PSFC/RR-12-1

Diagnosing Inertial Confinement Fusion Implosions at OMEGA and the NIF Using Novel Neutron Spectrometry

D. T. Casey

January, 2012

Plasma Science and Fusion Center
Massachusetts Institute of Technology
Cambridge MA 02139 USA

This work was supported in part by the U.S. Department of Energy (DE-NA0000877 and DE-FG52-09NA29553), the Fusion Science Center at the University of Rochester (PO #415023-G, UR Account #5-24431), the Laboratory for Laser Energetics at the University of Rochester (414090-G), and the Lawrence Livermore National Laboratory (B580243).

Diagnosing Inertial Confinement Fusion Implosions at OMEGA and the NIF Using Novel Neutron Spectrometry

by

Daniel Thomas Casey

B.S. Nuclear Engineering (2005)

University of New Mexico

SUBMITTED TO THE DEPARTMENT OF NUCLEAR SCIENCE AND ENGINEERING IN PARTIAL FULFILLMENT OF THE REQUIREMENTS FOR THE DEGREE OF

DOCTOR OF PHILOSOPHY IN NUCLEAR SCIENCE AND ENGINEERING

AT THE

MASSACHUSETTS INSTITUTE OF TECHNOLOGY

February 2012

Signature of Author:_____
Department of Nuclear Science and Engineering
February 15th, 2012

Certified by:_____
Richard Petrasso
Senior Research Scientist
Thesis Supervisor

Accepted by:_____
Ronald Parker
Professor of Nuclear Science and Electrical Engineering
Thesis Reader

Accepted by:_____
Mujid S. Kazimi
TEPCO Professor of Nuclear Science and Engineering
Chair, Department Committee on Graduate Students

Diagnosing Inertial Confinement Fusion Implosions at OMEGA and the NIF Using Novel Neutron Spectrometry

by Daniel Thomas Casey

Submitted to the Department of Nuclear Science and Engineering
on December 9, 2011, in partial fulfillment of the requirements for the degree of
Doctor of Philosophy

ABSTRACT

A novel neutron spectrometer, called the Magnetic Recoil Spectrometer (MRS), was designed, built, and implemented on the OMEGA laser facility and the National Ignition Facility (NIF) to measure the neutron spectra from inertial confinement fusion (ICF) implosions. Using the MRS, the down-scattered neutron (DSn) spectrum has been used to infer the areal density (ρR) of ICF implosions for the first time. The DSn technique is essential for diagnosing high ρR (>180mg/cm^2) cryogenic deuterium-tritium (DT) implosions, where most other methods fail. The MRS has helped to guide the cryogenic campaign toward the highest ρRs ever achieved at OMEGA. In addition, the MRS is currently being used to diagnose the DSn spectrum from cryogenic implosions at the NIF during the beginning phases of the National Ignition Campaign (NIC). MRS data have already been essential for tuning these implosions to the highest ρRs ever achieved in an ICF implosion (>1 g/cm^2), and thus for guiding the NIC toward the realization of thermonuclear ignition. The first measurements of the T(t,2n)^{4}He (TT) neutron spectrum in DT implosions at OMEGA have also been conducted using the MRS. The TT-neutron (TTn) spectrum was measured at low reactant central-mass energies of ~23 keV. The results from these measurements indicate that the TT reaction proceeds primarily through the direct three-body reaction channel, which is in contrast to the results obtained in higher energy accelerator experiments. Measurements of the TTn and DD proton yields were also conducted and compared to the DT neutron yield in DT implosions. From these measurements, it is concluded that the DD yield is anomalously low and the TTn yield is anomalously high, relative to the DT yield. These results have been explained by a stratification of the fuel in the core of an ICF implosion.

Thesis Supervisor:
Richard D. Petrasso
Senior Research Scientist
Plasma Science and Fusion Center,
Massachusetts Institute of Technology

Acknowledgments

First, I thank my advisor Richard Petrasso whose enthusiasm and scientific rigor are both motivating and, at times, even awe-inspiring. I also thank Johan Frenje, whose leadership of the OMEGA and NIF MRS projects directly led to their successful realization and whose supervision of my thesis research, was both supportive and educational. I also thank Johan for carefully reviewing this thesis manuscript. I am most appreciative for the many contributions of the entire high-energy-density physics division at MIT. This includes Fredrick Seguin, whose masterful experience and attention to detail was essential for many aspects of this project, including the development of the novel processing techniques of the MRS systems. I also thank Fredrick for his efforts in developing and maintaining the microscope and data analysis systems for all of the MIT diagnostics, including the MRS. I thank Chikang Li for always being available for questions and being supportive of this work. I thank Maria Gatu Johnson for developing powerful new analysis techniques and taking over most of the OMEGA and NIF MRS related responsibilities, while I was writing this thesis. I also thank my good friends Nathan Howard, Mario Manuel, Nareg Sinenian, (and so many others they cannot all be named here) for illuminating conversations both on physics and all facets of life. I also thank Jocelyn Schaeffer, Irina Cashen, Robert Frankel, and Ernie Doeg, who skillfully managed many aspects of the MIT etch/lab and are responsible for much of the data processing that was required to both commission the MRS diagnostics and perform the experiments described in this thesis.

This thesis work could not have been possible without the enormous support it received from LLE. The OMEGA operations, engineering, and scientific staff, along with their management, all supported this project. I thank David Meyerhofer and Craig Sangster for supporting the MRS projects, Vladimir Glebov for countless ride-along shot opportunities, Radha Bahukutumbi for enormous simulation support, and Michelle Burke and Joe Katz for managing the OMEGA MRS and the LLE etch/scan lab. I thank Jeff Ulreich and Bill Owens for providing the engineering support of the OMEGA MRS system. In particular, I also thank Sam Roberts, without whom, the OMEGA MRS would not have been successful. His experience and knowledge of OMEGA and its diagnostics are responsible for much of the success of this project. In addition, Sam's resilience and strength, after his terrible accident, will forever continue to inspire me.

At LLNL, I am very appreciative to Richard Bionta and Mark Mckernan for their support and for establishing and flawlessly running the LLNL MRS etch/scan lab. I also thank Mark for designing much of the NIF MRS detector hardware. I also thank Rick Ashabranner and Jason Magoon for their engineering support of the NIF MRS. I also thank Rick for his continued support of the NIF MRS. I also thank Dennis McNabb, whose involvement in the tt project contributed enormously to its success and fostered new collaborations in plasma nuclear science. I thank Ray Leeper at Sandia, for many insightful and entertaining conversations and for his continued interest in this work.

I thank my thesis reader, Professor Ron Parker, for reviewing this thesis, along with Professors Ian Hutchinson, Jeffrey Freidberg, and Miklos Porkolab for excellent courses in plasma physics and fusion energy.

I also thank my parents, Cheryl and Mike Horne, my brother Adam Horne, my Grandparents Don and Judi Horne and the many other members of my family, for their love, support, and pride, which inspired me to work hard. Lastly, and most importantly, I thank my beautiful and wonderful wife Maxine Casey. Her love and support during these long and arduous years of graduate school managed to make them the most rewarding and enjoyable years of my life.

TABLE OF CONTENTS

List of figures

1 - Introduction

Since the first people looked toward the sky, the power and wonder of the sun and stars, mystified humankind. Littered across a black canvas, twinkling stars rotated in familiar patterns, until the sun rose and banished the darkness of night. For thousands of years, people turned to religion and philosophy to help make sense of these celestial wonders. Even the great physicist Sir Isaac Newton, who was able to connect the laws of gravity on the ground to the celestial motion of planets and stars in our solar system, credited the source of the sun's energy to that of the divine.[1] The sun's mysteries lingered. In 1862, Lord Kelvin used a faulty estimate of the sun's age to argue against Charles Darwin's theory of evolution. Darwin estimated that the earth must be more than ~300 million years old, an estimate that was based on the erosion of the English Weald. This was a critical piece of his theory, as biological evolution required such long time scales. Kelvin, on the other hand, believed that the sun was powered by gravitational energy of primordial meteorites (as he realized no chemical reaction could suffice) and could not be more than a few tens of millions of years old. As Kelvin's argument was troubling to Darwin, he removed his discussion of time scales from the final editions of his book *On the Origin of the Species*.[2] It turns out though that Darwin's lower bound for the age of the earth was correct, as we now know the solar system formed some four billion years ago. Through evidence in the evolution of biological systems and geological erosion, both Darwin and Kelvin had unintentionally revealed that the current understanding of physics was insufficient to explain the apparent age of the sun. Something was missing.

The first piece of the puzzle emerged in 1905, when Einstein showed that mass and energy are equivalent through the famous equation $E=mc^2$.[3] A few years later in 1920, Aston measured the mass of the helium nucleus and found it weighed less than the sum of its constituents mass (two neutrons and two protons).[2] Immediately following, in that same year, Eddington realized that this difference in mass is the energy source of the sun, which fuses hydrogen into helium.[2, 4] Eddington could not, on the other hand, explain how the hydrogen nuclei overcome the Coulomb barrier and fuse into helium. This was instead provided by Gamow and his colleagues, who formulated a theory for quantum tunneling, which Atkinson and Houtermans recognized in 1929 to be the way for hydrogen nuclei to overcome the Coulomb barrier and fuse into helium in the center of the sun.[5] Three years later, fusion of light isotopes were first observed by Oliphant.[6] All this work laid the foundation to Bethe's seminal paper "Energy production in stars" in 1939,[7] for which he was awarded the Nobel Prize in 1967.

1.1Nuclear Energy

According to Einstein's famous equation $E= mc^2$, the energy released in the fusion process of light ions is simply related to the difference in mass between the reactants and fusion product(s). This mass difference is typically several MeV per nucleon (proton or neutron), making the energy released in fusion several orders of magnitude higher than in chemical reactions, which are fractions of eV/atom.[8] The underlying physics that dictates this mass difference is the strong

nuclear force, which increases the binding energy per nucleon with increasing mass number of the nucleus (A) for elements up to A=56 (Iron-56).[9] For elements heavier than Iron-56, the binding energy per nucleon starts to decrease due an increasing effect of the Coulomb repulsion. This means that breaking apart a heavier nucleus into lighter ones produces energy as well, which is called nuclear fission. This process can occur spontaneously if the nucleus is unstable enough. In Figure 1-1, the binding energy per nucleon[9] is plotted for the known range of elements. One striking feature is that the binding energy per nucleon is relatively flat (8-9 MeV/nucleon) for mass numbers above A~50.

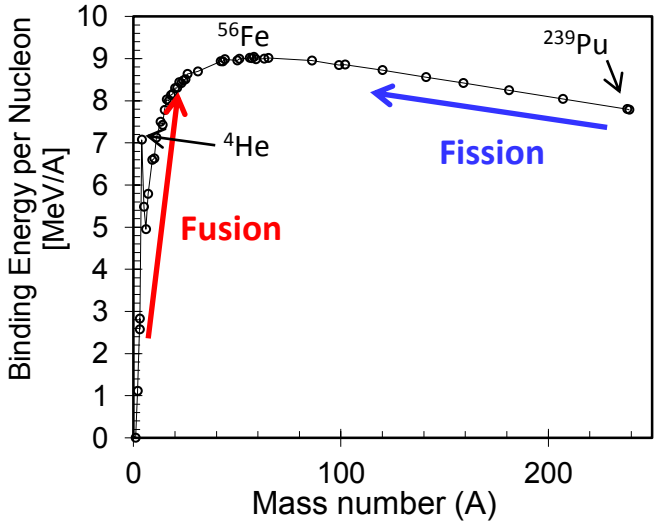

Figure 1-1: Binding energy per nucleon (MeV/A) as a function of mass number of the nucleus (A).[9] This curve illustrates that nuclear fusion of lighter elements, or nuclear fission of heaver elements, releases energy equivalent to the increased binding energy of the newly formed more stable nucleus or nuclei. As shown by the figure, the most stable element is ^{56}Fe.

1.2 Stellar nucleosynthesis

The formation of heavier nuclei through fusion is called nucleosynthesis. This process was initiated by the primordial big bang, which was responsible for the production of neutrons, protons, helium, and trace deuterium and lithium. All other nuclei are formed in stellar nucleosynthesis in stars either through the proton-proton (pp) cycle, CNO cycle, or through neutron capture.[10] The sun contains mostly hydrogen, which is gravitationally confined and supported by the heat and pressure generated by the thermonuclear-fusion process in its core. The pp cycle, which is the dominating reaction sequence in middle-aged yellow dwarf stars like our sun,[10] produces helium-4 from four hydrogen nuclei (protons) through a variety of intermediate reactions. Table 1-1 summarizes the important reactions in the pp cycle, which consists of four branches through which the hydrogen nuclei produce helium. Of particular interest is the neutrino emission along each branch, because a solar neutrino is the only direct observable of the sun's burning core. Other types of radiation emitted from the core are not directly observed, as they undergo numerous collisions before they reach the surface of the sun, which takes ~10^5 years.[11] For many years, the solar

nucleosynthesis models could not explain the solar neutrino flux, prompting doubts about the models and reaction cross-sections, until neutrino flavor oscillation was discovered to be source of the discrepancy.[10]

Table 1-1: Important reactions in the solar pp cycle, which is the main reaction sequence in yellow dwarf stars like our sun. In the pp cycle, four hydrogen nuclei (protons) fuse together through a variety of intermediate reactions to become one helium-4 nucleus. There are four branches that protons can follow to become a helium-4 nucleus. The reaction Q value for each reaction is indicated along with the pp-cycle branch.[10] It is noteworthy that the neutrino emission from each branch is the only direct observable that can be used to diagnose the sun's burning core, which makes solar neutrinos important to understanding stellar nucleosynthesis.

Reaction	Branch	Q (MeV)
$p + p \rightarrow D + {}^{+}\beta + \nu_e$	I-IV	0.4
$D + p \rightarrow He^3 + \gamma$	I-IV	5.5
$He^3 + He^3 \rightarrow \alpha + 2p$	I	12.9
$He^3 + He^4 \rightarrow Be^7 + \gamma$	II	1.6
$Be^7 + {}^{-}\beta \rightarrow Li^7 + \nu_e$	II	0.9
$Li^7 + p \rightarrow 2\,\alpha$	II	17.4
$Be^7 + p \rightarrow B^8 + \gamma$	III	0.1
$B^8 \rightarrow Be^8 + \beta + \nu_e$	III	17.0
$Be^8 \rightarrow 2\alpha$	III	2.9
$p + He^3 \rightarrow \alpha + {}^{+}\beta + \nu$	IV	18.8

1.3 Realization of thermonuclear energy on earth

From a net-energy production point of view, the most viable method for achieving fusion is to heat the fuel to high enough temperatures for significant fusion reactions to occur. This method is called thermonuclear fusion, which is the process that takes place in stars (the other method involves accelerators that produce "beam-target" fusion in cold solid targets. This method is not useful for energy purposes, as substantial amount of energy is transferred to the cold target by Coulomb scattering). By heating the fuel, the energy losses through Coulomb scattering are greatly reduced, as the Coulomb scattering just redistributes the energy among the ions rather than acting as a loss mechanism. Temperatures required for significant thermonuclear-fusion reactions to occur are in the keV range (1 keV= 1.16×10^7 Kelvin), at which the fuel is in a plasma state.

Several criteria exist for a viable fuel in a future thermonuclear-fusion reactor. The most important ones are: low-Z ions must be used to reduce the Coulomb repulsion and probability for Coulomb scattering to a minimum; low-Z ions must be used to reduce the X-ray emission losses (fusion of higher-Z ions requires higher temperatures, which results in increased X-ray emission losses); and finally the fusion reactions need to be exothermic and thus release substantial amount

of energy. Reactions that fit these criteria involve the isotopes of hydrogen and helium, i.e., deuterium (D), tritium (T), and helium-3 (^{3}He). Table 1-2 summarizes the most important reactions involving these elements. Among these reactions, the DT reaction is the most promising one due to its highest cross-section at temperatures that can be readily achieved (see Figure 1-3). The DT reaction releases a total kinetic energy of 17.6 MeV carried by an alpha particle and a neutron.

Table 1-2: Most important reactions in a thermonuclear-fusion experiment. The Q value for each reaction is also shown. Due to its relatively high cross section at temperatures readily achieved, the DT reaction is the most promising candidate for thermonuclear ignition.

Reaction	Q (MeV)
$D + T \rightarrow \alpha + n$	17.6
$D + D \rightarrow T + p$	4.0
$D + D \rightarrow n + He^3$	3.3
$T + T \rightarrow \alpha + 2n$	11.3
$T + T \rightarrow n + He^5$	10.4
$D + He^3 \rightarrow \alpha + p$	18.4

Figure 1-2 shows the cross-sections for the reactions in Table 1-2 as a function of center-of-mass (CM) energy of the reactants. The figure also shows a few reactions in the pp cycle shown in Table 1-1. As illustrated in Figure 1-2, the DT cross-section is the highest at CM energies below ~100 keV, which is partly due to the resonance at ~64keV[12] (see Appendix A for a discussion of differential cross sections in the CM and laboratory systems). Due to the small cross-section for the pp reaction, stars like our sun burn slowly, producing energy for billions of years.

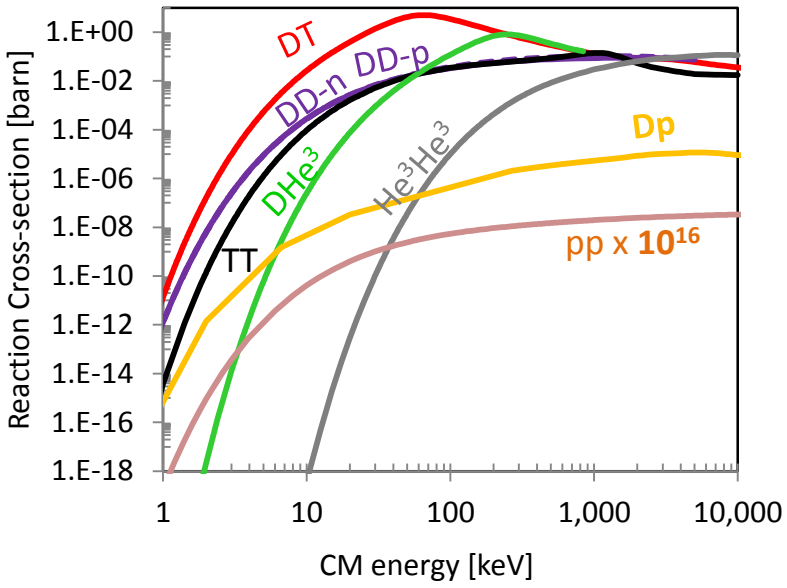

Figure 1-2: Reaction cross-sections as a function of center of mass (CM) energy in keV for commonly encountered fusion reactions, including those in the first branch of the solar pp cycle[13] [ENDF/B-VII.0 evaluated data (except pp which is generally regarded as too low to measure)].[14] The DT reaction is significantly higher at lower energies because of a resonance (~64keV),[12] making it an attractive reaction for controlled thermonuclear fusion. The pp reaction[15] is so much lower than the other reactions that it was multiplied by 10^{16} to fit on the graph.

To determine the power produced in a thermonuclear-fusion experiment, the first step is to calculate the reaction rate (R), which is a function of the reactant densities (n_1 and n_2) and the reactivity of the plasma $\langle\sigma v\rangle$[8] i.e.,

$$R = \frac{n_1 n_2}{1+\delta_{12}}\langle\sigma v\rangle. \tag{1-1}$$

Here, δ_{12} is the Kronecker delta used to prevent double counting of particles when n_1 and n_2 are the same reactant nuclei, and $\langle\sigma v\rangle$ is the cross section (σ) (shown in Figure 1-2), averaged over all relative velocities ($v = |\vec{v}_1 - \vec{v}_2|$) of the reactants, i.e., $\langle\sigma v\rangle = \int v\,\sigma(v) f_1(\vec{v}_1) f_2(\vec{v}_2) d\vec{v}_1 d\vec{v}_2$.[8] The reactivity can also be expressed as

$$\langle\sigma v\rangle = \sqrt{\frac{8}{\pi\, m_r}}\frac{1}{T^{3/2}}\int_0^\infty \sigma(E)\, E\, e^{-E/T} dE. \tag{1-2}$$

Here, E is the CM energy of the reactants. Equation (1-2) can be evaluated analytically[15] or numerically for a specified plasma ion temperature. Figure 1-3 shows the Maxwellian averaged reactivity as a function of the plasma ion temperature for the cross-sections shown in Figure 1-2. As expected, the DT reaction has the highest reactivity, making it the most likely candidate for the first ignition experiment and for the first-generation thermonuclear reactor.

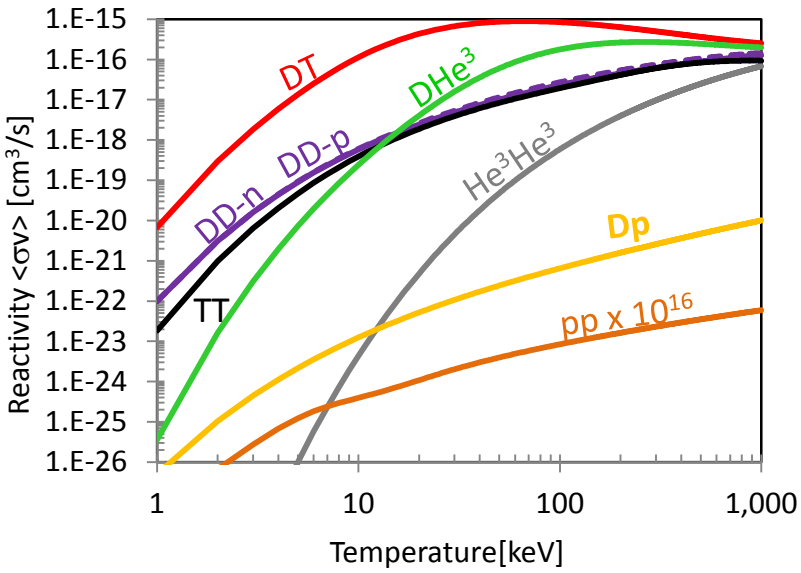

Figure 1-3: Maxwellian averaged reactivities as a function of ion temperature for reactions shown in Figure 1-2. [ENDF/B-VII.0 evaluated data (except for the pp reaction, which is generally regarded as too low to measure)].[13, 14]

As the Q value listed in Table 1-2, represents the energy released in a fusion reaction, the fusion power density (fusion power produced per unit volume) is determined by the reaction rate times the Q value, i.e.,

$$P/V = Q\frac{n_1 n_2}{1+\delta_{12}}\langle\sigma v\rangle\,. \tag{1-3}$$

Deriving the ignition condition for a fusion plasma can be done by balancing fusion power with the power losses, such as Bremsstrahlung and thermal conduction (or *pdV* expansion). Often referred to as the Lawson's criterion, the ignition condition is presented as a minimum product of density and confinement time (at some optimal temperature) at which the alpha heating can overcome the energy losses. Lawson's criterion states that $n\tau > 2\times10^{14}$ s/cm^3 at ~20keV.[16] Recent references[8, 17] have presented the ignition criterion as a product of the plasma pressure and the energy-confinement time requirement (equivalent to a $n\tau T$ criterion), illustrated by Equation (1-4).

$$P\tau > 8\ atm\ s \tag{1-4}$$

This expression indicates that a fusion plasma, or the energy in a fusion plasma, must be confined on a time-scale long enough for significant fusion reactions to occur or $\tau \sim \frac{1}{n} < \sigma v >$.[16] The sun's enormous mass m~2×10^{30} kg gravitationally confines the burning plasma by tremendous gravitational pressure balanced by the internal pressure.[10] The very long-energy confinement time in the sun is essential for a self-sustained burn, because the cross section for the pp reaction is extremely small, resulting in an extremely long average time between pp reactions. For thermonuclear fusion to be practical on earth, different confinement schemes must be applied. The most promising are magnetic confinement fusion (MCF), which uses powerful magnetic fields to

confine the plasma, and Inertial Confinement Fusion (ICF) where the plasma is confined by its own inertia over a short period of time. MCF will not be discussed further in this thesis but the interested reader is referred to several excellent textbooks on the subject.[8, 18]

1.4 Historical remarks on Inertial Confinement Fusion (ICF)

During World War II, when the first fission weapon was developed under the code name "Manhattan project," Teller and others realized that a fission bomb could potentially be used as a primary driver to implode a secondary thermonuclear-fusion package (which was initially called the "Super"). In 1949, when former Soviet Union detonated their first fission bomb, President Truman ordered an accelerated development of the thermonuclear-fusion bomb. This led to the United States' first test of a thermonuclear bomb on November 1, 1952. The Soviets were not far behind, as demonstrated by their first test in 1953.

The foundation of thermonuclear weapons rests on the concept of ICF, but to utilize the energy released for peaceful purposes (as an energy source), the energy output must be reduced roughly ten million times. This requires a radically different implosion driver, as the fission bomb cannot be appropriately scaled down.

With the realization of the first laser in 1960,[16] it was not long after when researchers at the Lawrence Livermore National Laboratory (LLNL) recognized that a laser could be potentially used as a driver for ICF. The first unclassified paper on ICF was written by Nuckolls in 1972,[19] in which he described a system where several lasers are used to implode a 1-mm sized spherical capsule to high densities and temperatures for significant thermonuclear fusion to occur. The main concepts of ICF and many of the original issues that were identified in that paper are still relevant today. However, that paper did predict that ignition would be achieved with a 1kJ driver (predictions today are ~1 MJ).[16, 19, 20] After Nuckolls paper, a substantial ICF program was established at LLNL. In 1976, the Argus laser was built to study laser-plasma interactions, and in the following year, the Shiva laser was built to demonstrate target compression using laser drivers. The results of these efforts led to the development of the NOVA laser in 1985, at which the first fully integrated indirect-drive experiments began. The experience gained from the NOVA effort paved the way for a larger MJ laser facility known as the NIF,[21] which was completed in 2009. In parallel with the LLNL program, the Laboratory for Laser Energetics (LLE) at the University of Rochester started an ICF program in the 1970s. The ZETA laser, built in 1978, was a six laser-beam prototype of the OMEGA 24 system, which was completed in 1980. OMEGA 24 was built to study spherical direct-drive compression of ICF capsules. The OMEGA-24 system was upgraded in 1996 to the OMEGA-60 system to achieve better uniformity and to validate the direct-drive approach to achieving ignition.[22] Much of the data obtained and described in this thesis were taken at OMEGA and the NIF. As these ICF laser facilities produce temperatures that are hotter than the core of sun and densities that are ~1000 times higher than solid density, specially designed diagnostics are required to probe these extreme conditions.

1.5 Thesis Overview

This thesis discusses a novel neutron spectrometer, called the Magnetic Recoil Spectrometer (MRS),[23-25] for diagnosing ICF-capsule implosions at OMEGA and the NIF. The primary objective with MRS is to measure the absolute neutron spectrum from which fuel assembly (areal density), ion temperature, and neutron yield (or "fusion energy" output) can be directly determined. Information about these parameters is essential for understanding the implosion performance. The MRS was first built, installed, and commissioned on OMEGA in 2007 to comprehensively test the technique and to bring a required diagnostic to the OMEGA cryogenic program.[26] In addition, the MRS has been uniquely used on OMEGA to address fundamental nuclear and plasma-physics questions, as discussed in this thesis. Another MRS was implemented and performance qualified on the NIF in 2010 to support the National Ignition Campaign (NIC).

Chapter 2 introduces the basic concepts of ICF. It also discusses OMEGA, the NIF, and the diagnostics used on these facilities.

Chapter 3 describes the nature of the ICF neutron spectrum and the information about the implosion that is carried by the spectrum. The principles of how charged particle data from low-ρR implosions can be used to validate the MRS data are also discussed.

Chapter 4 describes the basic principles of the MRS, and it elaborates in detail about the modeling of the MRS response function. This chapter also discusses measurements and modeling of the neutron background around the MRS and the optimal polyethylene-shielding design for the diagnostic on OMEGA and the NIF. This effort involved detailed characterization of the response functions for the different MRS configurations, using the Geant4 code; characterization of the fluence and spectrum of background neutrons at the MRS; and the design of the polyethylene shielding around both MRS systems. This work will be submitted to Rev. Sci. Instrum. in the paper D.T. Casey *et al.*

Chapter 5 presents measurements of the absolute primary DT neutron yield conducted with the MRS. These results are contrasted to other measurements at OMEGA and the NIF. This work will be submitted to Rev. Sci. Instrum. in the paper D.T. Casey *et al.* .

Chapter 6 describes the coincidence counting technique (CCT) that was developed to reduce the background in the MRS data (on both OMEGA and the NIF) to the required level for measurements of weak features in the emitted ICF-neutron spectrum, such as the down-scattered neutron (DS-n) component. The principle, implementation, and validation of the CCT are in particular discussed in this chapter. It also discusses the statistical uncertainty of the DS-n measurements at OMEGA and the NIF when utilizing the CCT. As an array of CR-39 is used as detectors in the MRS, the principal sources of background are neutron-induced tracks and intrinsic tracks (defects in the CR-39). Using the CCT, it was demonstrated that this type of background is reduced by a couple of orders of magnitude, which well exceeds the requirement for the DS-n measurements at both facilities. This work was published in the paper D.T. Casey *et al.*, Rev. Sci. Instrum. 82, 073502 (2011).[27]

Chapter 7 describes the MRS measurements of the DS-n spectrum, from which the areal density (ρR) is inferred and used to diagnose cryogenic DT implosions at OMEGA and the NIF.[26] As there are currently no other ways to diagnose ρR values larger than ~200 mg/cm^2 at OMEGA,[25] the ρR data obtained with the MRS have been essential for understanding how the assembly of the fuel occurs and for guiding the cryogenic program at OMEGA to ρR values up to ~300 mg/cm^2 .[26, 28] The MRS on the NIF has also provided data that have been critical to the progress of the NIC towards the goal of achieving thermonuclear ignition and net energy gain. Recent data obtained with the MRS in September 2011 indicate that the implosion performance, characterized by the Experimental Ignition Threshold Factor (ITFX),[29] has improved about 50× since the first cryogenic shot a year earlier. This work has been published in the following papers: J.A. Frenje *et al*., Rev. Sci. Instrum. 82, 073502 (2008);[24] J.A. Frenje *et al*. Phys. Plasmas 16, 042704 (2009);[30] V.N. Goncharov *et al*., Phys. Rev. Letters 104, 165001 (2010);[28] J.A. Frenje *et al*., Phys. Plasmas 17, 056311 (2010);[25] and T.C Sangster *et al*., Phys. Plasmas 17, 056312 (2010).[26]

Chapter 8 discusses the use of the MRS for novel studies of the T(t,2n)^{4}He reaction, which is an important mirror reaction to the ^{3}He(^{3}He,2p)^{4}He solar fusion reaction. The first high-resolution measurements of the TT neutron spectrum using high-energy-density-laboratory plasmas are presented in this chapter. As these spectra were obtained for a low average TT reactant energy of ~23 keV, which is the same as the solar peak reactant energy for the ^{3}He+^{3}He reaction, the results provided important nuclear-physics implications for the ^{3}He(^{3}He,2p)^{4}He solar fusion reaction. This work will be submitted to Phys. Rev. Letters in the paper D.T. Casey *et al.*

Chapter 9 discusses measurements of the D(d,p)T (DD) and T(t,2n)^{4}He (TT) reaction yields and how they compare to measurements of the D(t,n)^{4}He (DT) reaction yield in an ICF implosion. From these measurements, it was concluded that the DD yield is anomalously low and the TT yield is anomalously high relative to the DT yield, an observation most likely caused by stratification of the fuel in the implosion core. This effect may be present in ignition experiments planned on the NIF, potentially resulting in a more restrictive ignition threshold. This work was accepted for publication in *Phys. Rev. Letters* in the paper D.T. Casey *et al.*

Chapter 10 summarizes the thesis and presents some concluding remarks.

Appendix A discusses nuclear cross-sections and provides the relationships between center-of-mass and laboratory reference frames. Appendix B discusses the astrophysical S-factor parameterization of cross-sections, the reactant energy distributions for thermonuclear reactions, and the effects of electron screening. A summary of the down-scattered neutron data obtained at OMEGA is provided in Appendix C and at the NIF in Appendix D. Appendix E is a summary of the TT neutron data obtained at OMEGA. Appendix F describes the fitting algorithm used with MRS data. Appendix G provides a description of the coincidence counting analysis code, which was developed to process data according to the techniques described in Chapter 6. Appendix H discusses hydrodynamic simulations[31] of several OMEGA implosions relevant to this thesis.

2 - Inertial Confinement Fusion (ICF)

This chapter focuses on the concepts of ICF. Section 2.1 derives the ideal ignition conditions. In Section 2.2, different ICF-drivers are discussed. Section 2.3 elaborates on the challenges involved in achieving ignition. Section 2.4 provides details about the OMEGA laser facility, and section 2.5 discusses the NIF, which is the premier operational facility for ICF implosion experiments. A brief discussion of the diagnostic techniques for diagnosing the implosion is discussed in Section 2.6.

Additional reading on the physics of ICF can be found in the book "The physics of Inertial Fusion" by Atzeni and Meyer-ter-vehn.[16] In addition, a review of the principles of ICF ignition and a comparison to MCF can be found in the paper by Betti et al.[17], and a thorough discussion of ignition at the NIF can be found in the paper by Lindl et al.[32, 33]

2.1 Ideal ignition condition in ICF

In ICF, the energy-confinement time is essentially the time it takes for the burning core to disassemble itself. The disassembly time scales as: $\tau \sim R/3C_S$, where R is the fuel radius and C_s is the speed of sound. The fuel has typically a radius of ~50 μm and temperature of ~10keV, which corresponds to $C_s \sim 10^8$ cm/s, resulting in a confinement time τ of ~10 ps. It will be shown later that τ is linearly proportional to the ρR (see Equation (2-2)), which can be determined experimentally. For this reason, the ρR parameter is of critical importance in ICF. The ρR is typically expressed as

$$\rho R = \int_0^R \rho \, dr \tag{2-1}$$

Here, ρ is the fuel density. The relationship of ρR to the energy-confinement time (Equation(2-2)) is shown by first expressing pressure in terms of ion density n and temperature T ($P = 2nT$), and mass density ρ in terms of n ($\rho = n/\bar{m}$), where $\bar{m}$ is the average ion mass ($\bar{m}$=4.2×10^{-24} g for equimolar DT). Next, by using the confinement time $\tau \sim R/3C_S$, and $C_s \sim 3\times10^7 T^{1/2}$ (where T is given in keV) gives:[16]

$$P\tau \sim 2nTR/3C_s \sim \frac{2}{3}\rho R\, T/\bar{m}C_s \tag{2-2}$$

Incorporating Equation (2-2) into Equation (1-4) results in the inequality $\rho R > 0.3$g/cm^2, which is coincidentally near the range of the 3.5 MeV alphas that must be stopped (a necessary condition) to setup a self-sustaining burn.[17] In other words, achieving highest possible ρR is a prerequisite for an effective burn or high burn fraction (f_b) of the fuel. f_b in an ICF implosion can be derived from the reaction rate equation (Equation (1-1)) and expressed as

$$f_b = \frac{\rho R}{\rho R + 6 g/cm^2}. \quad (2\text{-}3)$$

Here, it is assumed that the plasma is at a temperature of ~10 keV. Equation (2-3) shows that efficient burn requires high compression and high ρR. For example, to burn 1/3 of the available DT fuel in a high gain implosion, the required ρR is ~3g/cm^2, which is an order of magnitude higher than the alpha particle range.

Ignition and self-sustaining burn occur when plasma self-heating (energy deposited from alpha particles) exceeds all energy loss mechanisms. The energy loss mechanisms in ICF are somewhat different from those in MCF. For example, thermal conduction and Bremsstrahlung loss, used in the derivation of Equation (1-4), are less important than the *pdV* expansion loss in an implosion.[16, 17, 34] These energy losses are treated by Betti et al.[17] who used 1D simulations to determine a power-law fit of the measurable burn-averaged ρR (in g/cm^2) and ion temperature T_i (in keV) necessary to achieve ignition (shown in Equation (2-4)).

$$\rho R \left(\frac{T_i}{4.4} \right)^{2.2} > 1 \ . \quad (2\text{-}4)$$

Equation (2-4) shows that high ρR and high T_i are required simultaneously to achieve ignition. For more details, the interested reader is referred to the papers by Zhou et al.[34] and Betti et. al.,[17] who describes an alternative analytical derivation of this ignition condition. Other references also discuss the required conditions for ignition both generally and in indirect-drive and fast ignition.[16, 32, 33] Betti et al.[17] have also extended this ignition condition to 3D by using measured yield (Y_{3D}) over calculated clean yield (Y_{1D}), which embodies 3D effects, such as Raleigh-Taylor (RT) mix that reduces the radius of the hot spot. However, this assumes that the 3D effects explain the discrepancy between the simulation and experiment. The underlying physics that govern ignition can be studied at ρR*'s* and T_i*'s* lower than this requirement. This can be done by using energy-scaled hydrodynamic implosions,[28, 32, 34, 35] which is important as few laser facilities have the potential of achieving ignition. Smaller laser facilities can therefore be used to study ignition conditions without actually igniting an implosion. Figure 2-1 shows a curve (black arrow) of a hydro-equivalent-implosion scaling with increasing laser energy (E_L). The starting point (black data point) is the energy-scaled implosion at ρR~0.3g/cm^2 and T_i~3.5keV that is obtained for a laser energy of E_L ~23kJ typically used on OMEGA. This implosion will marginally ignite in 1D for a ρR~1.0g/cm^2 and T_i~4.0keV when the laser energy is E_L~0.7MJ (this energy will be readily achieved on the NIF when operated in the polar-direct drive (PDD) configuration). To reach ignition, it is clear from Equation (2-4) that high compression and thus high ρR is required. Highest possible compression is achieved through an adiabatic (or isentropic) compression, which obeys $\rho/\rho_0 = (P/P_0)^{5/3}$ relationship, where ρ and P are the final density and pressure, respectively.[16] In contrast to isentropic compression, which in principle can lead to arbitrarily high compression, shock-induced compression is limited to $\rho/\rho_0 < 4$ because the remainder of the shock energy is lost to heating the plasma (raising the entropy) rather than compressing it. A common measure of compressibility (or the entropy) in an ICF implosion is the adiabat (α), which is defined in Equation (2-5) as the pressure (P) divided by the Fermi-degenerate pressure ($P_{deg} \propto \rho^{5/3}$),[16]

$$\alpha = \frac{P}{P_{deg}}. \tag{2-5}$$

In an isentropic compression, α is kept to a minimum, resulting in highest possible compression though *pdV* work. In principle, isentropic compression can be achieved through a carefully shaped continuously rising laser pulse, designed to gently compress without launching strong shocks. However, these continuous laser pulses have proven problematic to experimentally implement.[28] As an alternative, nearly isentropic compression can also be achieved through a sequence of carefully timed shocks using a multi-picket or multi-step laser pulse.[16, 28, 29, 32, 33] This is done by carefully timing a sequence of shocks to reach high compression.

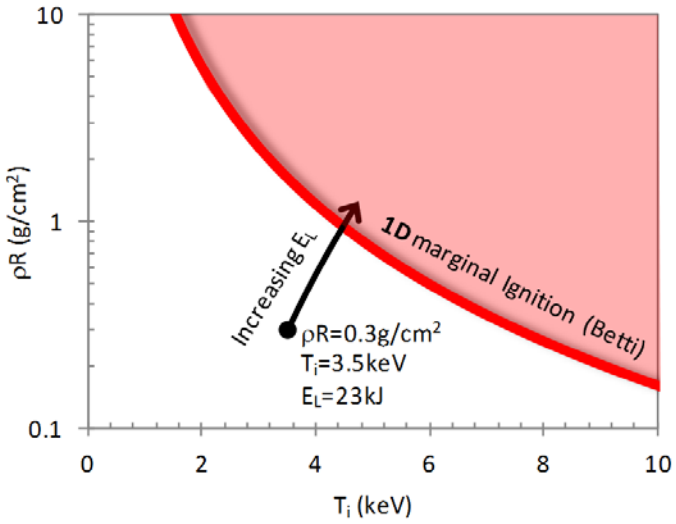

Figure 2-1: 1D-marginal ignition (red solid curve) as a function of ρR and ion temperature T_i (Equation (2-4)). These numbers are burn averaged ρR and T_i values required for self-sustained burn of the DT fuel in an implosion. The black data point represents an energy-scaled implosion, producing a ρR of ~0.3g/cm^2 and T_i~3.5keV for a laser energy of E_L ~23kJ. These numbers are the current goal of the cryogenic campaign at OMEGA.[26] The arrow shows a hydro-equivalent energy scaling[34] (described in more detail in the text) to a laser energy of E_L~0.7MJ[28] at which the implosion is predicted to marginally ignite at a ρR of ~1.0g/cm^2 and T_i~4.0keV. This laser energy will be readily achieved at the NIF operated in polar-direct-drive configuration.

2.2 ICF drive configurations

There are two main implosions schemes in ICF, which drive the capsule to high compression; namely direct-drive and indirect-drive, as illustrated in Figure 2-2. In the direct-drive scheme, the laser beams directly illuminate the capsule in a spherical geometry, and in the indirect-drive scheme, laser beams irradiate a cylindrical hohlraum, which produces x-rays that irradiate and implode the capsule. Direct-drive has better energy coupling to the capsule than indirect-drive, while indirect-drive has better symmetry and reduced sensitivity to the Raleigh-Taylor instability than direct drive.

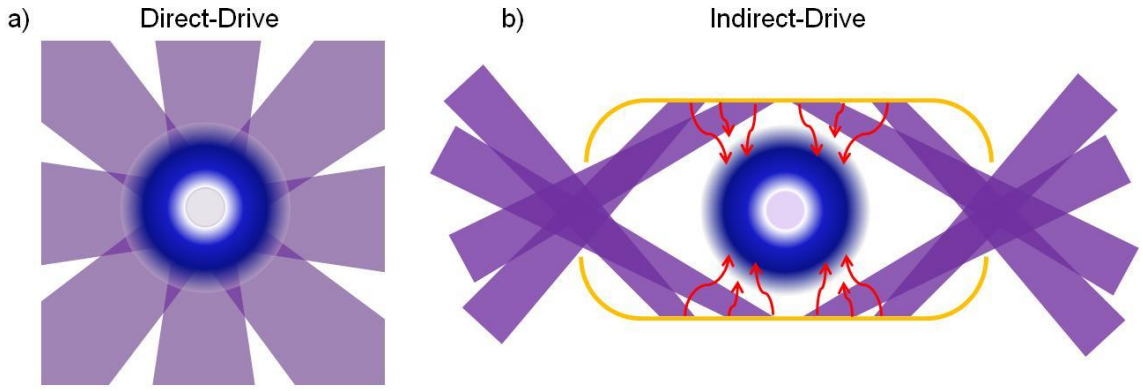

Figure 2-2: The two main implosion scenarios in ICF are direct-drive (a) and indirect-drive (b). In direct drive, the laser beams directly irradiate the capsule and in indirect drive, the laser beams produce x-rays in a cylindrical hohlraum, which irradiate the capsule. Unless otherwise specified, all experiments described in this thesis were performed using the direct-drive configuration (the only exception are cryogenic experiments at the NIF discussed in Chapter 7, which utilized indirect-drive).[16, 32]

In both direct and indirect-drive, the implosion process can be described as follows: the driver illuminates the capsule, ablating the outer part of the capsule shell, while the remaining shell compresses and eventually starts imploding inward. In the initial phase of the implosion, the shell accelerates, followed by a coasting phase and a deceleration phase. The implosion decelerates from the increasing internal pressure, and if some of the shell remains, it eventually stagnates at which time the peak fuel density and temperature have been achieved. At this time, the core temperature and density are high enough for thermonuclear-fusion reactions to occur. The internal pressure (tens of Gbar) will subsequently disassemble and quench the burn. Figure 2-3 illustrates the main phases of the implosion process.[16, 32]

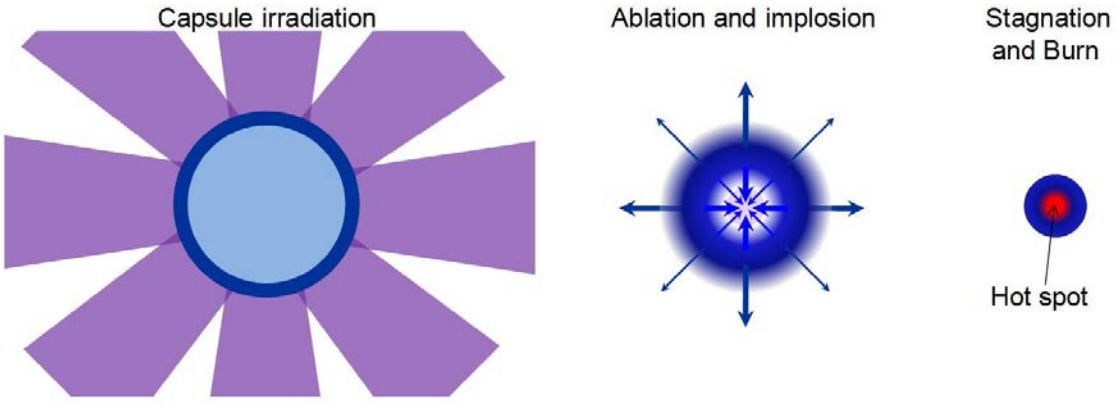

Figure 2-3: Illustration of the three main phases of the capsule-implosion process. Lasers or x-rays irradiate the capsule, ablating away the outer part of the shell. The remaining inner part of the capsule implodes inward, compressing and heating the core. A series of carefully timed shocks, coalesce at the inner surface of the high-density shell and propagate to the center of the implosion where they heat the hotspot just before stagnation, providing for significant fusion reactions to occur. A burn wave, supported by the DT alphas, then propagates through the main fuel.

2.3 Challenges in ICF

The ICF community is currently preparing to conduct the first credible ignition attempts at the NIF, and the word attempt is chosen to emphasize the challenges involved in these efforts. Issues such as, energy coupling, shock-timing, drive asymmetries, and hydrodynamic instabilities, must all be understood before ICF thermonuclear ignition can be realized. Understanding laser-plasma interactions is essential to efficiently deliver energy from the laser to the capsule. When the laser interacts with the capsule, it deposits energy at a critical density (also referred to as the critical surface), which is some distance away from the ablation front. The energy transport from the critical surface to the ablation front therefore relies on electron heat conduction. Laser-plasma instabilities can cause some of that energy to be reflected, reducing the capsule performance or producing hot electrons that deposit their energy past the ablation front, pre-heating the main part of the fuel and preventing effective compression. To understand how the energy flows from the critical surface to the ablation front, the electron heat conduction must be well understood. Recently, non-local heating models have been developed, which have improved the simulations of energy transport and subsequent mass assembly.[36] Comparisons between simulated and measured ρRs in implosions have been used to benchmark the energy-transport models.

Understanding shock timing is an essential prerequisite for achieving maximum compression in an implosion experiment. Poorly designed shocks, both in terms of timing and strength, may result in excessive shock heating, which raises the adiabat and severely limits the compression. Carefully shaped continuous laser pulses have also proven very difficult to implement due to the formation of a strong shock after a steepening of the compression wave that is not predicted in simulations.[16] One way to address this issue is to use a series of laser pickets before the main drive instead of a continuous low-adiabat laser pulse. These multi-shock laser pulses, which accurately launch the shocks, have been designed at OMEGA[28] and the NIF[33] (OMEGA and the NIF are discussed in the next sections) to compress the capsule. The optimal design of a laser-pulse shape is determined from a combination of efforts, such as direct measurements of the shock-timing[37] using VISAR,[37] and in fully integrated cryogenic experiments[26, 38] using measurements of ρR.

Hydrodynamic instabilities, such as the Raleigh-Taylor (RT) instability, must be considered as well in ICF. The RT instability occurs when the interface of two fluids, with different densities, accelerates toward the heavier fluid, which causes perturbations to grow in time. The RT instability threatens the implosion during the acceleration of the shell by the lighter ablator pushing the denser shell, and during the deceleration of the shell by the lighter fuel just before stagnation. Defects in the capsule and non-uniformities in the drive will cause RT growth, causing the cold shell-material spikes to quench some of the burning core and reduce (or eliminate) the effective hot spot. In severe cases, the RT instability can tear the shell apart and significantly truncate the implosion. The RT instability is primarily driven by high-mode non-uniformities, such as capsule imperfections and speckle pattern in a single laser-beam intensity (in the case of direct drive), while compression asymmetries are driven primarily by the overall laser-drive asymmetries. For example, capsule offsets due to vibration of the positioning system can lead to significant asymmetric laser drive, which reduces the compression and generates large compression asymmetries. These asymmetries can be probed by measuring the implosion ρR at different lines-of-sight using different diagnostics.

These physics challenges must be overcome before the implosion will ignite. As decades of experimental and theoretical work have significantly improved our understanding of these and other challenges, we are now in the position to finally start exploring conditions for ignition in an ICF implosion.

2.4 The OMEGA laser facility

The OMEGA laser facility at the LLE at the University of Rochester is a 351nm, 30kJ, 60 beam laser, which is capable of running in both direct and indirect drive.[22] The recently upgraded facility includes the OMEGA-EP laser, which is capable of delivering 1kJ in 1ps for advanced radiography and fast-ignition experiments. The OMEGA-EP laser operates independently but can also be directed into the OMEGA chamber for integrated experiments.[39] A large fraction of the experiments described in this thesis were performed at the OMEGA laser facility.

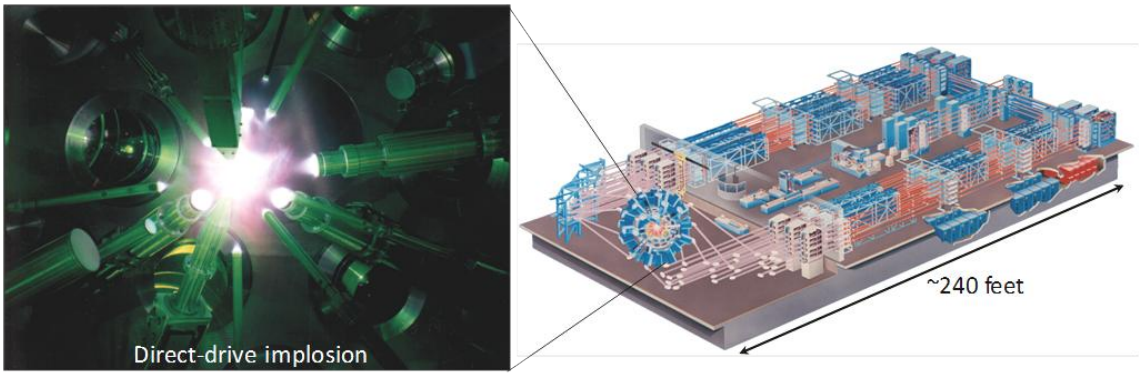

Figure 2-4 A diagram of the OMEGA laser facility at the Laboratory for Laser Energetics (LLE).[22] This 60 beam, 30kJ laser system implodes capsules in a spherical target chamber. An image of a direct-drive implosion is shown to the left (Images taken by LLE).

The spherical target chamber, which is made of aluminum, has a 1.56m inner radius with 92 laser and diagnostic ports. A schematic illustration of the chamber is shown in Figure 2-5. The laser ports are shown in red and the diagnostics ports relevant to this thesis are labeled. The ten-inch-manipulator (TIM) is a generic insertion module used to place diagnostics at precise locations inside the target chamber. The CPS1 and CPS2 diagnostics are the magnet based charged particle spectrometers discussed further in Chapter 3. The Magnetic Recoil Spectrometer (MRS), which is highlighted in yellow, is the diagnostic used for most of the data discussed in this thesis.

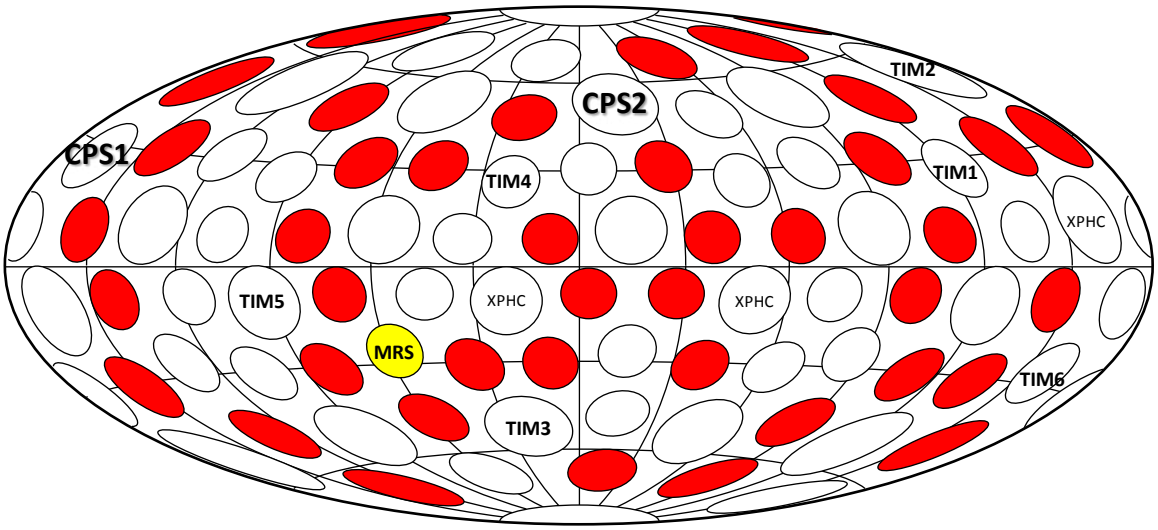

Figure 2-5: Schematic drawing of the OMEGA target chamber, illustrating laser and diagnostic ports. The red circles are the laser ports and the yellow port is for the MRS. The location of the CPS diagnostics and TIMs are also labeled. (Diagram from LLE)

2.5 The National Ignition Facility (NIF)

The NIF, at the Lawrence Livermore National Laboratory (LLNL), is a 192 beam, 1.8MJ laser facility (see Figure 2-6), designed to achieve ignition and energy gain using the indirect-drive scheme (Polar-direct drive[40] and future direct-drive upgrade capabilities also exist).[41] The NIF target chamber is 5m inner radius with a wall thickness of 60cm (50cm of borated Gunite and 10cm of aluminum). A schematic of the NIF facility, and an image inside the target chamber is shown in Figure 2-6. The ports for the laser beams (marked red) and diagnostics are schematically shown in Figure 2-7. The port for the MRS is marked yellow. The Diagnostic Inserter Manipulator (DIM) has the same function at the NIF as the TIMs have at OMEGA. It is worth noting that there are only three DIMs on NIF.

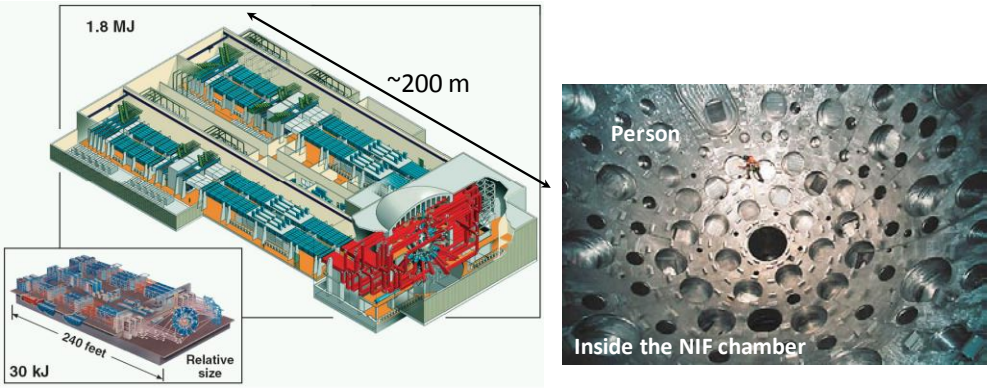

Figure 2-6: The National Ignition Facility (NIF) at the Lawrence Livermore National Laboratory is the most energetic laser in the world. This laser was built to demonstrate thermonuclear ignition and energy gain in a laboratory.[21] The NIF is a 1.8MJ laser with 192 laser beams, which are primarily configured in the indirect-drive configuration but can also be pointed in polar-direct-drive configuration (Images from LLNL).[40, 41]

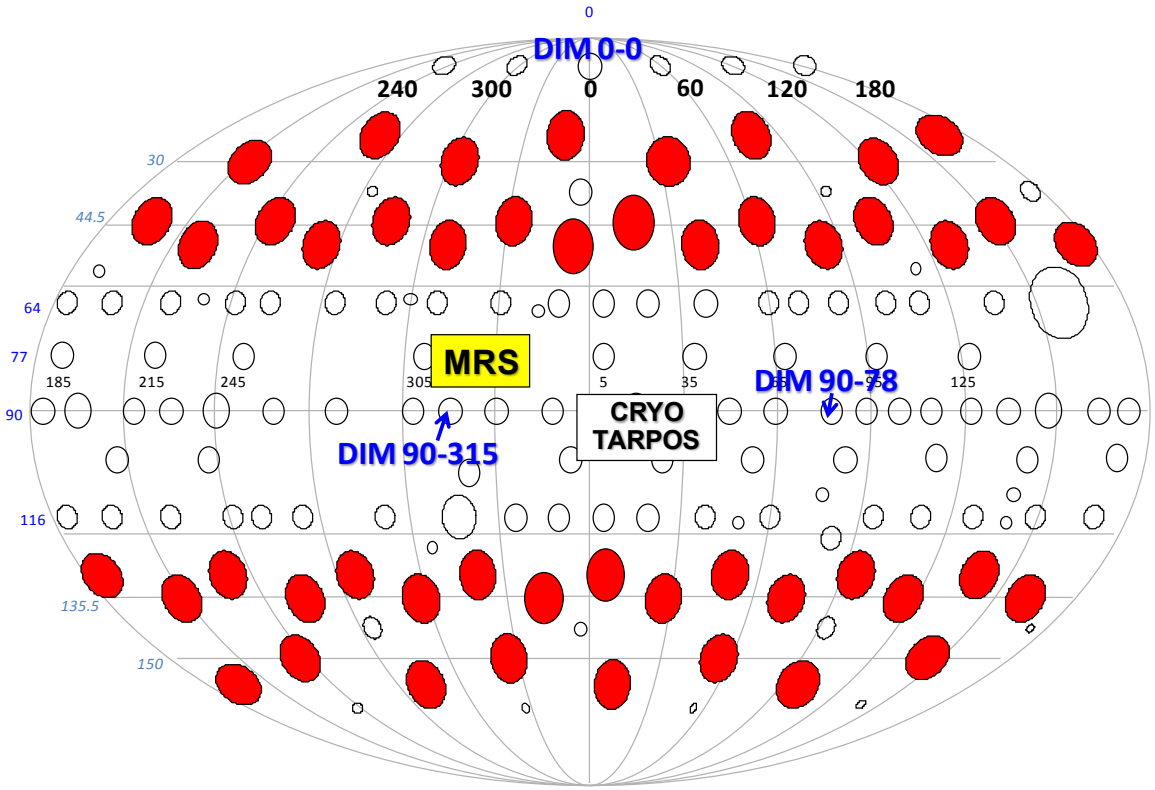

Figure 2-7: A schematic of the NIF target chamber with important locations highlighted (i.e. the MRS and DIM locations). Each red spot is a quad containing 4 laser beams. The MRS is located on the 77-324 line-of-sight, and the foil is inserted by the 90-315 DIM (Diagram from N. Izumi, LLNL). Because the NIF is an indirect-drive facility, the lasers irradiate the inside of the hohlraum from the top and bottom of the chamber.

Fully integrated target physics experiments began at the NIF in 2009. The first cryogenic THD implosion was conducted in September 2010, and the first cryogenic DT experiment was conducted in June 2011. At the time of writing this thesis, the first ignition attempt at the NIF was imminent (<1yr).

2.6 ICF Diagnostics

Diagnosing of an ICF implosion is critical for interpreting experimental success and for gaining insights of the underlying physics governing the implosion performance. At OMEGA, diagnostics such as X-ray, neutron, gamma-ray, and charged-particle techniques have been developed during decades of experiments. X-ray diagnostics are used to image the implosion using framing cameras and CCDs (or films),[42] to probe electron densities and temperatures in different regions of the implosion through the use of spectral measurements, and to determine X-ray bang time.[42] Nuclear-reaction yield, T_i, ρR, and bang time are measured by neutron diagnostics,[25, 43] which include techniques such as scintillator neutron time-of-flight (nTOF),[44] activation,[45] MRS,[24, 25] and streak-camera based particle temporal diagnostics.[46] Gamma rays can also be used for burn history and bang-time measurements.[47] Likewise, charged-particle diagnostics are used in the determination of reaction yields, ion temperature, and ρR.[48] Magnetic spectrometers, range filters,[48] radio-chromic film, and CVD (chemical-vapor-deposition) diamond detectors measure the charged particle emission[49] and in some cases spectra from implosions. Protons are also used for temporal measurements of the nuclear bang-time and burn width. Simulations are often used to predict the yield of a certain experimental configuration but rarely come close to predicting the actual yield observed in experiments. To fully diagnose an implosion, these different types of diagnostics are typically used simultaneously. The next chapter is devoted to charged-particle and neutron measurements.

3 - Probing ICF implosions using neutrons and charged-particles

Diagnosing ICF implosions is a non-trivial undertaking as the temperatures often exceed the core temperature of the sun and densities are often about 1000 times higher than solid-density. However, decades of work spanning many disciplines have established a solid suite of diagnostics capable of providing remarkable information about an ICF implosion. This chapter will, in particular, review how charged particles and neutrons can be used to diagnose an ICF implosion.[20, 25, 30, 43, 48, 50] Section 3.1 discusses briefly what implosion parameters can be determined from the primary DT neutron spectrum. Section 3.2 elaborates on what information is carried by the down-scattered neutrons. In Section 3.3, a more detailed discussion about the down-scattered-neutron measurement and how it relates to the implosion structure is presented. Section 3.4 discusses the complementary, well-established charged-particle measurements, which are often used to authenticate new types of measurements, such as the down-scattered neutron measurement.

3.1 Primary DT neutron spectrum and yield

The most likely fuel for the first ignited plasma in an ICF experiment and the first generation thermonuclear fusion reactor is the DT fuel. The DT reaction releases 17.6 MeV of kinetic energy, carried by an alpha particle (α) and a neutron (see Table 1-2). As discussed in detail in Appendix A, the neutron and α carry 80% and 20% of the kinetic energy released, respectively, when $T_i \ll Q$. When solving Equation (A-14) for thermonuclear reactants with Maxwellian energy distributions described by temperature T_i, the DT neutron spectrum broadens into a Gaussian distribution whose width is defined by T_i, as described by[51, 52]

$$f(E_n)dE_n \propto e^{-(E_n-\langle E_n\rangle)^2\frac{(m_n+m_\alpha)}{(4\,m_n\,T_i\langle E_n\rangle)}}dE_n. \tag{3-1}$$

Here, E_n is the neutron energy, m_n is the mass of the neutron, m_α is the mass of the α, and $\langle E_n\rangle$ is average neutron energy, which varies slightly with varying T_i (See Ballabio, et al.[53] for an empirical study of the $\langle E_n\rangle$ versus T_i dependence for different fusion reactions).[51] It is clear from Equation (3-1) that the Doppler broadened DT-neutron spectrum can be used to diagnose T_i ($T_i = 177\sigma_{DT}{}^2$, where T_i is in keV and σ_{DT} is in MeV).

The total number of DT neutrons released in an implosion is also called the DT neutron yield (Y_{DT}), which is the same as the DT reaction yield. In an ignited implosion, the DT α's are stopped, while the neutrons escape, carrying information about the condition of the implosion core and dense shell. Some of these neutrons will scatter in the fuel, providing additional information about the implosion, as discussed in the next section.

3.2 Down-scattered neutrons

Primary neutrons that elastically scatter and therefore lose energy in the fuel or shell (or high-density region) are called down-scattered neutrons (DSn). These DSn are the result of scattering processes in the high-density DT fuel or CH (or CD) plastic shell, where the primary neutrons lose energy to the charged particles in several types of processes, as summarized in Table 3-1. Either the neutrons can elastically scatter off hydrogen in the CH shell, producing scattered protons (or KO-p) with energies up to 14.1 MeV, or elastically scatter off the D and T fuel ions, producing knock-on deuterons (KO-d) and knock-on tritons (KO-t) with energies up to 12.5 MeV and 10.6 MeV, respectively.[20, 48] Some of the primary neutrons can also undergo inelastic n,2n reactions in D and T, producing protons and deuterons, respectively (at lower levels than the elastic scattering). As shown in Table 3-1, there are additional processes where primary neutrons elastically or inelastically scatter off C nuclei. In the latter process, kinetic energy of the neutrons goes into exciting the C nucleus (discussed further in Appendix A). Figure 3-1 illustrates the scattering of DT neutrons in the fuel and shell.

Table 3-1: Scattering processes of primary DT neutrons with the fuel and shell nuclei. Elastic-scattering processes produce charged particles called knock-on protons (KO-p), deuterons (KO-d), and tritons (KO-t). From the same reactions, elastically scattered neutrons or down-scattered neutrons (DSn) are produced and constitute a significant fraction of the ICF neutron spectrum.

Reaction	Observable	Inferable Quantity
$n + p \rightarrow n' + p'$	KO-p, DS-n	CH Shell ρR
$n + d \rightarrow n' + d'$	KO-d, DS-n	DT fuel ρR, CD Shell ρR
$n + d \rightarrow 2n + p$	DS-n, p	DT fuel ρR, CD Shell ρR
$n + t \rightarrow n' + t'$	KO-t, DS-n	DT fuel ρR
$n + t \rightarrow 2n + d$	DS-n, d	DT fuel ρR
$n + C \rightarrow n' + C'$	DS-n	CH Shell ρR
$n + C \rightarrow n' + C^*$	DS-n	CH Shell ρR

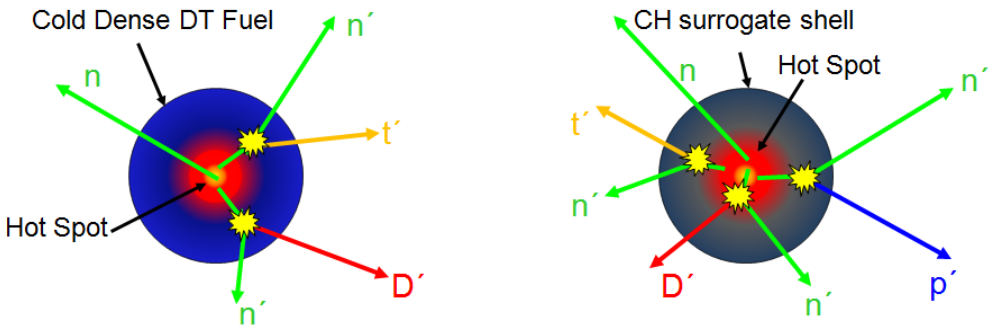

Figure 3-1: Primary DT neutrons produced in the implosion elastically or inelastically scatter off the fuel and shell nuclei, providing information about the amount of material, or the ρR, between the neutron source and the detector.

The DSn spectrum ($Y_{DSn}(E)$) can be expressed in terms of ρR and Y_{DT}, i.e.,

$$Y_{DSn}(E) = Y_{DT}\, N_a \frac{\sum_i \rho R_i \frac{d\sigma_i}{dE}(E) f_i}{\sum_i m_i f_i}. \tag{3-2}$$

Here, N_a is the Avogadro's number, m_i is the mass of the scattering nucleus, f_i is the atomic fraction, $d\sigma_i/dE$ is the differential cross section for the inelastic or elastic scattering process, ρR_i is the areal density of scattering material, i.e., ρR_{DT} for DT fuel, and ρR_{CH} for CH shell. The differential cross sections ($d\sigma_i/dE$) used here are calculated in Appendix A and presented in Figure A-2b for neutrons on carbon and Figure A-3b for neutrons on H, D, or T. It should be noted that the magnitude and shape of the DSn spectrum is to the first order defined by the radial-integrated ρR and differential cross sections for the different scattering processes (see Appendix A). Second-order effects, such as relative fraction of the different constituents in the fuel and shell, spatial ρR variations, and source size of the DT-primary neutrons, discussed in the next section, also play a role in defining the magnitude and shape of the DSn spectrum. The Y_{DSn} is determined by integrating the neutron spectrum over a specified energy range. Typically, Y_{DSn} is integrated over the energy range 10-12MeV to avoid the DT-primary-neutron and TT-neutron components, as shown and discussed in Figure 3-2. Evaluating Equation (3-2) for a low-density central DT fuel, surrounded by high-density DT shell for the specified energy range Y_{DSn} can be expressed as

$$Y_{DSn} \sim 0.05\, \rho R(g/cm^2)\, Y_{DT}. \tag{3-3}$$

The constant in Equation (3-3) will change if another energy range is used for the determination of Y_{DSn}. Figure 3-2 shows an example of a modeled ICF-neutron spectrum, which was constructed by assuming a T_i of 5 keV, ρR_{CH} of 50mg/cm^2 and ρR_{DT} of 10mg/cm^2. The thin solid curve represents the Doppler broadened DT-primary peak, the dashed curve represents the DSn component from the DT fuel, and the dotted curve represents the DSn component from the CH shell. As discussed in Appendix A, the shape of the DSn spectra is dictated by the well-known differential cross sections for the different processes. For instance, the structure observed for the DSn-CH component is primarily due to the differential cross section for inelastic scattering in carbon.

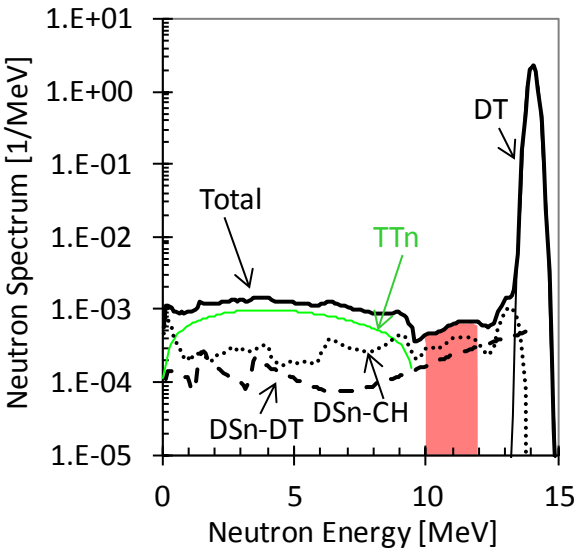

Figure 3-2: Modeled ICF-neutron spectrum for an implosion with a Ti of 5 keV, ρR_{CH} of 50mg/cm^2, and ρR_{DT} of 10mg/cm^2. The thin solid curve around 14.1 MeV represents the Doppler broadened DT-primary peak, the dashed curve represents the DSn component for the CH shell, the dotted curve represents the DSn component for the DT fuel, and the green curve represents the TTn spectrum, which limits the Y_{DSn} measurement to the energy range marked red. Measurements of the DSn spectrum are discussed in more detail in Chapter 7, and measurements of the TTn spectrum are discussed in detail in Chapters 8 and 9.

The TT reaction, shown in Table 1-2, releases an α and two neutrons, resulting in a broad TT-neutron spectrum (TTn) from 0-9.5 MeV, as shown in Figure 3-2.[54, 55] In the context of the DSn measurements at energies below 9.5 MeV, the TTn spectrum presents a background that needs to be well understood. Further discussions about measurements of the TTn spectrum are found in Chapters 8 and 9.

3.3 Path-integrated areal density (ρL) and its relation to ρR

The path-integrated areal density (ρL) determined from measurements is different from the radial-integrated ρR (Equation (2-1)), because ρL depends on the implosion geometry [i.e., primary-DT-neutron source and density profile ρ(r)] as described in detail by Seguin et al..[48] This needs to be considered when determining ρR_{fuel} and ρR_{shell} from the experimental data. To illustrate the significance of this effect, it is useful to look at the two extreme cases, i.e., the hot-spot model and the uniform model in which the fuel density is constant throughout the volume. In the hot-spot model, the primary DT-neutron source is entirely at the center, resulting in an integrated path length in the fuel that is the same as the radial distance through the fuel. In other words, $\rho L = \rho R$. In the uniform model, the primary DT-neutron source is evenly distributed throughout the fuel, resulting in an integrated path length that is 75% of the radial distance through the fuel. In this case, $\rho L = 0.75 \rho R$. Another scenario that is useful to look at, and perhaps more useful to describe in

the context of hot-spot ignition, is when the main-part of the fuel is distributed outside the primary DT neutron source. Then, the average path-length through the fuel is longer than the radial path length, resulting in the inequality $\rho L > \rho R_{shell}$. To account for these effects when determining the fuel or shell ρR in an implosion, simulated source and density profiles must be used. The neutron transport codes TART or MCNP[56, 57] are used to model the primary DT neutron source and to transport the neutrons through the density profile simulated by the 1D hydrodynamic code LILAC.[31] A comparison of DSn spectra calculated by using the hot-spot model and LILAC simulated source and density profiles is shown in Figure 3-3. This comparison shows that profile effects are subtle because the magnitude and shape of the DSn spectrum does not change significantly. It should be noted though that this modeling does not take into account 2D and 3D effects,[58, 59] which are considerably more complicated to address. However, as the solid angle for neutron scattering (which produces DSn) in the implosion is large,* the DSn measurements provide a decent average ρR, even when 3D asymmetries are significant.[26] Actual measurements of the DSn spectrum using the MRS are discussed in detail in Chapter 7.

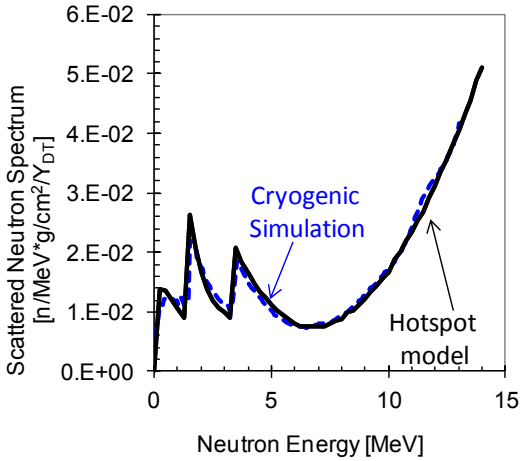

Figure 3-3 Calculated DSn spectra when using the hot-spot model, described in the text, and more realistic profiles for a cryogenic DT implosion at OMEGA. The 1D LILAC code [31]was used to calculate these profiles, which were used as input in the TART[56] modeling of the neutron transport through the fuel. As shown in the figure, the difference is subtle in this case because the cryogenic implosion produces a small primary DT neutron source.†

3.4 Charged-particle measurements for determination of ρL

Charged-particle techniques have been used extensively for decades to probe ρR in low to mediate ρR implosions.[30, 48, 60-63] These well-established techniques can therefore be reliably used

* The solid angle probed is ~20% of the total solid angle, when observing DSn in the range 10-12 MeV.

† This is not the case for all ICF implosions. For example, in cryogenic DT implosions at the NIF, these profile effects are important. This motivates use of the down-scatter ratio (DSR). DSR, which is equal to Y_{DSn}/Y_{DT}, removes the layer of modeling when inferring ρR from the data.

to authenticate new ρR techniques. This applies especially to the DSn measurement, as discussed thoroughly in Chapter 7. The reason for this is that the charged-particle measurement is a direct complement to the DSn measurement, as the elastically scattered charged particles and down-scattered neutrons are produced by the very same collision (see Figure 3-1). As shown in previous work,[30, 50,48, 50] ρR can be determined from the KO-d or KO-p yields as described by Equation (3-4) and Equation (3-5) below:[50]

$$\rho R \approx \frac{5\, m_p}{\sigma_{d\,eff}} \left(\frac{Y_{KO\text{-}d}}{Y_{DT}} \right), \tag{3-4}$$

$$\rho R \approx \frac{10\, m_p}{\sigma_{p\,eff}} \left(\frac{Y_{KO\text{-}p}}{Y_{DT}} \right). \tag{3-5}$$

Here, $\sigma_{p/d\ eff}$ is the effective cross section for proton or deuteron elastic scattering in the range of energies in which the knock-on yield is observed. The mass coefficients were evaluated for common fuel and shell compositions of f_T/f_D=1 DT for Equation (3-4) and f_H/f_C=1.38 for Equation (3-5).

3.4.1 Charged-particle diagnostics on OMEGA

A suite of charged-particle diagnostics have been used extensively over the last decade at OMEGA for diagnosing ICF implosions.[20, 48] Most of these diagnostics utilize CR-39, a clear plastic detector that is used for measurements of particles, such as alphas, protons, heavier ions, and neutrons. When implemented properly, CR-39 is also 100% sensitive to charged particles.[48] Besides being used in strictly charged-particle diagnostics, CR-39 is also used in the MRS to detect recoil deuterons (discussed in detail in this thesis). The insensitivity of CR-39 to x-rays, γ-rays, and electro-magnetic pulse (EMP) makes it ideal for the detection of charged-particles in the harsh environments at OMEGA and the NIF.

At OMEGA, two magnet-based charged-particle spectrometers (CPS1 and CPS2) have been used to diagnose a variety of implosions.[20, 48] These spectrometers cover a proton energy range of 0.1-30 MeV. As CR-39 is used in these spectrometers, both the track size on the CR-39 and the particle's gyroradius is used for particle identification and energy determination. This allows particles with the same gyroradius, such as protons and alphas with the same energy, to be separated. A CPS magnet is pictured in Figure 3-4. The CPS1 diagnostic, installed on the OMEGA target chamber, is shown in Figure 3-5. The CPS2 diagnostic during its installation on OMEGA is also shown in Figure 3-5.

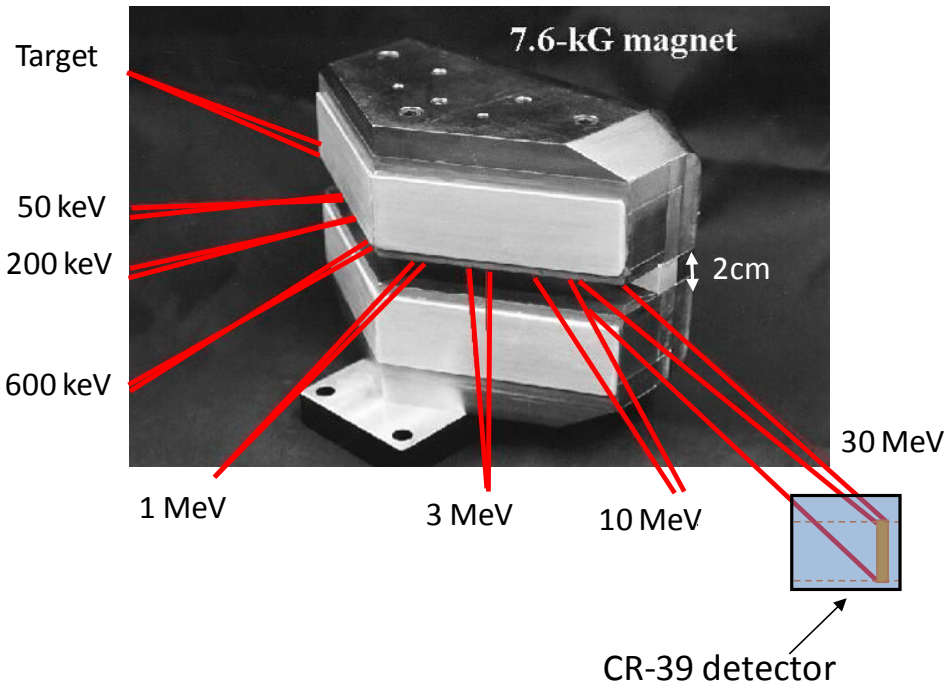

Figure 3-4: The Nd-Fe-B 7.6 kGauss permanent magnet for the charged-particle spectrometers (CPS1 and CPS2). This magnet disperses charged particles based on their momentum. A series of CR-39 detectors are used to detect charged particles from 0.1-30 MeV, proton equivalent energy. The locations and size of the induced tracks on the CR-39 detectors are subsequently used to determine particle species and to reconstruct the energy spectrum. More information about the CPS can be found in refs. Hicks and Seguin.[20, 48]

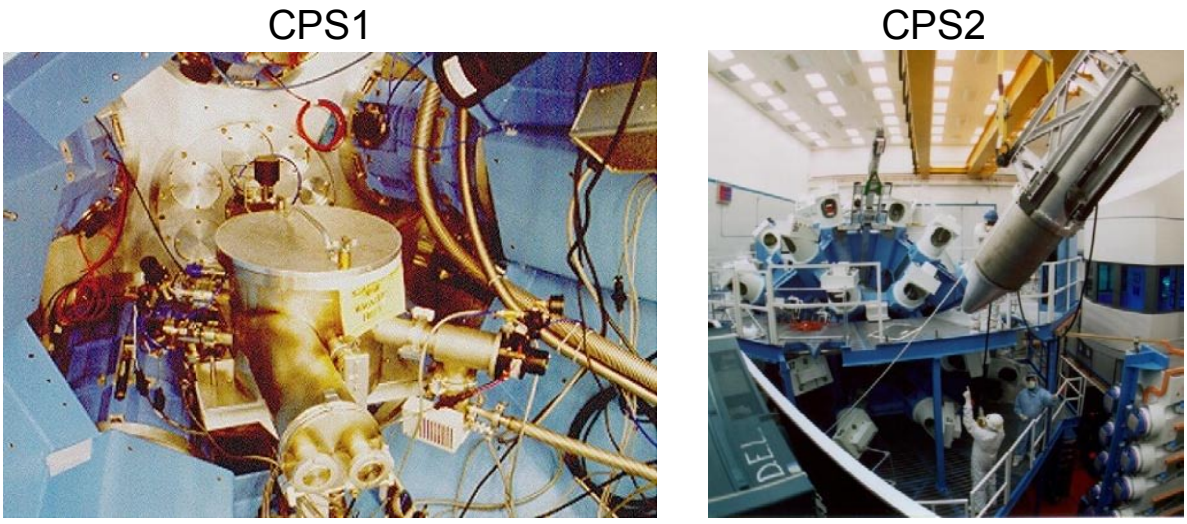

Figure 3-5: Left: the CPS1 spectrometer attached to the OMEGA target chamber. CPS1 is positioned 235cm from the implosion. Right: The CPS2 spectrometer as it is being hoisted and installed on the OMEGA target chamber. CPS2 is inserted inside the target chamber, allowing it to be positioned 100cm from the implosion.[20]

The wedge-range-filter spectrometer (WRF) is a compact proton spectrometer that consists of a aluminum wedge in front of a piece of CR-39.[48] Using the wedge thickness combined with well-known diameter versus particle energy relationship,[48] the proton energy spectrum can be determined. The passive and compact packaging allows the spectrometer to be fielded in a variety of ways (TIMs and NDIs at OMEGA and DIMs at the NIF), allowing several simultaneous measurements to be made in different directions.

The CPS and WRF diagnostics are ideal for measurements of the KO-p and KO-d spectra, which compliment the DSn measurements discussed at the beginning of this chapter. The CPS and WRF diagnostics have been used with much success in this regard.[20, 48, 50] Examples of measured KO-p and KO-d spectra obtained from a single CH shell implosion series at OMEGA is shown in Figure 3-6. The KO-p yield in the plateau of the spectrum is directly proportional to the ρR of the CH shell (given by Equation (3-5)), and the KO-d yield is proportional to the ρR of the DT fuel (given by Equation (3-4)). In addition, the energy downshift of the KO-d spectrum relative to the 12.5 MeV high-energy endpoint of the birth spectrum can also be used to determine the total ρR ($\rho R_{fuel} + \rho R_{shell}$), as described in Seguin et al.[48] and Frenje et al.[30]

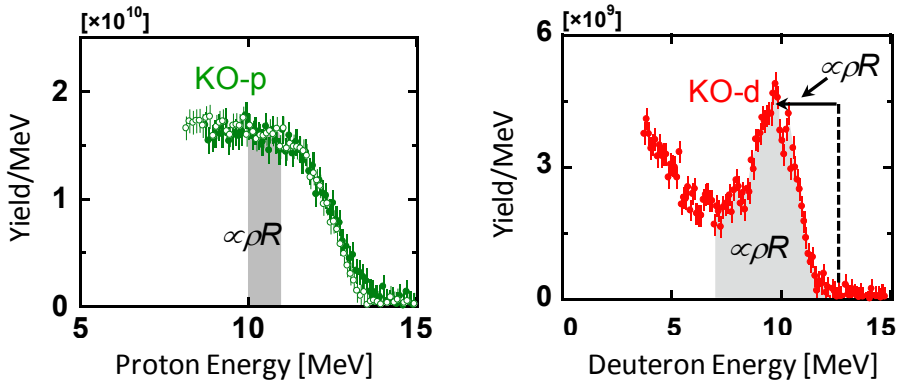

Figure 3-6: Examples of KO-p and KO-d spectra obtained at OMEGA by summing a series of 16um CH shell implosions with 18atm of DT gas. The CH shell ρR_{shell} is inferred from the plateau region of the KO-p spectrum shaded in grey.[48] The DT fuel ρR_{fuel} is inferred from the intensity of the KO-d peak (grey-shaded area that constitutes about ~15% of the total cross section). The measured KO-d energy down-shift from the 12.5 MeV high-energy endpoint of the KO-d birth spectrum can also be used to determine the total ρR.

In high ρR cryogenic DT implosions, the KO-d birth spectrum becomes sufficiently distorted by energy slowing-down in the implosion that the above method for determining the ρR from the high-energy KO-d peak does not work. In this case, the shape of the whole spectrum is therefore used to infer the ρR, as discussed in Frenje et al. [30]. In this work, it was established through Monte Carlo simulations that ρRs in cryogenic DT implosions at OMEGA can be determined accurately from the shape of the measured KO-d spectrum for ρRs up to about 180 mg/cm^2 (at higher values the techniques saturates as KO-d's do not escape the core). This can be done, as the shape of the KO-d spectrum depends mainly on ρR, and that effects of spatially varying density and temperature profiles play minor roles. Multi-dimensional features could, on the other hand, have an effect on the analysis and interpretation of the KO-d spectrum, as these effects would manifest

themselves by slightly smearing out the high-energy peak for low fuel ρRs (<100 mg/cm^2). For higher ρRs (>150 mg/cm^2), these effects should be less prominent as high-mode non-uniformities would not significantly alter the shape of the KO-d spectrum. Figure 3-7 shows examples of the KO-d spectra for different ρRs simulated for cryogenic DT implosions.

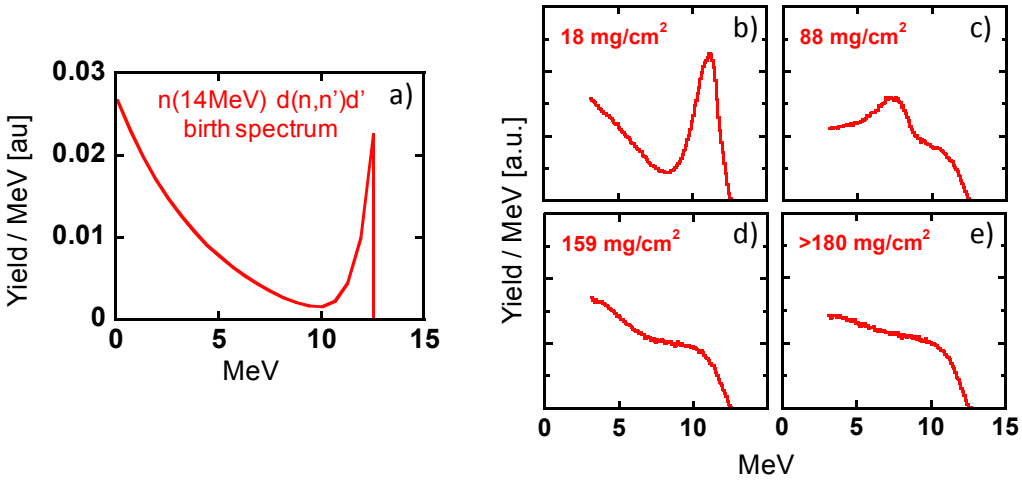

Figure 3-7 : Calculated KO-d birth spectrum (a) and simulated KO-d spectra for different ρRs in the cryogenic DT implosions ((b), (c), (d), and (e)). Frenje et al.[30] discuss this technique in detail, which has been very successful in diagnosing cryogenic DT implosions[26] when the ρR is below 180mg/cm^2. Above this value, the technique saturates.

4 - The Magnetic Recoil Spectrometer (MRS)

This chapter describes the Magnetic Recoil Spectrometer (MRS) on OMEGA[24] and the NIF. The MRS is a neutron spectrometer for measurements of the ICF neutron spectrum, from which ρR, T_i, and Y_n can be determined (Chapters 3, 5, 6, and 7), and for conducting basic science, as discussed in Chapters 8 and 9. An MRS was commissioned on OMEGA in 2007 and another was commissioned on the NIF in 2010. The main objective of the MRS is to diagnose implosions whose ρRs are too high (like in cryogenic DT implosions at OMEGA and the NIF) for the charged-particle techniques discussed in Chapter 3. This chapter describes these projects in detail, beginning with a discussion of the MRS principle in Section 4.1. Section 4.2 presents the final design of the MRS on both OMEGA and the NIF. Section 4.3 discusses the *ab initio* modeling of the MRS-response function and *in situ* calibration of the installed spectrometers. Section 4.4 elaborates on the detailed characterization of the different MRS parameters. Section 4.5 presents the complete MRS-response function simulated with the code Geant4.[64] Section 4.6 shows the modeling of the neutron-background and optimal shielding design for the MRS on both OMEGA and the NIF. Section 4.7 ties everything together by presenting a signal-to-background (S/B) calculation for the MRS DSn measurements at OMEGA and the NIF. Section 4.8 summarizes this chapter.

4.1 Principle

The MRS is a neutron spectrometer based on coupling of the neutron elastic scattering and the magnetic dispersion of recoil charged particles. This spectrometer is used in a similar fashion as in a wide variety of spectrometry applications in accelerator and tokamak experiments.[23, 65] The first design study of the MRS for ICF experiments was published in 2001 by Frenje et al.[23]. In that paper, the MRS concept is discussed for measurement of the ICF neutron spectrum, from which ρR, T_i, and Y_n can be determined.

The MRS consists of three main components (Figure 4-1). The first component is a CH_2 (or CD_2) foil positioned at 10cm and 26cm from the implosion at OMEGA and the NIF, respectively. The second component is a focusing magnet that is located outside the target chamber, and the third component is an array of CR-39 detectors positioned at the focal plane of the spectrometer. The principle of the system is the following: a small fraction of the neutrons emitted from the implosion hit the CH_2 or CD_2 foil, producing scattered recoil protons (or deuterons) in the forward direction. The energy relationship between the elastic scattered recoil (E_r) and the neutron (E_n) is described by:

$$E_r = \frac{4A}{(1+A)^2} E_n \mathrm{Cos}^2\theta_r \tag{4-1}$$

where θ_r is the angle between the direction of the incoming neutron and the direction of the outgoing recoil particle. Some of these forward scattered ($\theta_r \sim 0$) recoil protons or deuterons are

selected by an aperture, positioned in front of the magnet, which defines the MRS line-of-sight (LOS). The selected recoil particles are energy dispersed by their momentum, as described by Equation (4-2)

$$R_{Gyro} = \frac{p}{qB} = \frac{\sqrt{2mE_r}}{qB} \quad (4\text{-}2)$$

Here, R_{Gyro} is gyro radius, p is the momentum, q is the charge, m is the mass, E_r is the recoil particle energy, and B is the MRS magnetic field (perpendicular to the incident particle). The energy-dispersed particles are then focused onto the focal plane of the spectrometer. The focusing provides a clear mapping between position at the focal plane and the energy of the proton or deuteron and thus the energy of the neutron that scattered it. The CR-39 detectors record the position of each recoil particle with a detection efficiency of 100%. By measuring the spectrum of the recoil particles, the neutron spectrum is indirectly measured, as the MRS response function is well known. Note that deuterons have the same gyro radius as protons with energies twice as high (there is a slight relativistic correction at very high energy).

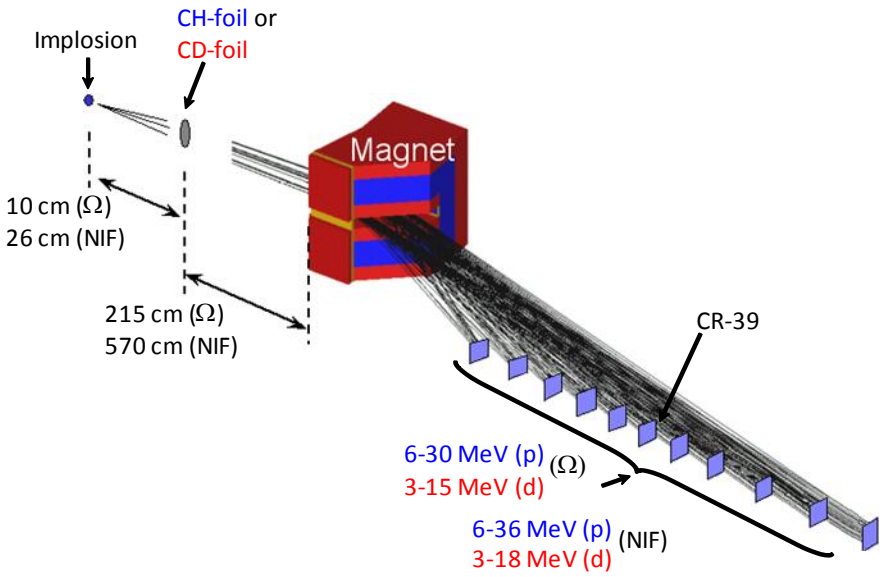

Figure 4-1: A schematic drawing of the MRS and its main components: a CH_2 (or CD_2) foil, magnet, and an array of CR-39 detectors. The MRS uses a CH_2 or CD_2 foil positioned 10 cm away from the implosion on OMEGA (and 26 cm on the NIF) to convert incident neutrons into recoil charged particles. Forward scattered recoil protons or deuterons are selected by an aperture in front of the magnet, positioned outside the target chamber at 215 cm (and 570 cm at the NIF) from the foil. Selected recoil particles are momentum analyzed and focused onto an array of CR-39 detectors, which record the position of each recoil particle with a detection efficiency of 100%. The measured recoil spectrum is then used to determine the neutron spectrum from the implosion. Proton energies of 6-30 MeV and deuteron energies of 3-15 MeV are detected at OMEGA and proton energies of 6-36 MeV and deuteron energies of 3-18 MeV are detected at the NIF.

An important characteristic to the MRS principle is that the detection efficiency [$\varepsilon_{MRS}(E_n)$], for a specified energy resolution [$\Delta E_{MRS}(E_n)$], is maximized (these parameters are discussed further in

the next sections). This is achieved because the differential cross sections for the elastic np- or nd-scattering in the laboratory system, peak in the forward direction and the average path length of the recoil particles in the foil is reduced to a minimum. In this context, it is also important to note that the magnet, which is made of Neodymium-Iron-Boron (NdFeB), is a focusing device with a pole gap of 3 cm producing a magnetic field up to ~0.9 Tesla and a field gradient of ~60 Gauss/cm. This feature is critical to the MRS design as it allows for the largest possible solid angle to be used, which maximizes ε_{MRS} for a specified ΔE_{MRS}. The entrance pole boundary is also angled relative to the incoming particles for increased focusing properties in both the transverse and dispersive planes, where the former prohibits the recoil particles from hitting the poles, and the latter provides for increased resolving power. The exit-pole boundary was chosen to minimize the magnet-space envelope and mass. However, this resulted in defocusing of the exiting particles in the transverse plane, which has an impact on the transmission function for the OMEGA-MRS as discussed in subsequent sections.

4.1.1 Efficiency

The detection efficiency of the MRS is given by

$$\varepsilon_{MRS}(E_n) = \frac{\Omega_n}{4\pi} \cdot T(E_r) \cdot n_i \cdot t \int^{"\Omega_r"} \frac{d\sigma(E_n)}{d\Omega_{lab}} d\Omega \tag{4-3}$$

Here, Ω_n is the solid angle subtended by the foil, $T(E_r)$ is the spectrometer transmission function, n_i is the number density in the foil, t is the foil thickness, Ω_r is the solid angle defined by the magnet aperture, and $d\sigma(E_n)/d\Omega_{lab}$ is the differential cross-section in the laboratory system for the elastic scattering. $T(E_r)$ is used if the particle distribution, perpendicular to the dispersive plane, extends beyond the CR-39 height (discussed in subsequent sections). In the case of OMEGA MRS, $T(E_r)$ depends on recoil-particle energy because the CR-39 detectors are further away from the magnet at higher energies. Also $d\sigma(E_n)/d\Omega_{lab}$ depends on the incident neutron energy (see Appendix A). As these parameters are well known, the MRS can be accurately characterized from first principles (*ab initio*), allowing quantitative calculations of the MRS response before the system has been built and installed. This is an important strength of the technique, but an *in situ* energy calibration is, however, required to check that the system has been built and installed according to specification. The *ab initio* characterization and *in situ* calibration experiments of the MRS on OMEGA and the NIF are discussed in Section 4.3.

4.1.2 Energy resolution

The spectrum of the recoil particles is related to the incident neutron spectrum through kinematic scattering process described in Chapter 3 and Appendix A. The MRS energy resolution [$\Delta E_{MRS}(E_n)$] can be approximated by

$$\Delta E_{MRS}(E_n) \approx \sqrt{\Delta E_{foil}^2(E_n) + \Delta E_{kin}^2(E_n) + \Delta E_{mag}^2(E_n)} \,. \tag{4-4}$$

Here, $\Delta E_{MRS}(E_n)$ is the total energy resolution of the system, $\Delta E_{foil}(E_n)$ is the energy broadening due to different path lengths in the foil resulting in different energy losses, $\Delta E_{kin}(E_n)$ is the kinematic broadening due to the dependence of the recoil energy on scattering angle θ_r ($E_r \propto \cos^2\theta_r$), and $\Delta E_{mag}(E_n)$ is the broadening due to the ion-optical aberrations of the magnet. $\Delta E_{foil}(E_n)$ is proportional to the thickness and the density of the foil. $\Delta E_{kin}(E_n)$ is proportional to the size of the foil because larger foils allow a larger spread of scattering angles to be selected by the aperture in front of the magnet. $\Delta E_{mag}(E_n)$ is weakly proportional to the size of the foil and magnet aperture because the focusing properties of the magnet are degraded for larger offsets from the central trajectory and therefore larger angle spreads of the recoil particles at the magnet aperture. This partially explains why the NIF MRS system boasts superior performance, because the foil (almost the same size as OMEGA) is further from the magnet aperture, resulting in a much smaller angular spread of the recoil particles. For the MRS to be both practical and useful at OMEGA and the NIF, built-in flexibility has been included in the design to effectively use it for different applications. This is important, as a tradeoff between ε_{MRS} and ΔE_{MRS} must be considered and chosen to suit the specific application. For instance, for practical implementation of low-yield applications, such as measurements of DSn at OMEGA for which yields are orders of magnitude smaller than the primary yield, it is necessary to degrade ΔE_{MRS} to substantially increase ε_{MRS}. For high-yield applications, on the other hand, such as measurements of primary neutron spectrum at OMEGA and the NIF, the MRS can be configured to operate in a high-resolution mode (low-ε_{MRS}). Several options are available for configuring the MRS. Either a CH_2 or CD_2 foil can be selected to produce recoil protons or deuterons (and thus the energy range covered for neutrons is 6 – 29.7 MeV with the CH_2 foil or 3.4 – 16.9 MeV with the CD_2 foil at OMEGA, and 6-35.5 MeV with the CH_2 foil and 3.4-20.3 with the CD_2 foil at the NIF). The foil area and thickness can also be adjusted to change the ε_{MRS} and ΔE_{MRS}. The area of the aperture in front of the magnet can be adjusted as well.

4.2 Final design of the MRS on OMEGA and the NIF

The MRS technique was first implemented on OMEGA in 2007, and then on the NIF in 2010. The philosophy behind this was first to comprehensively test the technique on OMEGA, and from the experience gained, insightfully design an optimal MRS for the NIF. There were other important reasons for taking this approach. First, ρR of both warm gas-filled CH-capsule and cryogenic DT implosions can be inferred from both the MRS and charged-particle spectrometry for moderate ρR implosions ($\rho R < 200$ mg/cm^2), which allowed for a definitive check of the MRS data (see Chapter 3 and Chapter 7). Second, as there are no other ways to determine cryogenic $\rho R > 200$ mg/cm^2 at OMEGA, the MRS brought the required diagnostic to the OMEGA cryogenic program. Images of the MRS fully installed on OMEGA and the NIF target chamber is shown in Figure 4-2a and Figure 4-2b, respectively. As shown by both images, the diagnostic is fully surrounded by polyethylene shielding to suppress the background of primary neutrons and neutrons scattered by the chamber wall, diagnostics, and other structures surrounding the MRS (in the case of the NIF MRS, grey aluminum plates are attached to the shielding). Additional shielding is obtained on the NIF by positioning the CR-39 detector array in the shadow of the 50 cm borated gunite, sitting on the 10 cm thick aluminum target chamber, or the 10 cm OMEGA aluminum chamber. As the CR-39 detector array is positioned on an off-axis detection plane that is well outside the target

chamber, enough space exists to position ~2200 lbs and ~6000 lbs of polyethylene shielding around the OMEGA MRS and NIF MRS, respectively. Detailed discussions about the shielding-design considerations are made in Section 4.6.

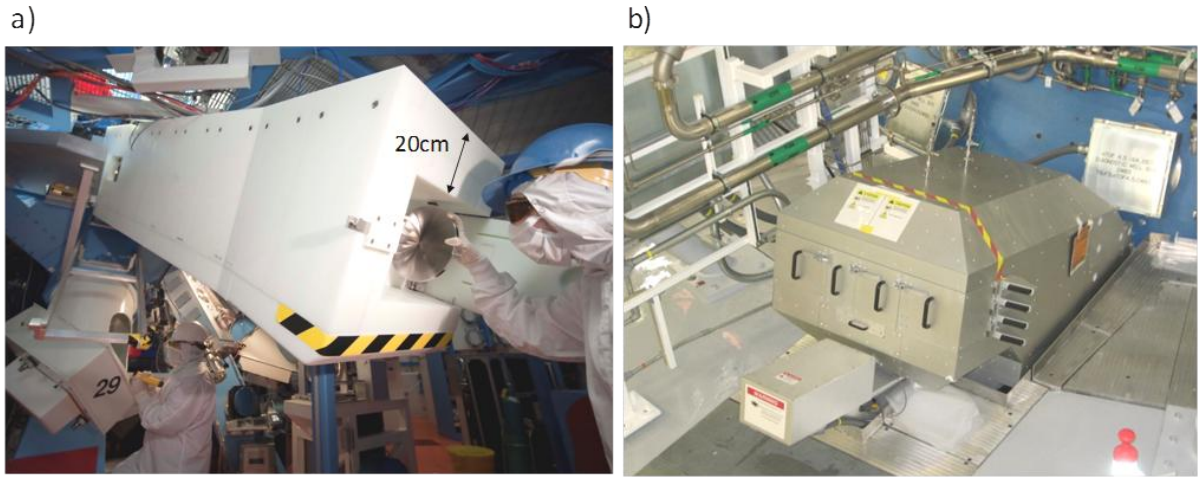

Figure 4-2: a) An image of the OMEGA MRS surrounded by ~20cm thick of polyethylene shielding. The shielding weighs ~2200lbs and primarily surrounds the detector housing to reduce the background neutron fluence to the required level for the DSn measurement (photo taken by Eugene Kowaluk). b) An image of the NIF MRS fully installed on the NIF-target chamber. The MRS detector array is located behind the blue borated gunite target-chamber wall and inside ~6000lbs of polyethylene shielding, which greatly reduces the background neutron fluence

A detailed cad drawing of the MRS on OMEGA and the NIF is shown in Figure 4-3a and Figure 4-3b, respectively. As shown in Figure 4-3a, the MRS is permanently attached to the OMEGA target chamber. The foil is inserted by the Nuclear Diagnostic Inserter (NDI). The magnet is surrounded by an aluminum vacuum chamber, which is isolated from the OMEGA target chamber by a gate-valve, allowing tritium vent/purge operations to be performed between shots before removal of the CR-39 detector array. The detector housing is connected directly to the magnet chamber and is surrounded by the polyethylene shielding. The NIF MRS is permanently attached to the 77°-324° port, which is close to the equator on the NIF target chamber. The foil is inserted to a distance of 26 cm from the implosion by the Diagnostic Insertion Manipulator (DIM) 90º-315º, which is not shown in this figure. The MRS is positioned close to the edge of the port to take advantage of gunite shielding (marked blue in the figure). The MRS vessel is also positioned between two floor boards (or “diving boards”). Substantial amounts of shielding (marked green and purple in the figure) surrounds the MRS. Prior to a shot, the CR-39 detector array is inserted into the MRS (see Figure 4-9). This typically happens an hour to a day before the shot, depending on shot schedule and facility. 30 minutes before a shot, the gate valve in front of the magnet is opened, which connects the MRS vacuum chamber to the target-chamber vacuum. After a shot, the CR-39 detector array is removed from the diagnostic for processing and analysis. The next sections describe the MRS parameters in detail.

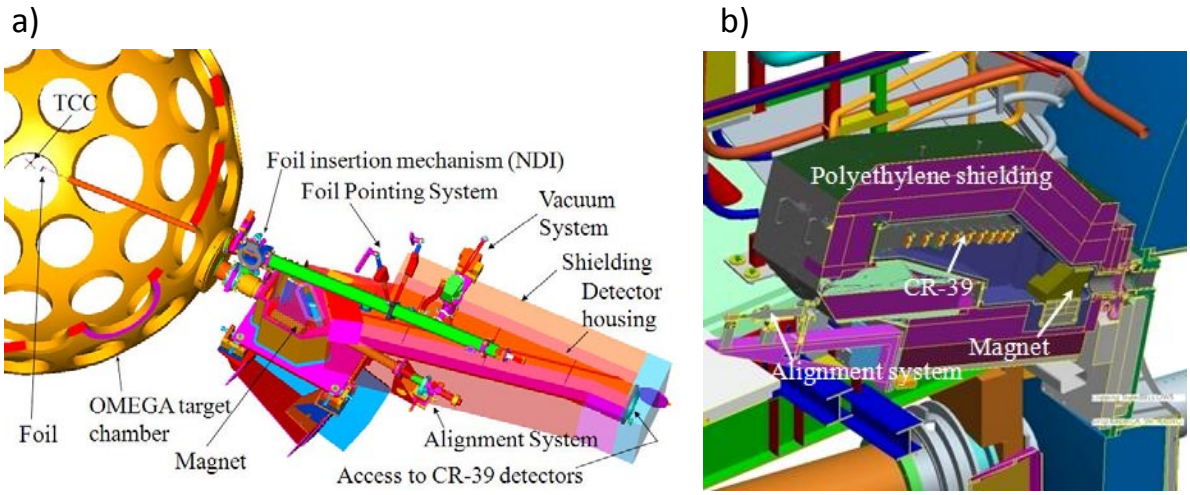

Figure 4-3: a) A CAD drawing of the OMEGA MRS, which is permanently mounted to the OMEGA target chamber. The foil is inserted to a distance of 10cm from the implosion by the nuclear diagnostic inserter (NDI). The magnet is enclosed by an aluminum vacuum housing, which is connected to the detector vacuum housing. The detector housing is surrounded by a ~2200 lbs of polyethylene shielding (shown here as a transparent material). Access to the CR-39 detector array is through the rear door. b) A CAD drawing of the NIF MRS positioned onto the target chamber at the line-of-sight 77°-324°. A vertical crosscut is made through the MRS to illustrate the various components in the system, i.e., the magnet, CR-39 detector array, alignment system, and shielding. The Diagnostic Insertion Manipulator (DIM) 90°-315°, not shown in this figure, is used to insert the foil to a distance of 26 cm from the implosion. The MRS is fully surrounded by ~6000 lbs of polyethylene shielding (marked grey and green) and is positioned in the shadow of the 50 cm borated gunite (marked blue) cladding on top of the 10 cm thick aluminum target chamber.

4.2.1 MRS configurations on OMEGA and the NIF

A summary of the MRS parameters and estimated errors are given in Table 4-1. The efficiency and energy resolution (for 14-MeV neutrons) for each MRS configuration are shown at the bottom of the table. Each MRS parameter, and how it is characterized, is discussed in detail in the subsequent sections.

Table 4-1: System parameters for the MRS on OMEGA and the NIF and associated errors.[25] The efficiency and energy resolution for each MRS configuration are also shown.

Spectrometer Parameters	OMEGA Med Res	OMEGA Low Res	NIF High Res	NIF Med Res	NIF Low Res
Foil Area (cm^2)	10.64	13.19	12.8 ± 0.1	12.8 ± 0.1	12.8 ± 0.1
Foil Distance (cm)	10.45 ± 0.3	10.55 ± 0.3	26.0 ± 0.3	26.0 ± 0.3	26.0 ± 0.3
Foil Thickness (μm)	164 ± 1	261 ± 1	47 ± 1	138 ± 1	259 ± 1
Foil Number density (d/cm^3 $x10^{22}$)	7.6 ± 0.3	7.6 ± 0.3	7.9 ± 0.1	7.9 ± 0.1	7.7 ± 0.1
$d\sigma/d\Omega$ (0°) at 14MeV (b/sr)	0.50 ± 0.01	0.50 ± 0.01	0.50 ± 0.01	0.50 ± 0.01	0.50 ± 0.01
Magnet Distance from Foil (cm)	215 ± 0.1	215 ± 0.1	570 ± 0.1	570 ± 0.1	570 ± 0.1
Magnet Aperture Area (cm^2)	21.3 ± 0.2	21.3 ± 0.2	20 ± 0.2	20 ± 0.2	20 ± 0.2
Interception correction	0.86 ± 0.013	0.86 ± 0.013	1 ± 0	1 ± 0	1 ± 0
Transmission at 14 MeV	0.79 ± 0.03	0.79 ± 0.03	1 ± 0	1 ± 0	1 ± 0
$\varepsilon_{MRS\ 14MeV}$	1.18E-09	2.14E-09	1.56E-11	4.61E-11	8.48E-11
Total Uncertainty at 14MeV	6.6%	6.5%	3.2%	3.2%	3.2%
ΔE_{MRS} FWHM at 14 MeV	1.31	1.77	0.69	0.80	1.56

4.2.2 Foil holder and blast-shield

On both the OMEGA MRS and NIF MRS, the foil is protected by a blast shield (Figure 4-4). For the OMEGA MRS, a 500μm thick stainless steel plate, positioned directly in front of the foil, is used as a blast shield. For the NIF MRS, a 1.57mm thick (on average) tantalum plate positioned 5mm in front of the foil is used as a blast shield. To withstand the impulse loading and debris from the NIF hohlraum, the thickness of the blast shield was tapered to improve the robustness. To assess the effect of these blast shields on the MRS primary and DSn measurements, MCNP was used to calculate the fluence, angle, and energy distributions of neutrons at the foil that have scattered from the blast shield. The number of primary neutrons absorbed or scattered away from the foil was also calculated. In these calculations, 14-MeV neutrons were emitted from the target chamber center and transported through the MRS foil-holder arrangements. The results from those calculations are shown in Figure 4-5a. The total OMEGA MRS fluence is higher than the NIF MRS because the foil is closer to the implosions (10cm at OMEGA compared to 26cm at the NIF). It is important to note that the simulated neutron fluences at the foil, shown in Figure 4-5a, are angle-integrated values. To assess the effect of the blast shield on the MRS DSn measurement, both the energy and the angle of the scattered neutron, and the differential cross section for the elastic n-d scattering must also be considered in the simulation. The results from MCNPX simulations that consider these effects are shown in Figure 4-5b, which give the recoil deuteron fluence at the MRS aperture. These calculations indicate that the blast shield adds an effective ρR of 1.7mg/cm^2 and 3mg/cm^2 to the observed ρR in a DT implosion at OMEGA and the NIF, respectively. Note that a 260μm CD foil alone, also adds about 0.7mg/cm^2 of ρR from internal scattering. These numbers are < 1% of typical cryogenic implosions (at each facility), but are

important for very low ρR implosions. Also from these calculations, it was also concluded that the blast shield attenuates the inferred primary yield by ~1% and 3.6%, at OMEGA and NIF respectively, an effect that must be corrected for when inferring the primary yield.

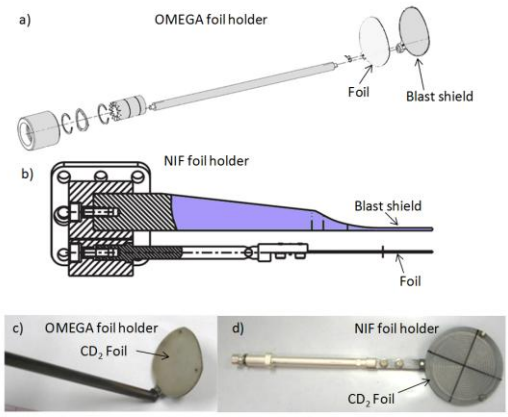

Figure 4-4: a) A CAD drawing of the OMEGA MRS foil holder, which illustrates the 500μm stainless steel blast shield, the foil, which is flush against the blast shield, and the insertion rod that attaches to the NDI. b) A CAD drawing of the NIF MRS foil holder, which illustrates, the tapered Ta blast shield (described in the text), the foil holder, which is attached directly to the foil and offset from the blast shield by 5mm, and the bracket that attaches to the DIM. c) OMEGA MRS foil holder with the 13.2 cm^2 low resolution CD_2 foil attached. d) NIF MRS foil holder with the12.8 cm^2 low-resolution CD_2 foil attached (blast shield not shown).

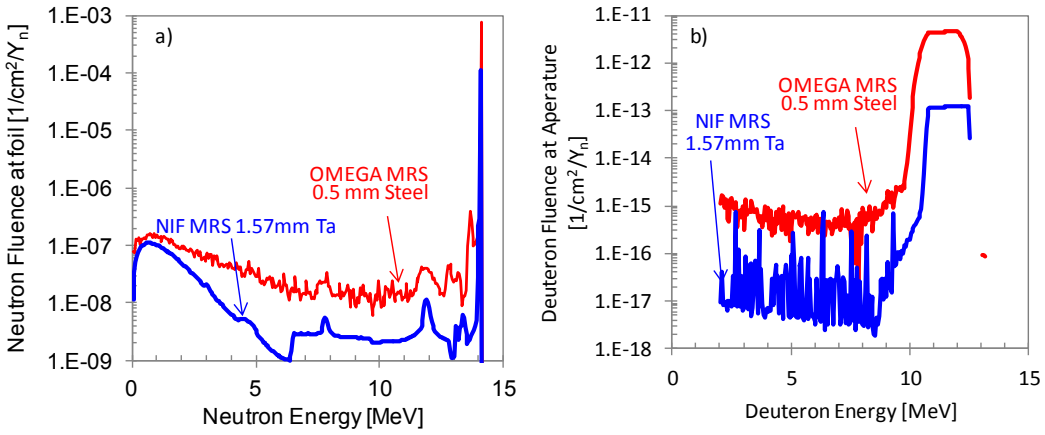

Figure 4-5: a) MCNPX simulated fluence of 14-MeV neutrons coming directly from the implosion and neutrons scattered by the foil blast shield for the OMEGA MRS (red curve) and the NIF MRS (blue curve). The OMEGA-MRS-foil blast shield is 500μm thick and made of stainless steel and NIF-MRS-foil blast shield is 1.57mm thick (on average) and made of tantalum. The total NIF MRS neutron fluence is lower than the OMEGA MRS because the foil is further away from the implosion than for OMEGA. b) MCNPX simulated fluence of recoil deuterons at the magnet aperture that originate from the neutron-fluence spectra shown in (a). Again, the total NIF MRS deuteron fluence is lower than the OMEGA MRS because the solid angle subtended by the NIF-MRS foil is smaller than the OMEGA-MRS foil. A 260μm thick CD_2 foil (low resolution) was used in these simulations. As described in the text, the fluence of these recoil deuterons is insignificant when diagnosing high-ρR implosions at OMEGA and the NIF.

4.2.3 Magnet and its properties

The magnets for the OMEGA MRS and NIF MRS are nominally identical wedge-shaped, rare-earth (Neodymium-Iron-Boron) permanent magnets manufactured by Dexter Magnetic Technologies, Inc.[66] Permanent magnets were selected, as they have several advantages over electro-magnets. They can be built much smaller and they do not require a power supply or cooling systems. In addition, they do not suffer from startup/hysteresis concerns. Some disadvantages include relatively expensive raw material and they cannot be adjusted or turned off when not in use. In addition, the strength of the magnet (B) field in permanent magnets depends slightly on the ambient temperature, which for these materials scales as -0.11% $(\delta B/B)/C°$.[67] The entrance and exit pole faces of the magnet are angled with respect to the incoming particle trajectories, creating a wedged-shaped field. This shaped-field focuses charged particles onto the detector plane, allowing the entrance aperture to be significantly larger for the same energy resolution.[23] This essential feature dramatically increases the detection efficiency (>10 times) over the CPS magnet designs, which is important when measuring very weak components in the neutron spectrum. The magnet pole-gap is 3cm across but the magnet aperture decreases the acceptance opening to 2cm in the direction perpendicular to the bending plane. The angled pole face relative to the direction of the incoming recoil particles produces a weak quadrapole moment that focuses particles in the transverse (non-dispersion) direction, helping to deflect particles away from poles (scattering of the poles would have a detrimental effect on the DSn measurement).[23] The magnet aperture is 11×2 cm^2 and 10×2 cm^2 in area for the OMEGA MRS and the NIF MRS, respectively. Other apertures are occasionally used for special experiments, which often involves measurements of charged particles coming directly from the implosion (when the foil is not fielded). In the case of the NIF MRS, very small apertures will be used for diagnosing very high-yield implosions.

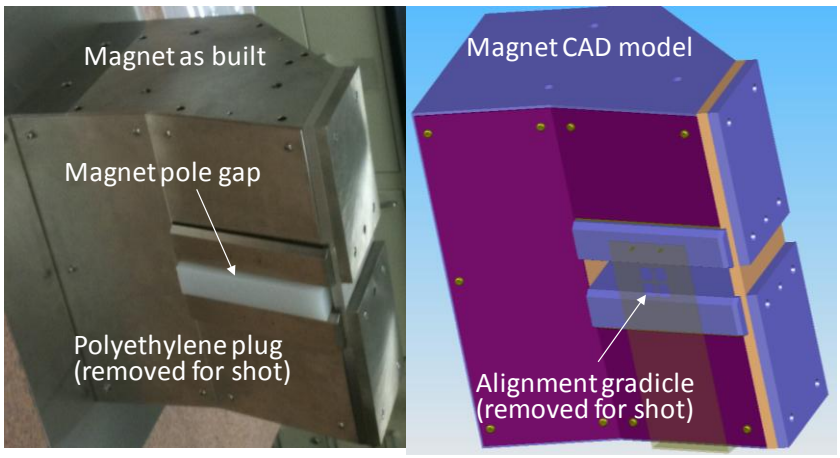

Figure 4-6: Left: image of the NIF MRS magnet, as built by Dexter Magnetic Technologies, Inc. The magnet pole gap has been plugged with polyethylene to prevent ferromagnetic objects from entering the ~0.9 Tesla field and possibly damaging equipment or causing injury (the plug was removed upon installation). Right: a CAD model of the MRS magnet with an image of the alignment gradicles used to position and orient the magnetic field with respect to foil and CR-39 detectors. The magnets for the OMEGA MRS and NIF MRS are nominally identical but have slightly different, as built, field strengths.

A finite element model of the magnetic field, developed by Dexter, is shown in Figure 4-7. The wedge shaped magnetic field that peaks at ~0.9 Tesla in the symmetry plane of the magnet is clearly visible. Also shown in the figure is the measured field map of the NIF MRS magnet. A comparison of the two field maps show that the measured magnetic field is in good agreement with the modeled one.

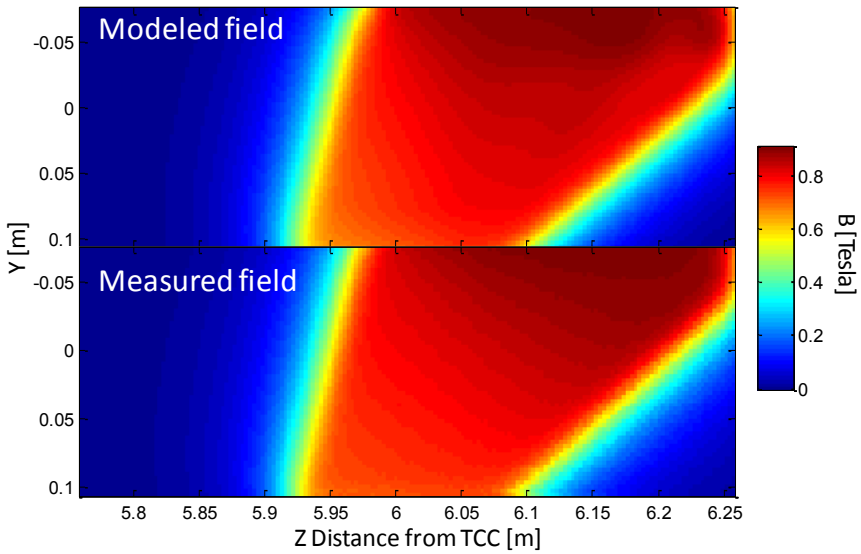

Figure 4-7: Modeled and measured magnetic-field maps of the main component of the field (B_x) for the NIF MRS (which is nominally identical to the OMEGA MRS magnet except for a slight difference in field strength, see Figure 4-8). A comparison of the images shows a very similar overall shape and maximum field strength. The magnet modeling and field measurements were performed by Dexter Magnetic Technologies Inc.

A quantitative comparison between the measured OMEGA MRS and NIF MRS fields clearly shows that the as-built NIF-MRS magnetic field is stronger by ~6% than the OMEGA MRS magnetic field, as illustrated by Figure 4-8. Despite this difference, both magnets perform differently but very well (the differences are accounted for in the *in situ* calibration and modeling of the MRS).

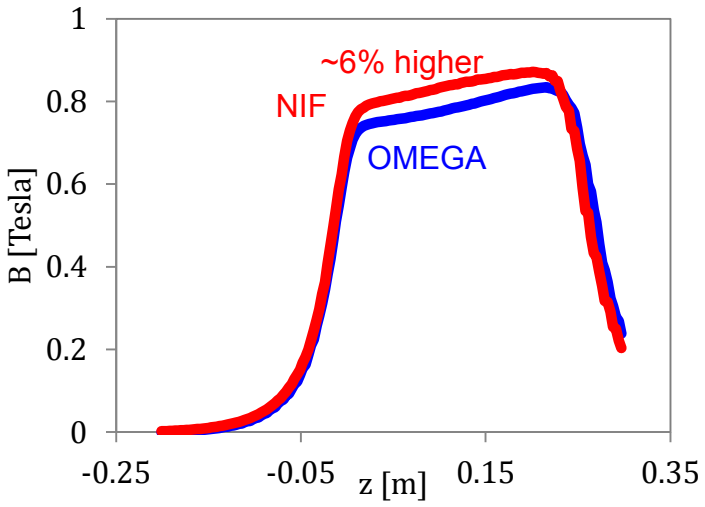

Figure 4-8: A comparison of the OMEGA MRS and NIF MRS measured magnetic field strength. This line-out was taken through the center of the MRS line-of-sight. Z=0 cm corresponds to the location of the magnet aperture at the pole entrance side, which is at 2.25m at OMEGA and 5.96m at NIF (Z=0 is also the location of the cross-hair in Figure 4-6).

4.2.4 CR-39 detector array

As previously mentioned an array of CR-39 detectors, positioned at the focal plane of the MRS, is used to detect the recoil particles produced in the conversion foil. CR-39 is a clear optical-quality plastic with a density of 1.3 g/cm^3 and molecular formula $C_{12}H_{18}O_7$ (all CR-39 detectors used in this study were manufactured by TASTRAK Ltd).[68] Signal charged particles, such as protons or deuterons, create trails of molecular damage as they travel through the CR-39 plastic. These trails of damage are revealed through an 80°C, 6N NaOH etch, in which the damaged trails etch faster than the bulk material. The location, size, eccentricity, and contrast of the formed tracks on the CR-39 detectors are accurately recorded, using a microscope.[20, 48] From this information, a histogram of track positions along the whole MRS detector plane can be generated. As the CR-39 detectors in the array are very accurately positioned and oriented with respect to the other components of the system (i.e. magnet, aperture, and foil), an energy spectrum of the recoil deuterons can be determined from the position histogram. Figure 4-8 shows the two CR-39 detector arrays for the OMEGA MRS and the NIF MRS. The base for the OMEGA-MRS detector array is a cylindrical tube, which slides upward into the detector housing where the nose cone locates to an alignment pin. The alignment pin suffered from wear and tear during routine operations, and had to be replaced a few times, which motivated a new design for the NIF-MRS detector array (sometimes called “ironing board”). The NIF-MRS detector array slides downward into the detector housing on a fin, and its location relative to the other system components is defined by a flat stainless-steel hard-stop at the bottom of the array. Images of the insertion procedure of the CR-39 detector arrays for the OMEGA MRS and NIF MRS are shown in Figure 4-11.

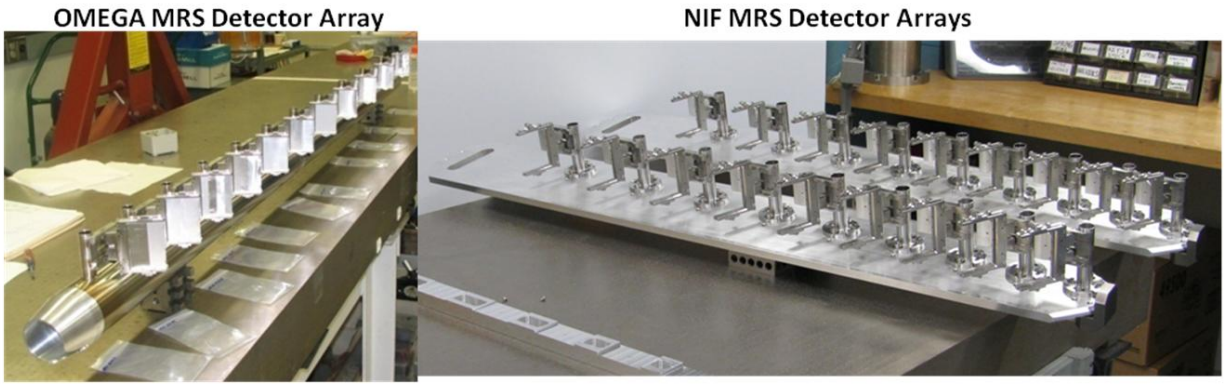

Figure 4-9: Left: CR-39 detector array for the OMEGA MRS. The base for the OMEGA MRS detector array is a cylindrical tube with a nose cone, which latches onto an alignment pin inside the detector housing. Right: Two CR-39 detector arrays for the NIF MRS. The NIF-MRS array is a flat "ironing board", which slides along a fin to a hard stop at the end of the array. Both systems use detector "flag poles," which position each CR-39 detector inside locking forks, described more in Figure 4-12

The CR-39 detectors are positioned at the focal plane of the MRS at which the recoil particles are at best magnetic focus (also best resolution). Each CR-39 detector is oriented to make sure the directions of the incoming recoil particles are nearly perpendicular to the detector surface, an important feature for optimal detection with CR-39 (also important for the coincidence counting technique discussed in Chapter 6). The eleven OMEGA-MRS detector locations are illustrated in Figure 4-10. The NIF-MRS detectors are located using the same guiding principles but due to different ion-optical focusing properties of the system, only nine CR-39 detectors, spaced much closer, are used to cover about the same energy range.

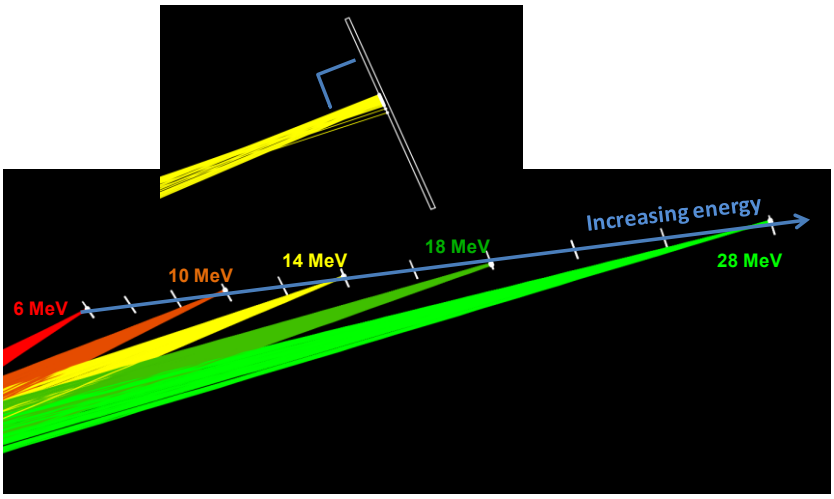

Figure 4-10: Position and orientation of the eleven OMEGA-MRS detectors (also called windows) along the MRS focal plane. The trajectories of recoil particles with proton equivalent energies of 6, 10, 14, 18, and 28 MeV are shown. Each CR-39 detector is oriented to make sure the directions of the incoming recoil particles are nearly perpendicular to the detector surface, an important feature for optimal detection with CR-39. The nine NIF-MRS detectors are located in a similar way but are spaced closer together due to different ion-optical focusing properties of the system.

Figure 4-11: The insertion of the CR-39 detector array for the OMEGA MRS (left) and NIF MRS (right). A door in the polyethylene shielding (described in detail in the next section) allows access to the MRS vacuum chamber.

The CR-39 detectors are held by forks that are attached to "flag poles," as depicted in Figure 4-12a. The forks also hold filters in front of the CR-39, which are used to slow incoming charged particles down to energies for optimal CR-39 detection. Typically deuteron with energies of <10MeV and proton with energies less <8MeV are readily detected in high signal-to-background (S/B) scenarios (S/B>>1).[48] In low signal-to-background scenarios (S/B<<1), the coincidence

counting technique (CCT) is used as described in detail in Chapter 6. The fork arrangement allows the CR-39 detector and appropriate filter in front to be inserted and locked into place. The position of the high-energy edge of the CR-39 detector is defined by two feet at the bottom of the fork. These are critical for the optimal position accuracy of the CR-39 detectors in the dispersive direction. Three dowel pins, two on the opposite side of the feet and one opposite the CR-39 label are used to roughly define the location of the CR-39 in the direction perpendicular to the dispersive direction. The CR-39 filters are made of thin strips of Mylar, Aluminum, or Tantalum filter laid out along the active area of the detector. The filter increases in thickness with increasing energy of the recoil particles along the array. Figure 4-12b shows a diagram of the filter layout for the NIF MRS CR-39 detector # 7, which detects recoil deuterons from primary DT neutrons. For this detector, a step filter made of Al, with thicknesses ranging from 150μm to 225μm is used. In front of the low-energy detectors ~3.5μm Mylar is used because it is more robust than Al or Ta, which are easily destroyed when the thickness is less than 10μm. Also note that the (n,p) proton production cross-section is about two times lower for Ta than for Al at14MeV,[69] making it an ideal filter when the neutron fluence at the MRS detector needs to be considered. However, Al is much less expensive than Ta and was therefore used in the initial commissioning experiments with the NIF MRS when the neutron fluence at the MRS detector was insignificant (such as in the detection of the primary DT peak where S/B>>1). The OMEGA MRS filter configuration for deuterons is summarized in Chapter 6 in Table 6-2, and the first-generation NIF MRS filter configuration for deuterons is summarized in Table 6-3. The first set of filters for the high-energy windows in the NIF MRS were made of Al for the commissioning experiments. The next set of filters will be constructed of Ta to improve S/B.

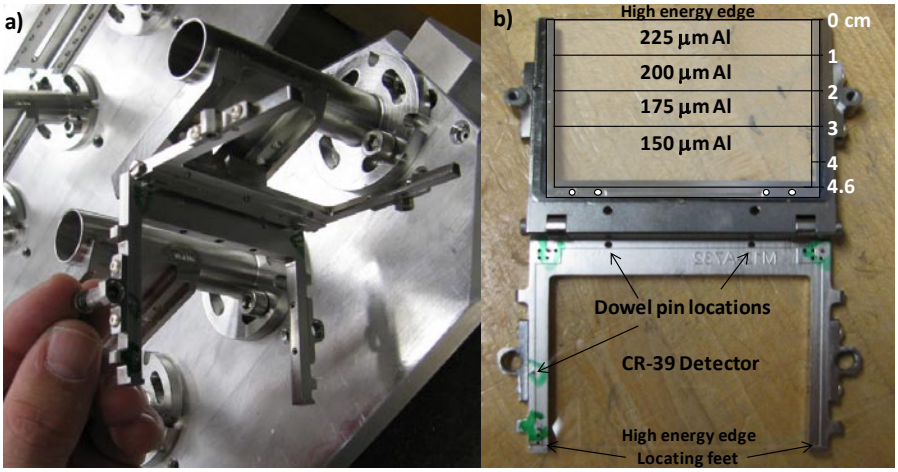

Figure 4-12: a) A CR-39 detector fork on the NIF-MRS detector array. This fork holds the CR-39 and filter in front. The filter is used to range down the energy of the recoil particles for optimal CR-39 detection. The two fork halves close together, locking the filter-CR-39 arrangement in place. b) A detector fork detached from the array to illustrate how the filter and CR-39 are mounted. In this case, the aluminum-filter arrangement is shown for the NIF-MRS CR-39 detector #7. The position of the CR-39 detector in the dispersive direction is accurately defined by two feet at the bottom of the fork. Three dowel pins, two on the opposite side of the feet and one opposite the CR-39 label are also used to roughly define the location of the CR-39 in the direction perpendicular to the dispersive direction.

4.2.5 Polyethylene neutron shielding

The background of primary neutrons and neutrons scattered by the chamber wall, diagnostics, and other structures around the MRS needs to be considered and reduced significantly. To suppress this neutron background, an extensive amount of polyethylene shielding was installed around the MRS. In the case of the OMEGA MRS, a stainless-steel plug was also used to more effectively suppress the unscattered primary neutrons. Designing the polyethylene shielding was a major undertaking, as it first required a detailed understanding of the neutron-fluence field in the OMEGA and NIF target bays, and secondly, many design iterations were required before an optimal shielding design was found that met the requirement. Both space and weight constraints had to be considered when designing the shielding. As CR-39, which is insensitive to γ-rays and x-rays, is the detector of choice for the MRS, polyethylene was chosen as the shielding material. This material is highly hydrogenous, which makes it an effective moderator and attenuator of neutrons (especially at lower neutron energies). It should be pointed out though that high Z materials are more effective at higher neutron energies (>10MeV) because inelastic processes provide greater moderation, on average, than elastic-scattering processes with hydrogen.[70] In the case of direct 14-MeV neutrons, it is advantageous to first use a high-Z material (like iron or steel) to entirely block the detector from direct 14-MeV neutrons. This type of material is very effective in attenuation and moderating un-scattered 14-MeV neutrons. A hydrogenous material is used downstream to more effectively moderate and attenuate the lower-energy neutrons that passed through the steel. Figure 4-13 shows the neutron mean-free path for several common shielding materials as a function of incident energy.

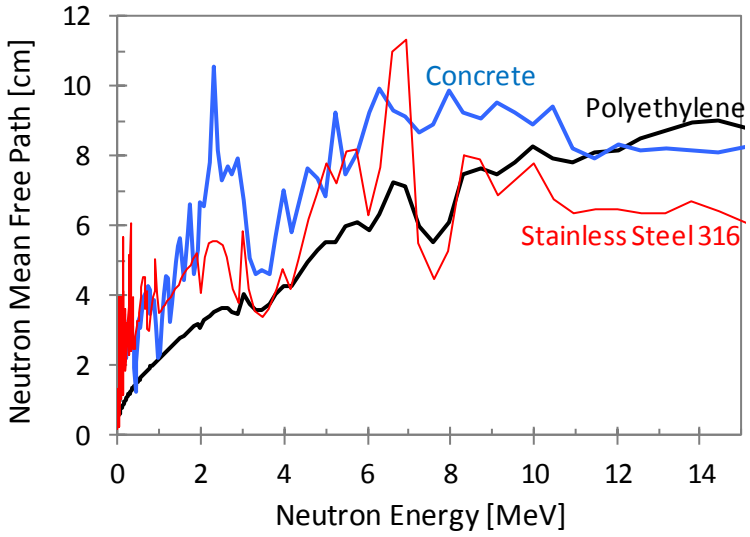

Figure 4-13: Neutron mean-free path as a function of neutron energy for concrete, polyethylene, and stainless steel 316.[56] This plot shows that stainless steel has the shortest mean-free path at 14 MeV, which makes it the best material for attenuating and moderating direct un-scattered 14 MeV neutrons from a DT implosion. Polyethylene is the best material for shielding neutrons with lower neutron energies.

Figure 4-14a show a schematic of the OMEGA-MRS shielding design, which features a ~20cm thick stainless steel plug that is used to attenuate direct 14 MeV neutrons from the implosion and

~20cm of polyethylene shielding placed around the detector housing that is used to shield scattered neutrons in the target bay. Figure 4-14b shows the NIF-MRS shielding design. The 50cm concrete (i.e. gunite) on top of the 10cm thick aluminum target chamber attenuates direct 14 MeV neutrons, and 40cm of polyethylene, surrounding the MRS, provides shielding from lower-energy scattered neutrons in the target bay.

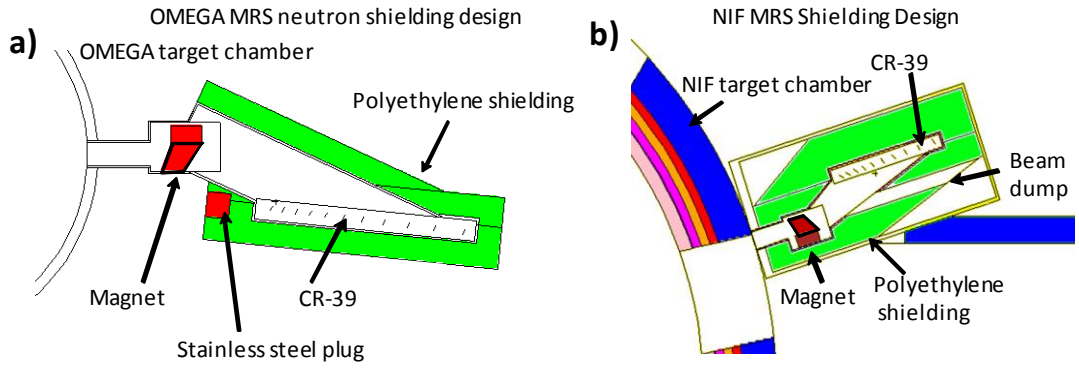

Figure 4-14: a) A schematic drawing of the OMEGA-MRS neutron shielding design. A stainless steel plug is used here to attenuate direct unscattered DT neutrons, while polyethylene around the MRS-detector housing is used to attenuate lower energy scattered neutrons. b) A schematic drawing of the NIF-MRS neutron shielding design. The NIF target chamber (10cm of aluminum and 50cm of concrete) significantly moderates and attenuates direct, unscattered 14-MeV neutrons, while the polyethylene around the whole diagnostic is used to moderate and attenuate lower-energy scattered neutrons.

4.2.6 Alignment procedure

The MRS system is aligned to the target chamber center (TCC) using a set of cross-hairs and a telescope system, as depicted in Figure 4-15 for the OMEGA MRS. Cross-hairs in the front and rear of the magnet define the MRS LOS. These cross-hairs are aligned to another set of cross-hairs in the alignment telescope. Using the aligned magnet cross-hairs, the MRS is pointed towards TCC where a 1-mm backlit gold ball is positioned. After the MRS is correctly aligned to TCC, the foil is inserted and centered on the MRS LOS at the specified distance from TCC. After the alignment process, the cross-hairs are removed and the magnet aperture is subsequently installed for shot operations. A similar procedure applies to the NIF MRS, except that a specially designed lighting system, which uses a scribed cross-hair on the foil and the cross-hairs of the alignment telescope, allows for the foil alignment to be verified before every shot.

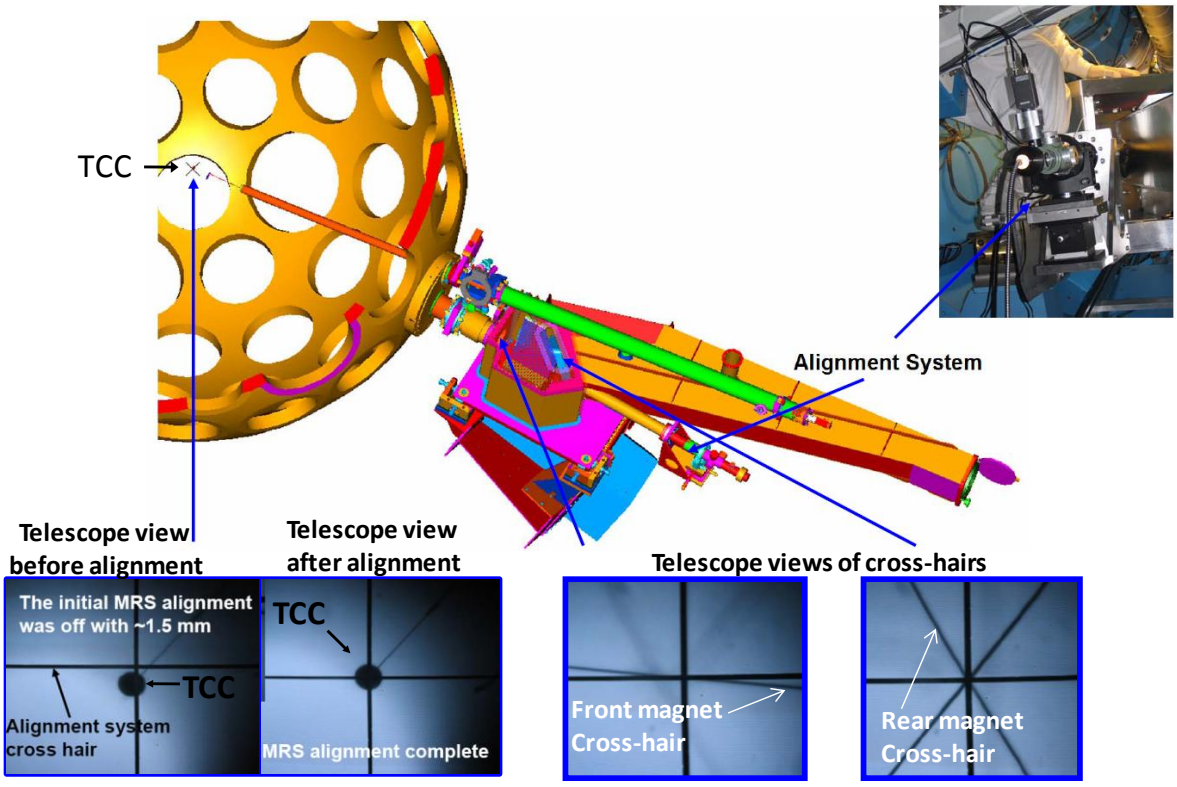

Figure 4-15: Alignment procedure for the OMEGA MRS. Cross-hairs in the front and rear of the magnet, which define the MRS LOS, are aligned to the cross-hair in alignment telescope that is behind the magnet. Using these cross-hairs, the MRS is pointed to TCC where a 1-mm backlit gold ball is positioned (see the bottom left images). When the MRS is pointing towards TCC, the foil is inserted and centered on the MRS LOS at the specified distance from TCC. This alignment procedure applies to the NIF MRS except for a minor difference, as described in the text.

4.3 *Ab initio* modeling and *in situ* calibration of the MRS

Through the MRS response function, the location of each recorded track on the CR-39 detectors can be related to the energy of the recoil particle and energy of the neutron, which produced the recoil particle. The MRS response is modeled using the Monte Carlo code Geant4,[64] which is a C++ based particle transport toolkit commonly used in the particle physics community. Its generality and powerful feature-base has made it a very useful tool for this application.

4.3.1 *Ab initio* modeling of the MRS on OMEGA and NIF using Geant4

Several Geant4 models of the MRS have been developed for a variety of configurations. An illustration of one such model is shown in Figure 4-16. As shown by the figure, neutrons are transported to the foil from a point source positioned at TCC. At the foil, a small fraction of the neutrons produce recoil protons or deuterons, some of which are forward scattered and selected by an aperture in front of the magnet. The selected recoil particles are transported through the 3D magnetic field map. As the magnet is a focusing device in the dispersive plane, the particle

trajectories for a specific energy are focused to a point at the focal plane of the spectrometer at which CR-39 detectors are positioned. When the recoil particles hit the CR-39 detectors, their energy and location are recorded and stored as well as the neutron energy.

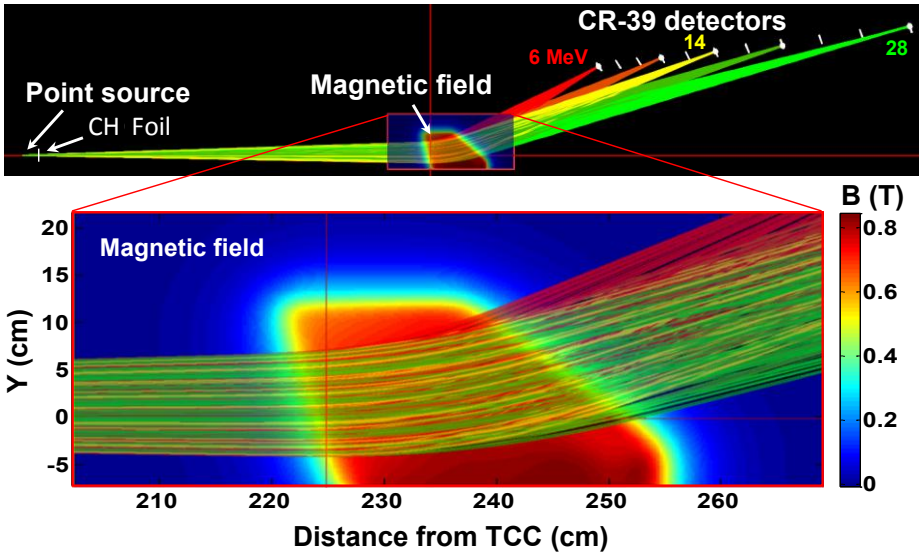

Figure 4-16: An illustration of a Geant4[64] model of the MRS response, featuring a simulation of 6, 10, 14, 18 and 28 MeV recoil protons from a CH_2 foil. The magnetic field has been designed to focus recoil protons (or deuterons) with very different trajectories through the system. The CR-39 detectors, which are oriented for normal particle incidence, are positioned at the focal plane of the spectrometer (the location of best focus).

Examples of *ab initio* modeled MRS-response functions for the medium and low-resolution CD-foil configurations, discussed in Table 4-1, are illustrated in Figure 4-17b. These recoil-deuteron spectra were calculated using the primary DT neutron spectrum shown in Figure 4-17a ($Y_n=3\times10^{13}$, $T_i=5$keV). Using the same neutron source spectrum as shown in Figure 4-17a, the MRS-response function for a 100μm CH_2 foil (high resolution) is shown in Figure 4-18b. Also shown in Figure 4-18b are the MRS-response functions for a 100μm CH_2 with a 140μm and 80μm tantalum filter behind to range down the recoil protons to an average energy of 10 MeV and 12 MeV, respectively. The idea of these measurements was to probe the MRS calibration at these energies.

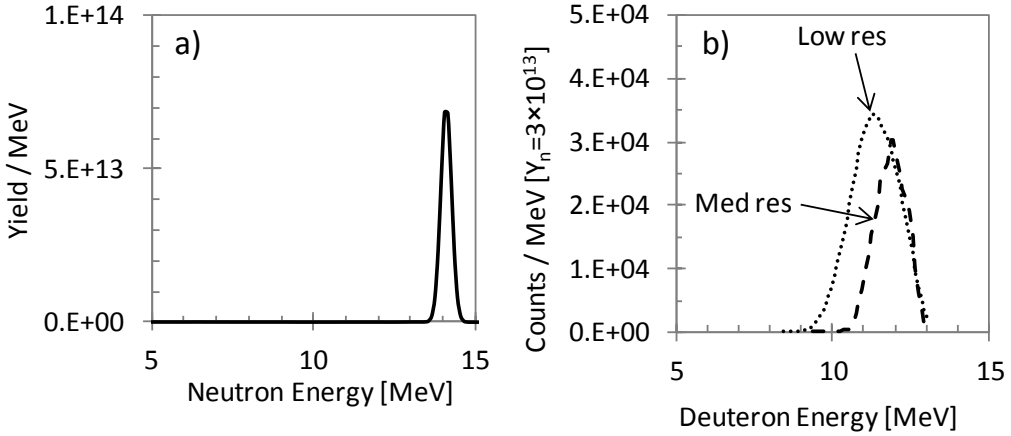

Figure 4-17: Examples of *ab initio* modeled MRS-response functions for the medium and low-resolution CD_2-foil configurations. a) Primary DT neutron spectrum (Y_n=3×10^{13}, T_i=5keV) used in these calculations. b) Recoil-deuteron spectra calculated for the CD_2 medium and low-resolution configurations (see Table 4-1). As shown by these two spectra, there is a tradeoff between efficiency and energy resolution.

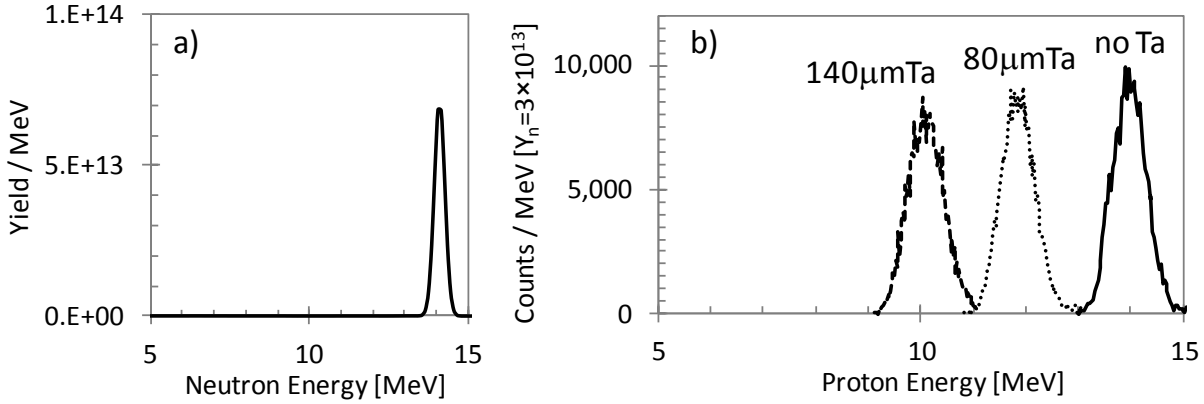

Figure 4-18: Examples of *ab initio* modeled MRS-response functions for 100μm CH_2 foil configurations with different amounts of tantalum filtering behind. a) Primary DT neutron spectrum (Y_n=3×10^{13}, T_i=5keV) used in these calculations. b) Recoil-proton spectra calculated for a 100μm CH_2 foil with a 140μm and 80μm tantalum filter behind to range down the recoil protons to an average energy of 10 MeV and 12 MeV, respectively. The recoil-proton spectrum generated without the Ta filter is also shown.

Ab initio modeling of the NIF-MRS response was also conducted for different configurations prior to installation. In Figure 4-19, the response for the MRS in high, medium, and low-resolution mode, discussed in Table 4-1, are shown. The DT neutron source spectrum (Y_n=10^{14}, T_i=5keV) used in these calculations is illustrated in Figure 4-19a.

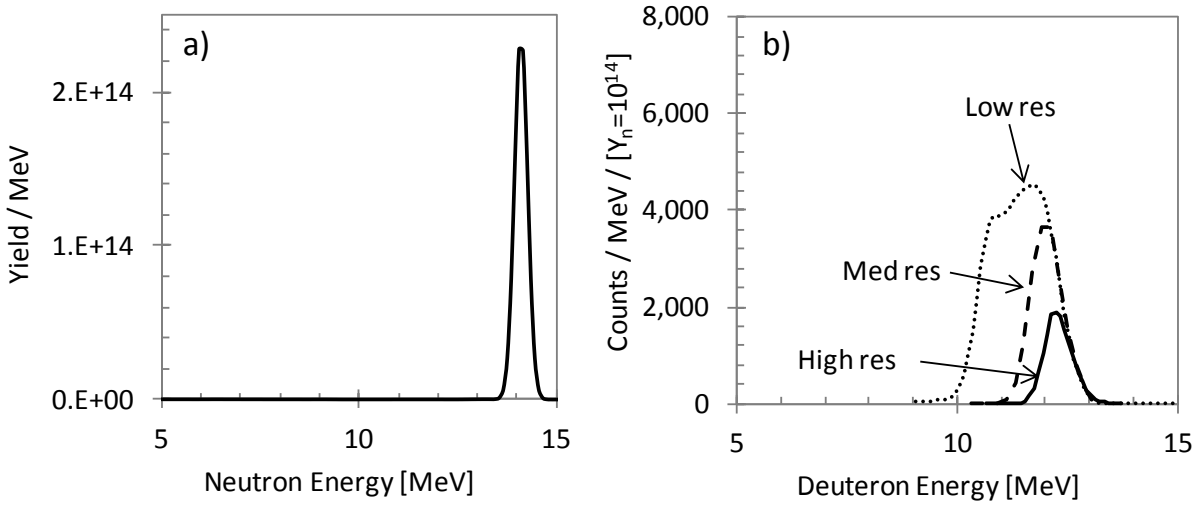

Figure 4-19: Examples of *ab initio* modeled MRS-response functions for the high, medium, and low-resolution CD_2-foil configurations. a) Primary DT neutron spectrum ($Y_n=10^{14}$, T_i=5keV) used in these calculations. b) Recoil-deuteron spectra calculated for these configurations (see Table 4-1). As shown by these three spectra, there is a tradeoff between efficiency and energy resolution for the NIF MRS.

4.3.2 *In situ* energy calibration of the MRS on OMEGA and the NIF

A series of *in situ* calibration experiments were conducted to check the performance of the as-built OMEGA MRS[24] and the NIF MRS. As the *ab initio* modeling used nominal spectrometer settings, this type of calibration experiment is required to quantify a possible misalignment of the magnet, detectors, and small changes in the magnetic field from the modeled one. For these experiments, a series of DT-gas filled CH capsules with a nominal diameter of 850 μm, a fill pressure of 15 atm, and shell thicknesses of 15 μm were imploded with a 1ns square laser pulse shape, delivering ~ 23 kJ of UV-energy at OMEGA. Primary neutron yields in the range of ~10^{13} to ~3×10^{13} and T_i in the range of 5-6 keV were produced in these implosions. An accurate yield and energy calibration of the MRS could therefore be obtained, as these yields were high enough to allow the MRS to operate in a high-resolution mode. The Doppler broadened primary DT neutrons were used to produce recoil protons and deuterons from a 100μm CH_2 foil and 60μm CD_2 foil, respectively. This provided two well-known calibration points at a proton energy of 13.9 MeV and a deuteron energy of 12.4 MeV. The deuteron energy corresponds to a proton equivalent of 24.6 MeV (this number is determined by the mass ratio times the deuteron energy with a small relativistic correction). These experiments were repeated with different thicknesses of tantalum foil positioned behind the CH_2 and CD_2 foils to obtain calibration points at various energies. Figure 4-20 shows the experimental results for three shots that used 100μm CH_2: one with no filter (13.9MeV), one with an 80μm Ta filter (11.8MeV), and one with a 140 μm Ta filter (10.1MeV). Figure 4-20 also compares the experimental results to the Geant4 simulated spectra, which were obtained after a -1.1% correction to the magnetic field had been applied to the model.

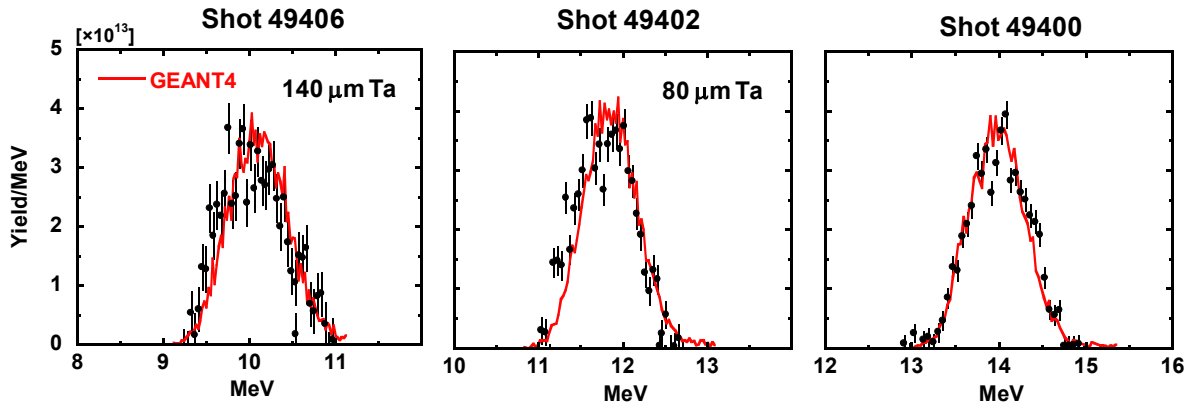

Figure 4-20: Examples of recoil-proton spectra obtained from the *in situ* energy calibration of the OMEGA MRS, using DT primary neutrons produced in DT-gas filled CH capsule implosions. A 100μm CH_2 foil with a 140μm or 80μm tantalum filter behind was used to probe the energy characteristics of the as-built MRS at ~10 MeV and ~12 MeV, respectively. A recoil-proton spectrum was also recorded when no tantalum was positioned behind the CH_2 foil (shot 49400). The spectra were explained by Geant4 modeling (red spectra) after a -1.1% uniform scale factor had been applied to the magnetic field.

This type of *in situ* energy calibration experiment was repeated by using CH_2 and CD_2 foils and different filters behind these foils. The results from those experiments are shown in Figure 4-21, in which the proton equivalent energy at the center of a CR-39 detector is plotted as a function of detector-window number (position along the focal plane could have been used as well on the x axis). The results are compared to the nominal *ab initio* simulated energy calibration (dashed curved) and the *in situ* energy calibration (solid curve). A -1.1% uniformly scaled field provided a better fit to the data over the entire array, improving the proton equivalent energy uncertainty from ±430 keV to ±160 keV. This translates to a neutron energy error of ±100keV when using the CD_2 foil.

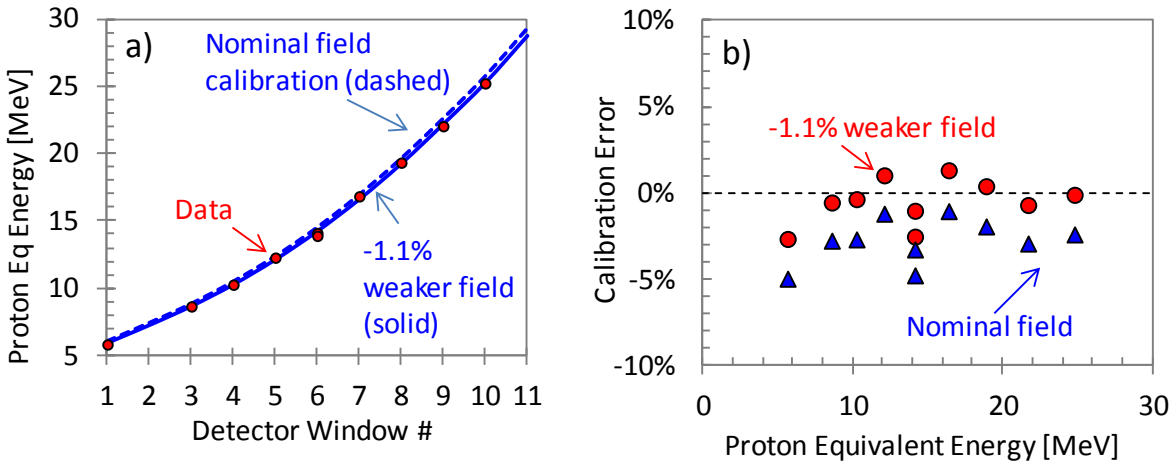

Figure 4-21: Measured and modeled energy (proton equivalent) as a function of detector window for the OMEGA MRS (as each CR-39 has a certain width, the energy representing the center of the CR-39 is plotted here). The dashed curve was determined from the *ab initio* modeling of the MRS, in which a nominal magnetic field was used. The solid curve represents the *in situ* energy calibration of the MRS, in which the strength of the magnetic field was reduced by 1.1%. The data were obtained using the primary DT neutron spectrum and CH_2 and CD_2 foils. The energies below 15 MeV were probed by recoil protons from a CH_2 foil, while energies above 15 MeV were probed with recoil deuterons from a CD_2 foil. b) Estimated calibration error calculated from the difference between the particle energy and the energy inferred from the calibration for the nominal field (blue triangles) and the -1.1% weaker field (red points). The estimated energy error is improved to ±160 keV from ±430 keV (proton equivalent energy) using the -1.1% field correction.

Similarly, *in situ* energy calibration data, shown in Figure 4-22, were obtained with the NIF MRS when operated with a medium resolution CD_2 foil (Table 4-1). In these experiments, the DT primary neutron spectrum from a DT gas-filled SiO_2 capsule implosion (N101212) and a cryogenic DT capsule implosion (N110914) was used. The solid red curve is the deuteron energy distribution entering the system. The measured deuteron spectrum for N110914 is shown by the red solid points. This spectrum revealed that the *ab initio* calibration was significantly off. By increasing the modeled magnetic field with about 5%, the modeled spectrum matches the measured recoil-deuteron spectrum very well. The other spectrum (solid blue points) for N101212 was obtained at lower energies using a 75μm thick Ta filter behind the foil, which ranged the average recoil-deuteron energy from 12.0 MeV to 8.4 MeV (23.8 MeV and 16.7 MeV proton equivalent energies). Once again, the magnetic field had to be increased by 5% to match the experimental observation. This modification of the *ab initio* modeling is not surprising, as the field in the NIF-MRS magnet was measured to be 6% higher than the field in the OMEGA-MRS magnet (see Figure 4-8). These experiments show that the corrected Geant4 modeling provides an accurate description of the as-built NIF-MRS performance.

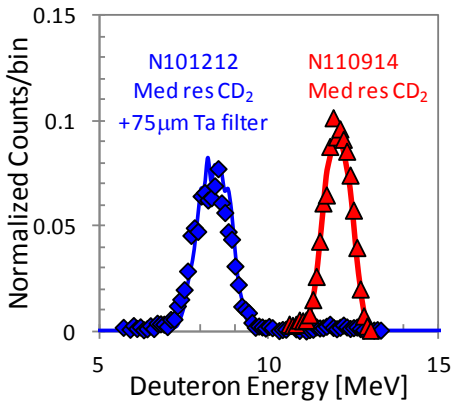

Figure 4-22: *In situ* calibration data obtained with the installed, as-built NIF MRS. For the calibration, DT primary neutrons from a DT-gas filled SiO_2 capsule implosion (N101212) and a cryogenic DT capsule implosion (N110914) were used. The medium resolution CD_2 foil (see Table 4-1) was used without a ranging filter (red solid points) and with a 75μm thick tantalum filter behind (blue solid points) to probe the energy characteristics of the as-built MRS around 12.0 MeV and 8.4MeV (23.8 MeV and 16.7 MeV proton equivalent energies), respectively. The *ab initio* calibration was corrected *in situ* using a 5% stronger modeled field (solid spectra).

Additional checks of the *in situ* energy calibration of the NIF MRS were conducted, and one of those experiments used D^3He protons from a D^3He gas-filled exploding-pusher implosion. In this experiment, a 196μm stainless steel filter with a rectangular hole in it, replaced the CD_2 to obtain two proton-energy calibration points at ~14.7 MeV and ~11.2 MeV. This split-filter is depicted in Figure 4-23a. In Figure 4-23b, the measured data obtained with the *in situ* energy calibration described earlier is shown. Excellent agreement between the modeled and measured spectra, illustrated in Figure 4-22 and Figure 4-23, show that the MRS provides excellent data from 11 – 24 MeV proton equivalent energies. Further, calibration data at lower energies were not available at the time when this thesis was written but data already taken show that the energy calibration of the NIF MRS is accurate to ±100keV proton equivalent energy, which corresponds to ±60 keV neutron energy when using the CD_2 foil.

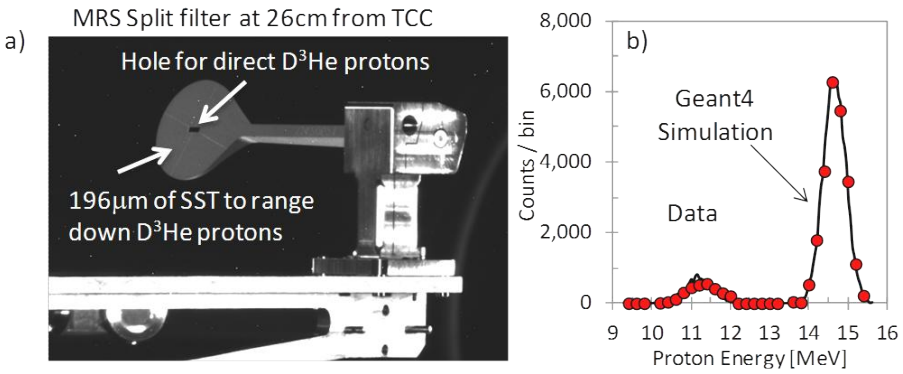

Figure 4-23: a) Image of the 196μm stainless steel filter with a rectangular hole in it, which replaced the CD_2 foil typically used in DT experiments. In this calibration experiment, D^3He protons were used from a D^3He gas-filled exploding-pusher implosion (N110722). The filter was used to obtain two energy calibration points by allowing direct ~14.7 MeV D^3He protons to go through the hole in the center, and ranging some D^3He protons down to ~11.2 MeV through 196μm stainless steel filter. b) Measured D^3He proton spectrum, which displays two peaks as expected. The measured spectrum is in excellent agreement (~100keV) with the *in situ* calibrated modeled spectrum.

Having established that the Geant4 model of the MRS can adequately describe the data measured with the MRS on OMEGA and the NIF, it can be used to construct a more detailed response of the systems. The coordinate along each individual CR-39 detector in the energy-dispersion direction is represented by $x_{CR\text{-}39}$ (shown in Figure 4-24). The signal region on each individual detector is 4.5 cm and 4.0 cm wide for the OMEGA MRS and NIF MRS, respectively, where the origin of the $x_{CR\text{-}39}$ coordinate is defined by the high-energy edge of each detector window.

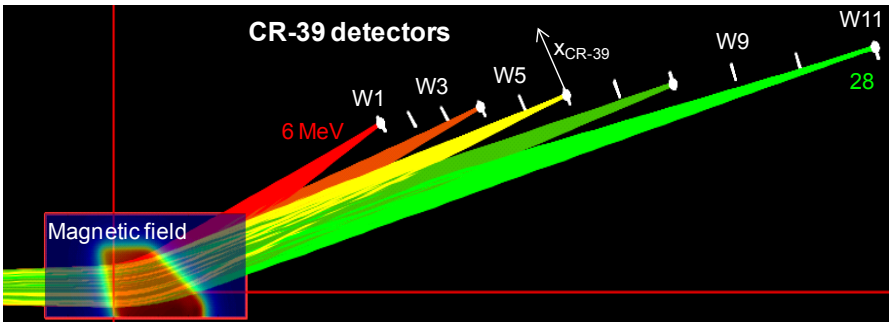

Figure 4-24: An illustration of the CR-39 detector arrangement for the OMEGA MRS. Simulated trajectories for protons with energies of 6, 12, 18, 22 and 28 MeV are also shown. The detector windows are identified as W1, W2,…, W11, where W11 detects protons (or deuterons) with the highest energies. The $x_{CR\text{-}39}$ coordinate along each individual CR-39 detector window increases with decreasing energy of the particle.

The initial plan was to operate the MRS in either CH_2 or CD_2 mode depending on application, but after the first set of *in situ* calibration experiments, it was clear that the MRS in CD_2 mode was far superior in performance to the MRS in CH_2 mode. It was therefore decided to run the MRS in CD_2 mode until the issues with the CH_2 mode, primarily due to small and relatively faint proton tracks

and high levels of intrinsic background in the CR-39 (defects), had been resolved. From this point on, only recoil-deuteron data is therefore discussed unless otherwise specified. In Figure 4-25a and Figure 4-25b, the detailed response of the OMEGA MRS operated in low-resolution mode and the NIF MRS operated in medium-resolution mode is shown, respectively. Also shown in Figure 4-25, as black dashed curves, are the best-fit polynomials to the simulated response (deuteron energy vs $x_{CR\text{-}39}$ for each window).

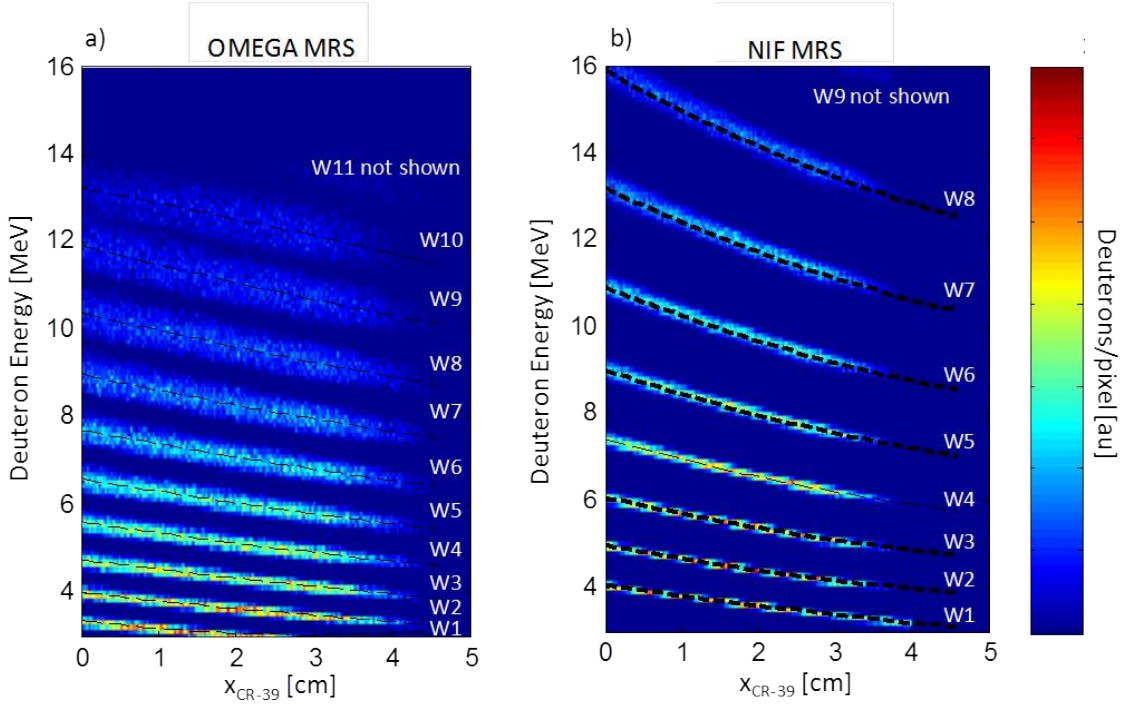

Figure 4-25: a) Geant4 simulated response of the OMEGA MRS when operated with a CD_2 foil in low-resolution mode. The simulated data is presented in the form of the number of recoil deuterons per pixel at a specified $x_{CR\text{-}39}$ and corresponding deuteron energy for a given detector window. The dashed black curves are polynomial fits to the simulated data, which are used to convert the recorded particle-track position into energy. As mentioned earlier, deuteron and proton energy calibrations are interchangeable through Equation (4-2), i.e. $E_p \sim 2E_d$. b) Geant4 simulated response of the NIF MRS when operated with a CD_2 foil in medium-resolution mode.

4. 4 Characterization of the MRS parameters

A summary of the spectrometer parameters and associated uncertainties are given in Table 4-1. The characterization of each parameter shown in that table is discussed in detail in this section. In addition, as the CD_2 foil is not an off-the-shelf item that can be purchased, this section also describes how they are manufactured to the required tolerances.

4.4.1 Manufacturing CD_2 foil

The CD_2 foils are manufactured from a deuterium powder that is manufactured by ISOTEC Sigma Aldrich.[71] From this powder, which contains 98% deuterium (atom percent), the first CD_2

foils for the OMEGA MRS were developed and produced by Dr. Kurt Fletcher et al. at Geneseo State University.[72] Two manufacturing methods were explored and used: the xylene and heated-press methods. In the xylene method, the CD_2 powder is dissolved into a xylene liquid solvent under heat. When exposed to the heat for a certain period of time (minutes to hours), the solvent evaporates, leaving a thin foil of CD_2 at the bottom of the container. In the heated-press method, the powder is pressed in a mold under high pressures at an elevated temperature, resulting in a uniform foil.[72] Both types of foils have been used for the OMEGA MRS and produced good data. The CD_2 foils for the NIF MRS have, on the other hand, been manufactured by General Atomics (GA),[73] who only used the heated-press method. From the experience gained at the Geneseo State University, they improved the manufacturing process and produced excellent foils that well exceeded the requirement. X-ray radiographs of the foils (see Figure 4-26) showed that the amount of voids in the foil, areal density variations, and amount of micro-structure defects and cracks are well within specifications. Therefore, the uncertainties in the deuterium-number density, effective foil area, and average foil thickness are within specifications. As a consequence, the xylene made CD_2 foils for the OMEGA MRS are being phased out and replaced by GA heated-press foils.

4.4.2 Characterization of the CD_2-foil density, area and thickness

The average density of the CD_2 foil is determined from mass and volume measurements. The determined density of the OMEGA low resolution foil is $1.03\pm0.03 g/cm^3$, which should be compared to the density of $1.08 g/cm^3$ for pure deuterated polyethylene.[74] This difference is due to the introduction of microscopic voids during the preparation of the foils (see Figure 4-26). The average density of the GA foils is $1.07\ g/cm^3$ and thus much closer to the literature value. The density variation of the GA foils was also as small as ±2%, which is due to a smaller fraction of voids in these foils.

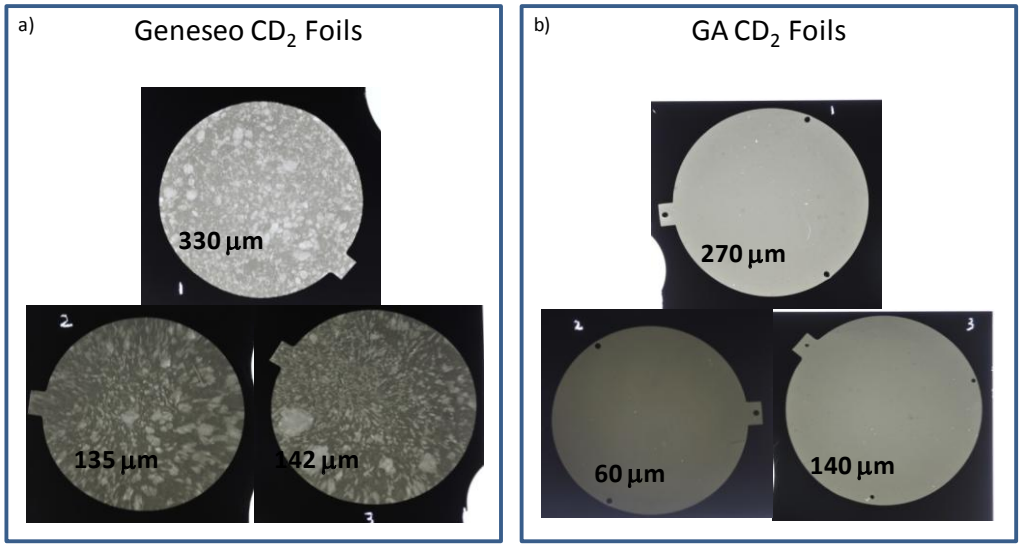

Figure 4-26: X-ray radiographs of the CD_2 foils produced by Geneseo and GA. These images show that the GA-produced CD_2 foils have smaller fractions of voids and thus more uniform density. Photos courtesy of Reny Paguio, GA LLC.[75]

The solid angle subtended by the foil is determined from the foil area (A) and foil distance from the implosion (d), i.e,

$$\Omega_n = \frac{\mathrm{A}}{4\pi d^2}. \tag{4-5}$$

At OMEGA, the NDI is used to position the foil at a nominal distance of 10cm from the implosion or TCC. However, as the foil holder tends to get warped over time (due to intense heat exposure), and the fact that the foil is often not attached flush-on to the holder (cupping), the actual distance of the foil to TCC is different from the nominal value, which must be accounted for in determination of the detection efficiency (recall Equation (4-3)). Due to the energy and impulse-loading constraints on the NIF, the foil for the NIF MRS is positioned at a distance of 26cm from TCC (DIM 90-315 is used for the positioning of the foil). The foil is also positioned behind a protective blast shield, which prevents the foil holder from getting bent or warped. As a consequence, only cupping of the foil is a slight issue for the NIF MRS, but this is less of a problem than for the OMEGA MRS as the NIF MRS foil is positioned further away from TCC. Although the cupping is only a minor issue for the NIF MRS, the foil holder is being redesigned with a new four-point mount to help mitigate this issue.

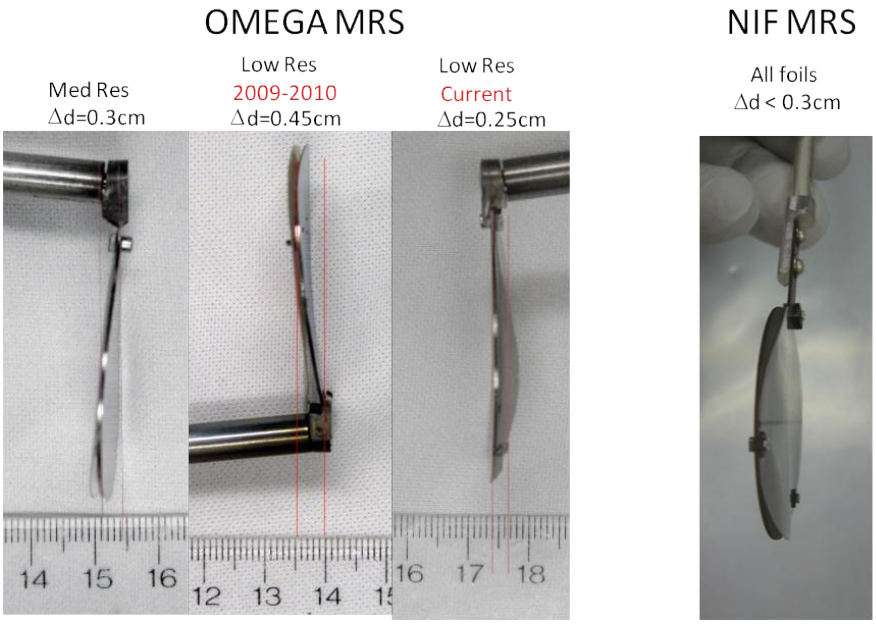

Figure 4-27: Images of the CD_2 foils for the OMEGA MRS and NIF MRS, which illustrate the foil-holder warping and foil-cupping issues. The warping issue, which is mainly caused by intense heat exposure, only exists for the OMEGA MRS, as no protective blast shield is positioned in front of the foil holder (a 500μm thick SST plate in front of and in direct contact with the foil). The foil-cupping issue, on the other hand, exists for both the OMEGA MRS and NIF MRS. These issues result in a distance offset of about 2-5mm from the nominal value for the OMEGA MRS and up to 2mm for the NIF MRS. In case of the NIF MRS, this is not a significant issue as the nominal foil distance is 26cm.

Two approaches have been used to determine the area of the CD_2 foil. In the first method, an image analysis was used to determine the area from a photo taken of the foil. This method was only applied to the OMEGA-MRS foils. In the analysis, a known area of reference, covering a certain number of pixels in the image, was used to convert the number of pixels covered by the foil into an area (see Figure 4-28a). Multiple measurements with different area references indicated an uncertainty of $\pm 0.1 cm^2$ associated with this method. Using this method, the low resolution foil for the OMEGA MRS was determined to be $13.19 cm^2 \pm 0.1 cm^2$. In the second method, the CD_2 foils were precision die cut by GA, and the uncertainty associated with this method was also estimated to be $\pm 0.1 cm^2$. This method was applied to all NIF-MRS foils.

The average thickness of the low-resolution OMEGA foil was measured with a micrometer and the average thickness was 261.3 μm with a standard deviation of 18μm (thickness map is shown Figure 4-28b). The uncertainty in the average thickness is ±1μm, which typically represents the uncertainty for the determined average thickness of foils for the OMEGA MRS. The NIF MRS foils were measured at GA using a similar method with an absolute uncertainty of ±1μm, see Figure 4-29b. The standard deviation of the low resolution GA foil thickness is 5 μm. The high-mode surface roughness of the foil was evaluated for a large sample of foils using an interferometry method. With this method, it was found that the roughness was on average 0.5-1μm (RMS) for the Geneseo manufactured foils and ~0.2μm for the GA manufactured foils.

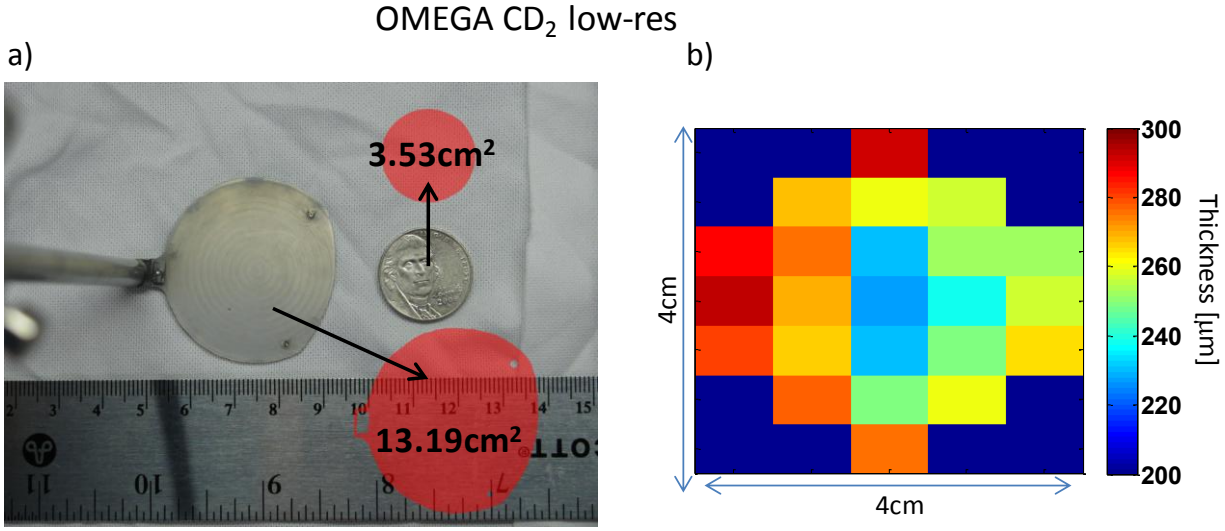

Figure 4-28: Image of the OMEGA-MRS low resolution CD_2 foil. The measured area of the foil is $13.19 \pm 0.1 cm^2$. To avoid interference between the foil and gate valve during the foil insertion process, the shape of the foil had to be non circular (this is only an issue for the foils larger than $11 cm^2$). Also shown, is a United States nickel (minted in 2006) used as a reference area for the foil area measurement, as described in the text. b) The measured thickness profile of the OMEGA low-resolution foil. The mean thickness is 261.3±1μm, and the thickness variation across the foil is characterized by a standard deviation of 18μm.

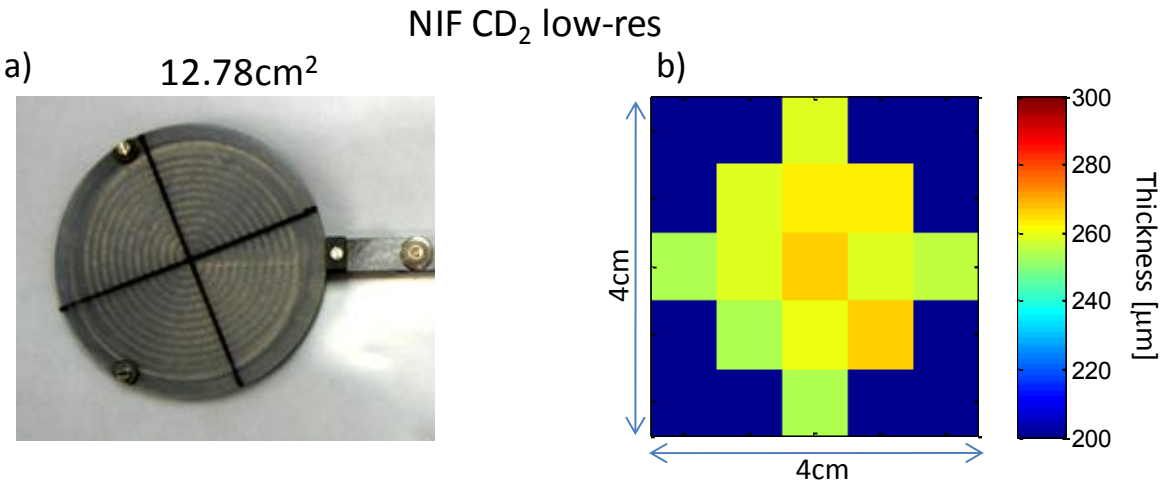

Figure 4-29: Image of the NIF MRS low resolution CD_2 foil (produced and characterized by GA). The area and average thickness of this foil is 12.78±0.1cm^2 and 259±1μm, respectively. The thickness variation across the foil is characterized by a standard deviation of 5 μm.

4.4.3 The differential cross section for elastic n-d scattering in the laboratory system

The differential cross-section for the elastic n-d scattering in the laboratory system for neutron energies in the range 3.5-18 MeV is an important parameter that needs to be considered when determining the detection efficiency for the MRS (see Equation (4-3)). The uncertainty in the evaluated cross-sections, obtained from the ENDF/B-VII.0 nuclear database,[13] also play an important role when determining the absolute spectrum from the measured recoil-deuteron spectrum. As these cross-sections are well known for the neutron energies of relevance, the MRS detection efficiency (and therefore the absolute neutron spectrum) can be determined with high accuracy. Figure 4-30a shows the angular differential cross-sections in the laboratory system for neutron energies of 5.6 and 14.1 MeV. Figure 4-30b shows the total cross section for the n-d elastic scattering as a function of neutron energy. See also Appendix A, for a detailed discussion of cross-sections in the center-of-mass (CM) and laboratory systems. The geometric consideration of the foil and magnet aperture of the cross-section is made using the Monte Carlo code MCNPX.[57] The uncertainty in the forward scatter differential cross-section at 14MeV is 2.3%.[76]

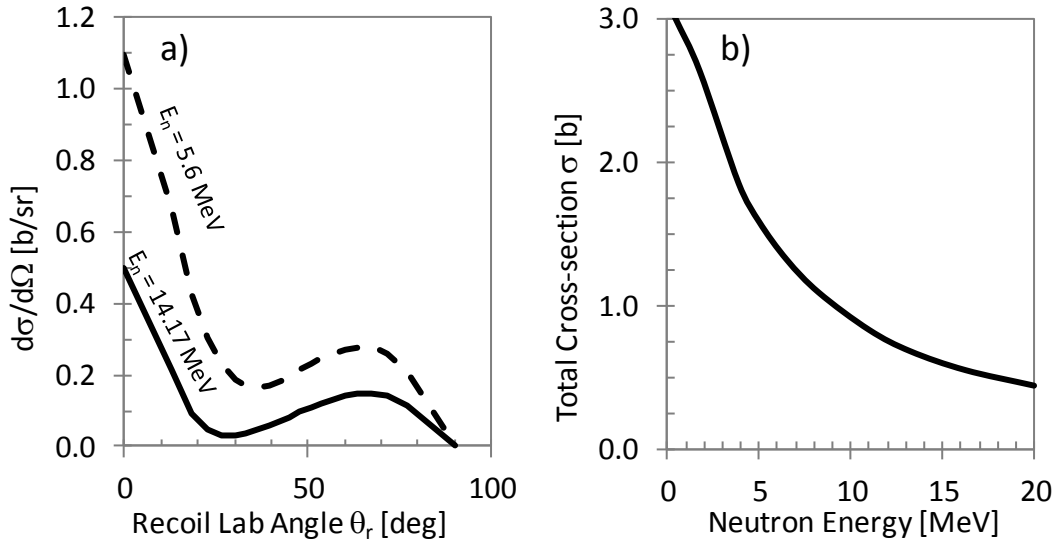

Figure 4-30: a) The differential cross-section for the elastic n-d scattering at neutron energies of 5.6 and 14.1 MeV as a function of laboratory scattering angle. The laboratory scattering angle θ_r is the angle between the incoming neutron and outgoing recoil deuteron. These cross-sections were obtained from the ENDF/B-VII.0[13] library. The location and geometry of the aperture with respect to the foil is such that only forward scattered recoil particles (θ_r~0) are accepted. b) The total cross section for the elastic n-d scattering, which can be obtained by integrating the angular differential scattering cross-sections, shown in a. The total cross sections were also obtained from the from the ENDF/B-VII.0[13] library.

4.4.4 The magnet aperture

For the OMEGA MRS and the NIF MRS, the magnet aperture is an 11×2cm^2 and 10×2cm^2 rectangular hole, respectively; cut out of a 500μm thick Tantalum plate. Highly accurate electrical discharge machining (EDM) was used to manufacture these apertures, and the estimated uncertainty in the aperture area is ± 0.2cm^2.[25] As the aperture is directly attached to the wedge shaped magnet (see Figure 4-31), it is tilted with 14.2° with respect to the incoming recoil protons or deuterons. This reduces the effective aperture area with 3%. More importantly, since the distance of the aperture relative to the CD_2 foil is 215cm and 570cm on the OMEGA MRS and NIF MRS, respectively, any error in the location of the aperture with respect to the MRS LOS and has an insignificant impact on the detection efficiency.

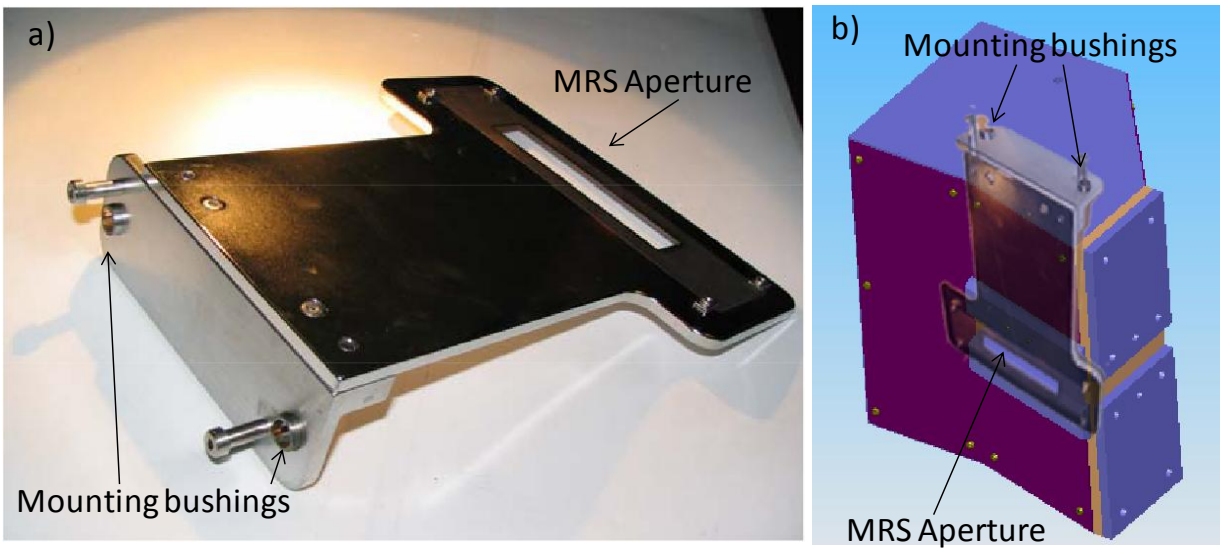

Figure 4-31: a) Image of the OMEGA MRS 11×2cm^2 aperture attached to the mounting plate, which attaches to the front of the magnet. b) Image of MRS aperture super-imposed on a CAD drawing of the MRS magnet to illustrate the relative location of the aperture on the magnet and where the aperture plate attaches.

4.4.5 The effect of the NDI-interception on the OMEGA-MRS data

It was recently found on OMEGA that the MRS-foil inserter, NDI, interferes slightly with the path of the recoil-deuteron beam, defined by the foil area and magnet aperture. The geometry is illustrated in Figure 4-32. As a consequence, a fraction of the produced recoil deuterons do not reach the aperture. This interception produces an asymmetric signal distribution in the direction perpendicular to the dispersion plane. Data obtained with the OMEGA MRS operated in medium resolution and low resolution that illustrates this asymmetric behavior is shown in Figure 4-33a and Figure 4-33b, respectively. These data were obtained when diagnosing DT-gas filled CH-capsule implosions. In the figures, the black dashed curves are simulated signal distributions when the NDI does not intercept the recoil-deuteron beam, and the blue dashed curves, which give the best fits to the data, are simulated signal distributions when the NDI intercepts the recoil-deuteron-beam path as shown in Figure 4-32. The best fits to the data indicate that a correction factor of 0.86 ± 0.013 should be applied to the MRS-detection efficiency for the low-resolution foil (uniformly over all energies) and 0.87 ± 0.013 for the medium-resolution foil. Engineering solutions to this issue are currently being implemented. This interception issue is not present at the NIF, as a totally different engineering solution is being used.

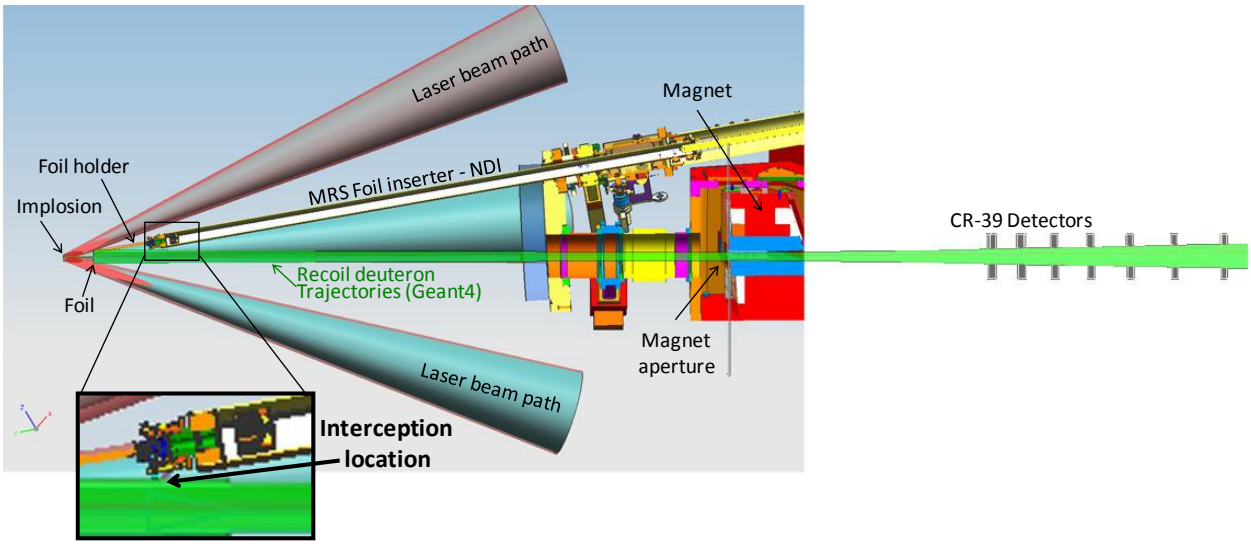

Figure 4-32: Illustration of the MRS and the MRS foil inserter (NDI) with super-imposed deuteron trajectories simulated with Geant4.The location where the NDI intercepts deuterons from the foil is illustrated in this drawing at the coupling between the foil holder and NDI.

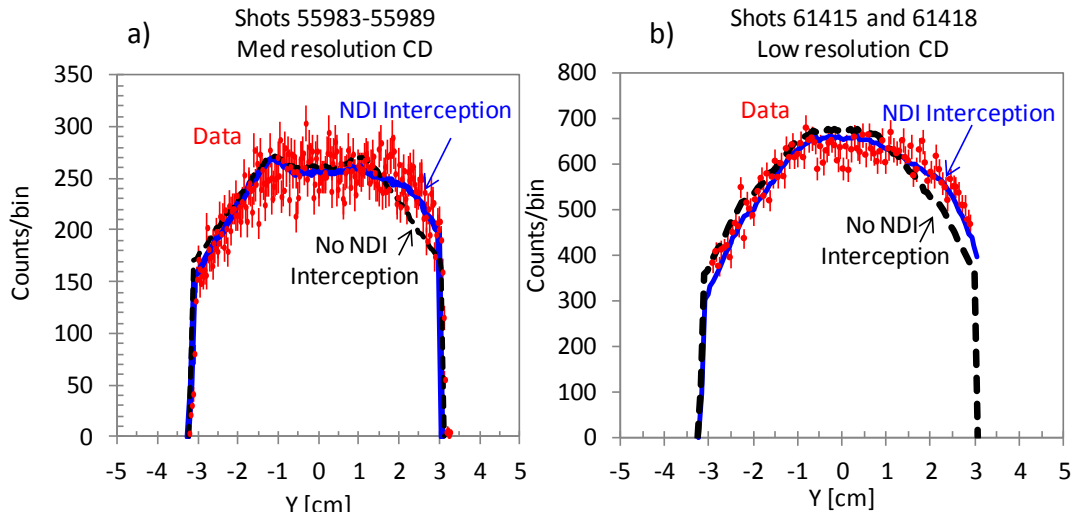

Figure 4-33: a) Measured and simulated signal distributions, in the direction perpendicular to the bending plane (geometry illustrated in Figure 4-32) for the MRS operated in medium resolution. The data was summed over shots 55983-55989. The black dashed curve represents a simulation with the NDI not intercepting the recoil-deuteron beam and the blue dashed curve represents a simulation with the NDI intercepting the recoil-deuteron beam. The simulation of the NDI interception was obtained by adjusting the height of NDI foil-holder coupling until the best fit to the data was found. b) Same modeling as in (a), but for the MRS operated in low resolution compared to data obtained from a summation shots 61415 and 61418. Both cases indicate a detection-efficiency reduction of 13-14% due to the NDI interception for all deuteron energies. An engineering solution to this issue is currently being implemented. This interception issue is not present at the NIF, as a totally different engineering solution is being used.

In addition, all deuterons that enter the aperture are not detected with the OMEGA MRS, as their spatial spread, in the direction perpendicular to the bending plane, is larger than the length of the CR-39 detectors. As a result, a fraction of the aperture-selected deuterons will not be recorded by the CR-39 detector array by design. This is accounted for in the detection-efficiency calculation, through the transmission parameter [$T(E_d)$]. $T(E_d)$ decreases with increasing deuteron energy because the deuteron-beam path diverges in the direction perpendicular to the bending plane and the CR-39 detectors covering higher energies are further away from the magnet. A simulated signal distribution in the non-dispersion direction of primary DT data using the OMEGA-MRS operated in low-resolution mode is shown and compared to data in Figure 4-34a. The simulation indicates that $T(12.5)$ = 0.79± 0.013 (averaged over the primary peak), and therefore 21% of the recoil deuterons are not recorded. For comparison, NIF-MRS data is shown Figure 4-34b, which illustrates that the T = 1.0 (this applies to all energies), which is due to better ion-optical properties of the NIF MRS. A plot of the transmission as a function of deuteron energy for OMEGA MRS and the NIF MRS is shown in Figure 4-35.

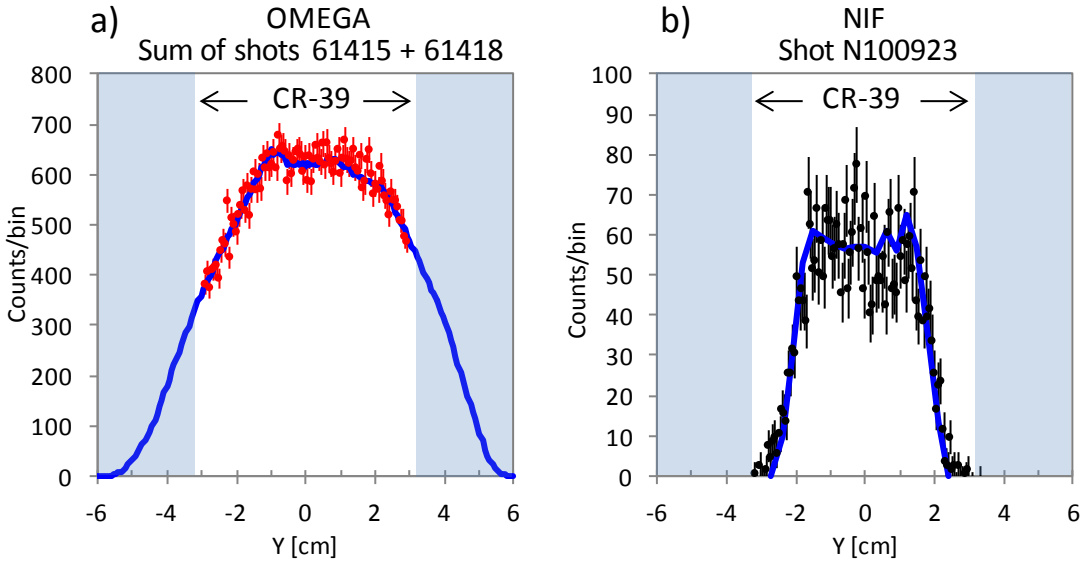

Figure 4-34: a) Measured and simulated signal distributions, in the direction perpendicular to the bending plane, for the OMEGA MRS, which indicate a transmission of $T(12.5)$ = 0.79±0.03 at about 12.5 MeV (which corresponds to a neutron energy of 14 MeV) (a) and the NIF MRS (b) operated in low resolution. These signal distributions were generated by primary DT neutrons. b) Measured and simulated signal distributions, in the direction perpendicular to the bending plane, for the NIF MRS. Due to the ion-optical properties of the NIF MRS, the transmission is 1.0 for all deuteron energies.

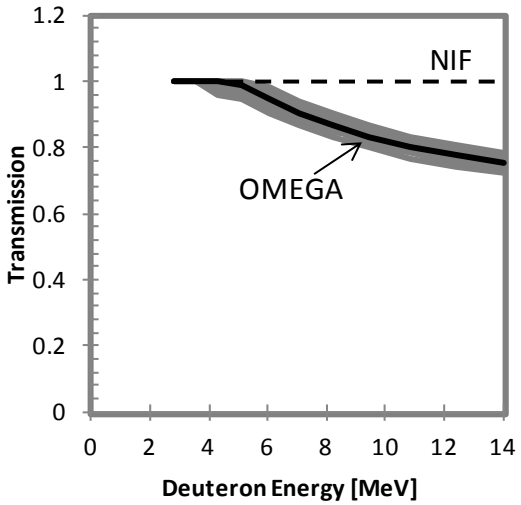

Figure 4-35: Transmission as a function of deuteron energy for the OMEGA MRS (solid line) and NIF MRS (dashed line). The uncertainty in the OMEGA MRS transmission function, inferred from experiments with different aperture sizes, is shown by the grey region around the solid line. Due to the ion-optical properties of the NIF MRS, the transmission is 1.0 for all deuteron energies.

4.5 Geant4 simulations of the complete MRS-response function

With an excellent understanding of the as-built MRS on OMEGA and the NIF, a complete MRS response function for the different configurations can now be generated with Geant4. This is accomplished by computing the deuteron spectrum at the CR-39 detector array, for neutron energies of 3.05, 3.105, …, 26.95 MeV. The energy calibration polynomials are used to convert position along the CR-39 detector plane into deuteron energy. The output of this calculation is a 240 × 240 response matrix. The utility of this matrix is that it allows a modeled neutron spectrum to be directly folded with the MRS-response function in one simple step, instead of running a full Geant4 simulation each time a measured MRS spectrum is analyzed. As each MRS configuration has a foil with different measured thickness and area, it must have its own specific response matrix. The OMEGA MRS-response matrices for the medium-resolution (10.64cm^2 area 164μm thick) and low-resolution (13.19cm^2 area 261μm thick) CD_2 foils are shown in Figure 4-36.

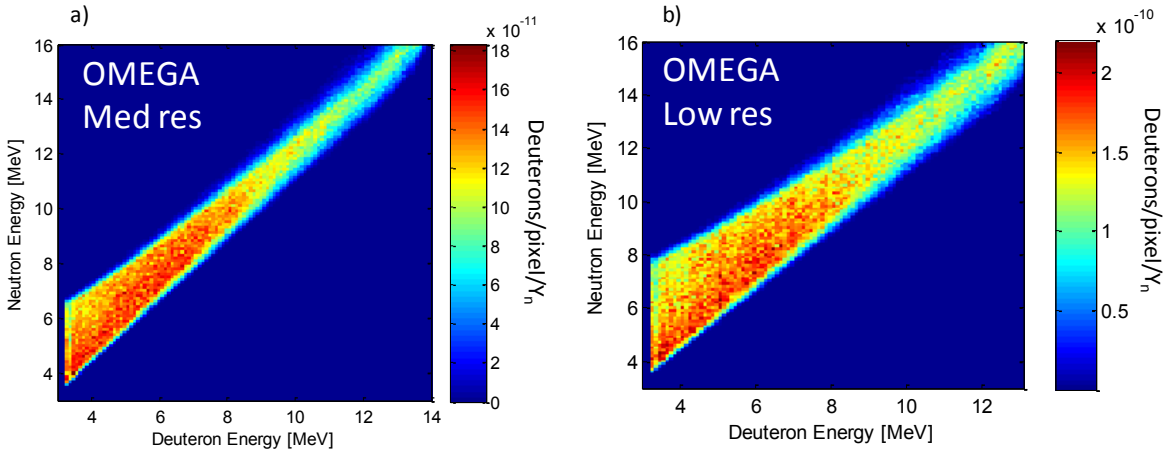

Figure 4-36: The response matrices for the OMEGA MRS operated in medium resolution (a) and low resolution (b) (see Table 4-1 for these spectrometer configurations). As shown by both matrices, the energy broadening is more significant at lower energies. The response matrix is used to determine the neutron spectrum from the measured recoil deuteron spectrum. This is done by folding a modeled neutron spectrum with the response matrix and by adjusting the neutron spectrum until best fit to the measured spectrum is found

Figure 4-38a illustrates MRS spectra summed over a series of 20μm CH-capsule implosions (shots 54472-54474) and 15μm CH-capsule implosions (shots 58165 & 58209-58210), which produced 3.2×10^{13} and 5.0×10^{13} primary neutrons, respectively (these yields were measured with the nTOF diagnostic).[44] The blue spectrum was obtained when the MRS was operated in medium resolution, and the red spectrum was obtained when the MRS was operated in low resolution. The modeled neutron spectra that provide the best fit to the measured spectra are shown in Figure 4-38b. Judging the data, the simulated and measured energy responses are in excellent agreement. Also, the total neutron yield determined the measured spectra are in agreement with the nTOF yields (discussed quantitatively in Chapter 5).

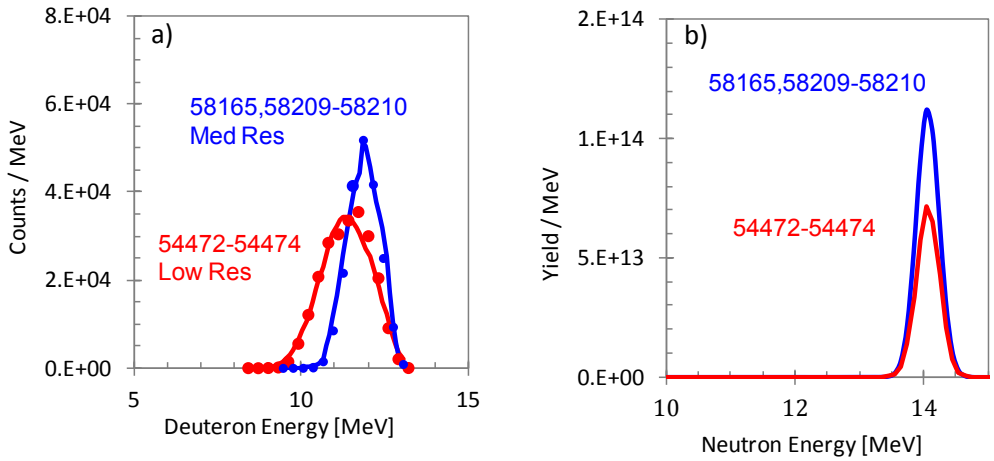

Figure 4-37: a) MRS spectra summed over a series of 15 μm CH-capsule implosions (blue spectrum) and 20 μm CH-capsule implosions (red spectrum), which produced 5.0×10^{13} and 3.2×10^{13} primary neutrons, respectively. Due to different average energy losses in the CD_2 foil, the average energy of the deuterons is 11.4 and 11.8 MeV for the low and med resolution foils, respectively. Energy kinematics (second term in Equation (4-4)) also causes some energy down shift of the recoil deuterons. b) Modeled neutron spectra that provide the best fits to the measured recoil-deuteron spectra.

The response matrices for the NIF MRS operated with a low-resolution ($12.78cm^2$ area and 259 μm thick), a medium resolution ($12.78cm^2$ area and 138μm thick), and a high-resolution ($12.78cm^2$ area and 47μm thick) CD_2 foil are shown in Figure 4-38.

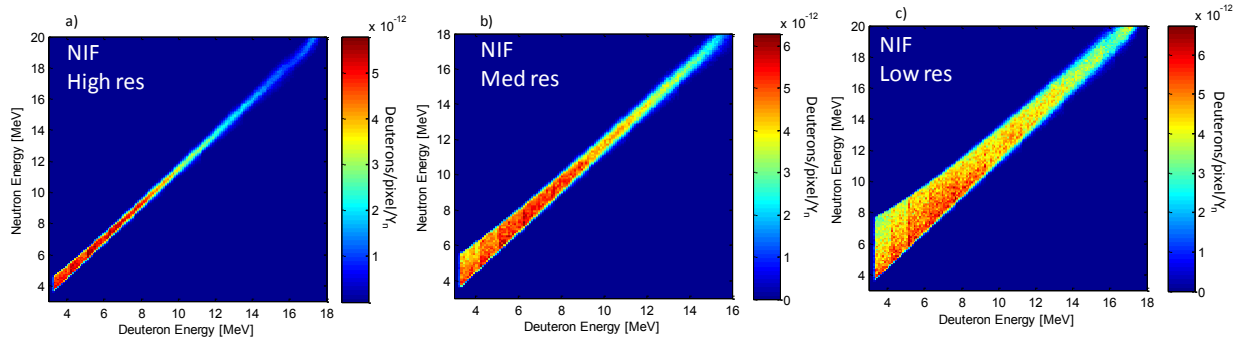

Figure 4-38: Response matrices for the NIF MRS operated in high (a), medium (b), low-resolution (c) modes.

Primary data obtained with the NIF MRS operated in different configurations are shown in Figure 4-39. These spectra were obtained from three 4μm thin-glass DT implosions (N100923, N1001030, and N110217), which produced yields of 4.8×10^{13}, 2.3×10^{14}, and 2.0×10^{14}, respectively. The green, blue, and red spectra were obtained when the MRS was operated in high-resolution, medium-resolution, and low-resolution mode (see Table 4-1), respectively. The modeled neutron spectra that provide the best fit to the measured spectra are shown in Figure

4-38b. Also, the total neutron yields determined from the measured spectra are in good agreement with the nTOF and activation yields (discussed in quantitatively in Chapter 5).

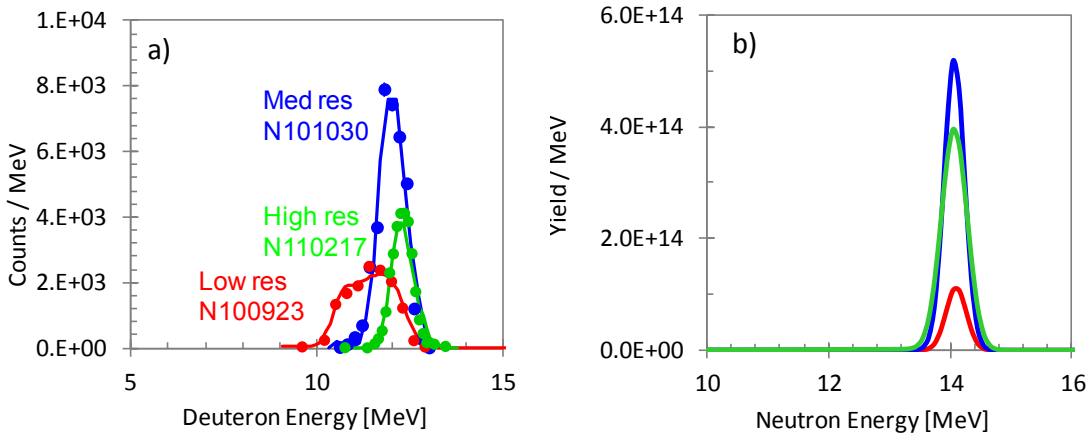

Figure 4-39: MRS spectra obtained from three 4 μm SiO_2-capsule implosions (N100923, N1001030, and N110217), which produced 4.8×10^{13}, 2.3×10^{14}, and 2.0×10^{14}, respectively. The green, blue, and red spectra were obtained when the MRS was operated in high-resolution, medium-resolution, and low-resolution mode. Due to different average energy losses in the CD_2 foil, the average energy of the deuterons is 11.4 MeV for low resolution, 12.0 MeV for medium resolution, and 12.3 MeV for high resolution. Energy kinematics (second term in Equation (4-4)) also causes an energy down shift of the recoil deuterons. b) Modeled neutron spectra that provide the best fits to the measured recoil-deuteron spectra.

4.6 Modeling of the neutron-background and optimal shielding design for the MRS

The choice of using CR-39 for the MRS detector was based on its insensitivity to x-rays, γ-rays, and EMP, and its 100% sensitivity to charged particles.[48] CR-39 is on the other hand somewhat sensitive to neutrons (>0.1MeV) according to Seguin et al,[48] and Frenje et al.[69]. The efficiency for detecting 14.1 MeV neutrons is 6×10^{-5} and 10^{-4} for 2.45 MeV neutrons,[69] which makes neutrons the primary source of background for low-signal applications such as down-scattered neutron measurements and TT neutron measurements (the other main source background is intrinsic noise, which will be discussed later in this section). It is therefore necessary to carefully model the neutron-background environment around the MRS and mitigate it by optimizing the shielding around the system (and use other means like the CCT discussed in Chapter 6). This section discusses the modeling of the neutron background and the optimal shielding design for both the OMEGA MRS and NIF MRS. In the case of the OMEGA MRS, modeling of the neutron background, with and without shielding, was also authenticated by measurements. The shielding built around the OMEGA MRS and the NIF MRS is shown in Figure 4-2.

4.6.1 Neutron interactions in CR-39

Neutrons interact with the CR-39 through nuclear elastic scattering, (n,p) reactions, (n,α) reactions, and carbon breakup. All these processes generate charged particles, as illustrated by Figure 4-40,[69] which leave trails of damage in the CR-39 that are revealed by the standard etching process described in Section 4.2.4 and in Chapter 6.

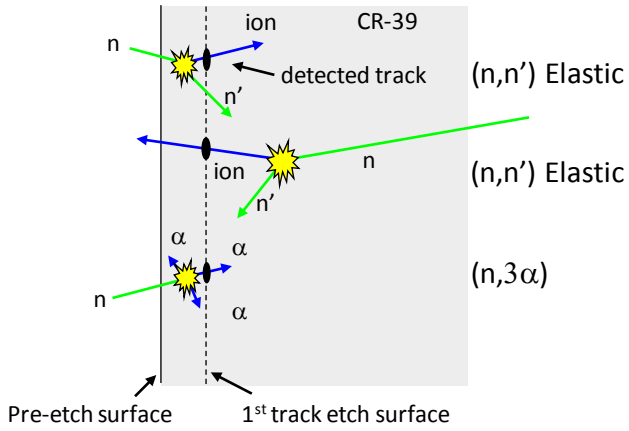

Figure 4-40: Schematic drawing (not to scale) of the CR-39 detector and the neutron-interaction processes that mainly take place in the CR-39 material. The neutrons can interact with the CR-39 material via nuclear elastic scattering, which produces recoil protons or recoil-carbon or recoil-oxygen nuclei in the forward direction in the laboratory system. Neutrons can also generate (n,p) reactions or (n,α) reactions in carbon and oxygen in the CR-39 material, producing charged particles that can generate tracks in the CR-39. Carbon-breakup (n, 3α), is another reaction that can occur in the CR-39.

4.6.2 Neutron background characterization and shielding design for the OMEGA MRS

The principal sources of background are direct primary neutrons and neutrons scattered by the chamber, target bay walls, diagnostics, and other structures surrounding the MRS. Although the CR-39 efficiency for detecting these neutrons is small, the MRS needs to be enclosed by polyethylene shielding to suppress the neutron background to the required level for measurements of DSn. To optimally design the shielding for the MRS, it is essential to first determine the fluence, directionality, and spectrum of the primary and scattered neutrons in the region around the MRS. The codes TART[56] and MCNP[57] simulated the neutron fluence using a model of the OMEGA target bay and target chamber. Measurements of the neutron fluence at various locations in the target bay were also conducted with several CR-39 detectors to benchmark the simulations. Figure 4-41a shows the locations of the CR-39 detectors used in this experiment, and the resulting data compared to simulations are shown in Figure 4-41b. Excellent agreement between the data and the simulation is observed, indicating that the modeling is accurate. For comparison, the $1/(4\pi R^2)$ curve, which represents the direct unscattered primary neutrons, is also shown in the figure. The difference between the measured fluence and the R^{-2} curve indicates the level of scattered neutrons at various distances from TCC.

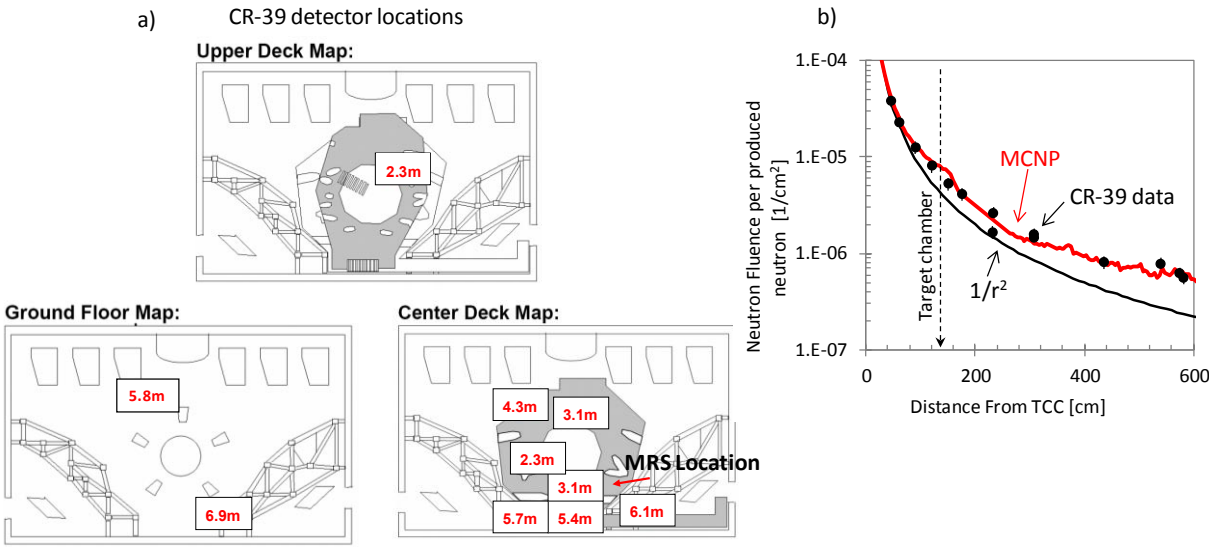

Figure 4-41: a) Schematic drawing indicating the locations of the CR-39 used in the OMEGA target bay for measurements of the neutron fluence. b) Measured and simulated neutron fluence per produced neutron as a function of distance from the implosion (or TCC). Data and simulations are contrasted to the $1/4\pi R^2$ scaling (black curve), which illustrates the effect of scattered neutrons.

The neutron fluence data, shown in Figure 4-41b, and the space-constraints information on OMEGA allowed us to optimally design the polyethylene shielding for the MRS that met the engineering requirements. The MCNP model used for this includes the MRS, the OMEGA target chamber, and the OMEGA target bay. A cut through image of the final MRS shielding design is shown in Figure 4-42a. This image has been rotated to have the x-axis parallel with the MRS LOS. In addition to the 20cm thick polyethylene shielding (marked green), a 20cm thick stainless steel plug was positioned between TCC and the detector to reduce the fluence of direct unscattered primary neutrons. Iron is often used to attenuate and moderate fast neutrons via inelastic scattering[70] but a non-ferromagnetic material must be used in proximity to the MRS magnet. Figure 4-42b shows the simulated neutron fluence per produced neutron in the region around and inside the MRS. As shown by the image, significant attenuation occurs in the magnet return yoke and the shielding in front of the detector. A beam of neutrons passes through the magnet pole gap and to some extent scatters inside the shielding. This is not optimal from a S/B point of view, but unavoidable due to space constraints. The fluence of background neutrons around the MRS shielding was simulated and measured to be ~10^{-6} n/cm^2 per produced neutron (see Figure 4-41b). Inside the shielding at the detector array, the neutron fluence was determined to be about 10^{-7} n/cm^2 and about 2×10^{-8} n/cm^2 per produced neutron at the low-energy and high-energy side of the MRS detector, respectively. Once again, the reason for this is that more shielding could not be placed in front of the detector and around the magnet housing due to the space constraints.

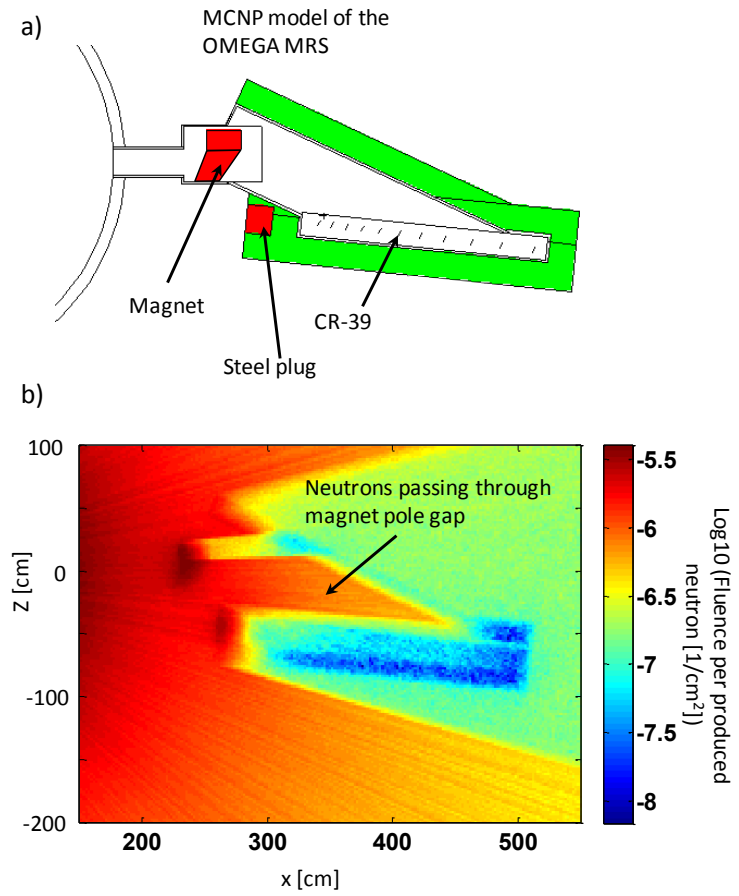

Figure 4-42: a) MCNP model of the OMEGA MRS, which includes the magnet, detector array, 20cm of polyethylene shielding that surrounds the detector array, and a 20cm thick piece of stainless steel positioned in front of the detector array to attenuate direct primary DT neutrons via inelastic collisions. b) Simulated map of neutron fluence per produced neutron in the region around and inside the MRS shielding. The neutron fluence inside the shielding at the detector array was determined to be $<10^{-7}$ Y_{DT} n/cm^2 per produced neutron. The implosion is located at the origin, and the MRS LOS is oriented along the x-axis. The MRS principle allows the detector array to be located off the main LOS providing significant shielding opportunities.

An additional check of the simulations and shielding design was conducted by measuring the neutron fluence at the MRS CR-39 detectors before and after the shielding was installed. The results are shown and contrasted to the simulations in Figure 4-43, which illustrate excellent agreement between the different measurements and simulations. Having benchmarked the modeling of the OMEGA MRS shielding, a similar modeling can now be applied with high level of confidence to the design of the NIF MRS shielding, which is discussed in the next section.

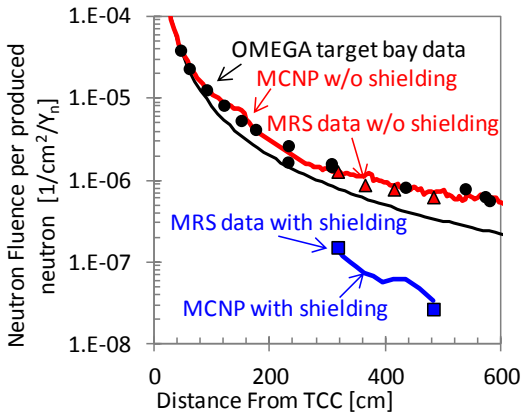

Figure 4-43: Measured and simulated neutron fluence (per produced neutron) along the MRS detector array with and without shielding around the MRS.

4.6.3 Neutron background characterization and shielding design for the NIF MRS

A detailed MCNP model of the NIF target bay, developed by Lawrence Livermore National Laboratory, was used as a starting point in the effort of optimizing the shielding for the NIF MRS. This model, which is shown in Figure 4-44a,[77] includes a complex representation of the NIF target chamber. In particular, it includes the 10cm thick spherical aluminum chamber, surrounded by 50cm of gunite shielding along with the laser and diagnostic ports. The concrete and stainless steel reinforced target-bay walls and floors are also included in the model. Using this model, the fluence of background neutrons was determined to be about 10^{-7} neutrons/cm^2 per produced neutron at the MRS location, which is close to the chamber equator at 77º-324º LOS (see Figure 4-44b). As shown by the neutron fluence map, neutrons stream relatively unaffected through the chamber ports. A detailed model of the MRS was incorporated into the NIF target bay model, as shown in Figure 4-45a.

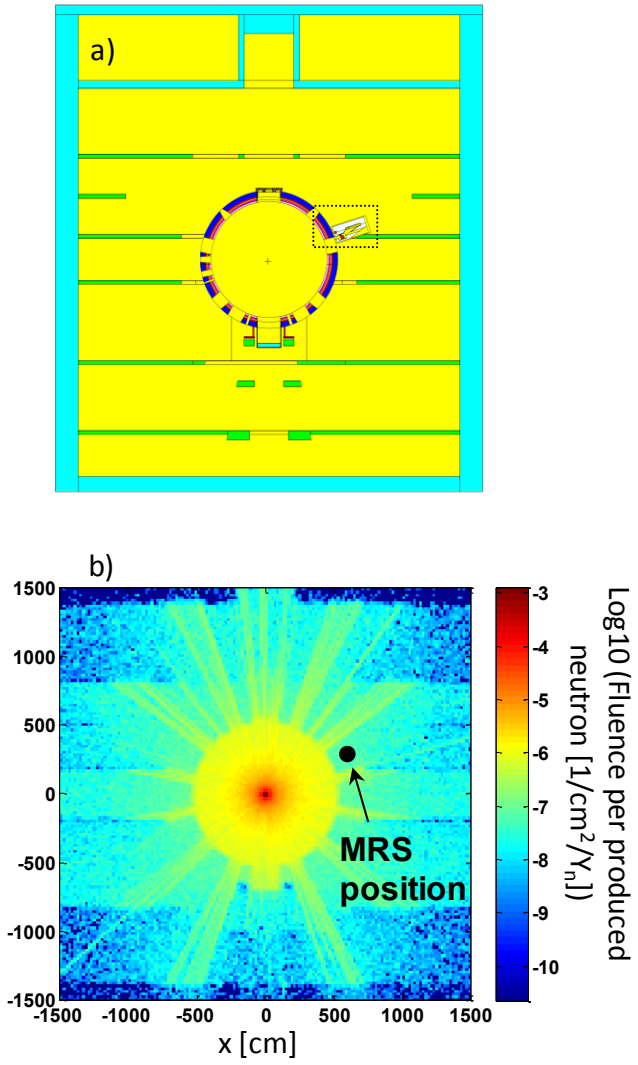

Figure 4-44: a) A detailed MCNP model of the NIF target bay, which includes the NIF target chamber with its laser and diagnostic ports, and the concrete and stainless steel reinforced walls and floors. This model was initially used to determine the neutron fluence at the MRS location. The NIF MRS was subsequently added to the model. b) Simulated neutron fluence inside the NIF target bay. The fluence is given in neutrons/cm^2 per produced neutron. A neutron fluence of ~10^{-7} n/cm^2 per produced neutron was determined at the MRS location.

A blown-up view of the MRS model with the final shielding design is shown in Figure 4-45a. This MCNP model was used to simulate the fluence map of background neutrons around and inside the MRS shielding (Figure 4-45b). As shown by the map, the simulated neutron background inside the shielding is ~2×10^{-9} neutrons/cm^2 per produced neutron, indicating that the shielding reduces the neutron fluence ~50 times. At the time of writing this thesis, this number could not be checked experimentally because the number of produced neutrons required for this needs to exceed ~$10^{15.69}$. And, the maximum produced yield to date is about 7×10^{14}. Also important to the shielding design is the neutron beam dump, which allows the beam of unscattered primary DT neutrons to pass freely through the NIF MRS. The total weight of the polyethylene shielding is about 6000 lbs.

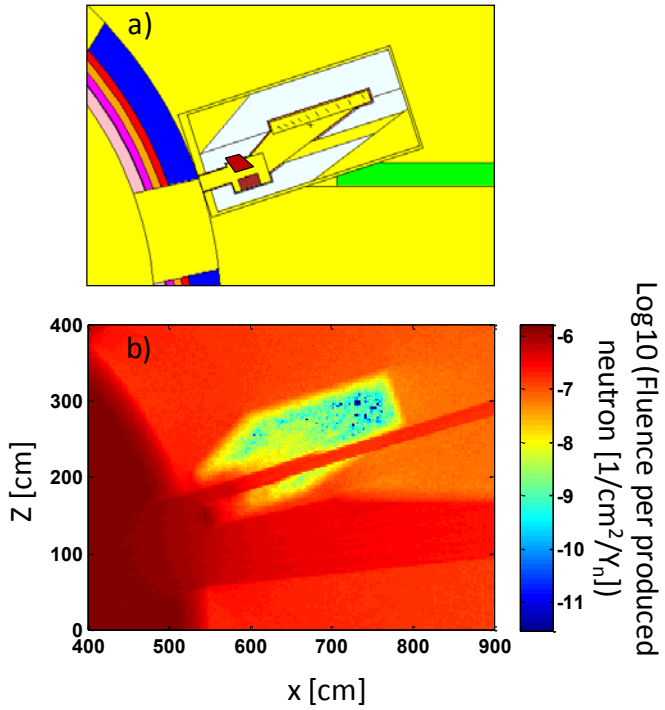

Figure 4-45: a) MCNP model of the final NIF MRS shielding design. The MRS detector array is located behind the target chamber shield, which provides excellent shielding. The detector array is also surrounded by ~40cm of polyethylene shielding, which reduces the fluence of scattered, ambient neutrons. An important feature to the shielding design is the neutron beam dump, which allows the neutron beam to freely pass through the system. b) Simulated neutron fluence (Log_{10}) around and inside the MRS shielding. The neutron fluence is given in neutrons/cm^2 per produced neutron. This simulation shows that the fluence is reduced inside the shielding by about a factor of 50 to ~2×10^{-9} n/cm^2 per produced neutron.

4.7 S/B for the MRS down-scattered neutron measurements at OMEGA and the NIF

Measurement of the DSn spectrum is quite challenging due to the low signal level relative to the intrinsic background and background of direct primary neutrons and scattered neutrons, as discussed in the previous sections. Using Equation (3-3), the DSn signal level (in the range 10-12MeV) from an OMEGA-cryogenic DT implosion can be approximately expressed as

$$S_{DSn} \sim 0.05\times\rho R\times 2.1\times10^{-9}\times 1.7\times Y_{DT} \sim 1.8\times10^{-10}\times \rho R\ (g/cm^2)\times Y_{DT}\,. \qquad (4\text{-}6)$$

This expression was determined for the MRS when operated in low-resolution mode (see Table 4-1). The factor of 1.7 accounts for the higher detection efficiency at DSn energies compared to 14 MeV (due to higher cross-section and higher transmission shown in Figure 4-35). The neutron background, calculated in the previous section, is on average ~$5\times10^{-8}\times Y_{DT}$ n/cm^2 (see Figure 4-43), and the CR-39 intrinsic background is ~50 tracks/cm^2.[48] With a CR-39 detector area of A~48cm^2, covering the DSn region and a CR-39 neutron detection efficiency[69] of 6×10^{-5} (this value can be

decreased to ~10^{-5} using careful track diameter, contrast, and eccentricity discrimination for deuteron signal), the neutron-background level and intrinsic background can be roughly expressed

$$B \sim 10^{-5} \times 48 \times 5 \times 10^{-8} \times Y_{DT} + 50 \times 48 \sim 2.4 \times 10^{-11} \times Y_{DT} + 2400. \quad (4\text{-}7)$$

For a typical cryogenic DT yield of 2×10^{12} and a ρR of 0.19g/cm^2, Equations (4-6) and (4-7) give a $S_{DSn}/B \sim 0.03$. Chapter 6 discusses the CCT, which is used to further reduce the neutron and intrinsic background to the required level for an accurate measurement of the DSn spectrum. It should be noted though that the shielding is adequate for measurements of the primary neutron spectrum. Applying a similar analysis to the NIF MRS data results in the following expressions

$$S_{DSn} \sim 0.05 \times \rho R \times 8.48 \times 10^{-11} \times 1.5 \times Y_{DT} \sim 6.4 \times 10^{-12} \times \rho R \text{ (g/cm}^2\text{)} \times Y_{DT} \quad (4\text{-}8)$$

$$B \sim 10^{-5} \times 48 \times 2 \times 10^{-9} \times Y_{DT} + 50 \times 48 \sim 10^{-12} \times Y_{DT} + 2400. \quad (4\text{-}9)$$

These expressions were determined for the MRS operated in low-resolution mode, and when using a DSn signal area of ~48cm^2 and a neutron fluence of 2×10^{-9} n/cm^2 per produced neutron (calculated in the previous section). Again, the detection efficiency is evaluated at DSn neutron energies, which are ~1.5 times higher than the efficiency for primary neutrons, but a transmission correction is not required. For a cryogenic yield of $Y_{DT} \sim 3 \times 10^{14}$ and ρR~1g/cm^2, the $S_{DSn}/B \sim 1$. This shows the background level is acceptable for a DSn measurement at $Y_{DT} \sim 3 \times 10^{14}$ meaning that for lower yields $Y_{DT} < 10^{14}$, the intrinsic background dominates and the S/B<1. In these cases, the CCT is required, as extensively discussed in Chapter 6.

Some of these points are nicely illustrated in Figure 4-46, which shows a MRS spectrum summed over OMEGA shots 54472-54474. Here, 23kJ of laser energy was delivered in 1ns to a series of 20μm CH-capsule implosions, filled with 17atm of DT gas. The total integrated yield was 3×10^{13}. Using a similar analysis as the one outlined above for the OMEGA MRS results in a predicted $S_{DT}/B \sim 20$ (where S_{DT} is the primary signal), which is reasonably close to the observed value for the primary spectrum shown in Figure 4-46. Using the estimates of the effectiveness of the CCT (75-100 reduction of the neutron and intrinsic background) derived in Chapter 6 (see Figure 6-10), and a typical ρR of ~0.07g/cm^2 for this type of implosion gives a $S_{DSn}/B \sim 15$, which is also close to the observed value.

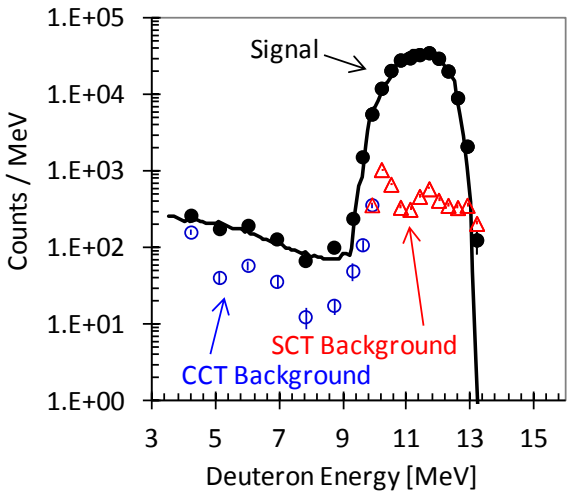

Figure 4-46: Recoil-deuteron spectrum (black data points) measured with the OMEGA MRS operated in low-resolution mode. The spectrum was summed over shots 54472-54474 ($Y_n=3\times10^{13}$). The open red triangles represent the background under the primary peak, which were obtained using the standard counting technique (SCT). The open blue circles represent the background under the DS-n spectrum, which were obtained using the CCT. SCT and CCT are discussed in detail in Chapter 6.

4.8 Summary

The MRS measures the absolute neutron spectrum at OMEGA and the NIF. The efficiency and resolution are functions of the MRS parameters summarized in Table 4-1. This chapter reviewed the final design of the MRS on OMEGA and the NIF, and the characterization of their system parameters. Using the Monte Carlo code Geant4, the full MRS-response function for various configurations (Table 4-1) has been characterized and discussed in detail. The response function is used to interpret the measured MRS spectrum. The neutron background for the MRS has been simulated, using the Monte Carlo code MCNP, and measurements of the neutron fluence at various locations in the OMEGA target bay have been used to benchmark the simulations. Although, the OMEGA-MRS polyethylene shielding decreases the neutron background by ~10 times, it is inadequate for DSn measurements. Further background reduction is required, and this is achieved with the CCT. The performance of the NIF MRS polyethylene shielding is expected to be adequate for DSn measurements for DT yields in excess of 10^{14}. For yields < 10^{14}, the CCT is also required (see Chapter 6 for details). Both the OMEGA-MRS and NIF-MRS perform well and have succeeded in their primary objective to measure the DSn spectrum, which is discussed in detail in Chapter 7. In addition to measuring the DSn spectrum, new physics about the stratification of deuterium and tritium fuel in ICF implosions is being inferred from the neutron spectrum, and this topic is discussed in Chapter 9. Furthermore, the emitted neutron spectrum from the TT reaction has been measured with the MRS for the first time at temperatures relevant to ICF conditions, and it is revealing interesting nuclear physics about the reaction at lower reactant energies than measured before.

5 - Absolute primary yield measurements at OMEGA and the NIF using the MRS

The absolute neutron yield from an ICF implosion is the most fundamental parameter that can be measured. As the number of neutrons produced by an implosion is directly related to the number of reactions and energy released, this quantity will directly indicate if ignition[17] has occurred. Although many different yield diagnostics exist, it is challenging to conduct an accurate absolute yield measurement. As the MRS detection efficiency is determined from first principles (see Chapter 4),[23-25] the absolute primary neutron yield from an ICF implosion is determined directly from the measured data without any cross calibration to other diagnostics data. This chapter focuses on that measurement. Section 5.1 discusses in some detail the diagnostics typically used to measure neutron yield from an ICF implosion. Section 5.2 describes the actual MRS yield measurements at OMEGA and the NIF, and Section 5.3 outlines future work. Section 5.4 summarizes this chapter.

5.1 Techniques for measuring neutron yield

As CR-39 is sensitive to neutrons[69] (see Chapter 4 and Chapter 6), it is sometimes used as a neutron yield detector in dosimetry and ICF applications. Two approaches have been developed to measure the neutron yield using CR-39; the first uses a cross-calibration method that is based on the associated particle technique;[45] the second method is based on *ab initio* simulations of the CR-39 response.[23] Using CR-39 as a neutron detector for ICF applications poses some constraints on the location or the setup of the CR-39 detector, because the CR-39 is sensitive to low-energy neutrons scattered by nearby structures. Either it needs to be positioned close to the implosion to minimize the effect of neutrons backscattered from the target chamber or it can be placed just behind an external charged-particle radiator (a polyethylene foil) that provides some directionality that is used do discriminate backscattered neutrons.

Activation diagnostics[43, 45, 78] are also used to measure the neuron yield from an ICF implosion by observing the neutron-induced radioactivity in samples. In principle, the neutron yield can be determined from the amount of activity in the sample. Information about the solid angle subtended by the fielded sample, activation cross-section, and radioactive decay between the time of shot and measurement of the radioactivity in the sample are also required for the determination of the neutron yield. In DD experiments, indium is used as sample material, while in DT experiments Cu and Zr are used because they have higher activation thresholds, making them less sensitive to scattered low-energy neutrons. In general, scattered neutrons pose a challenge for activation techniques because they can induce radioactivity that can be mistaken as signal coming directly from the implosion. It is therefore essential to select a clean LOS and to characterize the effect of the neutron scattering from nearby structures. In addition, attenuation of neutrons in materials in front of the sample (and within the sample) must be understood. The attenuation of the radiation emitted inside the sample must also be carefully considered when determining the activity in the

sample. Indium has the added complication of being sensitive to high-energy x-rays, which are often present in ICF experiments.[78]

The neutron yield is routinely measured with the nTOF diagnostic,[43, 79, 80] which is a neutron detector that can be based on a scintillator or a chemical vapor deposited (CVD) diamond. The interaction of neutrons with the scintillator-based detector produces light, which is transported to the photomultiplier system where it is converted to an electronic signal. This signal is subsequently transported to a data acquisition system (typically a computer controlled oscilloscope) where the signal is digitized. In the case of CVD based diagnostics, neutrons interact with the diamond generating electron-hole pairs that are separated by an applied voltage bias, whose electronic signal is digitized and recorded.[81] Calculating the response of a scintillator or CVD based nTOF detector from first principles is very complicated. The nTOF as a yield diagnostic is therefore cross-calibrated to other yield diagnostics such as Cu and Zr activation[80] or MRS (discussed in this thesis).

Another type of diagnostic that is used to measure neutron yield is the proton recoil detector (PROTEX)[82], which uses a pin diode to detect recoil protons from a thin CH_2 foil. In this diagnostic, the pin diodes are shielded from the direct radiation from the implosion but still sensitive to scattered protons from the CH_2 foil.

5.2 MRS measurements of the primary yield on OMEGA and the NIF

Y_{DT} can either be determined from the number of primary counts (S) in the MRS-measured spectrum divided by the primary detection efficiency (ε_{DT}) $Y_{DT}=S/\varepsilon_{DT}$*, or from the primary neutron spectrum that best fits the MRS-measured spectrum. As the detection efficiency is a function of neutron energy (caused by the energy dependence on the cross-section for the elastic nd-scattering), a primary-neutron-spectrum weighted ε_{DT} is used in the analysis. In the case of the forward-fit analysis of the MRS-measured spectrum, this is automatically done through the response function. Table 4-1 lists the ε_{DT} and the error budget for several MRS configurations on OMEGA and the NIF. The primary DT yield has been measured using the MRS for a wide range of DT implosions at these facilities. Discussed in Chapter 4, the total systematic error associated with the Y_{DT} determination is ~7% and ~3.2% for the OMEGA MRS and the NIF MRS, respectively. At OMEGA, the MRS is complimented by nTOF diagnostic,[43, 79, 80] which is the other main primary yield diagnostic. The total estimated systematic error of nTOF is ~10% at OMEGA.[83] Figure 5-1 shows the determined MRS primary yields compared to nTOF primary yields, ranging from $Y_{DT}\sim 2\times10^{12}$-$2\times10^{14}$. Four different CD_2 foils were used for these measurements. This plot shows excellent agreement between the two different types of measurements over several orders of magnitude. A closer look at the data reveals that the nTOF provides a yield that is on average 1±2% (statistical error only) higher than the MRS yield.

* This works only if there are no other significant sources of neutrons in the vicinity of the primary peak, such as the DSn component in very high ρR (>1g/cm^2) implosions.

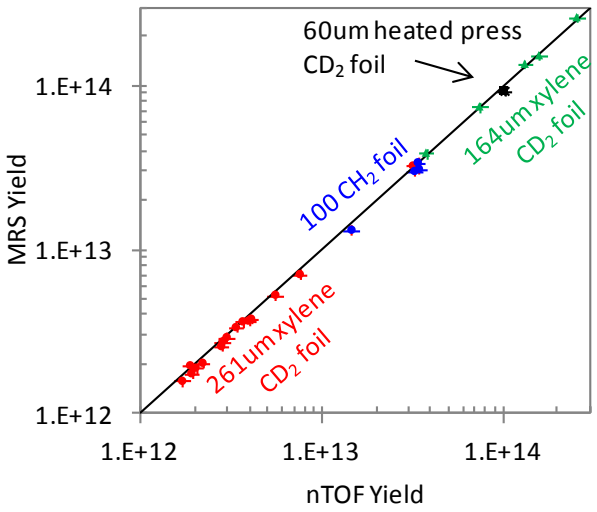

Figure 5-1: OMEGA MRS primary neutron yield as a function of nTOF primary neutron yield. Excellent agreement between the measurements is observed for a wide range of yields, which demonstrates that the data sets are of high quality. Three different CD_2 foils and one CH_2 foil were used in these experiments.

In the fall of 2010, the commissioning of a large suite of nuclear diagnostics on the NIF began. The diagnostics were the MRS, nTOFs,[80] Zr activation,[84, 85] Cu activation,[43, 78] and the Gamma-ray-burn-history (GRH) detector.[47] For these experiments, DT gas-filled exploding-pusher implosions were used. Cryogenic DT and THD implosions were also used to some extent for this purpose. After several series of implosions, it was clear that the MRS and activation techniques independently provided high-quality data, while the nTOFs provided yields that were about 20-30% higher. This yield discrepancy was eventually explained by an inaccurate transfer of the nTOF-yield calibration from OMEGA to the NIF environment.[86] The nTOFs were therefore cross-calibrated to the weighted average of the MRS and activation data. The yields determined from the MRS data as a function of the activation data are shown in Figure 5-2. Excellent agreement between the two sets of data is observed. On average, the MRS-to-activation-yield ratio is 1.003±0.03 (all DT shots from September 2010 to February 2011).

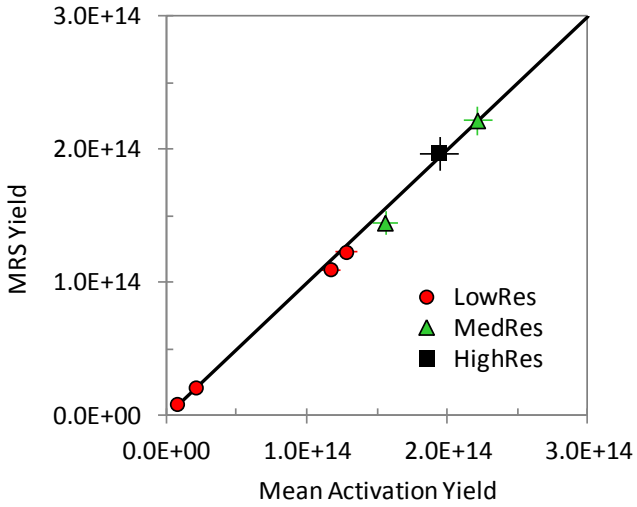

Figure 5-2: Absolute primary neutron yield measured by the NIF MRS as a function of the primary yield measured by Zr and Cu activation (uncertainty weighted mean). Given the absolute uncertainties, excellent agreement between the measurements is observed, giving confidence in the absolute primary yield measured at the NIF. The MRS was operated in the low-resolution, medium-resolution, and high-resolution modes.

5.3 Future work

As the systematic uncertainty typically dominates the statistical uncertainty in the MRS data, better characterization of the different MRS parameters will reduce the uncertainty in the determined primary neutron yield. We are therefore in the process of reducing the dominant sources of the systematic uncertainties. At both OMEGA and the NIF, the uncertainty in the differential cross-section for nd elastic scattering is important. Faddeev calculations of the nd elastic scattering cross section for neutron energies in the range 3-18 MeV were recently conducted by Dr. Evgeny Epelbaum to an accuracy of 1%.[87] These cross sections will replace the ENDF/VII-B cross sections used in the modeling of the MRS-response function, improving the systematic uncertainty in NIF-MRS yield data from 3.2% to 2.5%. For the OMEGA MRS, the uncertainty in the transmission function (4%), uncertainty in the deuterium number density (3%), and the distance of the foil to TCC due to positioning errors (3%) need to be considered as well when reducing the systematic yield uncertainty. Therefore, the foil holder for the OMEGA MRS is being redesigned to address the issue with the positioning of the foil. We are also in the process of better characterizing the transmission function. This is done by using magnet apertures of different sizes. In addition, the deuterium number density uncertainty is actively being improved by using GA manufactured CD_2 foils, discussed in Chapter 4. We anticipate that these improvements will reduce each individual source of uncertainty by about a factor of two, which will reduce the systematic yield uncertainty from 7% to 4%.

5.4 Summary

As the MRS detection efficiency is determined from first principles, the absolute primary neutron yield from an ICF implosion is determined directly from the measured data without any cross calibration to other diagnostics data. The results obtained at OMEGA and the NIF clearly demonstrate that the MRS provides very high-quality yield data. To further enhance the capability of the MRS, the systematic uncertainties associated with the MRS yield measurement is actively being reduced.

6 - The Coincidence Counting Technique for background reduction in MRS data

Measurements and calculations of the background in the MRS data (Chapter 4) have shown that the polyethylene shielding alone is not always sufficient to reduce the background to the required level for the DSn measurements at OMEGA and the NIF. Additional reduction of the background is therefore required for the DSn measurements for cryogenic DT and warm-capsules implosions at OMEGA and for the low-yield THD implosions at the NIF (yields $<10^{14}$). This is accomplished by using the CCT, discussed in this chapter. Section 6.1 provides an introduction and motivation for the CCT, while Section 6.2 describes the principle of the technique. Section 6.3 illustrates the application of the CCT to proton data obtained using our small linear accelerator.[88] Section 6.4 discusses the CCT application to MRS data obtained at OMEGA and the NIF, and in Section 6.5, concluding remarks are made.

6.1 The Coincidence counting technique (CCT)

As described in Chapter 4, CR-39 is used to detect recoil particles from the foil. Although the CR-39 efficiency for detecting background neutrons is small, Chapter 4 also showed that measures are required to significantly reduce the neutron background for successful measurements of DSn from cryogenic-DT[26] and plastic-capsules implosions at OMEGA,[50] and from low-yield tritium-hydrogen-deuterium (THD) implosions at the NIF.[21] This is achieved by surrounding the MRS with polyethylene shielding (Chapter 4), as a first step. Additional reduction of the background is accomplished by analyzing the MRS data using the CCT, which takes advantage of the fact that incident signal particles (protons or deuterons) penetrate deep inside the CR-39, producing correlated tracks on two surfaces. Using the CCT, these correlated signal tracks are searched for and distinguished from most of the background tracks, as the latter are generated anywhere in the CR-39 volume and are most likely to show up only on one surface or the other. More specifically, the CCT is implemented in a staged etch process, in which the CR-39 is etched in three steps; a sodium-hydroxide track etch, an ethanol-sodium-hydroxide based bulk etch, and a second track etch. The CCT has been applied to CR-39 in previous work[89-92] but to our knowledge this is the first staged-etch implementation of the CCT.

6.1.1 CR-39 as a charged-particle detector

When charged particles pass through the CR-39 material, they leave trails of molecular damage, related to their stopping power (dE/dx), where x is the distance along the trail. These trails of damage are revealed as tracks by a chemical-etching process.[48] As the CR-39 is a clear plastic with high optical quality, these tracks are readily observed and recorded with an optical microscope system.

6.1.2 The principle of the CCT

The CCT uses a three-step CR-39 etch process, which involves a sodium-hydroxide track etch, an ethanol-sodium-hydroxide bulk etch, and a second track etch.

When processed in this series of staged etches, the charged particles, which pass through the CR-39, leave microscopically visible tracks on each of the track-etched surfaces, resulting in coincident tracks. In contrast, most of the background tracks (both neutron-induced and intrinsic tracks) are generated randomly on each surface, as schematically shown in Figure 6-1.

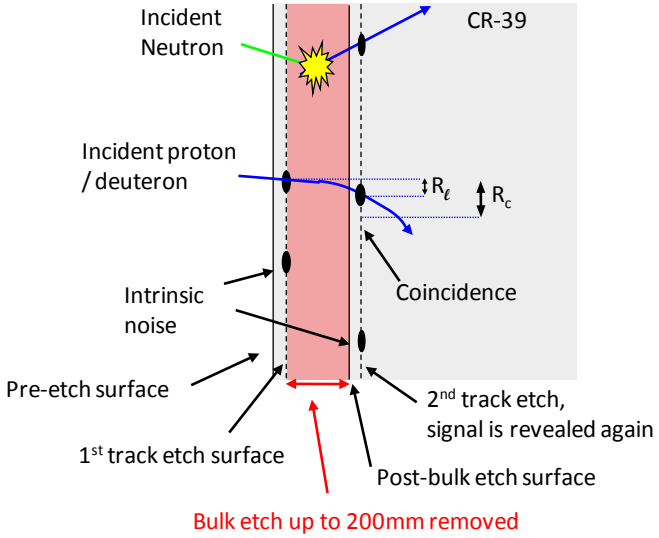

Figure 6-1: Schematic illustration of the three staged-etch process of the CR-39 used in the CCT (i.e. a track etch, an ethanol bulk etch, and a second track etch). When charged particles pass through the CR-39 they leave trails of molecular damage related to their stopping power (dE/dx). These trails of damage are revealed by a chemical-etching process that uses NaOH at 80°C. In this first step, the CR-39 is track etched and subsequently scanned using an optical microscope. The location, diameter, contrast, and eccentricity of each track are recorded. In the second step, an ethanol based bulk etch is used to remove significant amounts of CR-39 material and thus remove all tracks. This is done by tailoring the chemical etchant, etch temperature, and etch depth, as discussed in detail in the text. A second track etch is then conducted, which reveals the tracks again. Another scan is conducted, and tracks recorded in the first and second scans are then searched for within a correlation radius (R_c) that is chosen to be greater than R_l (caused by mainly lateral straggling, non-normal incidence and scan misalignment). Any tracks on the two surfaces within R_c are considered to be coincidence tracks. In contrast, the background is mainly distributed randomly on one surface or the other and can effectively be removed using the CCT.

6.1.3 First processing step – The sodium-hydroxide track-etch and scan

For the track-etch, the chemical etchant, concentration, and temperature is carefully chosen to maximize the ratio of the track-to-bulk etch rate. Typically, the CR-39 is etched for 6 hours in 6N NaOH at a temperature of 80 °C. This allows for more material to be removed in the damaged trails than around them (i.e., the CR-39 bulk material), resulting in particle-track growth. After the signal tracks have been revealed in the first track etch, the CR-39 is scanned and the location,

diameter, contrast, and eccentricity of each track are recorded. The location of pin-mark fiducials are recorded and stored so that the coordinate system can be related in the following steps. More detailed information about this process can be found in the papers by Hicks[20] and Seguin.[48]

6.1.4 Second processing step – The ethanol-sodium-hydroxide bulk etch

After this first track etch and scan, a second etch or the "ethanol bulk etch" is conducted to remove a significant amount of CR-39 material. The objective of the ethanol bulk etch is to, first, erase the tracks that were made visible in the first track etch, and secondly, remove significant amount of CR-39 material to ensure that intrinsic and neutron-induced tracks do not reappear within the correlation radius R_c (or the search radius). The chemical etchant, concentration, and temperature are chosen for this etch process, in such a way that the track etch and ethanol bulk etch rates are nearly equal.[93, 94] As a result, all visible tracks are removed if the ethanol bulk etch depth is significantly greater than the diameter of the tracks. For this etch process, a mixture of 2N NaOH/ethanol/water (made from 1 part of 10N NaOH/water and 4 parts pure ethanol) is used at a temperature in the range of 50-65 °C, resulting in a track-bulk-etch ratio of about one. Under these conditions, the ethanol bulk-etch rate (BER) is a strong function of temperature (Figure 6-2) but more importantly high enough to provide sufficiently deep etches with reasonable processing time and without destroying the CR-39 surface quality. It was concluded that a BER value faster than about 40μm/hr (~60°C) generated unacceptable deterioration of the surface quality when the etch times are longer than ~1hr.

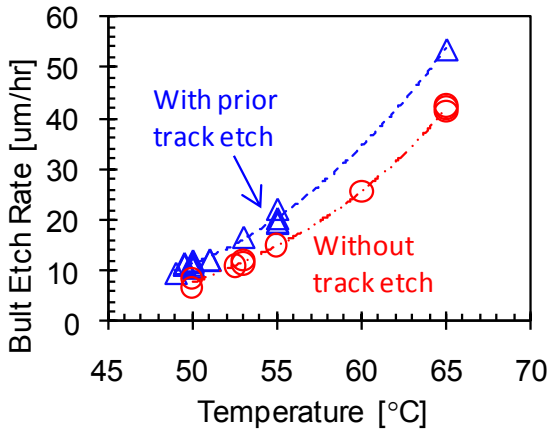

Figure 6-2: Ethanol bulk-etch rate (BER) as a function of etch temperature, when using a 2N NaOH/ethanol/water mixture made by diluting 1 part 10N NaOH/water in 4 parts ethanol. The blue triangles are for CR-39 that underwent a track etch (6 hours at 6N NaOH/water at 80 °C) prior to the bulk etch, as is typical for CCT data. The red circles are for CR-39 pieces that were placed directly in the bulk etch without a prior track etch. The difference between the curves show that CR-39, which undergoes a prior track etch, exhibits a 35-50% faster bulk etch rate during the ethanol bulk etch. In these experiments, 5.5-MeV alpha particles were used to estimate the track-etch rate while the BER was measured by comparing the CR-39 thickness before and after the etch process. As shown by the resulting data, the BER is a strong function of the etch temperature, which is a convenient control of the etch rate for a fixed etchant concentration.

A lower BER limit of ~10μm/hr (~50°C) was chosen on the basis of practical processing times for the CCT. As the BER depends on the CR-39 sensitivity, and the fact that differences in manufacturing and batch-to-batch differences in sensitivity cause overall shifts in the BER curve, it is always necessary to check this parameter for new batches of CR-39. Typical ethanol bulk-etch depths and times for the OMEGA and NIF MRS are illustrated in Table 6-1. When the CCT is used, the deuterons must also be detectable after having penetrated some 50-200μm into the detector (bulk etch depth); material which is removed by the bulk etch. The OMEGA MRS deuteron-filter configuration is summarized in Table 6-2, and the first-generation NIF MRS deuteron-filter configuration is summarized in Table 6-3. The filter configuration for the NIF MRS was made of Al for the commissioning experiments. The next deuteron-filter design will be constructed of Ta to improve S/B. The calculated pre and post-bulk etch deuteron energies for the OMEGA MRS-filter configuration, described in Table 6-2, is plotted as a function of detector window in Figure 6-3a. The pre and post-bulk etch deuteron energies for the NIF MRS-filter configuration, described in Table 6-3, is shown in Figure 6-3b.

Table 6-1 – Typical bulk etch depths for recoil deuterons measured with the MRS at OMEGA and the NIF. Each window represents a CR-39 detector position at a certain energy along the MRS focal plane. This means that each window covers a specific energy range, as described in Chapter 4. [24, 25] Ta filtering in front of each CR-39 detector is specifically designed for the CCT to optimize the energy of the incoming deuteron to be high enough to penetrate deeply into the CR-39 yet low enough for 100% detection efficiency.[48] Likewise, the ethanol bulk-etch depth is chosen to be shorter than the deuteron range in CR-39. The ethanol bulk-etch time is calculated on the basis of the selected bulk-etch depth and the bulk-etch rate shown in Figure 6-2, using an etch temperature of 55 °C. For windows 1-3, the CR-39 bulk-etch depth has to be smaller than 100 μm, which is the minimum etch depth to effectively remove the intrinsic-background tracks (see Figure 6-9). For etch depths smaller than 100 μm, intrinsic coincident background must be considered. All down-scattered neutron data obtained at OMEGA and the NIF are processed with ~200μm ethanol bulk etch and are therefore insensitive to this intrinsic coincidence background. †For efficient processing, a 200μm bulk etch is sometimes slowed to run overnight at 50 °C for ~16hr.

	OMEGA		NIF	
	Bulk-etch depth	Etch time	Bulk-etch depth	Etch time
Window	(μm)	(h)	(μm)	(h)
1	NA	NA	50*	2.5
2	70*	3.5	75*	3.5
3	90*	4.5	100	5
4	100	5	125	6
5	150	7.5	200	10†
6	200	10†	200	10†
7	200	10†	200	10†
8	200	10†	NA	NA

Table 6-2: OMEGA-MRS filter configuration for the CCT applied to recoil-deuteron data for CR-39 detector windows 1-8. The bulk-etch depth for each window is also listed.

Window	Filter Description [μm]	Bulk etch depth [μm]
1	3.5 Mylar	50
2	3.5 Mylar	70
3	3.5 Mylar	90
4	3.5 Mylar	100
5	3.5 Mylar	150
6	5/10 Ta	200
7	20/30/35 Ta	200
8	40/45/50/60 Ta	200
9	310/330/350/380 Al	none
10	410/430/460/490 Al	none
11	520/560/590/620 Al	none

Table 6-3: Preliminary NIF-MRS filter configuration for the CCT applied to recoil-deuteron data for CR-39 detector windows 1-7. The bulk-etch depth for each window is also listed.

Window	Filter Description [μm]	Bulk etch depth [μm]
1	3.5 Mylar	50
2	3.5 Mylar	75
3	3.5 Mylar	100
4	30 Aluminum	125
5	50/80 Al	175
6	100/120/140/160 Al	200
7	150/175/200/225 Al	200
8	400/420/450/500 Al	none
9	550/600/650/700 Al	none

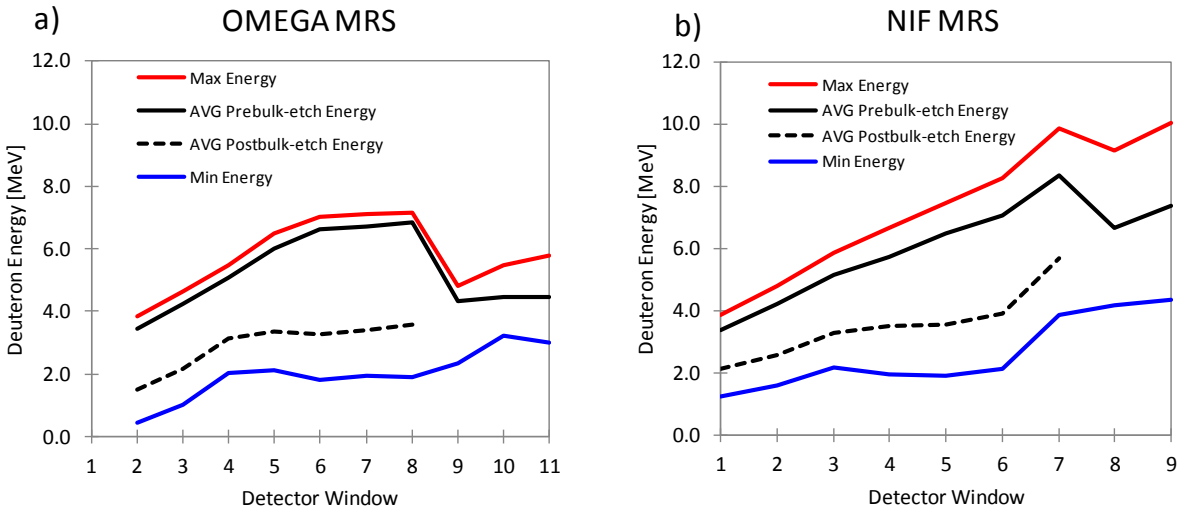

Figure 6-3: Calculated pre and post-bulk etch deuteron energies as a function of detector window for (a) the OMEGA MRS-filter configuration described in Table 6-2, (b) and for the NIF MRS-filter configuration described in Table 6-3. The CR-39 detectors must be sensitive to the deuterons on the pre-bulk-etch and post-bulk-etch surfaces, which are separated by 50-200μm of CR-39. This CR-39 material is removed in the bulk-etch process.

During the ethanol bulk etch, the solution turns orange, and then brown as salts and etch products build up in the solution. Significant etch-product build up on the CR-39 surface occurs as well, requiring frequent removal to prevent the insulation of the CR-39 from the etchant. Magnetic stirring units are therefore used to ensure that the build up on the CR-39 surface is continuously removed (see Figure 6-4).

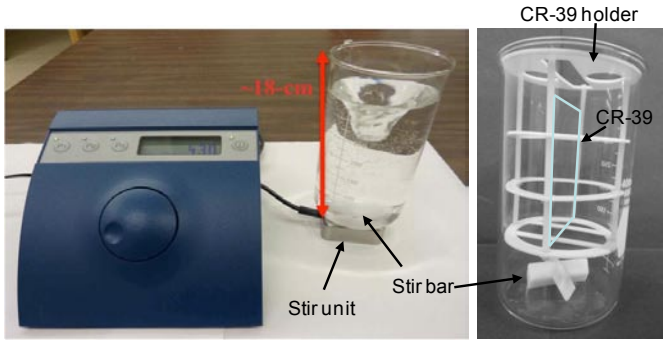

Figure 6-4: Magnetic stirring unit (ThermoScientific Micro20 submersible stirrer with Telemodul control) and beaker used in the CR-39 bulk-etch process. During the ethanol bulk etch, significant etch products are produced on the CR-39 surface, which must be removed. This is done by using a magnetic-stirring bar operated at ~410 RPM at the bottom of the beaker. A Teflon holder shown to the right is used to lift up CR-39 above the stirring bar in the beaker. Normally the beaker is put into a hot water bath, but for illustration purposes, the beaker has been lifted out from the bath.

6.1.5 Third processing step – The second track etch and scan

If the ethanol bulk etch is correctly executed, the amount of CR-39 material removed is smaller than the range of the incident charged particles (protons or deuterons). As a result, the particles' damage trails can be revealed again by a second track etch. A subsequent scan of this surface is conducted. The location of the pin-mark fiducials, that were located in the previous scan, are located and recorded once again and used to correct the coordinate systems of the pre and post-bulk etch scans.* By comparing the scans of the first and second track etched surfaces, correlated signal tracks can be searched for within some specified correlation radius R_c that must be larger than the lateral displacement (R_ℓ) of tracks (due to angle straggling in the CR-39, non-normal incidence, and possible scan shifts and scan misalignments). As neutron-induced and intrinsic tracks will reappear in new random locations on the second track-etched surface, the signal tracks can be distinguished from these background tracks using the CCT. Although some random-background coincidences (B_{CCT}) will be counted, this type of background can be characterized by misaligning the scans relative to each other by a distance significantly larger than R_c (see discussion in the next section). Figure 6-5a and b show the radial distribution of signal-coincident tracks and random-background-coincidences, respectively.

* Post-bulk etch scans tend to be more challenging for deeper bulk-etches, and therefore thinner CR-39, due to warping and auto-focus issues. Typically, CR-39 post-bulk etch thicknesses >0.5mm will maintain ideal focus throughout a scan (thinner detectors can be scanned with the aid of optical oil or pads). One-sided bulk-etches using a Teflon back-plate may also help alleviate some of these issues.

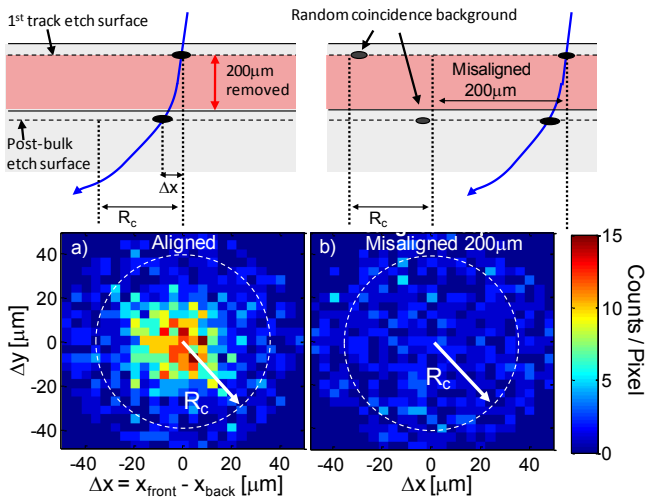

Figure 6-5: Distribution of signal deuteron coincidences (a) and random background coincidences (b) within the correlation radius R_c, obtained on OMEGA shot 50515 with the MRS. In this particular case, an R_c of 35 µm was used. The calculated straggling radius in the CR-39 is ~10µm, when neglecting lateral straggling in the filter and angular distribution of the incident deuterons. For the determination of the random background coincidences in b), the post-bulk-etch scan was misaligned 200 µm relative to the pre-bulk-etch scan, resulting in a random background coincidence level of ~35% of the total signal.

In this particular case, the scans were misaligned by ~200 µm to characterize the random-background coincidences. The net coincidence signal can then be determined by subtracting the random background data from the coincidence data. This background characterization and subtraction technique is a powerful feature of the CCT, as it allows the entire signal-scan area to be used for the background determination.

6.1.6 Random-Background Coincidences (BCCT)

The number of B_{CCT} within the correlation radius R_c can be expressed analytically as:

$$B_{CCT}/A = n_1 n_2 \pi R_c^2 \tag{6-1}$$

Here, n_1 is the total track density on the first track-etched surface (both signal and background), n_2 is the total track density on the second track-etched surface, and A is the total CR-39 signal area. The probability of finding a random track on the second track-etched surface within the correlation search area (πR_c^2) is then given by $n_2 \pi R_c^2$. The number of random coincidences per unit area then follows by multiplying by the track density on the first track-etched surface.

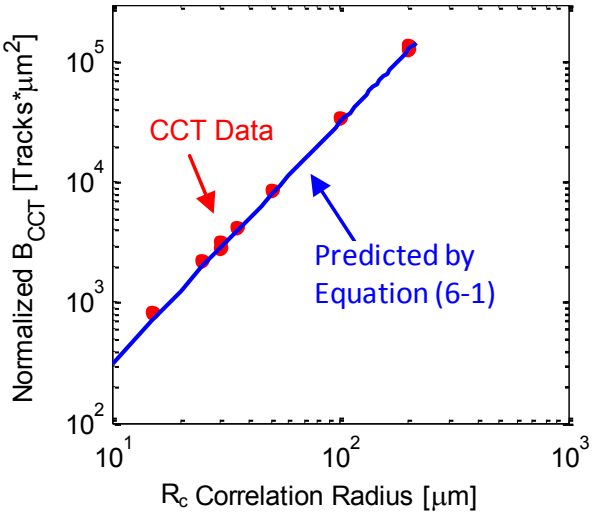

Figure 6-6: Normalized random background coincidences as a function of correlation radius R_c. A normalized number of CCT background counts (B/n_1n_2A) is plotted to allow for a comparison of different data with widely varying track densities. As shown by the data points, the observed number of random background coincidences is well described by Equation (6-1).

As shown by Equation 1, the number of random coincidences is proportional to the product of the total track densities and R_c^2. As a consequence, minimizing R_c is essential for the CCT to be effective. For instance, reducing R_c from 500 µm to 50 µm reduces the number of random coincidences with a factor of 100. As significant background reduction is required for the MRS (discussed in Chapter 4), i.e. a factor of ~50,[25, 95] the relative alignment of the two scans, as well as CR-39 movement during the scan, must be better than 15µm (which is comparable to the effect of angle straggling in the CR-39).

6.1.7 Neutron induced background coincidences

Although very unlikely, a background neutron can produce tracks on both the first and second track-etched surfaces within R_c, resulting in a real coincidence that cannot be eliminated by random background subtraction described in the previous section. These tracks are produced primarily through two processes: np-elastic scattering and carbon break up, which are both volumetric processes, producing a elastically-scattered proton and three alpha particles,[69] respectively. The minimum ethanol bulk-etch depth required to completely eliminate the carbon-breakup-alpha tracks is ~50 µm (the range of these particles in the CR-39 is ~45 µm). The tracks from the elastically-scattered protons, with a maximum energy of 14 MeV, cannot be removed completely by the ethanol bulk etch, as their maximum range is almost a factor of two larger than the thickness of the CR-39 (1 mm). However, most of these protons, if not all, are not detected as their scattering angles are larger than the solid angle Ω_C defined by R_C and the bulk etch depth (l_b) (see Figure 6-7).

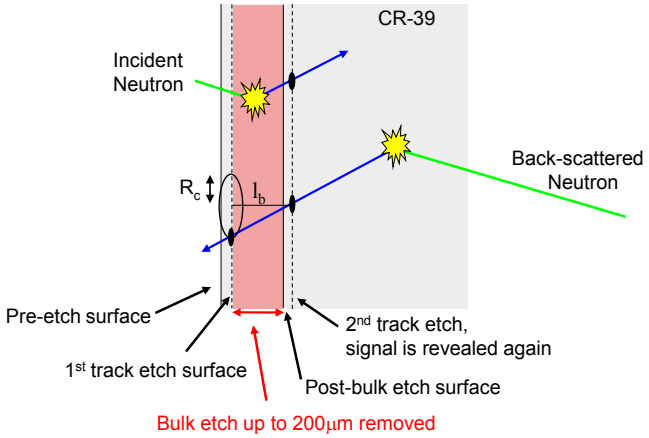

Figure 6-7: Illustration of two types of neutron interaction in the CR-39. Neutron scattered protons in between the pre and post-bulk-etch surfaces will only produce a recoil track on one of the etched surfaces, while neutrons coming from behind and interacting in the bulk CR-39 volume can scatter protons into a narrow solid angle, which could produce a neutron induced coincidence. The probability of this event is relatively small as it scales with ~R_c^2/l_b^2. Neutrons can also break up carbon nuclei, creating three alpha particles[69] with a range of <50 μm. As bulk etches are >50μm, the number of neutron-alpha coincidences is practically zero.

In addition, many protons elastically scattered within this solid angle are not detected, as their energies are too high for CR-39 detection (under typical conditions protons with energies > 10 MeV are not detected). Using these constraints, the number of neutron-induced coincidences (N_{CCT}) can be expressed as:

$$\frac{N_{CCT}}{A} \approx nx\int_{\Omega_c}\int_{E_{c-}(\theta)}^{E_c^+(\theta)} F_n(E,\theta)\frac{d^2\sigma}{d\Omega dE}dEd\Omega \approx F_n\frac{R_c^{\,2}}{l_b^{\,2}}nx\int_{E_{c-}(\theta(E))}^{E_c^+(\theta(E))}\frac{d\sigma(\theta(E))}{dE}dE \quad , \qquad (6\text{-}2)$$

where F_n is the neutron fluence, n is the hydrogen-number density in the CR-39, x is the average path length of the neutrons in the CR-39, and the integral evaluates the probability for producing a scattered proton that will generate a detectable track on the first and second track-etched surfaces within Ω_C. The neutron cutoff energies in the integral $E_c(\theta)_-^+ = (E_{p_-}^{\ +} + \int_{x_0}^{x_1}\frac{dE_p}{dx}dx)\cos^{-2}\theta$ are the neutron energies which can produce recoil protons within the limited energy range capable of producing a track ($E_{p\ -}$~0 and E_p^+~10MeV) accounting also for dE_p/dx energy loss from the interaction point to the etch surface and the kinematic scattering angle θ. As Equation (6-2) is extraordinarily difficult to evaluate analytically or numerically, the number of neutron-induced coincidences was instead experimentally determined as a function R_C and l_b, using high neutron fluence data obtained with the MRS on OMEGA. Applying this approach to the problem, Equation (6-2) can be rewritten as:

$$\frac{N_{CCT}}{A} \approx \varepsilon \, F_n \frac{R_c^{\,2}}{l_b^{\,2}}, \tag{6-3}$$

where ε was determined experimentally. From high-yield DT-implosion data obtained at OMEGA, ε was determined to be $2 \pm 1\times10^{-6}$ as shown in Figure 6-8.

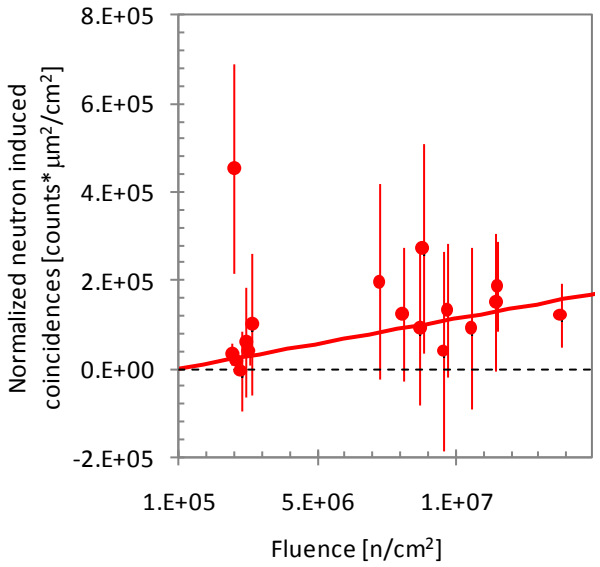

Figure 6-8: Number of neutron-induced coincidences (N_{CCT}/A) per unit area, normalized by the bulk etch depth (l_b) squared ($N_{CCT}*l_b^2/A$), as a function of neutron fluence for the OMEGA MRS. This data was obtained in a background region on the CR-39 detectors where signal particles from the MRS cannot reach the CR-39 detector. Bulk etch depths between 100 - 200 μm were used to process the data. The solid line represent the best fit to the data with Eq. (6-3) using a ε value of $2 \pm 1\times10^{-6}$. It is also noteworthy that this type of background is insignificant for OMEGA cryogenic DT implosions, typically producing a neutron yield of $\sim2\times10^{12}$, because the neutron fluence is $\sim10^5$ n/cm2 at the CR-39 detectors and thus two orders of magnitude below observable.

Given this scaling, the combination of a small solid angle and limited detectability of the scattered protons makes the CCT very effective at eliminating backscattered neutron-induced tracks**.** To quantify the potential impact of this background in MRS measurements at OMEGA and the NIF, the MCNP code was used to simulate the background neutron fluence at the MRS CR-39 detector array at both facilities. At OMEGA and the NIF, the scattered neutron fluence is strongly peaked near 14 MeV and was determined in Chapter 4 to be $\sim5\times10^{-8}\cdot Y_n$ neutrons/cm^2 and $\sim2\times10^{-9}\cdot Y_n$ neutrons/cm^2, respectively. When assuming a correlation radius of ~50 μm, an ethanol bulk-etch depth of 200 μm, and a detector area of ~30cm^2, the number of neutron-induced background coincidences per cm^2 for a given yield is $N_{CCT}/A \sim6\times10^{-15}\cdot Y_n$ at OMEGA and $N_{CCT}/A \sim 3\times10^{-16}\cdot Y_n$ at the NIF. As cryogenic DT implosions on OMEGA typically produce neutron yields less than 10^{13}, this type of background is not an issue for the MRS at OMEGA. At the NIF, this type of background can, on the other hand, be significant when neutron yields exceed $>10^{16}$. However, this will not be a problem as the CCT will not be applied to this type of data due to the high track densities, resulting in a large number of random coincidences as described by Equation (6-1). In

this scenario, the standard counting technique (SCT),[48] which is insensitive to this type of neutron induced background, will be applied because of strong signal levels.

6.1.8 Intrinsic background coincidences

The intrinsic background tracks are primarily due to surface and bulk defects in the CR-39, which after the first track-etch typically look like small faint tracks that can be mistaken as real signal tracks. Given this, it is essential that the ethanol bulk etch is deep enough to effectively remove these tracks, i.e., to reveal an entirely new layer of defects and thereby remove intrinsic background coincidences. To determine the impact of the intrinsic background coincidences for different ethanol bulk-etch depths, a series of experiments were conducted in which the ethanol bulk-etch depth was varied from 10 – 230 μm. The results from these experiments, which are shown in Figure 6-9, illustrate that a small number of intrinsic background tracks persist for about 100 μm of the ethanol bulk etch.

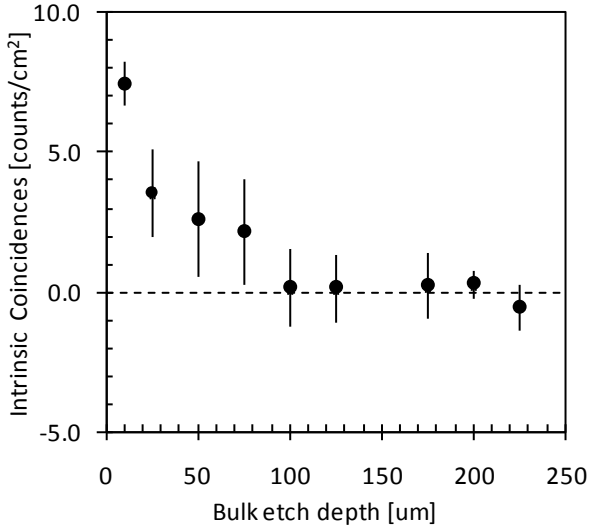

Figure 6-9: Number of intrinsic background coincidence tracks as a function of ethanol bulk-etch depth. Each point represents an average of multiple measurements and the error bar represents the standard deviation for those measurements. This data set shows that the ethanol bulk-etch depth has to be at least or larger than ~100 μm to effectively remove most of the intrinsic background tracks.

Beyond 100 μm, all these tracks are completely removed and new randomly distributed ones have appeared. However, these randomly distributed tracks are effectively removed by the CCT (see Figure 6-5).

6.2 Application of the CCT to D^3He-proton data obtained at the MIT linear accelerator

The CCT was validated by using D^3He-proton data obtained in well controlled experiments on the MIT linear accelerator.[88] In these experiments, a piece of CR-39 was exposed to ~5000 protons. The right-hand side of the piece was covered by a 960 μm thick aluminum filter to range the ~14.7 MeV protons to energies that are detectable on the first track-etched surface (5.7 MeV) and second track-etched surface (3.7 MeV). The left-hand side of the CR-39 was blocked by a 1440 μm thick aluminum filter to completely stop the D^3He protons. An under-filtered region (bottom part of the image in Figure 6-10a) used 480 μm of aluminum where the proton energy is too high (~11MeV) to be detected on the first track-etched surface of the CR-39. A 200 μm deep ethanol bulk-etch was used to process the data. The SCT, described in the paper by Séguin *et al*.[48] was applied to the data as well for comparison. This could be done, as the signal-to-background ratio was high in this experiment. An image of the scanned data is shown in Figure 6-10a, and the projected data on the y-axis is shown in Figure 6-10b. The CCT data is shown in black and the SCT data is shown in red. The over-filtered region shows no net counts, indicating that the CCT method properly subtracts the random background coincidences. Also, as expected the under-filtered region shows no net counts because the proton energy is too high. The signal distribution displays a parabolic shape, which is due to $1/R^2$ effect across the 7 cm high CR-39 that is positioned 7 cm from the target (the D^3He-proton source).

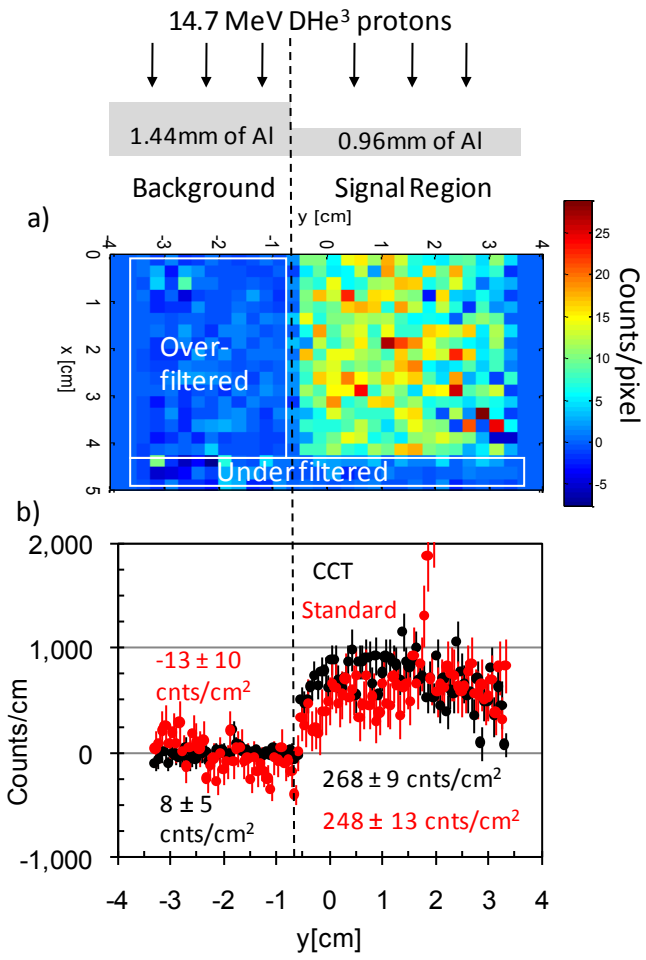

Figure 6-10: a) D^3He-proton data obtained on a piece of CR-39 fielded on the MIT linear accelerator on shot A2010012002. In this experiment, 14.7-MeV protons from D^3He reactions were used to expose the piece of CR-39 that had various types of filters in front. In front of the signal region, a 960 μm Al filter was used to range down the D^3He protons to energies detectable on the first and second track-etched surfaces. Two background regions were established as well by placing 1440 μm Al in front of one area (the over-filtered area in which the protons are ranged out) and 480 μm of Al in front of another area (the under-filtered area in which the protons have too high an energy to be detected on the first track-etched surface). b) Signal and background distributions projected onto the y-axis, where the black data points were obtained from the CCT analysis and the red data points were obtained from an analysis involving the standard counting technique. Both counting techniques could be applied to this data, as the signal-to-background level was high. Good agreement between the analysis techniques is shown, indicating that the CCT properly subtracts the background in the over-filtered background region, and thus provides high-fidelity data. Notice the spike at 2cm in the standard analysis, which is due to intrinsic noise, is removed by the CCT.

Considering the statistical uncertainties, the resulting data obtained with the two data-analysis techniques are in good agreement for both the signal and the background, indicating that the CCT is providing high-fidelity data. It is worth nothing that during this experiment, both SCT and CCT counted 37% lower D^3He protons than an independent measurement using a surface-barrier-detector (SBD). Subsequent experiments have confirmed that this was due to an error in the assumed geometry of the source. When using corrected dimensions, the SCT and the SBD agree within statistical error.

6.3 The application of the CCT to MRS data obtained at OMEGA and the NIF

As briefly discussed in the introduction, the background must be significantly reduced to meet the requirements for the MRS DSn measurements at OMEGA and for MRS DSn measurements in low-yield scenarios at the NIF.[25] According to neutron-background measurements and simulations, discussed in Chapter 4, a background reduction of ~50 times is required in addition to what the polyethylene shielding can provide.[25] To meet this requirement, the CCT is applied to the MRS DSn data.

The effectiveness of the CCT in reducing the background in the MRS data has been analytically evaluated by using Equation (6-1) as a starting point. Using this equation, the CCT background-reduction factor (f_{CCT}) can be expressed as the ratio between the SCT-background level and CCT-background level, i.e.,

$$\frac{\mathrm{B_{SCT}}}{\mathrm{B_{CCT}}} = f_{CCT} \approx \frac{F_n A \varepsilon_{CR-39} + IA}{A\left(F_n \varepsilon_{CR-39} + I\right)^2 \pi\ \mathrm{R_c}^2} = \frac{1}{\pi\ \mathrm{R_c}^2}\left(F_n\ \varepsilon_{CR-39} + \mathrm{I}\right)^{-1} . \tag{6-4}$$

Here, ε_{CR-39} is the CR-39 efficiency for detecting neutrons, I is the intrinsic noise level per square centimeter. Typically, the intrinsic noise level is ~100 tracks/cm^2 but it can vary from piece to piece between 50-200 tracks/cm^2. As stated before, the neutron fluence is F_n ~$5\times10^{-8}\cdot Y_n$ neutrons/cm^2 and ~$2\times10^{-9}\cdot Y_n$ neutrons/cm^2 at the OMEGA-MRS detector and the NIF-MRS detector, respectively. With an R_c of 50 μm, often used in the CCT analysis, f_{CCT} can be rewritten as:

$$\mathrm{f}_{CCT} \approx \frac{13000}{2.5\times10^{-12}\ Y_n + 100} \qquad \text{(OMEGA)} \tag{6-5}$$

$$\mathrm{f}_{CCT} \approx \frac{13000}{10^{-13}\ Y_n + 100} \qquad \text{(NIF)} \tag{6-6}$$

These expressions have been plotted in Figure 6-11 as a function of Y_n (solid lines). The dotted lines indicate the upper and lower limits for f_{CCT} when considering the intrinsic-background variation. Also shown, are measured data (red points) from OMEGA that are in good agreement with predictions, giving confidence in the predictions for the NIF. As shown by Equations (6-5) and (6-6), the CCT becomes less effective as Y_n increases.

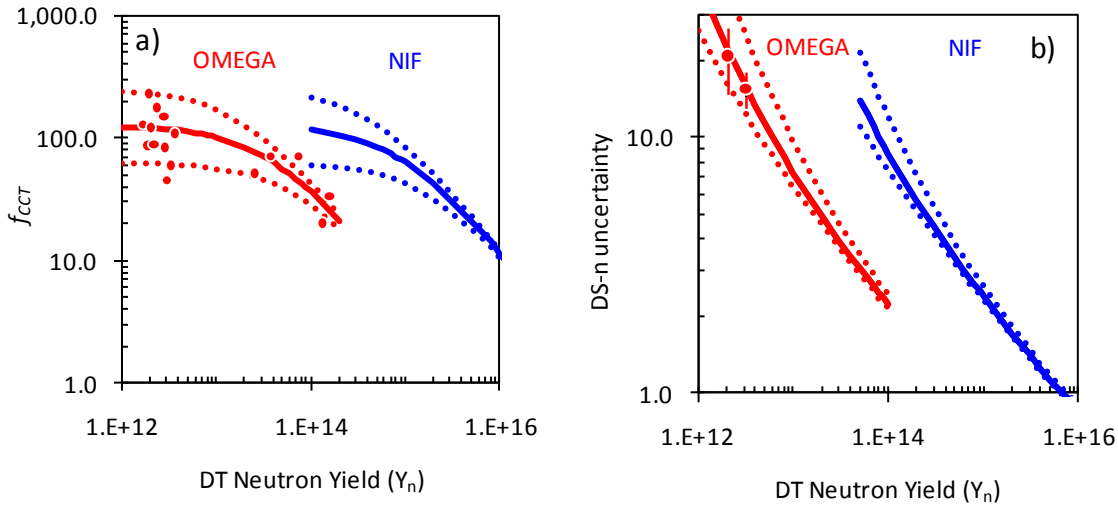

Figure 6-11: a) Background reduction factor (f_{CCT}) as a function of neutron yield (Y_n) when the CCT is applied to the MRS data at OMEGA (red) and the NIF (blue). In these calculations, the intrinsic background is assumed to be ~100 tracks/cm^2. The dotted lines represent the effect of typical intrinsic-background variations (a factor of two higher and lower).[48] The neutron background was determined using the results from Chapter 4. For comparison, experimental data are shown as well. b) Statistical uncertainty for the DSn yield, when applying the CCT, as a function of DT-primary-neutron yield (Y_n) for the OMEGA (assuming a typical cryogenic-DT areal density of ~0.19 g/cm^2 and the low resolution foil)[25, 26] and NIF MRS (assuming an areal density of ~1.0g/cm^2 during the THD and ignition campaigns and using the medium-resolution foil).[25] The red data points illustrate the observed DSn statistical uncertainty averaged over several MRS spectra obtained from different cryogenic-DT implosions at OMEGA (the inferred average areal density in these implosions is 190mg/cm^2). Good agreement between measured data and predictions indicate that the CCT background (a) and resultant DSn uncertainty (b) is well understood for the OMEGA MRS. As a consequence, the modeling of these parameters can be used with high confidence for the MRS at the NIF.

Using the f_{CCT} dependence on Y_n and the established DSn signal dependence on Y_n and ρR (see Appendix A), it is straightforward to determine the statistical accuracy for the DSn signal. The DSn signal scales with Y_n and ρR as 1.5×10^{-10} Y_n ρR(g/cm^2) when using a low-resolution foil for the OMEGA-MRS, and 2×10^{-12} Y_n ρR(g/cm^2) when using a medium-resolution foil for the NIF-MRS. Figure 6-11b illustrates the predicted statistical uncertainty for a ρR of ~0.19g/cm^2, which is a number that well represents cryogenic DT implosions at OMEGA,[26] and for a ρR of ~1g/cm^2 anticipated in THD implosions at the NIF.[25] Also shown in Figure 6-11b are averaged uncertainties determined from several OMEGA cryogenic DT implosions whose average ρR is ~0.19g/cm^2. As illustrated by the graph, these results are in good agreement with the prediction. In addition, it should be noted that the statistical accuracy improves with increasing neutron yield even though the CCT becomes less effective because of higher signal and background levels, causing increased random coincidences.

ρR data obtained from well-established charged-particle techniques[48, 50] were used to authenticate the MRS ρR data. The results from this authentication are shown in Figure 7-4 and they validate the MRS technique, which utilizes the CCT. This data is discussed more extensively in Chapter 7.

6.4 Conclusion

The CCT, which uses a staged etch scheme, has been developed for the MRS at OMEGA and for MRS DSn measurements in low-yield scenarios at the NIF to significantly reduce background. Background reductions of ~100 are regularly achieved when applying the CCT to DSn data obtained at OMEGA. The CCT will also be pivotal for DSn measurements in lower yield experiments anticipated in the THD campaign at the NIF.

7 - Down-scattered neutron measurements using the MRS on OMEGA and the NIF

To achieve ignition, a cryogenically layered DT capsule implosion must be significantly compressed to obtain high enough ρR to stop the DT-alpha particles and to allow for significant fusion reactions to occur before the implosion disassembles. Diagnosing ρR is therefore important for assessing the implosion performance, as discussed in Chapter 3. This chapter focuses on the actual measurement of the down-scattered neutron (DSn) spectrum, from which ρR can be inferred for cryogenic DT implosions at OMEGA and the NIF. In particular, it describes and expands upon the first measurements published by Frenje et al. 2010,[25] Sangster et al. 2010,[26] and Goncharov et al. 2010.[28] Section 7.1 describes the diagnosis of ρR and ρR asymmetries in OMEGA implosions. Section 7.2 discusses the authentication of the MRS measurement of the DSn spectrum. Section 7.3 describes the principles of how high compression (or high ρR) can be achieved in a cryogenic DT implosion. Section 7.4 and 7.5 discuss the MRS measurements of the DSn spectrum at OMEGA and NIF, respectively, and the importance of these measurements to the progress of the cryogenic programs at OMEGA and the NIF. Section 7.6 summarizes this chapter.

7.1 Diagnosing ρR in OMEGA implosions

ρR and ρR asymmetries in moderate ρR implosions (10-180mg/cm^2) at OMEGA are routinely diagnosed by the two charged particle spectrometers (CPS1 and CPS2) and the MRS. The CPS's measure the KO-d spectrum and the MRS measures the DSn spectrum from which the ρR can be inferred, as discussed in Chapter 3. Figure 7-1a illustrates the locations of these diagnostics on the OMEGA chamber, and Figure 7-1b illustrates the front end of the CPS2 diagnostic together with several compact Wedge-Range-Filter (WRF) spectrometers inside the target chamber. The WRF spectrometers are typically used to measure KO-p from which ρR and ρR asymmetries in the CH shell can be determined (see discussion in Chapter 3). Parts of the MRS and CPS2 are also visible in the image shown in Figure 7-2, which was taken inside the target chamber on cryogenic DT shot 55723. These diagnostics provide excellent coverage of a cryogenic DT implosion for an accurate determination of the average ρR.

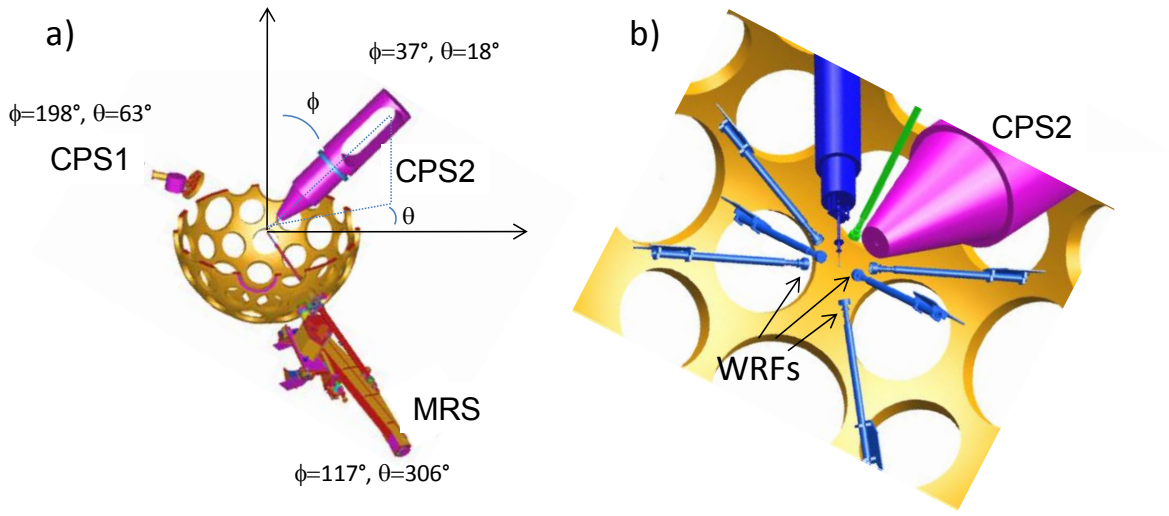

Figure 7-1: a) An illustration of the CPS1, CPS2, and MRS diagnostics on the OMEGA target chamber. The MRS is shown here without the 2000lbs shielding that surrounds the diagnostic. The LOS for each diagnostic is illustrated in terms of the polar angle ϕ and azimuthal angle θ. b) An illustration of the WRFs and CPS2 inside the OMEGA target chamber. Using these spectrometers, ρR and ρR asymmetries can be determined from the measured spectra of KO-d's (CPS1 and CPS2),[30, 48] KO-p's (WRF),[48] and DSn (MRS).

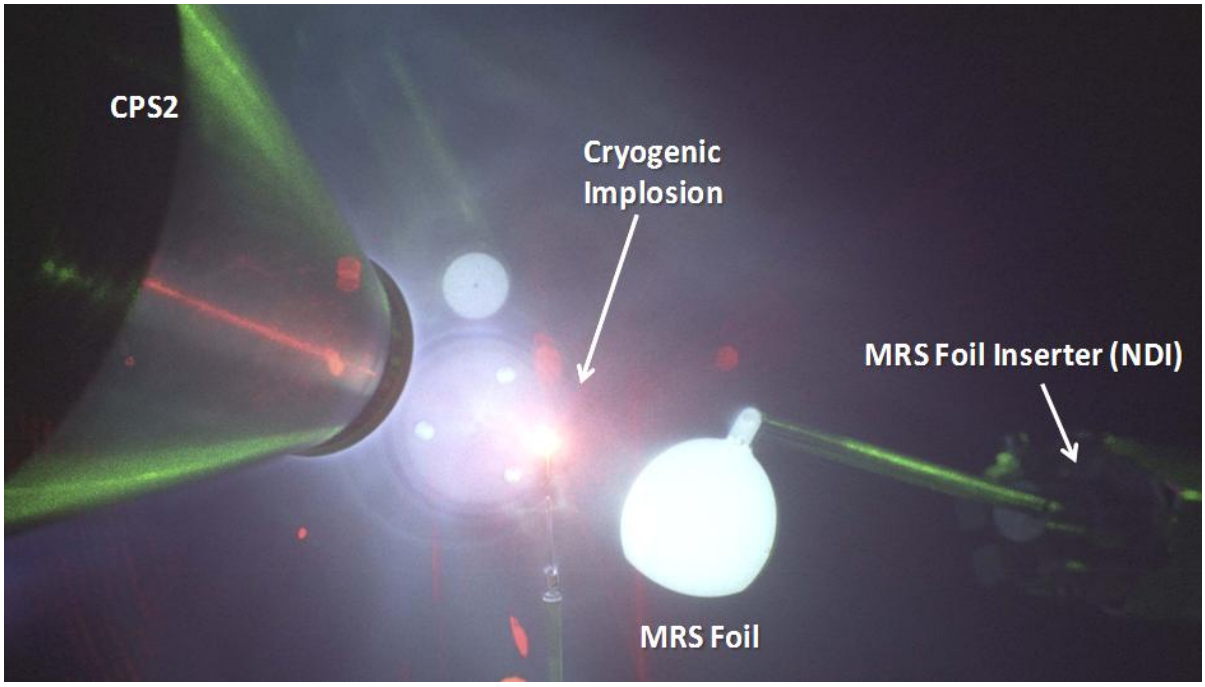

Figure 7-2: An image of cryogenic DT shot 55723, which holds the record ρR achieved at OMEGA. The CPS2 front end is shown to the left in the image and the MRS foil holder is shown to the right in the image. Photograph taken by Eugene Kowaluk.

7.2 Authentication of the MRS measurement of the DSn spectrum

For high ρR implosions (>180 mg/cm^2), only the DSn spectrum can be used to diagnose the ρR.[30] However, as previously mentioned, the well-established charged-particle techniques can be used to accurately diagnose moderate ρR implosions (10-180mg/cm^2) and authenticate the MRS measurement. An example of that authentication is shown in Figure 7-3. Here, a series of nominally identical implosions (shots 55074-55083) was summed to build up good statistics. This series used 16μm thick CH shell capsules, filled with 18atm of DT gas (see Figure 7-3), imploded with 23kJ of laser energy that was delivered in a 1ns square laser pulse. The MRS was fielded with the medium resolution CD_2 foil (see Table 4-1) to measure the DSn spectrum, and the CPS1 and CPS2 diagnostics were fielded to measure the KO-p and KO-d spectra, respectively. From the MRS data, a total areal density ($\rho R_{tot} = \rho R_{fuel} + \rho R_{shell}$) of 55 ± 10 mg/cm^2 was inferred, and from the CPS data a ρR_{tot}=56 ± 8 mg/cm^2 was inferred, which clearly illustrate that the MRS provides high-fidelity data.

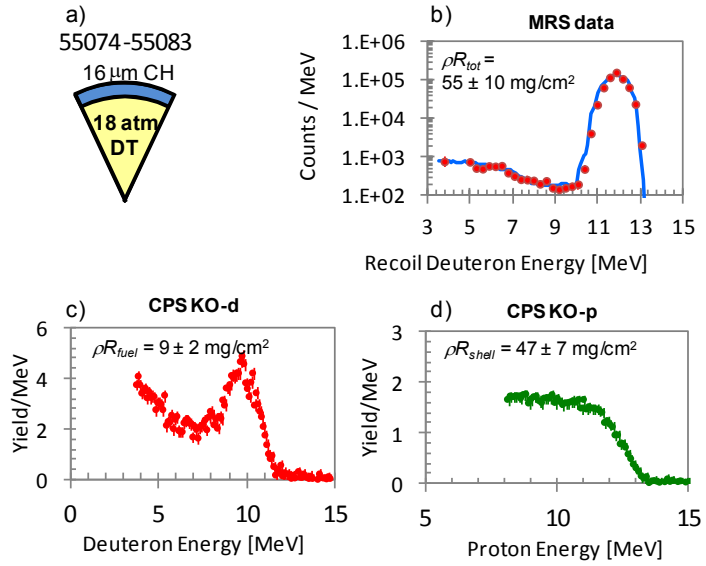

Figure 7-3: a) A schematic drawing of the capsules used for the OMEGA shot series 55074-55083. These shots were used to authenticate the MRS DSn measurement with the CPS measurements of the KO-p and KO-d spectra. In this series, 16μm thick CH plastic capsules, filled with 18 atm of DT gas, were imploded with 23kJ of energy that was delivered in a 1ns square laser pulse. This series produced a total neutron yield of 1.6×10^{14} and a burn-averaged T_i of 5.3 keV. b) Recoil deuteron spectrum (red points) measured with the MRS operated with the medium resolution foil (see Table 4-1). The best fit to the measured spectrum (blue line) was obtained as described in Chapter 3. From the fit to the DSn part of the spectrum (over which the TTn component is not important), a total areal density ($\rho R_{tot} = \rho R_{fuel} + \rho R_{shell}$) of 55 ± 10mg/cm^2 was inferred. The analysis of the TTn component is described in detail in Chapters 8 and 9. c) Knock-on deuteron (KO-d) spectrum measured by CPS2. A ρR_{fuel} of 9 ± 2 mg/cm^2 was inferred from the high-energy peak. d) Knock-on proton (KO-p) spectrum measured by CPS1. A ρR_{shell} of 47 ± 7 mg/cm^2 was determined from the plateau of the spectrum, giving a ρR_{tot} of 56 ± 8mg/cm^2, which is in excellent agreement with the MRS data, considering the statistical error and ±15% ρR asymmetries commonly encountered in this type of implosion.[30, 59, 62]

This authentication was repeated several times using different types of capsule implosions, which produced different ρR_{tot}. The capsules used in these experiments are schematically shown in Figure 7-4a, and the results are shown in Figure 7-4b. The data are in good agreement, considering the error bars and that ±15% ρR asymmetries typically observed in these types of implosions.[30, 59, 62] These results indicate that the MRS technique provides high-fidelity ρR data for a wide range of primary neutron yields (10^{12}-10^{14}) and ρRs (>10mg/cm^2).[24, 25]

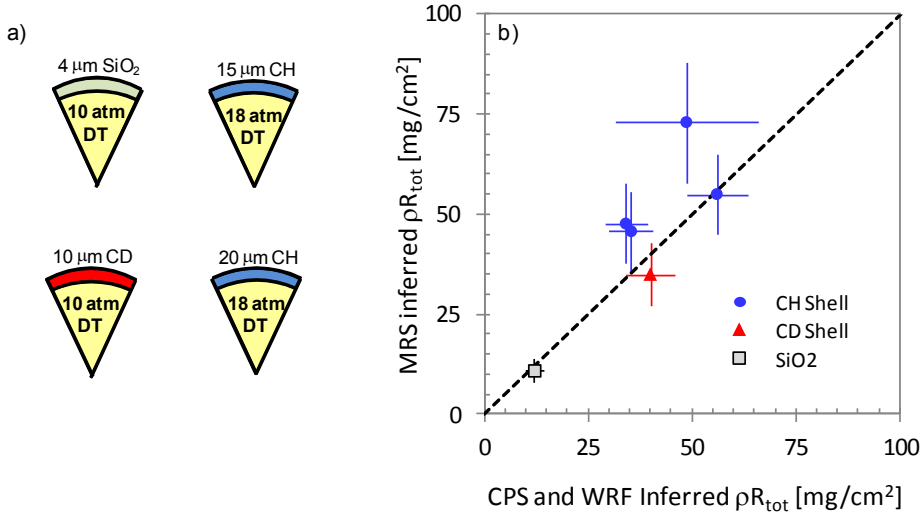

Figure 7-4: a) Schematic drawings of the capsules used to authenticate the MRS DSn measurement. The well-established CPS and WRF techniques were used for the authentication.[48] b) ρR inferred from MRS data as a function of ρR inferred from CPS and WRF data. Considering the error bars and ±15% ρR asymmetries typically observed for these types of implosions,[30, 59, 62] good agreement between the measurements is observed, indicating that the MRS provides high-fidelity ρR data.

7.3 Achieving high ρR_{tot} in OMEGA cryogenic implosions

To achieve high ρR_{tot} (>100mg/cm^2) at OMEGA, the laser pulse shape must be carefully tailored to control the dynamics of the implosion process.[17, 28, 32, 96] The 1D radiation-hydrodynamics code LILAC[31] is often used to design such an implosion. Figure 7-5 shows a LILAC simulation for OMEGA cryogenic DT implosion 55952 (more details of this simulated implosion and other implosions are provided in Appendix H). The top plot in Figure 7-5 shows the laser power profile used in this shot.[26] Notice the three pickets ("triple-picket" pulse)[28] in front of the main drive. These pickets are designed to begin compressing the shell without significantly raising the adiabat, as discussed in Chapter 2, before the main drive breaks out of the shell, into the gas, and drives the implosion to maximum compression (low-adiabat implosion). The lower plot shows the simulated trajectories of different fluid elements (of fixed mass) during the implosion. The thick blue curve is the outer ablator boundary. The plastic CD ablator is located between the blue and green curves, the DT ice-shell is between the green and red curves, and the DT gas lies within the red curve. The first picket at ~0.1ns begins ablating the outer CD layer and sends a

shock through the DT ice that starts at 0.3ns. The second picket at 0.9ns launches a second shock, which travels faster than the first shock because of the higher temperature generated by the first shock. The third picket at ~1.6ns launches a third and even faster shock. The shocks from the three pickets approximately coalesce and break out at the inner surface of the DT ice shell at ~2.1ns. The shell begins to decelerate at around 3.6ns and peak compression and heating of the gas occur at ~3.8ns.

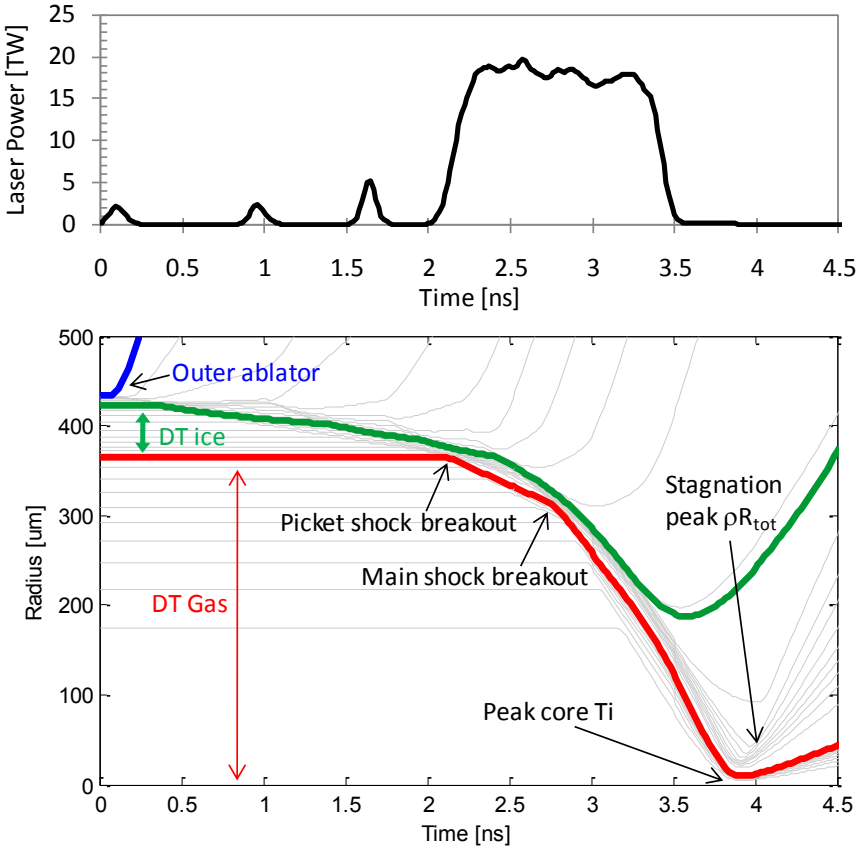

Figure 7-5 Top: Measured laser pulse shape for OMEGA cryogenic DT shot 55952. This implosion used a triple picket designed by Goncharov et al.[28] Bottom: 1D hydro-dynamic LILAC[31] simulation of this implosion. Each contour shows a group of fluid elements (of fixed mass) during the implosion. The blue curve represents the outer capsule ablator surface. The green curve is the outer shell ice layer, the DT gas lies within the red curve, which is the inner ice layer surface[4] (LILAC Simulation of OMEGA cryogenic DT shot 55952 performed by P. B. Radha, LLE).

Figure 7-6 shows the simulated DT core-averaged temperature and ρR_{tot} (fuel and shell) as a function of time for the OMEGA cryogenic DT implosion 55952. As the shell begins to approach stagnation, significant pdV work heats the core, causing the ion temperature to peak slightly before 4ns, while the peak ρR_{tot} occurs at ~4ns. The reason for this is that the core rebounds and cools slightly, reducing the burn rate, just as the shell reaches complete stagnation. All measured ρR_{tot} values discussed in this thesis are burn averaged values (because this is what is measured by the MRS), which are less than the peak ρR_{tot}. See Appendix H for additional information about this simulated implosion and other simulated implosions.

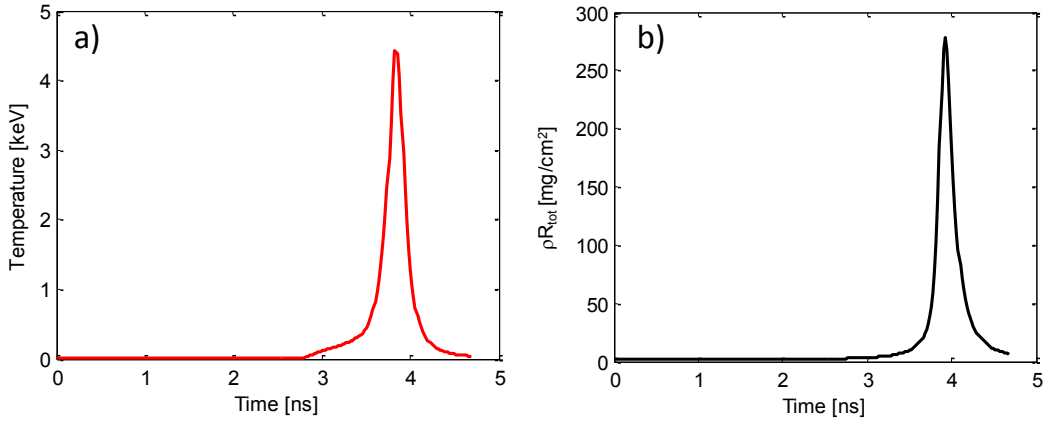

Figure 7-6 1D LILAC[31] simulation of OMEGA cryogenic DT implosion 55952. Simulated fuel ion temperature (a) and ρR_{tot} (b). Notice that the peak ion temperature occurs slightly before the peak ρR_{tot} because the core starts to expand before the shell stagnates. This is due to the finite sound speed effectively truncating the burn before peak ρR_{tot} occurs (simulation provided by P. B. Radha at LLE).

7.4 Diagnosing performance of cryogenic DT implosions at OMEGA using the MRS

7.4.1 Diagnosing average ρR_{tot}

Obtaining high compression requires careful tailoring of the capsule and laser pulse, as discussed in the previous section. It also requires a good understanding of how the assembly of the fuel occurs for that particular design. The ρR data obtained with the MRS have been essential for understanding the fuel assembly and for guiding the cryogenic program at LLE to ρR_{tot} values up to ~300 mg/cm^2. Examples of MRS data obtained for three low-adiabat cryogenic DT implosions illustrate this in Figure 7-7a. These spectra are normalized by the primary neutron yield Y_{DT} to visualize the differences in the DSn energy region. As the relative intensity of the DSn signal (neglecting profile effects) is proportional to ρR_{tot}, the differences between the different spectra indicate differences in the ρR_{tot}. A triple picket laser pulse shape (shown in Figure 7-8) was used to implode these capsules.[28] These pulse shapes were designed to carefully launch sequential shocks, experimentally tuned by varying intensity and timing.[26] The 55723 implosion (blue line) features an additional step in the main drive designed to reduce the strength of the main pulse shock.[28] Best compression is achieved if the picket and main drive shocks are timed to coalesce at the fuel shell boundary. If the shocks coalesce too early, they will form a stronger shock, which will raise entropy in the main fuel and reduce compression. This makes shock timing critical in the effort of achieving highest possible ρR_{tot}. Shot 55723 (blue data in Figure 7-7) produced the highest ρR_{tot} (295 ± 44 mg/cm^2) yet measured at OMEGA, which was achieved through a careful experimental tuning of the multi-picket pulse shape.[26, 28] In addition, Goncharov et al.[8] have designed a direct-drive capsule implosion that is expected to ignite when the laser energy is scaled to direct-drive conditions on the NIF (NIF is currently an indirect-drive facility, but it is capable of polar direct-drive after some modifications to the facility have been made).[40,41]

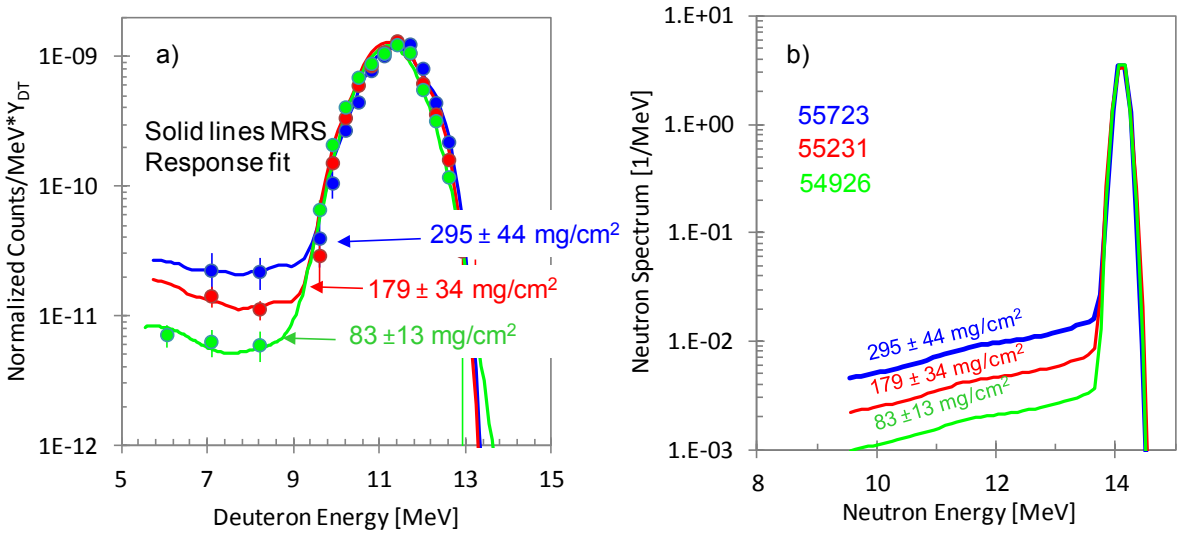

Figure 7-7: a) MRS measured recoil deuteron spectra for three cryogenic DT implosions on OMEGA. In these experiments, the MRS was operated in low-resolution mode (see Table 4-1). These spectra, which are convolutions of the neutron spectra and MRS response function, are normalized by the primary neutron yield Y_{DT}. The inferred ρR_{tot} values and associated errors from the chi-squared determined fits are also shown. b) Neutron spectra that give the best fits to the measured recoil-deuteron spectra, when convolved with the MRS response function. A summary of the MRS measurements of the DSn spectrum from all cryogenic DT implosions are shown in Appendix C.

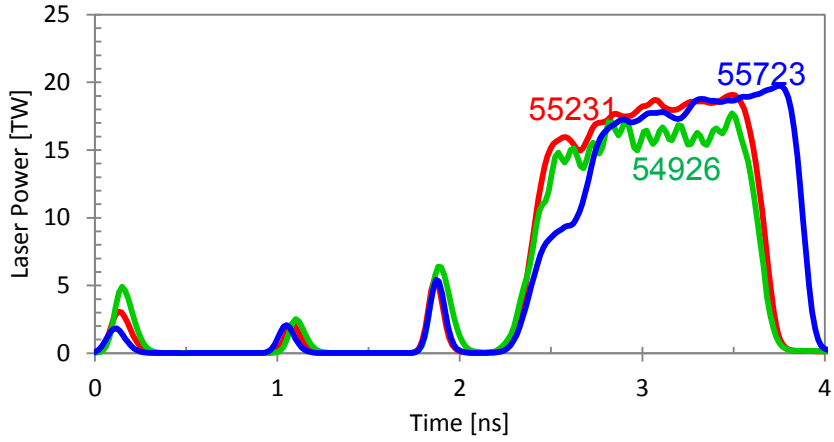

Figure 7-8: Triple picket laser-pulse shapes used to implode the cryogenic DT capsules discussed in the text. The red and green pulse shapes launch four shocks while the blue launches five. The shocks are timed to coalesce at the inner surface of the main fuel. Shock mistiming can cause the shocks to coalesce early, forming a stronger shock that raises the entropy in the main fuel and reduces compression. The MRS was used to diagnose these implosions and help find the proper pulse shape for reaching high compression or ρR_{tot}. Shot 55723 (blue pulse shape with triple-pickets and step) has produced the highest ρR_{tot} so far observed at OMEGA.[26, 28]

The uncertainty of the inferred ρR_{tot} from the MRS data obtained at OMEGA is dominated by the statistical uncertainty in the DSn spectrum. This is because most of the systematic uncertainties associated with the MRS setup cancel in the DSn-to-primary ratio used to infer the ρR_{tot} (see Equation (3-2)). The uncertainties that do not cancel are associated with the nd-cross-sections and in the different transmission values at the DSn and primary-neutron energies. The uncertainty due to the cross-sections is determined to be ±4.3%[25,97] and the uncertainty due to transmission differences is determined to be ±3.8%, resulting in a total systematic error of ±7%. According to the analysis in Chapter 6, the statistical uncertainty will continue to dominate the uncertainty of the inferred ρR_{tot} until $Y_{DT}>10^{13}$ and ρR_{tot} >200mg/cm^2 have been achieved simultaneously, which has not yet occurred at OMEGA by the time this thesis was being written.

7.4.2 Diagnosing ρR_{tot} asymmetries

Implosion symmetry is important to achieving high compression in cryogenic implosions. Controlling and minimizing ρR_{tot} asymmetry is therefore essential. On OMEGA, ρR_{tot} asymmetries are mainly generated by capsule offsets from TCC and large-scale capsule defects (usually in the ice layer).[26, 58] Capsule offsets are due to vibrations of the stalk caused by the removal of the cryogenic shroud, moments before the implosion. This puts the target in a non-uniform irradiation field (see Figure 7-9). As a consequence, the implosions will be asymmetrically driven, leading to large ρR_{tot} asymmetries that reduce the overall implosion performance.

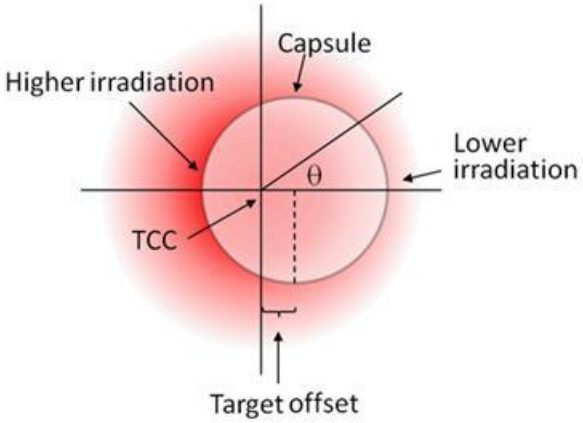

Figure 7-9: Illustration of how the capsule offset affects the symmetry of the laser irradiation. When the capsule is offset from the center of chamber (or the center of the irradiation field), the laser intensity increases on the side closest to the center, which increases the compression on that side. Capsule offsets[26] in direct-drive implosions at OMEGA are measured using time integrated X-ray pinhole cameras.[42]

Figure 7-10 shows a plot of the ρR_{tot} inferred from the CPS data (average of CPS1 and CPS2) as a function of ρR_{tot} inferred from the MRS data. Excellent agreement is shown between the two techniques for implosions with small capsule offsets (<30μm), smooth ice layers (ice layer RMS <3μm), and for ρR_{tot} values below the saturation of the CPS technique (180mg/cm^2).[25] Above ~180mg/cm^2, the CPS diagnostics can only give a lower bound on the inferred ρR_{tot}, while the MRS can continue to provide accurate values. Implosions with large capsule offsets (>30μm) or

with rough ice layers show significant variations in the inferred ρR_{tot} between the techniques, which are caused by spatial asymmetries established by these perturbations (shown by grey boxes and blue triangle). This was demonstrated using charged-particle measurements in previous plastic surrogate capsule experiments by Li et al.[61] and Seguin et al.,[62] and in cryogenic implosions by Frenje et al.[30] Hu et al. have also studied these effects using 2D DRACO hydrodynamic simulations.[58] The post-shot simulated ρR asymmetries, using measured ice roughness and capsule offsets, are in agreement with those observed in these experiments.[26]

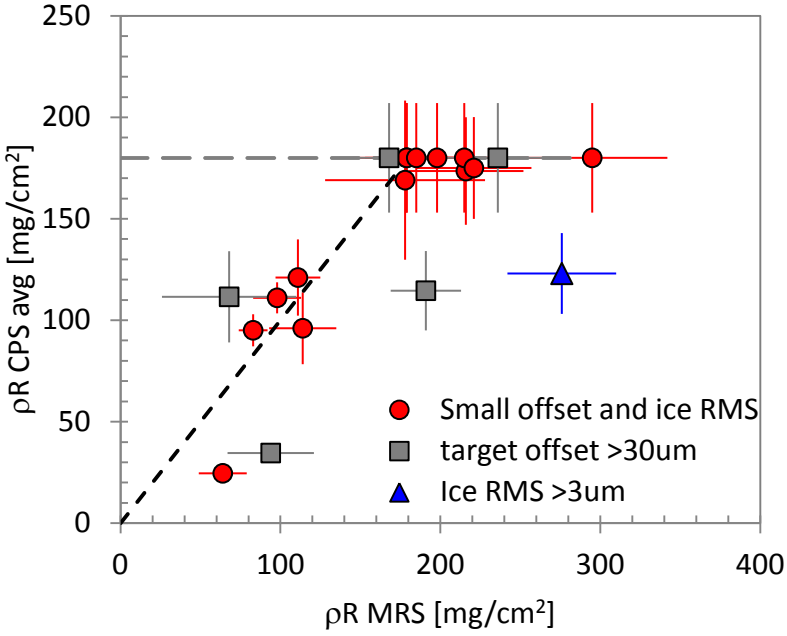

Figure 7-10: ρR inferred from the CPS data (average of CPS1 and CPS2) as a function of ρR inferred from the MRS data. Good agreement is observed for symmetrical implosions with small capsule offsets and small RMS ice roughness up to the CPS saturation limit of ~180mg/cm^2, where only the MRS can accurately diagnose the implosion.[25]

7.5 Diagnosing cryogenic DT implosion performance at the NIF using the MRS

The MRS on the NIF plays a critical role in guiding the NIC towards the demonstration of thermonuclear ignition and net energy gain. At the time of writing this thesis, the MRS has provided data that has been essential to addressing issues with the shock timing and drive symmetry in the first two cryogenic implosion campaigns using both THD and DT fuel mixtures. These experiments have already achieved record high values of Y_{DT} and ρR_{tot} in ICF experiments. Although, this work is still ongoing, some of these results are discussed in the following section.

Examples of MRS spectra are shown in Figure 7-11 for NIF cryogenic implosions N110121, N110201, and N110608. Shot N110121 (taken on January 21, 2011) was imploded with a 1MJ

pulse, while N110201 and N110608 shots were imploded with a 1.3MJ pulse. Two of these implosions (N110121 and N110201) used THD fuels designed to decrease the primary DT neutron yield to enable the use of sensitive x-ray diagnostics, while one implosion (N110608) used equimolar DT. The recoil-deuteron spectra obtained with the NIF MRS on these shots are shown in Figure 7-11a. These recoil spectra are normalized by Y_{DT} to directly show the different levels of DSn (and therefore differences in ρR_{tot}). The neutron spectra, which provide the best fits to the measured spectra, are shown in Figure 7-11b. On the basis of the DSn levels, these implosions clearly performed differently. For shots N110121, N110201, and N110608, the determined down-scattered ratios (DSRs)* from the MRS data was 3.5±1.3%, 2.4±0.3%, and 4.7±0.4%, respectively. Utilizing the expression derived in Appendix A, the areal density of N110608 is ~1g/cm^2, more than three times higher than the record value obtained at OMEGA.[26]

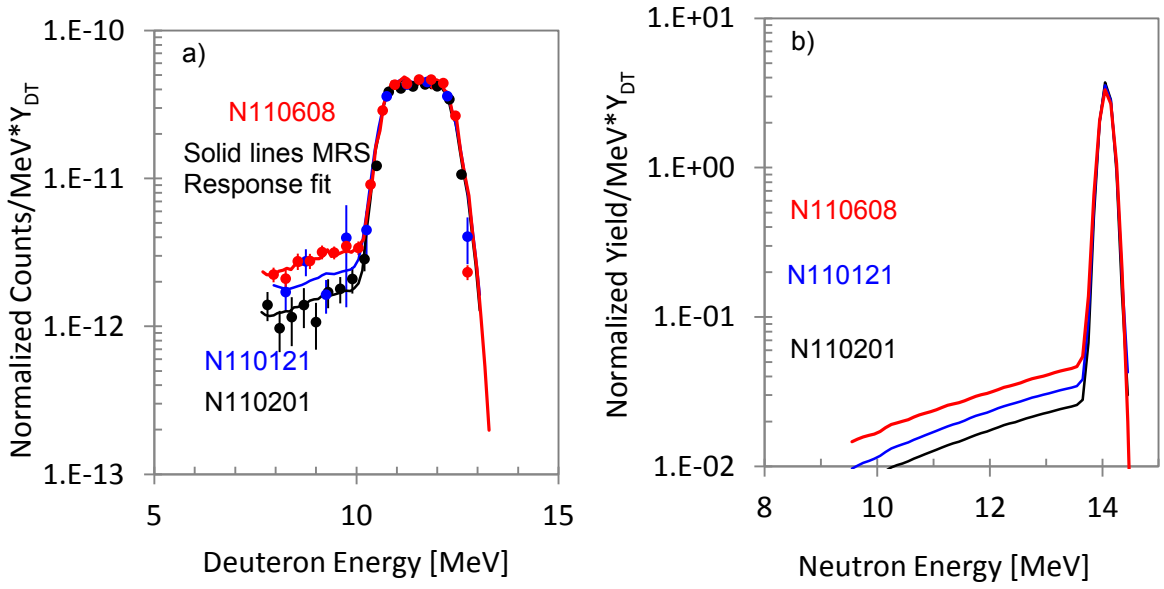

Figure 7-11: a) Y_{DT}-normalized MRS recoil-deuteron spectra for NIF cryogenic implosions N110121, N110201, and N110608. Two of these shots (N110121 and N110201) used THD fuels, while shot N110608 used equimolar DT. The MRS spectra were obtained with the low resolution CD_2 foil described in Chapter 4. b) Neutron spectra that give best fits to the recoil-deuteron spectra (solid curves, which are convolutions of the neutron spectra and the MRS-response function). From these neutron spectra, a DSR of 3.5±1.3%, 2.4±0.3%, and 4.7±0.4% was determined for shot N110121, N110201, and N110608, respectively. On the basis of these values, shot N110608 performed the best (highest compression).

Figure 7-12 shows the laser pulse shapes used to drive the implosions described in Figure 7-11.[32, 98-100] The tuning of the implosion drive was performed by adjusting the intensity and timing

* The ρR_{tot} of an ICF implosion can be determined from the yield ratio between DSn and primary neutrons, commonly called down-scattered ratio (*DSR*). Derived in Appendix A, the ρR_{tot} scales with DSR as ρR_{tot} (g/cm^2) = 20 × DSR when neglecting profile effects. This relationship also neglects any remaining ρR_{shell}. Efforts to experimentally determine any remaining ρR_{shell} have not yet been done but are currently underway. It should be noted though that the neutron scattering cross-sections for typical ablator materials, i.e. CH, are significantly lower in the 10-12 MeV range than for DT for the same ρR (see Appendix A), significantly reducing the effect of the ablator ρR_{shell} on the measured DSR.

of the first two pickets as well as the main drive and its shoulder. The first two implosions were not tuned correctly, resulting in relatively low DSR (and ρR_{tot}) values, as discussed in the previous section. The third shot shown here (N110608) was conducted after the shock-tuning campaign in May 2011, resulting in almost a factor of two higher DSR value and compression. The main reason for this was that the laser drive for N110608 provided better timing for shock-coalescence near the gas/ice boundary, which is required to maintain a low implosion adiabat and therefore reach maximum compression.

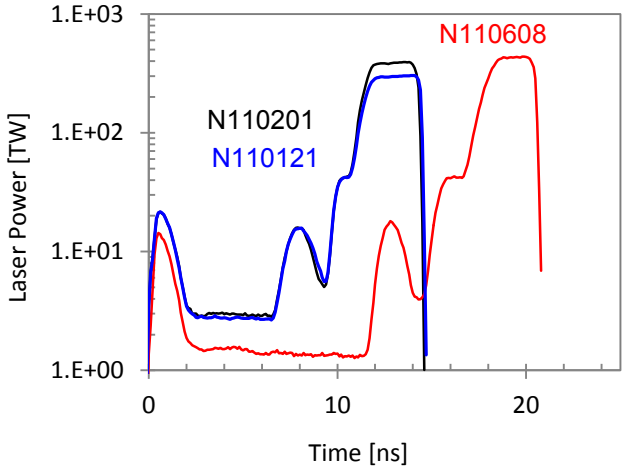

Figure 7-12: Laser pulses used to drive the N110121, N110201, and N110608. The intensity and timing of the first two pickets, the shoulder, and the main drive are adjusted to tune the implosion. The shock timing must be optimized to minimize the adiabat in the main fuel to reach maximum compression. The major change in the timing of the main pulse for shot N110608 was partly due to revised shock-timing data obtained during specially designed key-hole experiments in May 2011,[37] resulted in significant improvement of the implosion performance, as shown in Figure 7-11a.

The MRS on the NIF has provided data that have been essential to the progress of NIC. The most recent MRS data obtained in September 2011, indicate that the implosion performance, characterized by the experimental Ignition Threshold Factor (ITFX),[29] has improved about 50× since the first shot a year earlier. The ITFX is defined by

$$ITFX = \frac{Y_{DT}}{Y_0}\left(\frac{DSR}{0.07}\right)^{2.3}, \tag{7-1}$$

where Y_0 normalizes the ITFX metric to be equal to ~1 (based on thousands of 2D simulations) for a 50% probability of achieving a gain of one in an equivalent equimolar-DT implosion.[29] Here, gain is defined as the ratio of thermonuclear energy produced to laser energy incident on the hohlraum. For hydro-equivalent THD implosions, the normalization factor $Y_0=3\times10^{15} f_d$ (3-2f_d), where f_d is the deuterium fraction (atom %) of the core normalized so that $f_h + f_d + f_t=1$. The ITFX is a metric derived from a large simulation database to assess implosion performance in the context of achieving ignition. The main reason for the improvement in ITFX was the improved shock timing.[101] In addition, going from a germanium-doped ablator to a silicon-doped ablator also improved the implosion performance, as the implosion velocity improved 10-15%.[102] It is worth

noting that this analysis assumes the DT fuel of the core remains "un-stratified," an assumption tested in non-cryogenic plastic-shell implosions at OMEGA in Chapter 9.

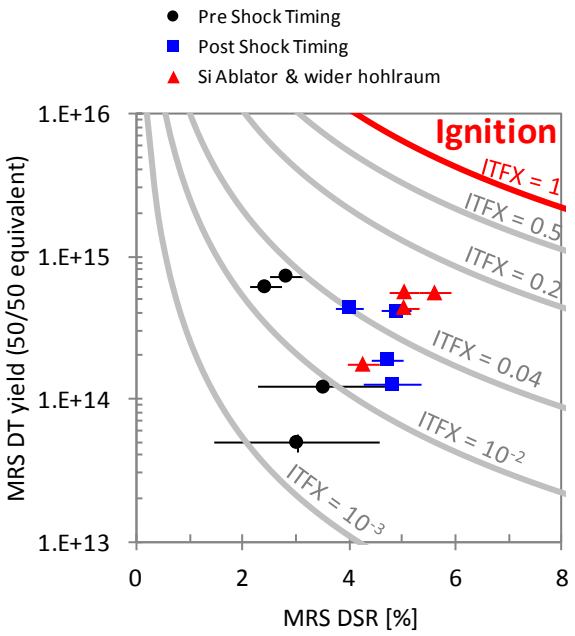

Figure 7-13: DT equivalent yield as a function of DSR (both values obtained from the NIF MRS), which is proportional to ρR. For hydro-equivalent THD implosions, the equimolar DT equivalent yield is equal to $Y_{DT\text{-}eq.} = Y_n / f_d\,(3\text{-}2f_d)$, when neglecting alpha particle heating. From yield and DSR, measured by the MRS, the implosion performance (characterized by ITFX)[29] was determined. From September 2010 to September 2011, the ITFX improved about 50 times.

7.6 Summary

For the first time, the DSn spectrum has been used to infer the ρR_{tot} in ICF implosions. DSn measurements made with the MRS have played an essential role in diagnosing cryogenic DT implosion performance at OMEGA. New capsules and carefully tuned laser pulses have been designed[28] and implemented[26] to achieve ρR_{tot} of ~300mg/cm^2 at OMEGA. DSn measurements with the MRS at the NIF have already played an important role in tuning the implosions to the highest ρR_{tot} values ever achieved in ICF (about 70-80% of the compression required for ignition).

8 - Measurements of the TT neutron spectrum at low reactant energies

This chapter presents the first measurements of the absolute neutron spectrum from the T(t,2n)4He (or tt) reaction using ICF implosions. In these experiments, which were carried out at the OMEGA laser, deuterium-tritium (DT) gas-filled capsules were imploded to probe the tt reaction in thermonuclear plasmas at low reactant center-of-mass (CM) energies. As the tt reaction is a mirror reaction to the ^{3}he^{3}he solar fusion reaction, this study could have important implications to stellar nucleosynthesis. In addition, these spectral measurements lay the foundation for the tt yield measurement, which is discussed in Chapter 9. This chapter is structured as follows, Section 8.1 provides an introduction, Section 8.2 discusses measurements of the tt neutron spectrum at higher reactant energies, Section 8.3 shows measurements of the tt spectrum at OMEGA, and finally Section 8.4 summarizes.

8.1 Introduction

In Inertial Confinement Fusion (ICF) experiments at the OMEGA laser facility at the University of Rochester[22] and the National Ignition Facility (NIF) at Lawrence Livermore National Laboratory,[21] capsules are irradiated with lasers to compress and heat the fuel to high enough temperatures and densities for fusion reactions to occur. These thermal plasma environments more closely resemble the burning core in a star (e.g. thermonuclear reactant energy distributions and electron screening environment),[14] than the conditions in accelerator experiments, thereby providing unique opportunities to explore new areas of low-energy plasma-nuclear science[87] and stellar nucleosynthesis.[10] One reaction of interest to both these areas is t(t,2n)^{4}he (or tt). The tt reaction is a mirror reaction[103-106*] to the stellar ^{3}he(^{3}he,2p)^{4}he (or ^{3}he^{3}he) reaction,[107] which is the dominate energy-producing step in the solar proton chain.[10] Therefore, studying the tt reaction also provides information about the ^{3}he^{3}he reaction, as mirror reactions have very similar nuclear behavior (after correcting for the difference in the coulomb potential and isospin).[10, 13, 107] One probe of this nuclear behavior is the shape of the emitted particle spectra, which is sensitive to the final-state interactions between the emitted particles. The tt neutron spectrum is a broad continuum of energies due to the 3-body kinematics that govern the two neutrons and ^{4}he, emitted per reaction. The n-n and n-^{4}he final-state interactions modify the spectrum from an otherwise elliptical energy spectrum (if these interactions are insignificant†).[108] Therefore, measuring the tt

* Mirror nuclei have the same number of nucleons with the special relationship that the number of protons in one mirror is equal to the number of neutrons in the other. The charge symmetry of the strong force causes wave-functions with a given isospin to be the same when some number of neutrons are replaced by protons (or vice versa). This property gives mirror nuclei very similar energy levels and state properties (these closely related states are also called isobaric analogue states). The small differences (typically) that do exist between mirror states are due to the Coulomb force and the smaller but also important charge-symmetry breaking (CSB) effect.

† Even with zero final-state interactions the emitted spectrum will not be exactly elliptical because of the triton wave function in the entrance channel. For simplicity, this effect will be neglected in this chapter but *ab initio* calculations will treat this properly.

neutron spectrum provides information that can be used to constrain models of these final-state interactions. In addition, a quantitative understanding of the tt neutron spectrum is important to ICF, as the spectrum must be well understood to make inferences of other important features in the ICF-neutron spectrum. In particular, the tt spectrum overlaps with part of the down-scattered neutron (DSn) spectrum, an essential gauge of implosion performance.[26]

Using the implosion capabilities on OMEGA, the tt reaction can be studied in ICF implosions at reactant center-of-mass (CM) energies from 10-45 keV.[24, 43] This chapter presents measurements of the absolute neutron spectrum from the tt reaction utilizing a variety of deuterium-tritium (DT) gas-filled capsule implosions at the OMEGA laser facility. From these measurements, the tt neutron spectrum is found to differ significantly from accelerator experiments conducted at CM energies >100keV.[55, 109] More specifically, the "low-energy" ICF thermonuclear experiments herein show a negligible n+^{5}he resonance (or n-^{4}he final-state interaction).

8.2 The tt neutron spectrum and previous measurements

As the tt reaction produces three particles in the final-state, the tt neutron energy spectrum is challenging to calculate theoretically.[107] *Ab initio* methods[110] can be used to determine the spectral shape but are computationally intensive and are presently ongoing for the tt reaction at these energies.[111] The neutron spectrum can be approximated using a three-body resonance model.[13] This model includes the n+n+^{4}he, the ground-state n+^{5}he(GS), and the excited-state n+^{5}he*(ES) resonances, summarized in Equations (8-1) to (8-3).

$$\mathrm{T} + \mathrm{T} \rightarrow 2\,\mathrm{n}(0 - 9.4\mathrm{MeV}) + {}^{4}_{2}\mathrm{He} \quad \mathrm{Q}=11.3\ \mathrm{MeV}, \tag{8-1}$$

$$\mathrm{T} + \mathrm{T} \rightarrow \mathrm{n}(\sim 8.7\mathrm{MeV}) + {}^{5}_{2}\mathrm{He} \tag{8-2}$$

$$\mathrm{T} + \mathrm{T} \rightarrow \mathrm{n}(\sim 7.7\mathrm{MeV}) + {}^{5}_{2}\mathrm{He}^{*} \tag{8-3}$$

The n+n+^{4}He resonance channel (Equation 8-1) emits two neutrons over an energy range of 0-9.4MeV. As mentioned previously, if the neutrons and ^{4}he nuclei do not interact and the initial-state wave functions are ignored, the neutron spectrum takes the form of an elliptical spectrum.[54] However, this spectrum is modified by the n-n interaction, skewing the neutron spectrum towards lower energies as calculated by Lacina et al.[54] and shown in Figure 8-1. The n+^{5}he(GS) resonance modifies the neutron spectrum through the formation of the short-lived ^{5}he nucleus in the ground-state and results in a neutron with a peak energy of 8.7 MeV (Eq. 2). Similarly, the excited-state resonance n+^{5}he*(ES) modifies the neutron spectrum through the formation of an excited ^{5}he* nucleus (whose energy level is 1.27MeV[112] above the ground-state) and results in a neutron with an energy-distribution peak ~7.7MeV.* The relative amplitudes of these resonance contributions have traditionally been determined from accelerator experimental data (> 100 keV).[13, 109]

* This neutron has a broad emission spectrum due to the very short lifetime of ^{5}he*.

One such experiment often used to normalize these resonance amplitudes[13] was performed by Wong et al.[109] who measured the tt neutron spectrum at a CM energy of 250 keV (see Figure 8-1b). These authors determined that all three resonance contributions were observable in the ratios of 70% n+n+^{4}he (using Lacina[54] calculated spectra), 20% n+^{5}he(GS), and 10% n+^{5}he*(ES). In addition, at a CM energy of 110 keV, Allen et al.[55] measured a n+^{5}he(GS) ratio to n+n+^{4}he of about 5%, indicating that the branching ratio is smaller at 110 keV than observed at 250 keV.

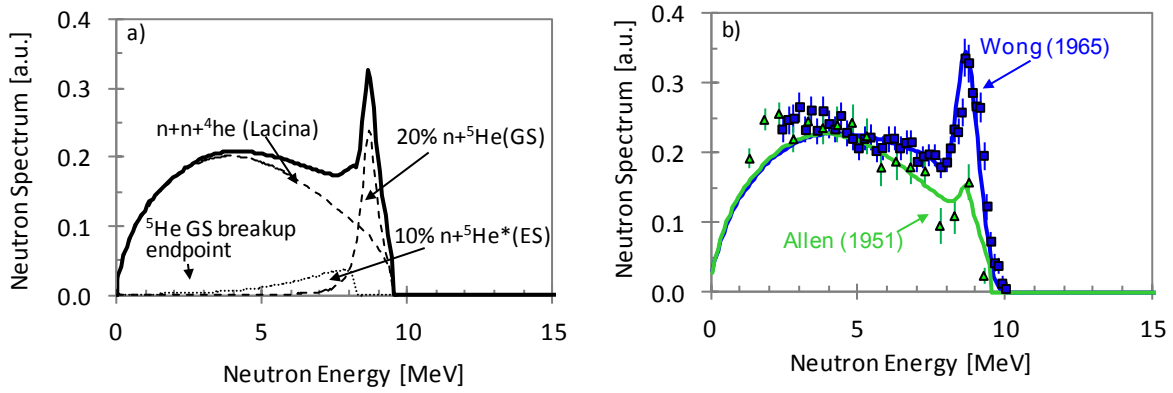

Figure 8-1: a) Model neutron spectrum for the tt reaction including contributions from the n+n+^{4}he, n+^{5}he(GS), and n+^{5}he*(ES) resonances.[54] The n+^{5}he resonance shapes were calculated using ^{5}He data from Tilley et al.[112] and resonance amplitudes determined by the Wong spectrum. Contributions from the ^{5}He-breakup neutrons are neglected because the GS is below the detection limit for the data discussed in this paper and the ES contribution is minimal (contributions from ^{5}He are shown *a posteriori* to be negligible). b) Measured tt neutron spectrum at 90° from Allen et al.[55] (green triangles) and Wong et al.[109] (blue squares) at CM reactant energies of 110 keV and 250 keV, respectively. The best fits to the two data sets are also shown (solid lines) using the model described in part a.

This apparent reactant-energy dependence of these resonance amplitudes poses the question of what happens at even lower reactant energies. To address this issue, the tt neutron spectrum has been obtained at lower reactant CM energies in the thermonuclear conditions for ICF implosions. To compare data from such an implosion to accelerator data, it is necessary to convert the observed implosion ion temperature (T_i) into the reactant CM energy. The peak (also called Gamow peak energy) of the reactant energy distribution can be expressed as $E_{cm} = (b\,T_i/2)^{2/3}$, which has a $1/e$ full-width of $\Delta = 4(E_{cm}T_i/3)^{1/2}$. Here, the Gamow penetration factor (b), is $b = \sqrt{2m_r}\pi e^2 Z_1 Z_2/\hbar$. For tt, b =38.5 keV$^{1/2}$ and for ^{3}he^{3}he b=154 keV$^{1/2}$(T_i and E_{cm} are expressed in keV).[10] Using T_i's readily achievable in an OMEGA ICF implosion (2-15keV), it is seen that CM energies of 10-45 keV can be explored.

8.3 Measurements of the tt neutron spectrum at OMEGA

The ICF experiments presented herein were conducted at the 60 beam, 30kJ OMEGA laser facility.[22] The absolute neutron spectrum, including the tt neutron component, is measured at OMEGA with the Magnetic Recoil Spectrometer (MRS), discussed in detail in Chapter 4. This is

accomplished by first converting neutrons, incident on a 164μm thick CD_2 foil positioned close to the implosion, into elastically scattered recoil deuterons. Next, forward scattered recoil deuterons are selected, momentum-analyzed, and focused by a magnetic spectrometer onto an array of CR-39 detectors. The CR-39 array records the deuteron energy spectrum, which is finally used to determine the original neutron spectrum.*

Figure 8-2a shows MRS data summed over the nominally identical† OMEGA shots 55641-55647. In this series, six‡ 10μm thick CD capsules filled with 12 atm of DT fuel (f_T/f_D=0.63[113], where f_T and f_D are the tritium and deuterium fuel fractions, respectively) were imploded with 23kJ of energy delivered in 1ns-square laser pulses, resulting in a total neutron yield of 2.6×10^{14}. A burn averaged ion temperature of 8.0keV was determined from the neutron time-of-flight (nTOF) diagnostic suite[79] for this implosion series. The MRS measured recoil deuteron spectrum is shown in Figure 8-2a, where the black points represent the primary dt and DSn data, and the red points represent mostly the tt data (some DSn signal exist in this region as well, indicated by the DSn fit). The primary 14 MeV dt peak is evident in Figure 8-2a at a deuteron energy of ~11.6MeV; the energy shift is a result of kinematics and energy loss in the CD_2 foil. The DSn spectrum is visible, isolated from other spectral components, in the deuteron-energy range 8-10 MeV. The solid line in Figure 8-2a represents the best fit of the primary dt and DSn components to the measured black data points.

In the fitting process, the neutron spectrum (Figure 8-2b) is folded with a Monte Carlo generated MRS-response function to create a modeled recoil deuteron spectrum. The magnitude of the DSn spectrum is used as a fit parameter to the measured data, and the fixed DSn shape is defined by the fuel and shell mixture and the differential cross section for n-D, n-T, and n-C scattering. To ensure that this fitted DSn level is sound, the inferred total (fuel and shell) areal density (ρR) from the DSn spectrum§ can be compared to well-established charged particle measurements.[48] The DSn inferred ρR is 35±5mg/cm^2, which is in acceptable agreement with the complimentary charged particle inferred ρR of 40±6mg/cm^2.[**,61, 62] As already indicated, the tt spectrum dominates at deuteron energies below 8 MeV and is absent from the neutron model in Figure 8-2b; it will be determined directly from the data.

---

* For the experiments described in this chapter, the MRS was operated with a medium-resolution configuration, with a resolution of about 0.55 MeV (sigma).

† Six implosions were integrated to obtain better statistics because the neutron detection efficiency is relatively low. Nominally identical shell thickness, diameter, fill pressure, and laser profiles within an implosion series result in very similar nuclear-burn-averaged ion temperatures and DT yield. In this series, the shot-to-shot ion temperature varied by 3% and the DT yield varied by 39%.

‡ OMEGA shot 55645 was not a target shot and produced no yield.

§ The DSn spectrum is linearly proportional to the imploded capsule areal density.

** Areal density asymmetries of 15-20% are commonly encountered for these types of capsule implosions.

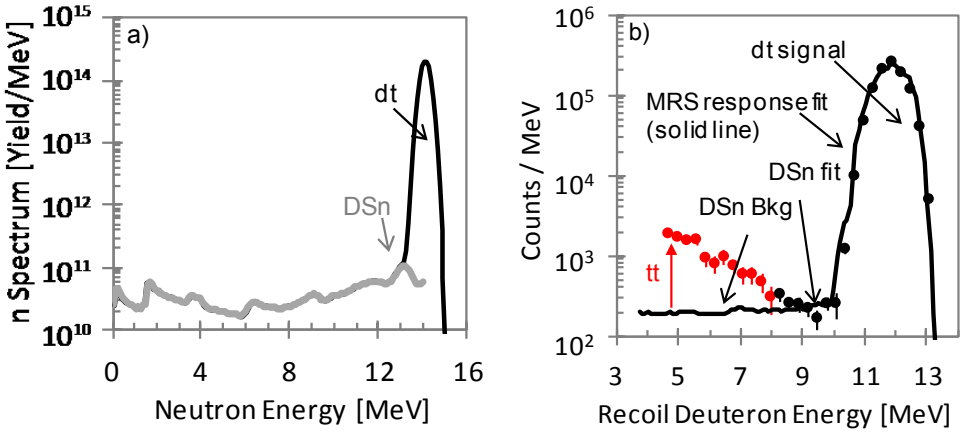

Figure 8-2: a) MRS measured recoil deuteron spectrum summed over OMEGA shots 55641-55647 (points). The deuteron peak at ~11.6 MeV is due to the primary 14 MeV dt neutrons. The width of the dt peak is primarily due to the MRS resolution. The DSn component is observed in the deuteron-energy range of 8-10 MeV. A best fit to the black data points for the dt and DSn components is shown by the solid black line. The remaining tt neutron signal (red data points) rises above the DSn background below 8 MeV. b) Modeled neutron spectrum for dt and down-scattered neutron (DSn) components that gives the best fit to the measured recoil deuteron spectrum for OMEGA shots 55641-55647 (black points discussed in part a).

The tt neutron spectrum is obtained by subtracting the best-fit contribution from DSn and then converting recoil deuteron energy to neutron energy through the MRS response function. This procedure was repeated for six different implosions series, utilizing capsules with shells made of 3.8μm thick SiO_2, 10μm CD, and 15-20μm CH, providing a range of T_i between 3.5 - 8keV with an average of 5.8keV. Figure 8-3 shows the average-tt-neutron spectrum obtained from this analysis. Also shown are modeled neutron spectra, convolved with the MRS resolution, for the n+n+^{4}He resonance (solid red),[54] along with 5% (dashed red) and 20% (dotted red) intensities of n+^{5}He(GS) resonance.* The measured data shows that the n+^{5}He(GS) resonance is insignificant, given the uncertainty of about ~2% that is based on a χ^2 sensitivity analysis.†

* The n+^{5}He*(ES) resonance is neglected since the n+^{5}He(GS) is not observed.

† The spectrum determined in Fig. 3 is qualitatively supported by unpublished nTOF measurements of the tt neutron spectrum from T_2-gas filled implosions, conducted by V. Yu Glebov et al.[Bull. of Am. Phys. Soc. 2006, APS.2006.DPP.GO2.11], that suggested a spectrum dominated by the n+n+4he resonance. It should, however, be noted that this data was only suggestive as a complicated nTOF detector response and neutron scattering made a quantitative measurement of the tt neutron spectrum very challenging.

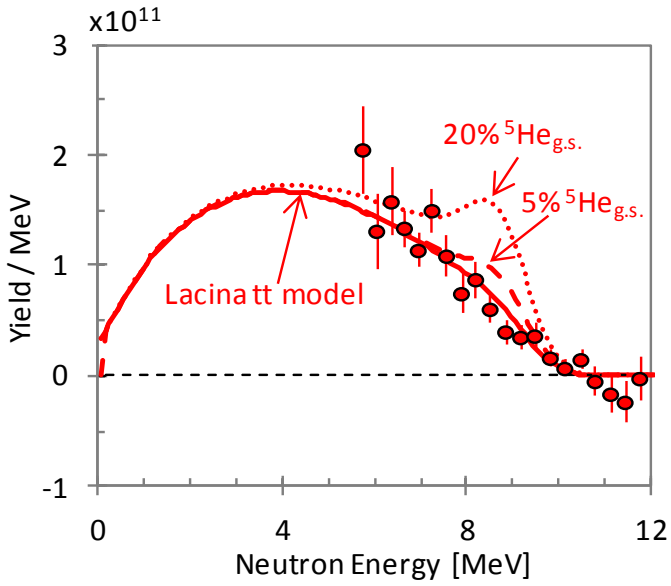

Figure 8-3: The tt neutron spectrum averaged over six different implosion series consisting of two 4 μm thick SiO_2, six 10μm CD, and seventeen 15μm CH, and five 20μm CH capsules, all filled with DT gas. The solid line shows the modeled n+n+^{4}He resonance,[54] while the dashed and dotted lines represent 5% and 20% contributions of n+^{5}He(GS), respectively. All three models were convolved with the MRS resolution for direct comparison to the measured data (the neutron energy resolution is 0.55MeV). As indicated by the plot, no n+^{5}He(GS) resonance is observable in the neutron spectrum.

Utilizing the results of Figure 8-3, the relative intensity of n+^{5}he(GS) to the n+n+^{4}he resonance can be compared to accelerator experiments at higher CM energy, as shown in Figure 8-4. For this comparison, the average T_i 5.8 keV for the data in Figure 8-3 corresponds to a peak reactant energy distribution of E_{CM} = 23keV. The data at 23keV (CM energy) suggests a trend with the data obtained in the accelerator experiments at 110 keV and 250 keV.[55, 109] The negligibly small n+^{5}he(GS) resonance apparent in Figure 8-3 along with the suggested trend of Figure 8-4 implies that n+^{5}he(GS) is suppressed at these low reactant CM energies. Such an effect might be due to the dominance of a tunneling mechanism, where a proton tunnels from one triton to the other, thus excluding the n+^{5}he(GS) reaction. *Ab initio* calculations of the tt spectrum currently underway will help to explore this idea.

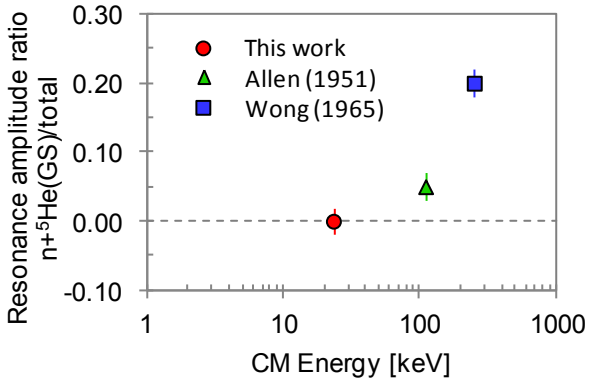

Figure 8-4: The n+^{5}he(GS) to n+n+^{4}he reaction branching ratio as a function of CM energy. The red data point was determined from the neutron spectrum shown in Figure 8-3. This data set is compared to accelerator experiments (both at 90°) by Wong [109] (blue square) and Allen [55] (green triangle). The general trend in the observed accelerator data agrees with the measurements in this work, which shows an insignificant n+^{5}He resonance at ICF relevant energies.

The relative strength of the n+^{5}he(GS) resonance amplitude shown in Figure 8-4 is of immediate relevance in ICF applications. Specifically, hydrodynamic simulations of ICF implosions using LASNEX indicate that the tt reaction significantly contributes to the total neutron spectrum in tritium-rich THD implosions at the NIF.[29] In particular, LASNEX simulates the tt neutron emission using the resonance amplitudes obtained by Wong et al.[109] at 250keV CM energy.[114] In contrast, Figure 8-4 indicates that the n+^{5}he(GS) contribution to the tt neutron emission is negligible for ICF. It is also interesting to note that the relative amplitudes of ^{3}he^{3}he resonance channels (p+p+^{4}he and p+^{5}li) have been determined from the Wong spectrum in some situations.[109] This is for the reason that tt and ^{3}he^{3}he are mirror reactions.[13] The results of Figure 8-4 additionally pose the question as to whether a similar relationship exists for ^{3}he^{3}he in the case of the p+^{5}li resonance. To that end, experiments have begun to directly measure the ^{3}he^{3}he proton spectrum in OMEGA implosions.[115]

To improve upon the measurements of the tt neutron spectrum at OMEGA, future experiments using pure T_2-gas filled capsules are proposed that will greatly reduce the dt yield and thereby the DSn background. This will eliminate the principle source of background in these measurements and reduce the uncertainty in the measured spectrum. In addition, plans are underway to construct a low-energy neutron spectrometer (LENS)[116] that will extend measurements of the tt neutron spectrum to 0.1-5MeV. This will directly illuminate the n-n final-state interaction in the tt spectrum, whose affect should be most apparent at neutron energies of ~4MeV.

8.4 Summary

In summary, the tt neutron spectrum has been measured at low reactant energies in thermonuclear plasmas using a variety of ICF capsule implosions at OMEGA. The results show that, in contrast to accelerator data at higher CM energies (>100keV), the n+^{5}he resonance is

insignificant at reactant energies relevant to ICF. This result is of immediate relevance in the interpretation of the ICF neutron spectrum at the NIF and raises the question about the resonance amplitudes for the he^3he reaction, which is the dominant energy-producing step in the solar proton-proton chain.

9 – Evidence for stratification of DT fuel in ICF implosions

Neutrons released in fusion provide a window into the burning core, which reveal a wealth of information that cannot be obtained through any other means. Implosions that contain deuterium and tritium generally produce copious dt reactions and subsequent 14.1 MeV neutrons. These primary dt neutrons are discussed extensively in Chapter 5. Primary dt neutrons also undergo elastic scattering, producing down-scattered neutrons, which are used to infer areal density as discussed in Chapter 7. However, other primary reactions occur in the burning core (like dd and tt), when deuterium and tritium are present, but in much lower numbers because of their lower reactivity (recall Figure 1-3). In typical temperature ranges (2-15keV) the reactivity is $< 10^{-2}$ times lower for dd and tt, making the measurements of these reactions quite challenging in DT implosions, because of the very high dt background. Despite the difficulty, new physics can be discovered by studying these reactions. For example, the tt reaction is now revealing new insights in both basic nuclear physics and in studying the dynamics of ICF implosions. This chapter discusses the measurements of the tt neutron spectrum, in DT implosions, and expands upon the results, which have been accepted for publication in the *Physical Review Letters*. This chapter is structured as follows, Section 9.1 provides an introduction, Section 9.2 derives the predicted dd/dt and tt/dt yield ratios, Section 9.3 shows the observed yield ratios and Section 9.4 discusses the role of fuel stratification, while Section 9.5 summarizes.

9.1 Introduction

In laser-driven Inertial Confinement Fusion (ICF), spherical capsules are compressed and heated to high enough temperatures and densities for fusion reactions to occur.[16, 32] The fusion products from these reactions carry information about the core, and can be used to diagnose the underlying implosion physics. For instance, measurements of fusion products from the D(d,p)T (dd) and D(^{3}he,p)^{4}He (d^{3}he) reactions in D^{3}He gas-filled capsule implosions at OMEGA[22] have shown anomalous yield behavior, indicating that aspects of the underlying physics governing an ICF implosion are not completely understood.[35] Based on scaling of D_2 implosions with the same mass and particle density (which are "hydro-equivalent"),* it was shown by Rygg et al.[35] that the d^{3}he proton and dd neutron yields were about 50% lower than the expected in equimolar D^{3}He gas-filled capsule implosions. In another study, non-hydro-equivalent DT^{3}He gas-filled capsule implosions have shown anomalous D(t,n)^{4}He (dt) reaction yield behavior that was ~50% lower than expected.[47] A third study showed indirect-drive experiments, with trace Ar dopants in D_2 capsule implosions, which also had observed dd yields that were 30-50% of expectation.[33, 117] The

* Hydro-dynamic behavior was predicted to be the same for implosions with the same mass density, total particle density, and equation of state, despite having different fuel compositions.

results from these studies suggest species diffusion effects, as proposed by Amendt et al.[117] These effects, which are to the best of our knowledge not included in simulations, appear to measurably degrade the nuclear yields of lighter ion species in an ICF implosion. Generalizing these observations from the different elemental mixtures (different Z) of previous work[35, 47, 117] to include isotopic mixtures of the same Z (e.g, Z=1 for hydrogen, deuterium, tritium), is of fundamental interest. The latter case is particularly important, as it is directly relevant to current ignition experiments at the National Ignition Facility (NIF), where different mixtures of H, D and T are being utilized.

To address questions about ion diffusion in DT implosions, this chapter reports on measurements of the dd and tt reaction yields (Y_{dd} and Y_{tt}) and how they contrast to the measured dt reaction yield (Y_{dt}). Spherical thin-glass (SiO_2) and thick-CH capsules were filled with DT-gas, and imploded using 23-30 kJ of energy delivered by the OMEGA laser in 1-ns square laser pulses. The absolute dd proton spectrum was measured by two magnet based charged particle spectrometers (CPSs),[48, 118] and the dt neutron yield and ion temperature were measured with the suite of neutron time-of-flight (nTOF) detectors.[44] The absolute dt and tt neutron spectra were measured with the Magnetic Recoil Spectrometer (MRS), discussed in detail in Chapter 4. The different reactions utilized in this study are summarized below.

$$\mathrm{D} + \mathrm{D} \rightarrow \mathrm{T} + \mathrm{p}(3.0\mathrm{MeV}) \qquad \text{Q=4.0 MeV} \tag{9-1}$$

$$\mathrm{D} + \mathrm{T} \rightarrow \mathrm{n}(14.1\mathrm{MeV}) + {}^{4}_{2}\mathrm{He} \qquad \text{Q=17.6 MeV} \tag{9-2}$$

$$\mathrm{T} + \mathrm{T} \rightarrow 2\,\mathrm{n}(0 - 9.4\mathrm{MeV}) + {}^{4}_{2}\mathrm{He} \qquad \text{Q=11.3 MeV} \tag{9-3}$$

As shown by Equations ((9-1) through (9-3)), the dd reaction produces a 3 MeV proton and a triton, and the dt reaction produces a 14.1 MeV neutron and an alpha particle. At ICF relevant conditions, the tt reaction produces two neutrons and an alpha particle (Equation (9-3)). The spectrum of these tt neutrons can be described by a 3-body continuum that is modified by the n-n and n-alpha final-state interactions.[54]

9.2 Predicted dd/dt and tt/dt yield ratios in ICF implosions

The yield (Y_{12}) for the different reactions is determined by integrating the spectrum of the dd protons, tt neutrons, and dt neutrons. To relate Y_{12} to the conditions in an ICF implosion, the reaction yield can be expressed as

$$Y_{12} = \int \frac{f_1 f_2}{1+\delta_{12}} \frac{\rho(\vec{r},t)^2}{\bar{m}^2} \langle \sigma v \rangle_{12}\, d\vec{r}\, dt, \tag{9-4}$$

where $<\sigma v>$ is the Maxwellian averaged reactivity, f_1 and f_2 are the atomic fractions of the reactants, ρ is the fuel-mass density, $\bar{m}$ is the average reactant mass, and the Kronecker delta (δ_{12}) accounts for double counting of identical reactants.[16] Using Equation (9-4), the reaction yield ratio (Y_{11}/Y_{12}) can be expressed as

$$\frac{Y_{11}}{Y_{12}} = \frac{1}{2}\frac{\int {f_1}^2 \rho(\vec{r},t)^2 \langle\sigma v\rangle_{11}\, d\vec{r}\, dt}{\int f_1 f_2 \rho(\vec{r},t)^2 \langle\sigma v\rangle_{12}\, d\vec{r}\, dt}. \tag{9-5}$$

This expression can be simplified if the reactivity ratio for the two reactions is slowly varying within the temperature range of the reacting fuel, which is the case for the Y_{dd}/Y_{dt} and Y_{tt}/Y_{dt} measurements discussed in this paper (T_i=9-18keV for dd/dt, and T_i=2-15 keV for tt/dt).[13] With this condition met, the reactivity ratio can be removed from the integral in Equation (9-5). Also, as hydrodynamic models of an ICF implosion often assume that the reactant density ratio (f_1/f_2) is spatially and temporally constant during the implosion (although, we will show this to be inconsistent with the data herein), f_1 and f_2 can also be removed from the integrals. Now, the integrals cancel and the reaction yield ratio can be expressed as

$$Y_{11}/Y_{12} \cong \frac{1}{2}\frac{f_1}{f_2}\frac{\langle\sigma v\rangle_{11}}{\langle\sigma v\rangle_{12}}. \tag{9-6}$$

Using the known reactivities (obtained from the ENDF/B-VII.0 database)[13] for the dd, dt, and tt reactions in the temperature range specified above, the expected Y_{dd}/Y_{dt} and Y_{tt}/Y_{dt} ratios in a DT implosion are given by

$$Y_{dd}/Y_{dt} \cong 2.6\times10^{-3}(f_\mathrm{T}/f_\mathrm{D})^{-1} \quad (T_i\text{=9-18 keV}) \tag{9-7}$$

$$Y_{tt}/Y_{dt} \cong 1.7\times10^{-3}\,(f_\mathrm{T}/f_\mathrm{D}) \quad (T_i\text{=2-15 keV}). \tag{9-8}$$

Here, f_T is the fraction of tritium in the core, f_D is the deuterium fraction in the core, and Y_{tt} is the tt reaction yield, which is half of the tt neutron yield because the 3-body branch emits two neutrons per reaction. Unless otherwise specified, all yields described herein refer to the reaction yield.

9.3 Measurements of the dd/dt and tt/dt yield ratios at OMEGA

To test this prediction, Y_{dd} can be determined in a DT implosion from the measured dd proton spectrum; an example is shown in Figure 9-1. This spectrum was obtained for OMEGA shot 39794 in which a 2.8μm thick SiO_2 capsule filled with 20 atm of DT gas (f_T=0.39, f_D=0.56, and trace hydrogen impurity, or f_T/f_D =0.69)[119] was imploded. A Y_{dd} of 5.0×10^{10} was determined from the spectrum, and a Y_{dt} of 3.9×10^{13} and T_i of 11.8keV were determined from the nTOF measurement. This results in a yield ratio of Y_{dd}/Y_{dt} = $(1.3\pm0.2)\times10^{-3}$ for this implosion, which is about a factor of three lower than 3.7×10^{-3} predicted by Equation (9-7).

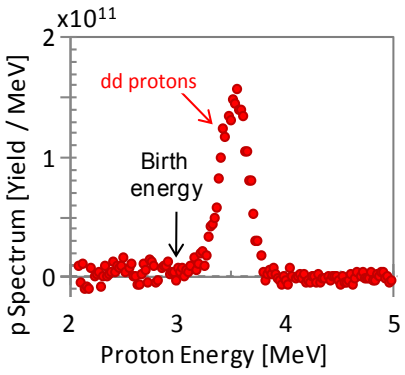

Figure 9-1: Absolute dd proton spectrum measured with the CPS on OMEGA implosion 39794. The proton peak is energy upshifted ~0.5 MeV from its birth energy due to electric fields, as discussed by Hicks et al.[118]

Similarly, Y_{tt} can be determined in a DT implosion from the measured tt neutron spectrum; an example is shown in Figure 9-2. Figure 9-2a shows the neutron spectrum that best describes the recoil deuteron spectrum measured by the MRS (Figure 9-2b). This spectrum was obtained by integrating nine nominally identical OMEGA implosions (shots 55074-55083),* using 16 μm CH capsules filled with DT fuel ($f_T/f_D = 0.63$) at 17.5 atm. A total Y_{DT} of 1.6×10^{14} and a burn averaged ion temperature of 5.3 keV were measured with the nTOF detector. As shown by Figure 9-2, the neutron spectrum consists of a dt neutron component, a tt neutron component and DSn component. The shape and magnitude of the DSn component are determined by the differential cross-sections for the n-d, n-t, n-c, and n-h elastic and inelastic scattering. From this neutron spectrum, a yield ratio of $Y_{tt}/Y_{dt} = (4.1\pm0.5)\times10^{-3}$ was determined, which is more than a factor of three larger than 1.1×10^{-3} predicted by Equation (9-8).

* Nine implosions were integrated to obtain better statistics because the neutron detection efficiency is relatively low when compared to charged particle measurements. Nominally identical shell thickness, diameter, fill pressure, and laser profiles result in very similar nuclear-burn-averaged ion temperatures and DT yield. In this series, the shot-to-shot ion temperature varied by 5% and the DT yield varied by 28%.

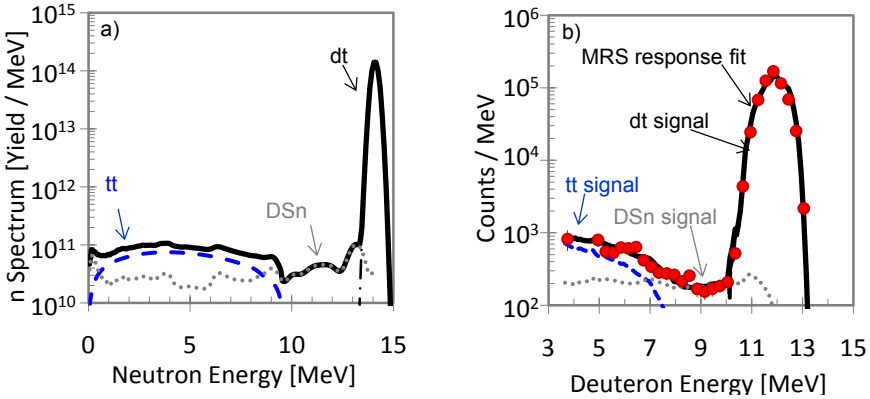

Figure 9-2: a) Neutron spectrum (black curve) that gives the best fit to the recoil deuteron spectrum measured with the MRS. b) Measured recoil deuteron spectrum (red points) obtained with the MRS. The spectrum is a convolution of the MRS-response function and neutron spectrum shown in part a. The deuteron peak at ~11.6 MeV is due to the primary dt neutrons. The width of this peak is primarily due to the MRS resolution. A DSn component is also observed in the deuteron-energy range 8-10 MeV, where other neutron sources are absent. The tt neutron spectrum dominates at deuteron energies below 7 MeV.

As an extension of the above study, the Y_{dd}/Y_{dt} and Y_{tt}/Y_{dt} ratios were determined for several series of different types of capsule-implosions, resulting in different burn averaged ion temperatures (T_i). In the case of the Y_{dd}/Y_{dt} study, thin-glass capsules with thicknesses in the range of 2.4-3.7 μm were used, and in the case of the Y_{tt}/Y_{dt} study, thin-glass capsules with thicknesses of 3.8 μm and CH (or CD) capsules with thicknesses of 10μm, 16μm, and 20μm were used. The initial DT fuel mixture was on average $f_{\mathrm{T}}/f_{\mathrm{D}} \cong 0.75$ for the Y_{dd}/Y_{dt} study and $f_{\mathrm{T}}/f_{\mathrm{D}} \cong 0.62$ Y_{tt}/Y_{dt} study. The differences in the initial $f_{\mathrm{T}}/f_{\mathrm{D}}$ are due to tritium decay and refueling of the DT inventory at OMEGA. The observed Y_{dd}/Y_{dt} data are shown in Figure 9-3a as a function of ion temperature. For comparison, the expected yield ratios calculated using Equation (9-6) for these dt implosions are shown by the solid black curve. 1D LILAC hydrodynamic simulations[31] were also used to calculate the yield ratios (blue triangles) and the results are in excellent agreement with Equation (9-6), as shown in Figure 9-3a. This comparison demonstrates that the observed ratios are significantly lower than expected from known reactivities alone, indicating a lower deuterium fraction in the core than expected. Similarly, Figure 9-3b illustrates the observed Y_{tt}/Y_{dt} ratios, which are compared to the expected ratio (black solid curve) as a function of ion temperature. The observed reaction yield ratio is anomalously 3 to 6 times higher than predicted at ~4 keV and ~8 keV, respectively.

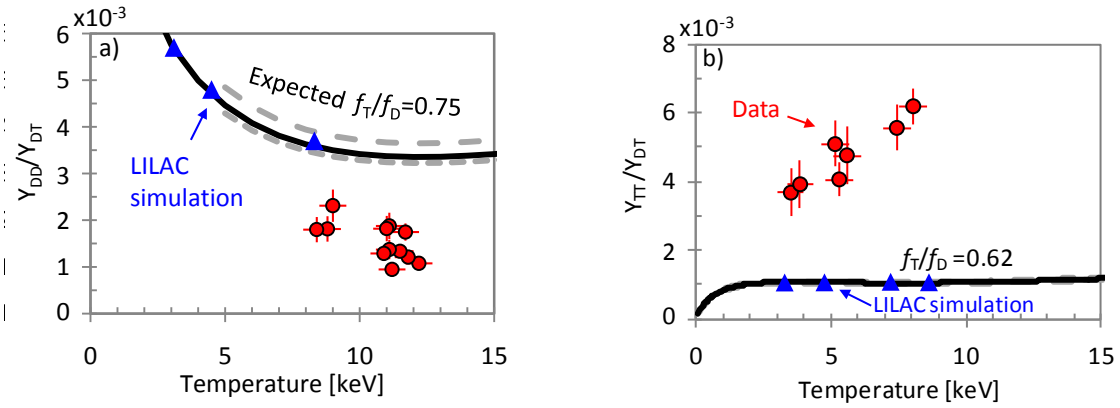

Figure 9-3: a) Measured Y_{dd}/Y_{dt} yield ratios as a function of ion temperature (red points). The solid line represents the expected yield ratio calculated using Equation (9-6) for the average initial DT fuel mixture ($f_T/f_D \cong 0.75$) used in this study. The grey dashed lines show the variation in the initial f_T/f_D due to tritium decay between these shots, which were obtained over a two-year period. 1D hydrodynamic simulations using LILAC (blue triangles) are also shown (for constant $f_T/f_D \cong 0.75$). The results show a suppression of the Y_{dd}/Y_{dt} yield ratio, indicating a lower deuterium fraction in the core than expected. b) Measured Y_{tt}/Y_{dt} reaction yield ratios as a function of ion temperature (red points). The solid line represents the expected yield ratio for the ($f_T/f_D \cong 0.62$) DT fuel mixture used in this study. The anomalously high Y_{tt}/Y_{dt} is consistent with a lower deuterium fraction in the core than expected, as suggested by the results in Figure 9-3a.

9.4 The potential role of fuel stratification

The relatively constant tt/dt (and dd/dt) reactivity ratio over the range of observed temperatures, and the consequential insensitivity to complex time-evolving density and temperature profiles strongly suggests this yield anomaly is due to a change in the reacting-fuel fractions f_T/f_D induced by deuterium leaving the center of the implosion. These anomalies, which are stronger for Y_{tt}/Y_{dt} than for Y_{dd}/Y_{dt}, could be caused by the combined effect of the centrally-peaked temperature profile and stratified fuel-species (recall the yield ratio is insensitive to the temperature profile only if f_T/f_D is fixed). As the temperature profile is peaked at the center of the compressed core, where the fuel is tritium rich, the effective tt reactant temperature relative to dt and dd is higher. Because the reactivity is a strong function of temperature, this will further enhance Y_{tt}/Y_{dt} and likewise suppress Y_{dd}/Y_{dt}. Therefore, these anomalous yield ratios indicate that f_T/f_D has changed but cannot be directly used to infer f_T/f_D without a self-consistent model of the density change in the core. However, implosion temperature and density profiles simulated using LILAC can be used to estimate the $\langle f_T/f_D \rangle$ (averaged over the DT burn region) required to produce the observed yield ratios in Figure 9-3. This work suggests that $\langle f_T/f_D \rangle$ has been increased by ~40-70% above its pre-shot value during the implosion. More detailed estimates for $\langle f_T/f_D \rangle$ will be the subject of further study.

Some insight as to when stratification begins, may come from the fact that anomalous yield behavior is observed (Figure 9-3) in two different implosion types; thin-shell (2.4-3.8μm SiO_2) shock-driven "exploding-pusher" and thick-shell (10-20μm CH or CD) ablatively-driven implosions. In both the exploding-pusher and ablative implosions, the laser launches a strong-

shock, significantly heating the gas and producing a "shock-yield" after rebounding off the center. By the time the shock-yield is produced, the shell is mostly ablated away for the exploding-pusher case and no additional yield is produced. However, for the ablatively-driven case much of the shell remains, which continues imploding inward until stagnation, where *pdV*-work heats the gas producing an additional "compression-yield." Because both of these implosion types show an apparent change in f_T/f_D in the core, this implies the change begins relatively early in the implosion process, shortly after the first shock breaks out of the shell and certainly by the time the shock rebounds off the center and the shock-yield is produced. This stratification may continue between the shock and compression-yield for the ablative implosions, but without temporal measurements of the relative yields, this cannot yet be definitively established.

A possible mechanism for the fuel stratification is plasma baro-diffusion, recently proposed by Amendt et al.[117] to explain the previously mentioned d^3he and dt^3he yield anomalies, which causes lighter ions to diffuse away from the implosion center (and the heavier nuclei into the center). We propose future experiments with the aim of studying this possible mechanism and determining the role of the mass and charge of the fuel constituents. The first is to observe $^3he^3he$ protons (which have recently been observed for the first time in ICF implosions),[120] produced in different mixtures of $^3He^4He$ gas-filled implosions. This combination will feature same the Z but different constituent masses, which will directly complement this study but at Z=2. A second experiment would be to measure t^3he deuterons using different mixtures of T^3He gas-filled implosions. T^3He deuterons have been observed in previous DT^3He gas-filled implosions,[48] but not with the aim of studying possible diffusion effects. Any inferred stratification in t^3he would then be isolated to the difference in charge as these constituents feature the same mass. A third experiment would look at the DD yield in hydro-equivalent THD fuel mixtures, analogous to the previously mentioned D^3He study.[35]

9.5 Summary

In summary, the dd and tt reaction yields are anomalously low and high, respectively, when compared to the dt reaction yield. We hypothesize that this discrepancy is caused by a stratification of the fuel, which causes f_T/f_D to increase at the center of the compressed core, an effect that becomes stronger with higher temperature. The anomaly is larger for Y_{tt}/Y_{dt} than for Y_{dd}/Y_{dt}, which may be the result of the combined effect of the temperature profile and stratified fuel. This stratification of the fuel may be driven by plasma baro-diffusion[117] of the fuel ions, which pushes the lighter ions from the imploding ICF core. The implications of these anomalous yields have bearing on other dt experiments in ICF including the ignition experiments planned on the NIF, potentially resulting in a more restrictive ignition threshold[17, 121] and reduced dt yield.

Summary

We stand on the frontier of a new era in fusion energy research, the era of alpha-particle heating and burning plasmas. In diagnosing burning plasmas, nuclear diagnostics like the Magnetic Recoil Spectrometer (MRS) are key, as they directly provide information about the burning core. In addition, nuclear diagnostics will excel in performance at high neutron yields, while most other diagnostics will fail.

The MRS was installed and commissioned on OMEGA in 2007. The interpretation of the MRS data is made through the response function, which was generated by a detailed Geant4 model, and is used to infer the original neutron spectrum. Reducing the background to the required level for the different measurements is a key challenge, as the most interesting features of the neutron spectrum, like down-scattered neutrons (DSn) and TT neutrons (TTn) are orders of magnitude below the primary DT neutrons, which constitute the main background. Significant polyethylene shielding around the MRS was used to directly attenuate the neutron background around the detector as much as possible. To reduce the background even further, the coincidence counting technique was developed to mitigate both intrinsic and neutron induced background. This new processing technique enables accurate low-signal measurements of the DSn or TTn components in the neutron spectrum.

For the first time, the DSn spectrum has been used to infer the areal density (ρR) of ICF implosions. DSn spectra were accurately measured in a variety of low to moderate ρR implosions and are in excellent agreement with the well-established charged particle[48] measurements. This authenticates the DSn technique, which is important for diagnosing high ρR (>180mg/cm^2) cryogenic DT implosions, where most other techniques fail. Cryogenic DT implosions at OMEGA[26] are now regularly diagnosed using the DSn spectrum measured with the MRS. These measurements helped lead to a new triple-picket pulse design,[28] which provided improved compression, resulting in the highest ρRs ever achieved at OMEGA.[26, 28] In addition, the MRS has been used to diagnose the DSn spectrum from THD and DT implosions at the NIF, during the beginning phases of the National Ignition Campaign. These results have already been central in tuning these implosions to the highest ρRs achieved in ICF (>1 g/cm^2), which is over three times the range of the DT alphas.

The first measurements of the TTn spectrum in equimolar DT implosions at OMEGA have been conducted using the MRS. Both the TTn and the DD proton yield were compared to the DT neutron yield in DT implosions. From these measurements, it is concluded that the DD yield is anomalously low and the TTn yield is anomalously high, relative to the DT yield, an effect that is enhanced with increasing ion temperature. These results can be explained by a stratification of the fuel in the core of an ICF implosion, an effect that may be present in ignition experiments planned on the National Ignition Facility. In addition, the spectral measurements of the TT-neutron emission were conducted for the first time at reactant central-mass energies in the range of 15-30

keV. The results from these measurements indicate that the TT reaction proceeds primarily through the direct three-body reaction channel, producing a continuous TT-neutron spectrum in the range 0 – 9.5 MeV.

The MRS has already provided valuable and elucidating data that have been essential to the ICF program. However, its contribution in the years ahead, promise to be even more rewarding, as it continues to be a primary diagnostic in the ignition campaign when the yields will be significantly higher at the NIF.

Bibliography

1. E. Harrison, A. L. A. Marschall and Reviewer, American Journal of Physics **69** (4), 523-524 (2001).
2. J. N. Bahcall, SLAC Beam Line **31N1**, 2-12 (2001).
3. A. Einstein, Annalen der Physik **323** (13), 639-641 (1905).
4. J. R. Rygg, Massachusetts Institute of Technology Thesis, 2006.
5. R. Atkinson and F. Houtermans, Z. für Physik **54**, 656 (1929).
6. M. L. E. Oliphant, B. B. Kinsey and L. Rutherford, Proceedings of the Royal Society of London. Series A **141** (845), 722-733 (1933).
7. H. A. Bethe, Phys Rev **55** (5), 434-456 (1939).
8. J. P. Freidberg, *Plasma physics and fusion energy*. (Cambridge University Press, Cambridge, 2007).
9. R. D. Evans, *The atomic nucleus*. (R.E. Krieger, Malabar, Fla., 1982).
10. R. N. Boyd, *An introduction to nuclear astrophysics*. (University of Chicago Press, Chicago, 2007).
11. R. S. Mitalas, K. R., Astrophysical Journal, Part 1 **401** (2), 759-760 (1992).
12. H. S. Bosch and G. M. Hale, Nuclear Fusion **32** (4), 611 (1992).
13. M. B. Chadwick, P. Oblozinský, M. Herman, N. M. Greene, R. D. McKnight, D. L. Smith, P. G. Young, R. E. MacFarlane, G. M. Hale, S. C. Frankle, A. C. Kahler, T. Kawano, R. C. Little, D. G. Madland, P. Moller, R. D. Mosteller, P. R. Page, P. Talou, H. Trellue, M. C. White, W. B. Wilson, R. Arcilla, C. L. Dunford, S. F. Mughabghab, B. Pritychenko, D. Rochman, A. A. Sonzogni, C. R. Lubitz, T. H. Trumbull, J. P. Weinman, D. A. Brown, D. E. Cullen, D. P. Heinrichs, D. P. McNabb, H. Derrien, M. E. Dunn, N. M. Larson, L. C. Leal, A. D. Carlson, R. C. Block, J. B. Briggs, E. T. Cheng, H. C. Huria, M. L. Zerkle, K. S. Kozier, A. Courcelle, V. Pronyaev and S. C. van der Marck, Nuclear Data Sheets **107** (12), 2931-3060 (2006).
14. E. G. Adelberger, A. Balantekin, D. Bemmerer, C. Bertulani, J. Chen, H. Costantini, M. Couder, R. Cyburt, B. Davids, S. Freedman, M. Gai, A. Garcia, D. Gazit, L. Gialanella, U. Greife, M. Hass, K. Heeger, W. C. Haxton, G. Imbriani, T. Itahashi, A. Junghans, K. Kubodera, K. Langanke, D. Leitner, M. Leitner, L. E. Marcucci, T. Motobayashi, A. Mukhamedzhanov, K. M. Nollett, F. M. Nunes, T. S. Park, P. D. Parker, P. Prati, M. Ramsey-Musolf, R. Robertson, R. Schiavilla, E. Simpson, K. Snover, C. Spitaleri, F. Strieder, K. Suemmerer, H. P. Trautvetter, R. Tribble, S. Typel, E. Uberseder, P. Vetter, M. Wiescher and L. Winslow, Reviews of Modern Physics **83**, 195 (2011).
15. E. G. Adelberger, S. M. Austin, J. N. Bahcall, A. B. Balantekin, G. Bogaert, L. S. Brown, L. Buchmann, F. E. Cecil, A. E. Champagne, L. de Braeckeleer, C. A. Duba, S. R. Elliott, S. J. Freedman, M. Gai, G. Goldring, C. R. Gould, A. Gruzinov, W. C. Haxton, K. M. Heeger, E. Henley, C. W. Johnson, M. Kamionkowski, R. W. Kavanagh, S. E. Koonin, K. Kubodera, K. Langanke and T. Motobayashi, Reviews of Modern Physics **70** (4), 1265 (1998).

16. S. Atzeni and J. Meyer-ter-Vehn, *The physics of inertial fusion*. (Oxford University Press, Oxford, 2004).
17. R. Betti, P. Y. Chang, B. K. Spears, K. S. Anderson, J. Edwards, M. Fatenejad, J. D. Lindl, R. L. McCrory, R. Nora and D. Shvarts, Physics of Plasmas **17** (5), 058102 (2010).
18. J. Wesson, *Tokamaks*, 3rd ed. (Oxford University Press., Oxford, 2004).
19. J. Nuckolls, L. Wood, A. Thiessen and G. Zimmerman, Nature **239** (5368), 139-142 (1972).
20. D. G. Hicks, Massachusetts Institute of Technology Thesis, 1999.
21. E. I. Moses, Journal of Physics: Conference Series **112** (1), 012003 (2008).
22. T. R. Boehly, D. L. Brown, R. S. Craxton, R. L. Keck, J. P. Knauer, J. H. Kelly, T. J. Kessler, S. A. Kumpan, S. J. Loucks, S. A. Letzring, F. J. Marshall, R. L. McCrory, S. F. B. Morse, W. Seka, J. M. Soures and C. P. Verdon, Optics Communications **133** (1-6), 495-506 (1997).
23. J. A. Frenje, K. M. Green, D. G. Hicks, C. K. Li, F. H. Seguin, R. D. Petrasso, T. C. Sangster, T. W. Phillips, V. Y. Glebov, D. D. Meyerhofer, S. Roberts, J. M. Soures, C. Stoeckl, K. Fletcher, S. Padalino and R. J. Leeper, Review of Scientific Instruments **72** (1), 854-858 (2001).
24. J. A. Frenje, D. T. Casey, C. K. Li, J. R. Rygg, F. H. Seguin, R. D. Petrasso, V. Y. Glebov, D. D. Meyerhofer, T. C. Sangster, S. Hatchett, S. Haan, C. Cerjan, O. Landen, M. Moran, P. Song, D. C. Wilson and R. J. Leeper, Review of Scientific Instruments **79** (10), 10E502 (2008).
25. J. A. Frenje, D. T. Casey, C. K. Li, F. H. Seguin, R. D. Petrasso, V. Y. Glebov, P. B. Radha, T. C. Sangster, D. D. Meyerhofer, S. P. Hatchett, S. W. Haan, C. J. Cerjan, O. L. Landen, K. A. Fletcher and R. J. Leeper, Physics of Plasmas **17**, 056311-056319 (2010).
26. T. C. Sangster, V. N. Goncharov, R. Betti, T. R. Boehly, D. T. Casey, T. J. B. Collins, R. S. Craxton, J. A. Delettrez, D. H. Edgell, R. Epstein, K. A. Fletcher, J. A. Frenje, Y. Y. Glebov, D. R. Harding, S. X. Hu, I. V. Igumenschev, J. P. Knauer, S. J. Loucks, C. K. Li, J. A. Marozas, F. J. Marshall, R. L. McCrory, P. W. McKenty, D. D. Meyerhofer, P. M. Nilson, S. P. Padalino, R. D. Petrasso, P. B. Radha, S. P. Regan, F. H. Seguin, W. Seka, R. W. Short, D. Shvarts, S. Skupsky, V. A. Smalyuk, J. M. Soures, C. Stoeckl, W. Theobald and B. Yaakobi, Physics of Plasmas **17**, 056312-056317 (2010).
27. D. T. Casey, J. A. Frenje, F. H. Séguin, C. K. Li, M. J. Rosenberg, H. Rinderknecht, M. J.-E. Manuel, M. G. Johnson, J. C. Schaeffer, R. Frankel, N. Sinenian, R. A. Childs, R. D. Petrasso, V. Y. Glebov, T. C. Sangster, M. Burke and S. Roberts, Review of Scientific Instruments **82** (7), 073502 (2011).
28. V. N. Goncharov, T. C. Sangster, T. R. Boehly, S. X. Hu, I. V. Igumenshchev, F. J. Marshall, R. L. McCrory, D. D. Meyerhofer, P. B. Radha, W. Seka, S. Skupsky, C. Stoeckl, D. T. Casey, J. A. Frenje and R. D. Petrasso, Physical Review Letters **104** (16), 165001 (2010).

29. M. J. Edwards, J. D. Lindl, B. K. Spears, S. V. Weber, L. J. Atherton, D. L. Bleuel, D. K. Bradley, D. A. Callahan, C. J. Cerjan, D. Clark, G. W. Collins, J. E. Fair, R. J. Fortner, S. H. Glenzer, S. W. Haan, B. A. Hammel, A. V. Hamza, S. P. Hatchett, N. Izumi, B. Jacoby, O. S. Jones, J. A. Koch, B. J. Kozioziemski, O. L. Landen, R. Lerche, B. J. MacGowan, A. J. MacKinnon, E. R. Mapoles, M. M. Marinak, M. Moran, E. I. Moses, D. H. Munro, D. H. Schneider, S. M. Sepke, D. A. Shaughnessy, P. T. Springer, R. Tommasini, L. Bernstein, W. Stoeffl, R. Betti, T. R. Boehly, T. C. Sangster, V. Y. Glebov, P. W. McKenty, S. P. Regan, D. H. Edgell, J. P. Knauer, C. Stoeckl, D. R. Harding, S. Batha, G. Grim, H. W. Herrmann, G. Kyrala, M. Wilke, D. C. Wilson, J. Frenje, R. Petrasso, K. Moreno, H. Huang, K. C. Chen, E. Giraldez, J. D. Kilkenny, M. Mauldin, N. Hein, M. Hoppe, A. Nikroo and R. J. Leeper, Physics of Plasmas **18** (5), 051003 (2011).
30. J. A. Frenje, C. K. Li, F. H. Seguin, D. T. Casey, R. D. Petrasso, T. C. Sangster, R. Betti, V. Y. Glebov and D. D. Meyerhofer, Physics of Plasmas **16** (4), 042704 (2009).
31. J. Delettrez, R. Epstein, M. C. Richardson, P. A. Jaanimagi and B. L. Henke, Phys Rev A **36** (8), 3926 (1987).
32. J. D. Lindl, *Inertial confinement fusion : the quest for ignition and energy gain using indirect drive*. (Springer, New York, NY, USA, 1998).
33. J. Lindl, et al., Physics of Plasmas **11**, 339 (2004).
34. C. D. Zhou and R. Betti, Physics of Plasmas **15** (10), 102707-102712 (2008).
35. J. R. Rygg, J. A. Frenje, C. K. Li, F. H. Seguin, R. D. Petrasso, J. A. Delettrez, V. Y. Glebov, V. N. Goncharov, D. D. Meyerhofer, S. P. Regan, T. C. Sangster and C. Stoeckl, Physics of Plasmas **13** (5), 052702 (2006).
36. V. N. Goncharov, T. C. Sangster, P. B. Radha, R. Betti, T. R. Boehly, T. J. B. Collins, R. S. Craxton, J. A. Delettrez, R. Epstein, V. Y. Glebov, S. X. Hu, I. V. Igumenshchev, J. P. Knauer, S. J. Loucks, J. A. Marozas, F. J. Marshall, R. L. McCrory, P. W. McKenty, D. D. Meyerhofer, S. P. Regan, W. Seka, S. Skupsky, V. A. Smalyuk, J. M. Soures, C. Stoeckl, D. Shvarts, J. A. Frenje, R. D. Petrasso, C. K. Li, F. Seguin, W. Manheimer and D. G. Colombant, Physics of Plasmas **15** (5), 056310-056318 (2008).
37. T. R. Boehly, D. Munro, P. M. Celliers, R. E. Olson, D. G. Hicks, V. N. Goncharov, G. W. Collins, H. F. Robey, S. X. Hu, J. A. Morozas, T. C. Sangster, O. L. Landen and D. D. Meyerhofer, Physics of Plasmas **16** (5), 056302-056309 (2009).
38. R. L. McCrory, D. D. Meyerhofer, R. Betti, T. R. Boehly, R. S. Craxton, J. A. Delettrez, D. H. Edgell, V. Y. Glebov, V. N. Goncharov, D. R. Harding, S. X. Hu, J. P. Knauer, F. J. Marshall, P. W. McKenty, P. B. Radha, S. P. Regan, T. C. Sangster, W. Seka, R. W. Short, D. Shvarts, S. Skupsky, V. A. Smalyuk, J. M. Soures, C. Stoeckl, W. Theobald, B. Yaakobi, J. A. Frenje, C. K. Li, R. D. Petrasso, F. H. Séguin and D. T. Casey, Journal of Physics: Conference Series **244** (1), 012004 (2010).
39. D. D. Meyerhofer and et al., Journal of Physics: Conference Series **244** (3), 032010 (2010).

40. R. S. Craxton, F. J. Marshall, M. J. Bonino, R. Epstein, P. W. McKenty, S. Skupsky, J. A. Delettrez, I. V. Igumenshchev, D. W. Jacobs-Perkins, J. P. Knauer, J. A. Marozas, P. B. Radha and W. Seka, Physics of Plasmas **12** (5), 056304-056308 (2005).
41. R. L. McCrory and et al., Nuclear Fusion **45** (10), S283 (2005).
42. F. J. Marshall, T. Ohki, D. McInnis, Z. Ninkov and J. Carbone, Review of Scientific Instruments **72** (1), 713-716 (2001).
43. V. Y. Glebov, D. D. Meyerhofer, T. C. Sangster, C. Stoeckl, S. Roberts, C. A. Barrera, J. R. Celeste, C. J. Cerjan, L. S. Dauffy, D. C. Eder, R. L. Griffith, S. W. Haan, B. A. Hammel, S. P. Hatchett, N. Izumi, J. R. Kimbrough, J. A. Koch, O. L. Landen, R. A. Lerche, B. J. MacGowan, M. J. Moran, E. W. Ng, T. W. Phillips, P. M. Song, R. Tommasini, B. K. Young, S. E. Caldwell, G. P. Grim, S. C. Evans, J. M. Mack, T. J. Sedillo, M. D. Wilke, D. C. Wilson, C. S. Young, D. Casey, J. A. Frenje, C. K. Li, R. D. Petrasso, F. H. Seguin, J. L. Bourgade, L. Disdier, M. Houry, I. Lantuejoul, O. Landoas, G. A. Chandler, G. W. Cooper, R. J. Leeper, R. E. Olson, C. L. Ruiz, M. A. Sweeney, S. P. Padalino, C. Horsfield and B. A. Davis, Review of Scientific Instruments **77** (10), 10E715 (2006).
44. V. Y. Glebov, C. Stoeckl, T. C. Sangster, S. Roberts, G. J. Schmid, R. A. Lerche and M. J. Moran, Review of Scientific Instruments **75** (10), 3559-3562 (2004).
45. C. L. Ruiz, R. J. Leeper, F. A. Schmidlapp, G. Cooper and D. J. Malbrough, Review of Scientific Instruments **63** (10), 4889-4891 (1992).
46. J. A. Frenje, C. K. Li, F. H. Seguin, J. Deciantis, S. Kurebayashi, J. R. Rygg, R. D. Petrasso, J. Delettrez, V. Y. Glebov, C. Stoeckl, F. J. Marshall, D. D. Meyerhofer, T. C. Sangster, V. A. Smalyuk and J. M. Soures, Physics of Plasmas **11** (5), 2798-2805 (2004).
47. H. W. Herrmann, J. R. Langenbrunner, J. M. Mack, J. H. Cooley, D. C. Wilson, S. C. Evans, T. J. Sedillo, G. A. Kyrala, S. E. Caldwell, C. S. Young, A. Nobile, J. Wermer, S. Paglieri, A. M. McEvoy, Y. Kim, S. H. Batha, C. J. Horsfield, D. Drew, W. Garbett, M. Rubery, V. Y. Glebov, S. Roberts and J. A. Frenje, Physics of Plasmas **16** (5), 056312 (2009).
48. F. H. Seguin, J. A. Frenje, C. K. Li, D. G. Hicks, S. Kurebayashi, J. R. Rygg, B. E. Schwartz, R. D. Petrasso, S. Roberts, J. M. Soures, D. D. Meyerhofer, T. C. Sangster, J. P. Knauer, C. Sorce, V. Y. Glebov, C. Stoeckl, T. W. Phillips, R. J. Leeper, K. Fletcher and S. Padalino, Review of Scientific Instruments **74** (2), 975-995 (2003).
49. H. Rinderknecht, to be published.
50. C. K. Li, F. H. Seguin, D. G. Hicks, J. A. Frenje, K. M. Green, S. Kurebayashi, R. D. Petrasso, D. D. Meyerhofer, J. M. Soures, V. Y. Glebov, R. L. Keck, P. B. Radha, S. Roberts, W. Seka, S. Skupsky, C. Stoeckl and T. C. Sangster, Physics of Plasmas **8** (11), 4902-4913 (2001).
51. H. Brysk, Plasma Physics **15** (7), 611 (1973).
52. I. H. Hutchinson, *Principles of plasma diagnostics*, 2nd ed. (Cambridge University Press, 2002).
53. L. Ballabio and et al., Nuclear Fusion **38** (11), 1723 (1998).
54. B. Lacina, J. Ingley and D. W. Dorn, Report No. UCRL-7769, 1965.

55. K. W. Allen, E. Almqvist, J. T. Dewan, T. P. Pepper and J. H. Sanders, Phys Rev **82** (2), 262 (1951).
56. D. E. Cullen, LLNL, UCRL-ID-126455 (2003).
57. F. B. Brown, R. F. Barrett, T. E. Booth, J. S. Bull, L. J. Cox, R. A. Forster, T. J. Goorley, R. D. Mosteller, S. E. Post, R. E. Prael, E. C. Selcow, A. Sood and J. Sweezy, Transactions of the American Nuclear Society **87**, 273 (2002).
58. S. X. Hu, V. N. Goncharov, P. B. Radha, J. A. Marozas, S. Skupsky, T. R. Boehly, T. C. Sangster, D. D. Meyerhofer and R. L. McCrory, Physics of Plasmas **17** (10), 102706-102713 (2010).
59. C. K. Li, F. H. Seguin, J. A. Frenje, R. D. Petrasso, J. A. Delettrez, P. W. McKenty, T. C. Sangster, R. L. Keck, J. M. Soures, F. J. Marshall, D. D. Meyerhofer, V. N. Goncharov, J. P. Knauer, P. B. Radha, S. P. Regan and W. Seka, Physical Review Letters **92** (20), 205001 (2004).
60. J. A. Frenje, C. K. Li, J. R. Rygg, F. H. Seguin, D. T. Casey, R. D. Petrasso, J. Delettrez, V. Y. Glebov, T. C. Sangster, O. Landen and S. Hatchett, Physics of Plasmas **16** (2), 022702 (2009).
61. C. K. Li, F. H. Séguin, J. A. Frenje, R. D. Petrasso, R. Rygg, S. Kurebayashi, B. Schwartz, R. L. Keck, J. A. Delettrez, J. M. Soures, P. W. McKenty, V. N. Goncharov, J. P. Knauer, F. J. Marshall, D. D. Meyerhofer, P. B. Radha, S. P. Regan, T. C. Sangster, W. Seka and C. Stoeckl, Physics of Plasmas **10** (5), 1919-1924 (2003).
62. F. H. Séguin, C. K. Li, J. A. Frenje, S. Kurebayashi, R. D. Petrasso, F. J. Marshall, D. D. Meyerhofer, J. M. Soures, T. C. Sangster, C. Stoeckl, J. A. Delettrez, P. B. Radha, V. A. Smalyuk and S. Roberts, Physics of Plasmas **9** (8), 3558-3566 (2002).
63. C. K. Li, F. H. Seguin, J. R. Rygg, J. A. Frenje, M. Manuel, R. D. Petrasso, R. Betti, J. Delettrez, J. P. Knauer, F. Marshall, D. D. Meyerhofer, D. Shvarts, V. A. Smalyuk, C. Stoeckl, O. L. Landen, R. P. J. Town, C. A. Back and J. D. Kilkenny, Physical Review Letters **100** (22), 225001 (2008).

64. S. Agostinelli, J. Allison, K. Amako, J. Apostolakis, H. Araujo, P. Arce, M. Asai, D. Axen, S. Banerjee, G. Barrand, F. Behner, L. Bellagamba, J. Boudreau, L. Broglia, A. Brunengo, H. Burkhardt, S. Chauvie, J. Chuma, R. Chytracek, G. Cooperman, G. Cosmo, P. Degtyarenko, A. Dell'Acqua, G. Depaola, D. Dietrich, R. Enami, A. Feliciello, C. Ferguson, H. Fesefeldt, G. Folger, F. Foppiano, A. Forti, S. Garelli, S. Giani, R. Giannitrapani, D. Gibin, J. J. Gómez Cadenas, I. González, G. Gracia Abril, G. Greeniaus, W. Greiner, V. Grichine, A. Grossheim, S. Guatelli, P. Gumplinger, R. Hamatsu, K. Hashimoto, H. Hasui, A. Heikkinen, A. Howard, V. Ivanchenko, A. Johnson, F. W. Jones, J. Kallenbach, N. Kanaya, M. Kawabata, Y. Kawabata, M. Kawaguti, S. Kelner, P. Kent, A. Kimura, T. Kodama, R. Kokoulin, M. Kossov, H. Kurashige, E. Lamanna, T. Lampén, V. Lara, V. Lefebure, F. Lei, M. Liendl, W. Lockman, F. Longo, S. Magni, M. Maire, E. Medernach, K. Minamimoto, P. Mora de Freitas, Y. Morita, K. Murakami, M. Nagamatu, R. Nartallo, P. Nieminen, T. Nishimura, K. Ohtsubo, M. Okamura, S. O'Neale, Y. Oohata, K. Paech, J. Perl, A. Pfeiffer, M. G. Pia, F. Ranjard, A. Rybin, S. Sadilov, E. Di Salvo, G. Santin, T. Sasaki, N. Savvas, Y. Sawada, S. Scherer, S. Sei, V. Sirotenko, D. Smith, N. Starkov, H. Stoecker, J. Sulkimo, M. Takahata, S. Tanaka, E. Tcherniaev, E. Safai Tehrani, M. Tropeano, P. Truscott, H. Uno, L. Urban, P. Urban, M. Verderi, A. Walkden, W. Wander, H. Weber, J. P. Wellisch, T. Wenaus, D. C. Williams, D. Wright, T. Yamada, H. Yoshida and D. Zschiesche, Nuclear Instruments and Methods in Physics Research Section A: Accelerators, Spectrometers, Detectors and Associated Equipment **506** (3), 250-303 (2003).
65. J. Källne and H. Enge, Nuclear Instruments and Methods in Physics Research Section A: Accelerators, Spectrometers, Detectors and Associated Equipment **311** (3), 595-602 (1992).
66. (Dexter Magnetic Technologies, Inc., 400 Karin Lane, Hicksville, NY 11801 USA).
67. M. Devine, personal communication.
68. Track Analysis Systems Ltd., H. H. Wills Physics Lab., Tyndall Ave., Bristol BS8 1TL, United Kingdom.
69. J. A. Frenje, C. K. Li, F. H. Seguin, D. G. Hicks, S. Kurebayashi, R. D. Petrasso, S. Roberts, V. Y. Glebov, D. D. Meyerhofer, T. C. Sangster, J. M. Soures, C. Stoeckl, C. Chiritescu, G. J. Schmid and R. A. Lerche, Review of Scientific Instruments 7**3** (7), 2597-2605 (2002).
70. E. M. Lent, Report No. LLNL UCRL-50857, 1970.
71. ISOTEC Inc., 3050 Spruce St., St. Louis, MO 6310
72. K. Fletcher, (To be published).
73. (General Atomics LLC, 3550 General Atomics Court, San Diego, CA 92121-1122).
74. J. Mark, P*hysical Properties of Polymers Handbook.* (Springer, 2006).
75. R Paguio, personal communication.
76. J. Frenje, personal communication.
77. H. Khater, personal communication
78. G. W. Cooper and C. L. Ruiz, Review of Scientific Instruments 7**2** (1), 814-817 (2001).

79. M. A. Russotto and R. L. Kremens, Review of Scientific Instruments 6**1** (10), 3125-3127 (1990).
80. V. Y. Glebov, T. C. Sangster, C. Stoeckl, J. P. Knauer, W. Theobald, K. L. Marshall, M. J. Shoup, Iii, T. Buczek, M. Cruz, T. Duffy, M. Romanofsky, M. Fox, A. Pruyne, M. J. Moran, R. A. Lerche, J. McNaney, J. D. Kilkenny, M. J. Eckart, D. Schneider, D. Munro, W. Stoeffl, R. Zacharias, J. J. Haslam, T. Clancy, M. Yeoman, D. Warwas, C. J. Horsfield, J. L. Bourgade, O. Landoas, L. Disdier, G. A. Chandler and R. J. Leeper, Review of Scientific Instruments 8**1** (10), 10D325-326 (2010).
81. G. J. Schmid, R. L. Griffith, N. Izumi, J. A. Koch, R. A. Lerche, M. J. Moran, T. W. Phillips, R. E. Turner, V. Y. Glebov, T. C. Sangster and C. Stoeckl, Review of Scientific Instruments 7**4** (3), 1828-1831 (2003).
82. M. J. Moran, V. Y. Glebov, C. Stoeckl, R. Rygg and B.-E. Schwartz, Review of Scientific Instruments 7**6** (2), 023506-023506-023505 (2005).
83. V. Glebov, personal communication.
84. O. Landoas, V. Y. Glebov, B. Rossé, M. Briat, L. Disdier, T. C. Sangster, T. Duffy, J. G. Marmouget, C. Varignon, X. Ledoux, T. Caillaud, I. Thfoin and J.-L. Bourgade, Review of Scientific Instruments 8**2** (7), 073501 (2011).
85. D. Bleuel, to be published.
86. J. Frenje, private communication.
87. J. A. Frenje, C. K. Li, F. H. Seguin, D. T. Casey, R. D. Petrasso, D. P. McNabb, P. Navratil, S. Quaglioni, T. C. Sangster, V. Y. Glebov and D. D. Meyerhofer, Physical Review Letters 1**07** (12), 122502 (2011).
88. S. C. McDuffee, J. A. Frenje, F. H. Seguin, R. Leiter, M. J. Canavan, D. T. Casey, J. R. Rygg, C. K. Li and R. D. Petrasso, Review of Scientific Instruments 7**9** (4), 043302 (2008).
89. S. Kacenjar, L. M. Goldman, A. Entenberg and S. Skupsky, Journal of Applied Physics 5**6** (7), 2027-2032 (1984).
90. I. Lengar, J. Skvarc and R. Ilic, Nuclear Instruments and Methods in Physics Research Section B: Beam Interactions with Materials and Atoms 1**92** (4), 440-444 (2002).
91. H. Azechi, N. Miyanaga, R. O. Stapf, K. Itoga, H. Nakaishi, M. Yamanaka, H. Shiraga, R. Tsuji, S. Ido, K. Nishihara, Y. Izawa, T. Yamanaka and C. Yamanaka, Applied Physics Letters 4**9** (10), 555-557 (1986).
92. S. W. Barwick, K. Kinoshita and P. B. Price, Physical Review D 2**8** (9), 2338 (1983).
93. Matiullah, S. Rehman and W. Zaman, Radiation Measurements 3**9** (3), 337-343 (2005).
94. D. Nikezic and K. N. Yu, Materials Science and Engineering: R: Reports 4**6** (3-5), 51-123 (2004).
95. D. T. Casey, (To be published).
96. P. B. Radha, R. Betti, T. R. Boehly, J. A. Delettrez, D. H. Edgell, V. N. Goncharov, I. V. Igumenshchev, J. P. Knauer, J. A. Marozas, F. J. Marshall, R. L. McCrory, D. D. Meyerhofer, S. P. Regan, T. C. Sangster, W. Seka, S. Skupsky, A. A. Solodov, C. Stoeckl, W. Theobald, J. A. Frenje, D. T. Casey, C. K. Li and R. D. Petrasso, Plasma Science, IEEE Transactions on 3**9** (4), 1007-1014 (2011).

97. J. Frenje, personal communication.
98. S. H. Glenzer, To be published. (2011).
99. O. L. Landen, T. R. Boehly, D. K. Bradley, D. G. Braun, D. A. Callahan, P. M. Celliers, G. W. Collins, E. L. Dewald, L. Divol, S. H. Glenzer, A. Hamza, D. G. Hicks, N. Hoffman, N. Izumi, O. S. Jones, R. K. Kirkwood, G. A. Kyrala, P. Michel, J. Milovich, D. H. Munro, A. Nikroo, R. E. Olson, H. F. Robey, B. K. Spears, C. A. Thomas, S. V. Weber, D. C. Wilson, M. M. Marinak, L. J. Suter, B. A. Hammel, D. D. Meyerhofer, J. Atherton, J. Edwards, S. W. Haan, J. D. Lindl, B. J. MacGowan and E. I. Moses, Physics of Plasmas 1**7** (5), 056301-056308 (2010).
100. S. W. Haan, D. A. Callahan, M. J. Edwards, B. A. Hammel, D. D. Ho, O. S. Jones, J. D. Lindl, B. J. MacGowan, M. M. Marinak, D. H. Munro, S. M. Pollaine, J. D. Salmonson, B. K. Spears and L. J. Suter, Fusion Science and Technology 5**5** (3), 227-232 (2009).
101. H. Robey et al., submitted to Physical Review letters 2011.
102. A. Mackinnon, to be published.
103. G. A. Miller, B. M. K. Nefkens and I. Šlaus, Physics Reports 1**94** (1-2), 1-116 (1990).
104. G. A. Miller, A. K. Opper and E. J. Stephenson, Annual Review of Nuclear and Particle Science 5**6** (1), 253-292 (2006).
105. C. R. Howell, Q. Chen, T. S. Carman, A. Hussein, W. R. Gibbs, B. F. Gibson, G. Mertens, C. F. Moore, C. Morris, A. Obst, E. Pasyuk, C. D. Roper, F. Salinas, I. Slaus, S. Sterbenz, W. Tornow, R. L. Walter, C. R. Whiteley and M. Whitton, Physics Letters B 4**44** (3-4), 252-259 (1998).
106. S. S. M. Wong, I*ntroductory Nuclear Physics.* (Wiley-VCH Verlag GmbH, 2007).
107. A. Csótó and K. Langanke, Nuclear Physics A 6**46** (3), 387-396 (1999).
108. R. J. Slobodrian, Reports on Progress in Physics 3**4** (1), 175 (1971).
109. C. Wong, J. D. Anderson and J. W. McClure, Nuclear Physics 7**1** (1), 106-112 (1965).
110. A. F. Lisetskiy, B. R. Barrett, M. K. G. Kruse, P. Navratil, I. Stetcu and J. P. Vary, Physical Review C 7**8** (4), 044302 (2008).
111. I. J. Thompson, private communication.
112. D. R. Tilley, C. M. Cheves, J. L. Godwin, G. M. Hale, H. M. Hofmann, J. H. Kelley, C. G. Sheu and H. R. Weller, Nuclear Physics A 7**08** (1-2), 3-163 (2002).
113. W. Shmayda, private communication.
114. G. Zimmerman, private communication.
115. J. Frenje et al., to be published.
116. M. Gatu Johnson, to be published.
117. P. Amendt, O. L. Landen, H. F. Robey, C. K. Li and R. D. Petrasso, Physical Review Letters 1**05** (11), 115005 (2010).
118. D. G. Hicks, C. K. Li, F. H. Seguin, A. K. Ram, J. A. Frenje, R. D. Petrasso, J. M. Soures, V. Y. Glebov, D. D. Meyerhofer, S. Roberts, C. Sorce, C. Stockl, T. C. Sangster and T. W. Phillips, Physics of Plasmas 7 (12), 5106-5117 (2000).
119. W. Shmayda, personal communication.
120. J. A. Frenje, private communication.

121. S. W. Haan, J. D. Lindl, D. A. Callahan, D. S. Clark, J. D. Salmonson, B. A. Hammel, L. J. Atherton, R. C. Cook, M. J. Edwards, S. Glenzer, A. V. Hamza, S. P. Hatchett, M. C. Herrmann, D. E. Hinkel, D. D. Ho, H. Huang, O. S. Jones, J. Kline, G. Kyrala, O. L. Landen, B. J. MacGowan, M. M. Marinak, D. D. Meyerhofer, J. L. Milovich, K. A. Moreno, E. I. Moses, D. H. Munro, A. Nikroo, R. E. Olson, K. Peterson, S. M. Pollaine, J. E. Ralph, H. F. Robey, B. K. Spears, P. T. Springer, L. J. Suter, C. A. Thomas, R. P. Town, R. Vesey, S. V. Weber, H. L. Wilkens and D. C. Wilson, Physics of Plasmas 1**8** (5), 051001 (2011).
122. A. Michalowicz, K*inematics of Nuclear Reactions.* (Lliffe Books Ltd. , London, 1967).
123. Z. G. Ge, Y. X. Zhuang, T. J. Liu, J. S. Zhang, H. C. Wu, Z. X. Zhao and H. H. Xia, International Conference on Nuclear Data for Science and Technology (2008).
124. W. R. Arnold, J. A. Phillips, G. A. Sawyer, E. J. Stovall, Jr. and J. L. Tuck, Phys Rev 9**3** (3), 483-497 (1954).
125. E. M. Balabanov, I. I. Barit and et al., Journal Name: Soviet J. Atomic Energy (English Translation); Journal Volume: Vol: Suppl. No. 5; Other Information: Orig. Receipt Date: 31-DEC-59, Medium: X; Size: Pages: 43-52 (1958).
126. A. Galonsky and C. H. Johnson, Phys Rev 1**04** (2), 421-425 (1956).
127. S. J. Bame, Jr. and J. E. Perry, Jr., Phys Rev 1**07** (6), 1616-1620 (1957).
128. M. D. Goldberg and J. M. Le Blanc, Phys Rev 1**22** (1), 164-168 (1961).
129. E. Magiera, M. Bormann, W. Scobel and P. Heiss, Nuclear Physics A 2**46** (2), 413-424 (1975).
130. R. E. Brown, N. Jarmie and G. M. Hale, Physical Review C 3**5** (6), 1999-2004 (1987).
131. H. M. Agnew, W. T. Leland, H. V. Argo, R. W. Crews, A. H. Hemmendinger, W. E. Scott and R. F. Taschek, Phys Rev 8**4** (4), 862 (1951).
132. A. M. Govorov, K. Li, G. M. Ostetinskii, V. I. Salatski and I. V. Sozor, Sov. Phys. JETP 1**5** (1962).
133. V. I. Serov, S. N. Abramovich and L. A. Morkin, Atomic Energy 4**2** (1), 66-69 (1977).
134. N. Jarmie and R. E. Brown, Nuclear Instruments and Methods in Physics Research Section B: Beam Interactions with Materials and Atoms 1**0-11** (Part 1), 405-410 (1985).
135. M. R. Dwarakanath and H. Winkler, Physical Review C 4 (5), 1532 (1971).
136. M. Junker, A. D'Alessandro, S. Zavatarelli, C. Arpesella, E. Bellotti, C. Broggini, P. Corvisiero, G. Fiorentini, A. Fubini, G. Gervino, U. Greife, C. Gustavino, J. Lambert, P. Prati, W. S. Rodney, C. Rolfs, F. Strieder, H. P. Trautvetter and D. Zahnow, Physical Review C 5**7** (5), 2700 (1998).
137. A. Krauss, H. W. Becker, H. P. Trautvetter and C. Rolfs, Nuclear Physics A 4**67** (2), 273-290 (1987).
138. D. D. Clayton, P*rinciples of stellar evolution and nucleosynthesis: with a new preface.* (University of Chicago Press, 1968).
139. H. J. Assenbaum, K. Langanke and C. Rolfs, Zeitschrift für Physik A Hadrons and Nuclei 3**27** (4), 461-468 (1987).

140. M. Aliotta, F. Raiola, G. Gyürky, A. Formicola, R. Bonetti, C. Broggini, L. Campajola, P. Corvisiero, H. Costantini, A. D'Onofrio, Z. Fülöp, G. Gervino, L. Gialanella, A. Guglielmetti, C. Gustavino, G. Imbriani, M. Junker, P. G. Moroni, A. Ordine, P. Prati, V. Roca, D. Rogalla, C. Rolfs, M. Romano, F. Schümann, E. Somorjai, O. Straniero, F. Strieder, F. Terrasi, H. P. Trautvetter and S. Zavatarelli, Nuclear Physics A 6**90** (4), 790-800 (2001).
141. U. Schröder, S. Engstler, A. Krauss, K. Neldner, C. Rolfs, E. Somorjai and K. Langanke, Nuclear Instruments and Methods in Physics Research Section B: Beam Interactions with Materials and Atoms 4**0-41** (Part 1), 466-469 (1989).
142. Y. Avni, Astrophysical Journal 2**10,** 642 (1976).
143. P. R. Bevington and D. K. Robinson, D*ata reduction and error analysis for the physical sciences.* (McGraw-Hill, 2003).
144. J. R. Taylor, A*n introduction to error analysis: the study of uncertainties in physical measurements.* (University Science Books, 1997).
145. W. H. Press, N*umerical recipes: the art of scientific computing.* (Cambridge University Press, 2007).

Appendix A - Nuclear cross-sections and center-of-mass vs laboratory frame

Nuclear cross-section data is used throughout this thesis to calculate important parameters such as scattering probabilities in the MRS foil, and scattered neutron spectra in imploded ICF capsules. Nuclear databases present data in many forms and often in the center-of-mass (CM) frame. This section will provide a basic discussion of some relationships, which can be used to manipulate nuclear data into appropriate forms for several topics discussed in this thesis. Here, the focus will be on non-relativistic two-body problems. The interested reader is referred to the *Kinematics of Nuclear Reactions* by Michalowicz,[122] for an extension to relativistic and many-body problems.

Many problems in nuclear physics are often cast and solved in the CM reference frame, even though experiments are performed in the more familiar laboratory (lab) reference frame. The CM frame moves with the center-of-mass of the reactants. Figure A-1 illustrates a reaction between a particle with mass m_1 and kinetic energy E_1 that moves toward another particle with mass m_2, which is at rest in the lab frame.

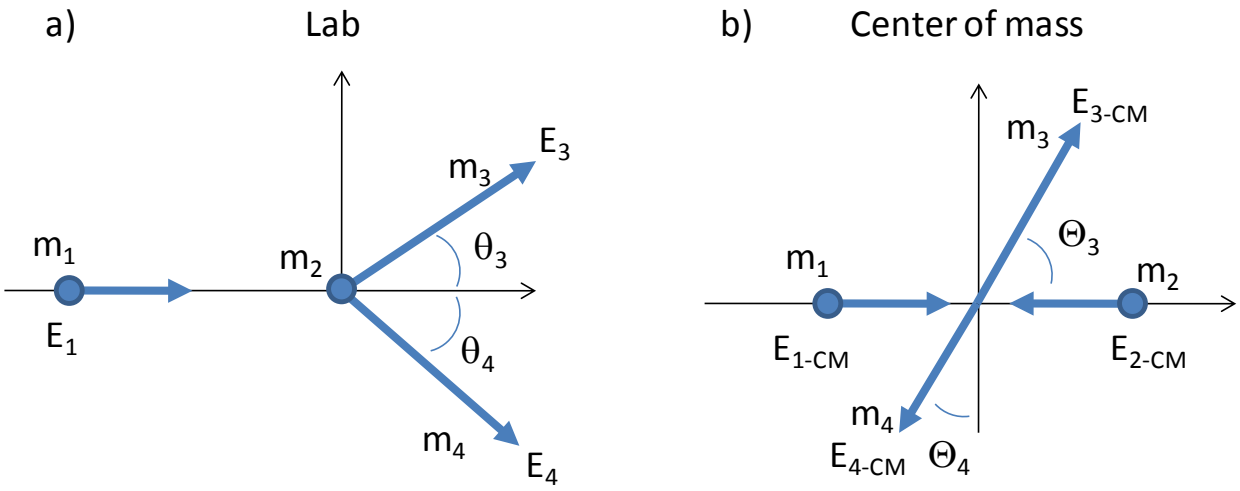

Figure A-1: a) Illustration of a reaction between two particles with masses m_1 and m_2 in the laboratory (lab) reference frame. Particle 1 has the kinetic energy E_1 in the lab frame and is moving toward partile 2, which is at rest in this frame. The reaction products (particles 3 and 4) have have the masses m_3 and m_4 and kinetic energies E_3 and E_4. b) Same reaction given in the and center-of-mass (CM) reference frame. In an elastic collision, $m_1 = m_3$ and $m_2 = m_4$.

The CM velocity (*V*) is given by

$$V = \frac{m_1 v_1}{m_1 + m_2}. \tag{A-1}$$

Here, v_1 is velocity of particle 1. Similarly, the CM frame velocities of particle 1 ($v_{1-\mathrm{CM}}$) and particle 2 ($v_{2-\mathrm{CM}}$) are given by

$$v_{1-\mathrm{CM}} = \frac{m_2 v_1}{m_1 + m_2} \tag{A-2}$$

$$v_{2-\mathrm{CM}} = \frac{m_1 v_1}{m_1 + m_2} = V. \tag{A-3}$$

The kinetic energy of the CM ($E_{t\text{-}CM}$) frame is given by

$$E_{t-\mathrm{CM}} = \frac{m_2 E_1}{m_1 + m_2}. \tag{A-4}$$

The kinematic relationtionships between the pre and post-reaction parameters are derived by using conservation of energy and momentum. In the non-relativistic limit, $E_1 << m_1$, the post-reaction CM angle (Θ) can be related to the lab angle (θ) using the constant of motion K for both particle 3 and particle 4.[122]

$$K_3 = \frac{V}{v_{3-\mathrm{CM}}} = \sqrt{\frac{m_1 m_3 E_{t-\mathrm{CM}}}{m_2 m_4 (E_{t-\mathrm{CM}} + Q)}} \tag{A-5}$$

$$K_4 = \frac{V}{v_{4-\mathrm{CM}}} = \sqrt{\frac{m_1 m_4 E_{t-\mathrm{CM}}}{m_2 m_3 (E_{t-\mathrm{CM}} + Q)}} \tag{A-6}$$

$$\mathrm{Tan}\ \theta_3 = \frac{\mathrm{Sin}\Theta_3}{\mathrm{Cos}\Theta_3 + K_3} \tag{A-7}$$

$$\mathrm{Tan}\ \theta_4 = \frac{\mathrm{Sin}\Theta_4}{\mathrm{Cos}\Theta_4 + K_4}. \tag{A-8}$$

The angular differential cross-section in the CM frame (most nuclear databases tabulate cross-sections in the CM frame) can be related to the differential cross-section in the lab frame through

$$\frac{d\Omega_{3-\mathrm{CM}}}{d\Omega_{3-\mathrm{lab}}} = \frac{\mathrm{Sin}\Theta_3}{\mathrm{Sin}\theta_3}\frac{d\Theta_3}{d\theta_3}, \tag{A-9}$$

where

$$\frac{d\Theta_3}{d\theta_3} = \frac{\frac{d\mathrm{Tan}\theta_3}{d\theta_3}}{\frac{d\mathrm{Tan}\theta_3}{d\Theta_3}} = \frac{(1+\mathrm{Tan}^2\theta_3)(\mathrm{Cos}\Theta_3 + K_3)^2}{(1+K_3\,\mathrm{Cos}\Theta_3)} = \frac{1+{K_3}^2+2K_3\,\mathrm{Cos}\Theta_3}{1+K_3\,\mathrm{Cos}\Theta_3} \tag{A-10}$$

and

$$\frac{\mathrm{Sin}\Theta_3}{\mathrm{Sin}\theta_3} = \frac{\mathrm{Sin}\Theta_3}{\frac{\mathrm{Sin}\Theta_3}{\mathrm{Cos}\Theta_3+K_3}\Big/\sqrt{1+\left(\frac{\mathrm{Sin}\Theta_3}{\mathrm{Cos}\Theta_3+K_3}\right)^2}} = (1+{K_3}^2+2K_3\,\mathrm{Cos}\Theta_3)^{1/2}. \tag{A-11}$$

Combining (A-10) with (A-11) yields

$$\frac{d\sigma}{d\Omega_{3-\mathrm{lab}}} = \frac{(1+{K_3}^2+2K_3\,\mathrm{Cos}\Theta_3)^{3/2}}{1+K_3\,\mathrm{Cos}\Theta_3}\frac{d\sigma}{d\Omega_{\mathrm{CM}}}. \tag{A-12}$$

Applying a similar analysis to particle 4 gives

$$\frac{d\sigma}{d\Omega_{4-\mathrm{lab}}} = \frac{(1+{K_4}^2+2K_4\,\mathrm{Cos}\Theta_4)^{3/2}}{1+K_4\,\mathrm{Cos}\Theta_4}\frac{d\sigma}{d\Omega_{\mathrm{CM}}}. \tag{A-13}$$

A useful relationship between the CM angles of particle 3 and particle 4 is $\Theta_4 = \pi - \Theta_3$, which follows from the conservation of momentum in the CM frame. To derive the energy differential cross-section $\left(\frac{d\sigma}{d\mathrm{E}}\right)$ in the lab frame as a function of CM angular differential cross-section $\left(\frac{d\sigma}{d\Omega_{\mathrm{CM}}}\right)$, it is useful to first relate the energy of the reactants in the CM frame ($\mathrm{E}_{3-\mathrm{CM}}$ and $\mathrm{E}_{4-\mathrm{CM}}$) to $\mathrm{E}_{\text{t-CM}}$ (A-4). Following from the velocities of particle 3 and 4 in the CM frame, $\mathrm{E}_{3-\mathrm{CM}}$ and $\mathrm{E}_{4-\mathrm{CM}}$ can be expressed as

$$\mathrm{E}_{3-\mathrm{CM}} = \frac{1}{2}m_3{v_{3-\mathrm{CM}}}^2 = \frac{m_4(\mathrm{E}_{\mathrm{t}-\mathrm{CM}}+\mathrm{Q})}{(m_3+m_4)} \tag{A-14}$$

$$\mathrm{E}_{4-\mathrm{CM}} = \frac{1}{2}m_4{v_{4-\mathrm{CM}}}^2 = \frac{m_3(\mathrm{E}_{\mathrm{t}-\mathrm{CM}}+\mathrm{Q})}{(m_3+m_4)}. \tag{A-15}$$

From conservation of momentum in the direction perpendicular to the incident particle, we can express the following relationship

$$\mathrm{m}_3 v_{3-\mathrm{lab}}\,\mathrm{Sin}\theta_3 = \mathrm{m}_3 v_{3-\mathrm{CM}}\,\mathrm{Sin}\Theta_3. \tag{A-16}$$

Now, the lab energies (E_3 and E_4) can be expressed as functions of constants of motion (K_3 and K_4 from Equations (A-5) and (A-6)) and CM scattering angles (Θ_3 and Θ_4). These can be expressed as

$$\mathrm{E}_3 = \mathrm{E}_{3-\mathrm{CM}}\left(\frac{\mathrm{Sin}\Theta_3}{\mathrm{Sin}\theta_3}\right)^2 = \mathrm{E}_{3-\mathrm{CM}}\left(1 + {K_3}^2 + 2K_3\,\mathrm{Cos}\Theta_3\right). \tag{A-17}$$

Following the same procedure for particle 4 yields

$$\mathrm{E}_4 = \mathrm{E}_{4-\mathrm{CM}}\left(1 + {K_4}^2 + 2K_4\,\mathrm{Cos}\Theta_4\right). \tag{A-18}$$

The energy differential cross-section $\left(\frac{d\sigma}{d\mathrm{E}}\right)$ in the lab frame can now be expressed in terms of the CM angular differential cross-section $\left(\frac{d\sigma}{d\Omega_{\mathrm{CM}}}\right)$ via the constant K, using the relationship

$$\frac{d\mathrm{E}_3}{d\Omega_{\mathrm{CM}}} = \frac{\mathrm{E}_{3-\mathrm{CM}}\,2\,K_3\,\mathrm{Sin}\Theta_3}{2\,\pi\,\mathrm{Sin}\Theta_3}, \tag{A-19}$$

which yields

$$\frac{d\sigma}{d\mathrm{E}_3} = \frac{d\Omega_{\mathrm{CM}}}{d\mathrm{E}_3}\frac{d\sigma}{d\Omega_{\mathrm{CM}}} = \frac{\pi}{K_3 E_{\mathrm{CM}-3}}\,\frac{d\sigma}{d\Omega_{\mathrm{CM}}}. \tag{A-20}$$

Similarly for particle 4:

$$\frac{d\sigma}{d\mathrm{E}_4} = \frac{\pi}{K_4 E_{\mathrm{CM}-4}} \frac{d\sigma}{d\Omega_{\mathrm{CM}}}. \tag{A-21}$$

The MRS often diagnoses implosions of plastic capsules that contain carbon. This requires a good understanding of the spectrum of scattered neutrons from carbon. The elastic and inelastic angular differential cross-sections in the CM frame for 14MeV neutrons on carbon, obtained from the (Evaluated Nuclear Data File) ENDF/B-VII.0[13] database, are shown in Figure A-2a. Figure A-2b shows the conversion of the CM angular differential cross-sections to the lab energy differential scattering cross-section for 14MeV neutrons using Equation (A-20).

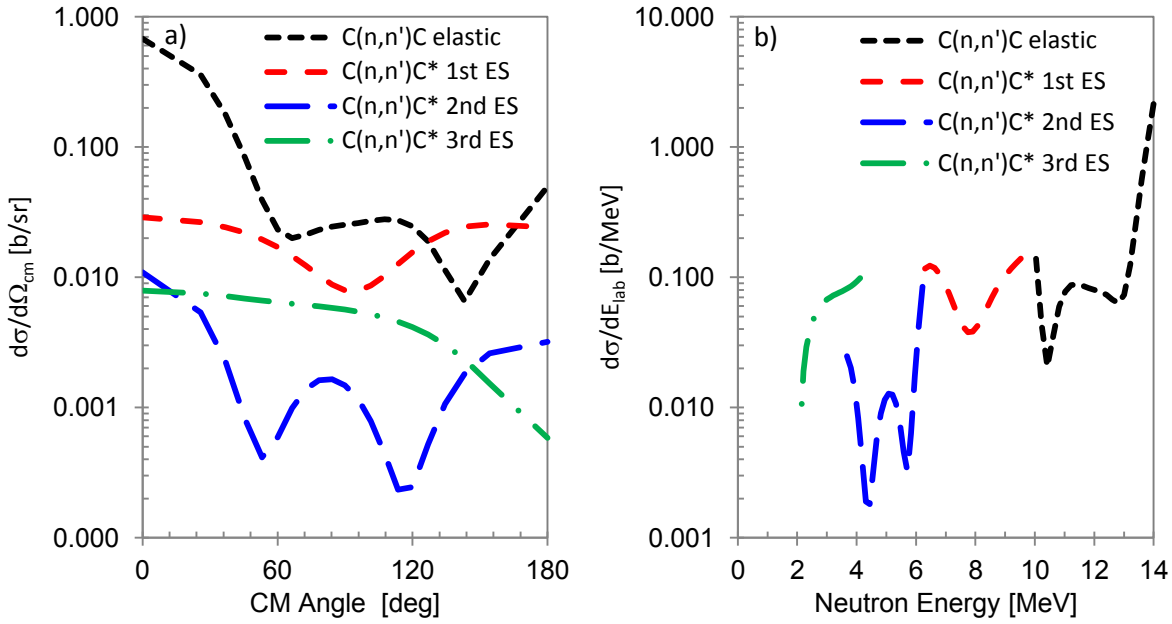

Figure A-2 a) Angular differential scattering cross-section for 14MeV neutrons on carbon as a function of CM angle for elastic and inelastic scattering from the first three excited states in C-12. These cross sections were obtained from the ENDF/B-VII.0 database.[13] b) Energy differential scattering cross-section for 14MeV neutrons on carbon for elastic and inelastic scattering from the first three excited states in C-12 is plotted as a function of laboratory energy. These cross-sections were derived from the CM angular differential cross-sections shown in figure (a) using Equation (A-20).

The expressions derived above are valid for any non-relativistic two-body reactions. However, these kinematic expressions are greatly simplified in the case of elastic (Q=0) neutron scattering. If we identify particle 3 as the neutron and particle 4 as the recoil nucleus, then $m_1 = m_3 = 1$ and $m_2 = m_4 = A$, where A is the mass number of the recoil nucleus. In this case, the relationship between the recoil angular differential cross-section $\left(\frac{d\sigma}{d\Omega_{\mathrm{lab}-4}}\right)$ (which is useful in determining the MRS detection efficiency) and CM angular differential cross-section $\left(\frac{d\sigma}{d\Omega_{\mathrm{CM}}}\right)$ is given by

$$\frac{d\sigma}{d\Omega_{\text{lab}-4}} = 4\,\text{Cos}\,\theta_4 \frac{d\sigma}{d\Omega_{\text{CM}}} \tag{A-22}$$

The relationship between the energy differential scattering cross-section $\left(\frac{d\sigma}{d\text{E}_3}\right)$ for the neutron and $\frac{d\sigma}{d\Omega_{\text{CM}}}$ is also simplified and is given by

$$\frac{d\sigma}{d\text{E}_3} = \frac{\pi(1+A)^2}{A\ \text{E}_3} \frac{d\sigma}{d\Omega_{\text{CM}}}. \tag{A-23}$$

The relationship between the recoil scattering angle (θ_4) and CM neutron scattering angle (Θ_3) can also be simplified, and expressed as

$$\text{Cos}\,\theta_4 = \sqrt{\frac{1-\text{Cos}\,\Theta_3}{2}}. \tag{A-24}$$

The energy of the recoil nucleus (E_4) can now be simply expressed in terms of θ_4, i.e.,

$$E_4 = \frac{4A}{(1+A)^2}\text{E}_1\text{Cos}^2\theta_4. \tag{A-25}$$

The $d\sigma/d\Omega_{\text{CM}}$ curves for elastic scattering of 14 MeV neutrons off H, D, and T are shown in Figure A-3a. These cross sections were also obtained from the ENDF/B-VII.0[13] database. The energy differential cross-sections for elastic neutron scattering are derived from Equation (A-23) and are shown in Figure A-3b. The n,2n reactions in D and T are also shown in this figure, and these cross sections were obtained from the CENDL-3.1 database.[123] $d\sigma/d\Omega_{\text{CM}}$ for elastic n-d scattering can be converted to the lab frame, using Equation (A-22), as shown in Figure A-4 for neutron energies of 5.6 MeV and 14.17 MeV. This quantity is important in computing the MRS detection efficiency, as discussed in Chapter 4.

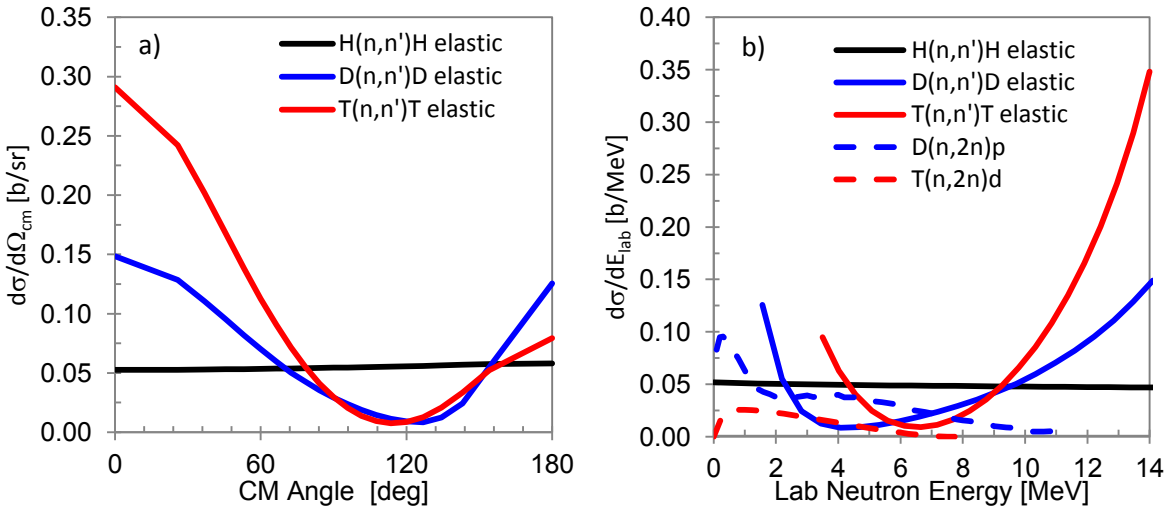

Figure A-3: a) Angular differential cross-section for 14 MeV neutron elastic scattering off H, D, and T as a function of CM energy. These cross sections were obtained from the ENDF/B-VII.0[13] database. b) The lab-energy differential cross-sections (solid lines) derived using Equation (A-23) for elastic scattering of 14 MeV neutrons off H, D, and T using the cross-sections shown in figure (a). Also shown are the n,2n reactions in D and T, which were obtained from the CENDL-3.1 database (dashed lines).[123]

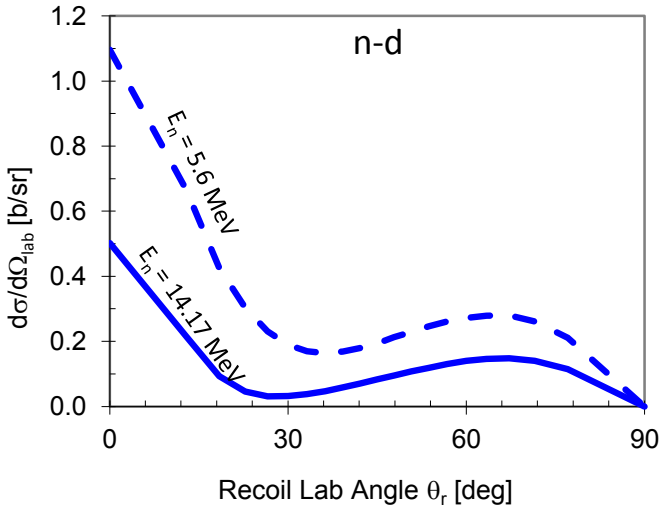

Figure A-4: Angular differential cross section for elastic n-d scattering as a function of the recoil deuteron angle in the lab frame for neutron energies of 14.17MeV (solid line) and 5.6MeV (dashed line). The MRS detects forward scattered recoil deuterons (θ_r~0). The two curves show that the $d\sigma/d\Omega_{lab}$ cross-section is higher at lower incident neutron energy, indicating that the MRS-detection efficiency is a function of neutron energy.

The scattered neutron spectrum from an ICF implosion (discussed in Chapter 3) can be calculated from the energy differential cross-section and the path integrated areal density (ρL), as expressed by

$$\frac{\mathrm{Y_{DSn}}(E)}{\mathrm{Y_{DT}}} = N_a \frac{\sum_i \rho L_i \frac{d\sigma_i}{d\mathrm{E}} f_i}{\sum_i m_i f_i}. \tag{A-26}$$

Here, N_a is Avogadro's number, m_i is the atomic mass, and f_i is atomic fraction. Recall from Chapter 3 that $\rho L = \rho R$ for a hot-spot implosion model (where all neutrons are produced at the center of the implosion). The scattered neutron spectrum for an equimolar DT implosion is shown in Figure A-5a. The different components, from each individual reaction, contributing to the spectrum are also shown. The scattered neutron spectrum for a CH plastic (H/C = 1.38/1) implosion is shown in Figure A-5b. This spectrum, which was normalized by the scattering material's ρL, was calculated using Equation (A-26). The components for the n-p elastic scattering and neutron-inelastic scattering in carbon, which contribute to the scattered neutron spectrum, are also shown in the figure. The down scattered neutron yield (Y_{DSn}) can be calculated by integrating Equation (A-26) or by integrating the curves in Figure A-5. The neutron energy range used for detecting DSn at OMEGA is 9.5-12.5 MeV, as discussed in Chapter 7. The relationship between Y_{DSn} and the ρL for an equimolar DT implosion is given by

$$Y_{DSn} = \int_{9.5\mathrm{MeV}}^{12.5\mathrm{MeV}} Y(E)dE \sim 0.07\, \rho L(g/cm^2)\, Y_{DT}. \tag{A-27}$$

At the NIF, Y_{DSn} is typically defined as the down-scattered ratio (DSR), which is simply Equation (A-26), integrated over the energy range 10-12MeV. The relationship between DSR and ρL for an equimolar DT implosion is given by

$$DSR = \frac{Y_{DS-n}}{Y_{DT}} = \frac{1}{Y_{DT}} \int_{10\mathrm{MeV}}^{12\mathrm{MeV}} Y(E)dE \sim 0.05\, \rho L(g/cm^2) \tag{A-28}$$

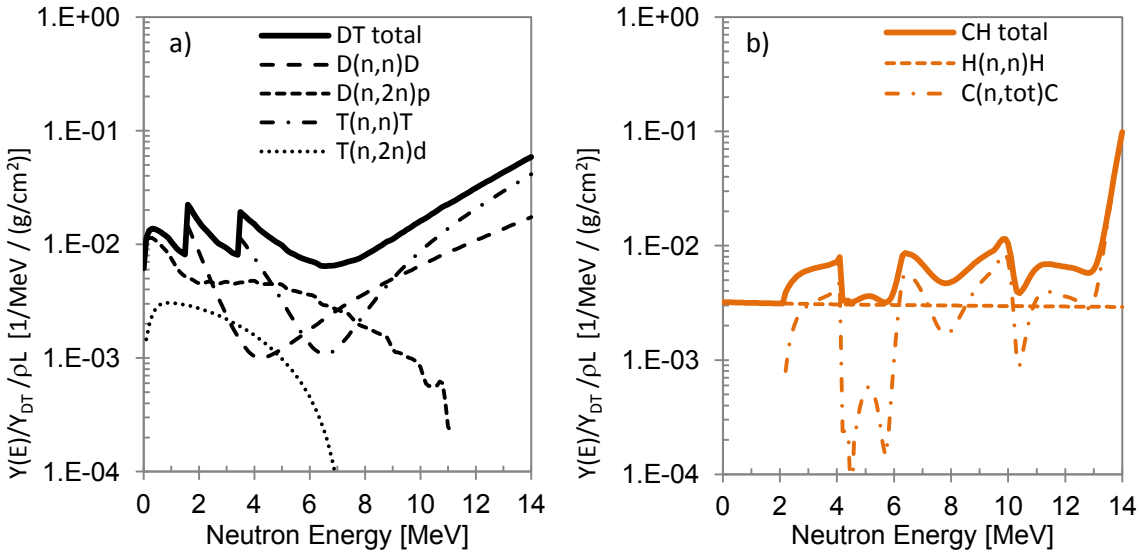

Figure A-5: a) The scattered neutron spectrum for an equimolar DT implosion, which is normalized by ρL. b) The scattered neutron spectrum for a CH plastic implosion The different components, associated with the different reactions (or scattering) processes, contributing to the scattered neutron spectrum are also shown in the figures.

Appendix B – Astrophysical S-factor, reactant distributions, and electron screening

Cross-sections for fusion reactions are extremely important for both nucleosynthesis and for fusion experiments like those discussed throughout this thesis. This section will discuss the "astrophysical S-factor" parameterization of the cross-section. This section will also show how the S-factor can be used to derive the thermonuclear reactant distribution of a burning plasma. In addition, the effect of electron screening on reaction cross-sections is also discussed.

A convenient and illuminating way of displaying and tabulating the reaction cross-sections is to use the astrophysical S-factor parametrization,[16] which can be expressed as

$$\sigma(E) = \frac{S(E)}{E} e^{-\sqrt{E_G/E}}. \tag{B-1}$$

Here, E_G is the Gamow penetration energy that is expressed as $E_G = 2\left(\pi\, \alpha_f\, Z_1 Z_2\right)^2 m_r c^2$, where E is the reactant energy in the CM frame, α_f is the fine structure constant, m_r is the reduced mass, and c is the speed of light. The utility of this parameterization is that the nuclear scale size (de Broglie wavelength squared $\lambda^2 = (\mathrm{h}/p)^2 = \mathrm{h}^2/(2mE)$) and Coulomb barrier penetration-factor, which vary extremely fast with CM energy, are separated from the slower varying nuclear component or S-factor.[10, 16] As an important example, the measured and evaluated cross-sections for the DT reaction[124-130] are plotted as a function of the CM energy in Figure B-6a and the corresponding astrophysical S-factors are given in Figure B-6b. Notice a broad resonance evident in the DT S-factor. Figure B-6c and Figure B-6d show the astrophysical S-factors for the TT[13, 131-134] and ^{3}He^{3}He[135-137] reactions, respectively. Both the TT and ^{3}He^{3}He reactions are non-resonant in this energy range and therefore their S-factors vary slowly with energy. Additional cross-sections and astrophysical S-factors for several reactions of interest are given in Figure B-7.

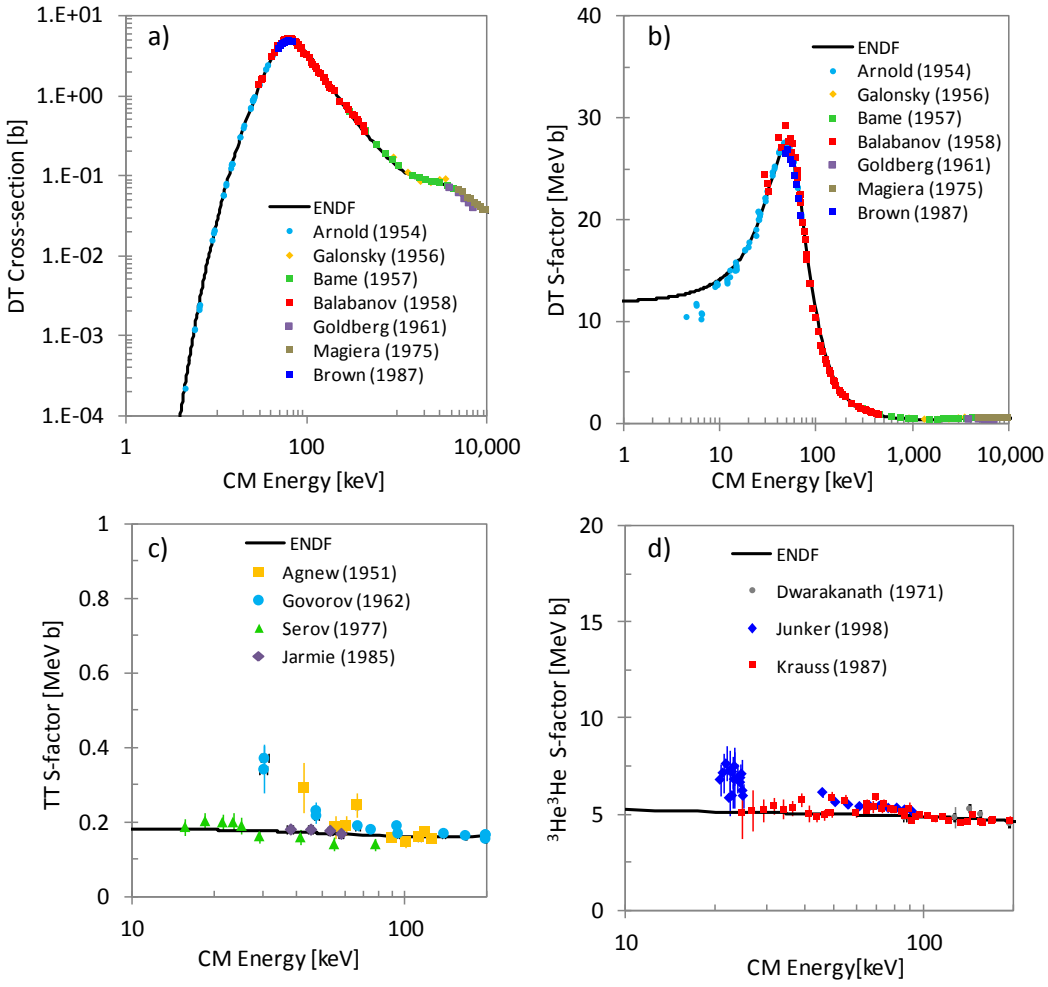

Figure B-6: a) Measured[124-130] and evaluated (ENDF/B-VII.0)[13] DT reaction cross-section as a function of CM energy. b) Measured and evaluated (ENDF/B-VII.0) S-factor for the DT reaction.[124-130] The S-factor provides a convenient way to display the reaction cross-sections as it separates the fast varying Coulomb penetration and de Broglie wavelength (nuclear size) from the slower varying nuclear physics component. b) Measured and evaluated (ENDF/B-VII.0) S-factor for the TT reaction.[13, 131-134] d) Measured[135-137] and evaluated (ENDF/B-VII.0)[13] S-factor for the ^{3}He^{3}He reaction.

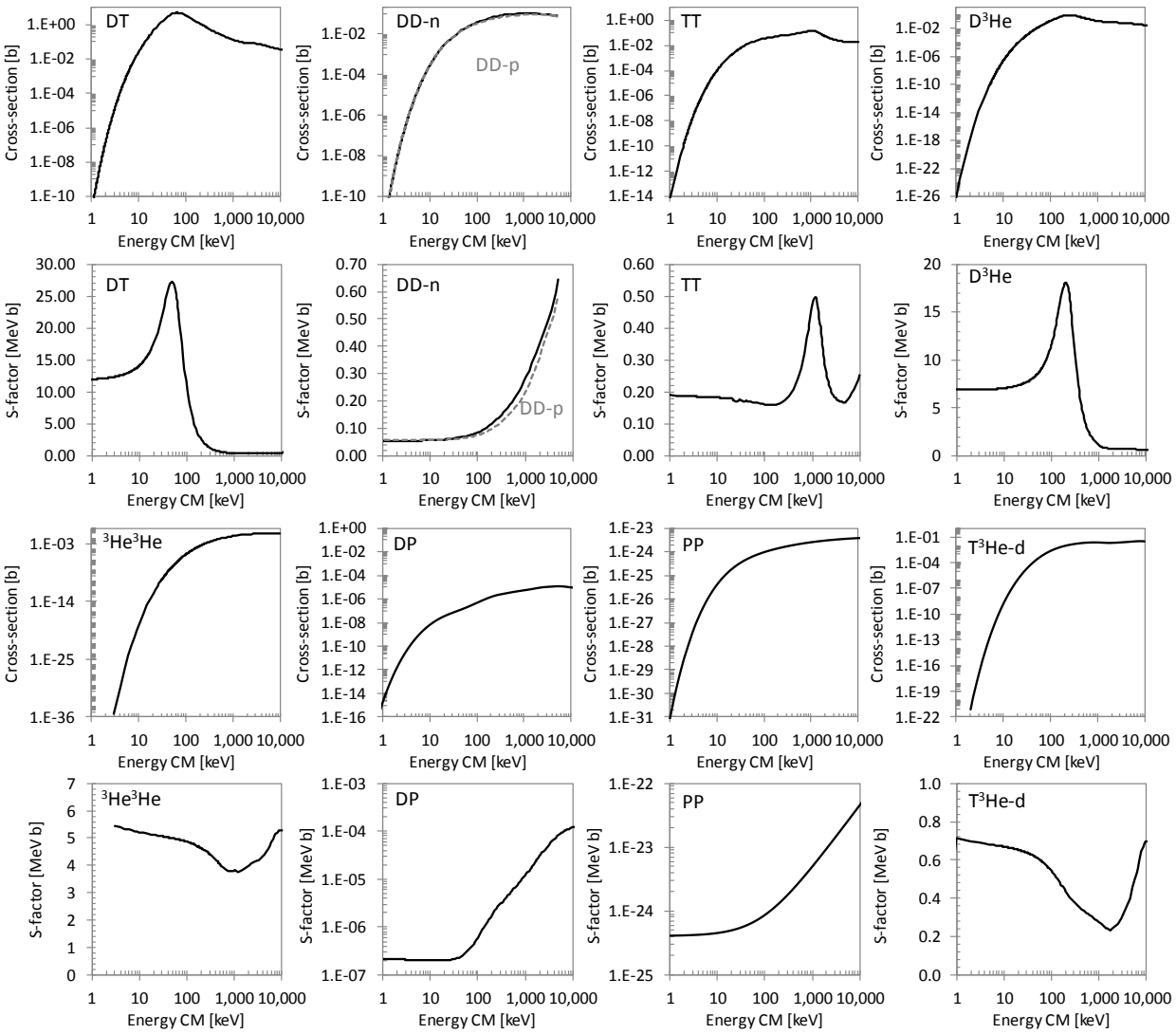

Figure B-7: Evaluated (ENDF/B-VII.0)[13] reaction cross-section data (except the pp reaction which was derived from Adelberger et al.[14]) and the corresponding astrophysical S-factor as a function of CM energy for several reactions of interest.

To illustrate the utility of the non-resonant S-factor, we consider the following calculation of the reactant energy distribution of a thermonuclear burn. This energy distribution can be derived directly from the Maxwellian averaged reactivity $\langle \sigma v \rangle$ given by Equation (1-2). Figure B-8 shows the components inside the energy integral of Equation (1-2) and the resultant energy distribution of TT reactants at T_i=5keV. The peak of this distribution (E_0) is also called the Gamow peak energy.[10, 16] Additionally, Figure B-9 shows the numerically calculated reactant energy

distributions for several reactions of interest at four ion temperatures [1keV, 5keV, 50keV, and 200keV].

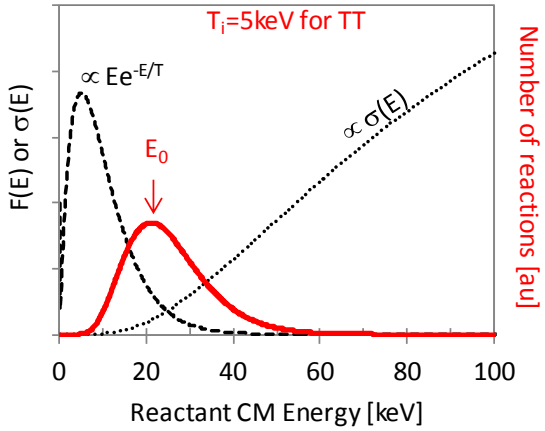

Figure B-8: Plot of the reactant energy distribution (red) of a T_i=5keV TT fusion burn, as a function of CM energy. The components of Equation (1-2), whose product make up this reactant distribution, are the velocity weighted Maxwellian distribution (dashed) and the cross-section (dotted). The peak of this distribution (E_0) is called the Gamow peak energy.

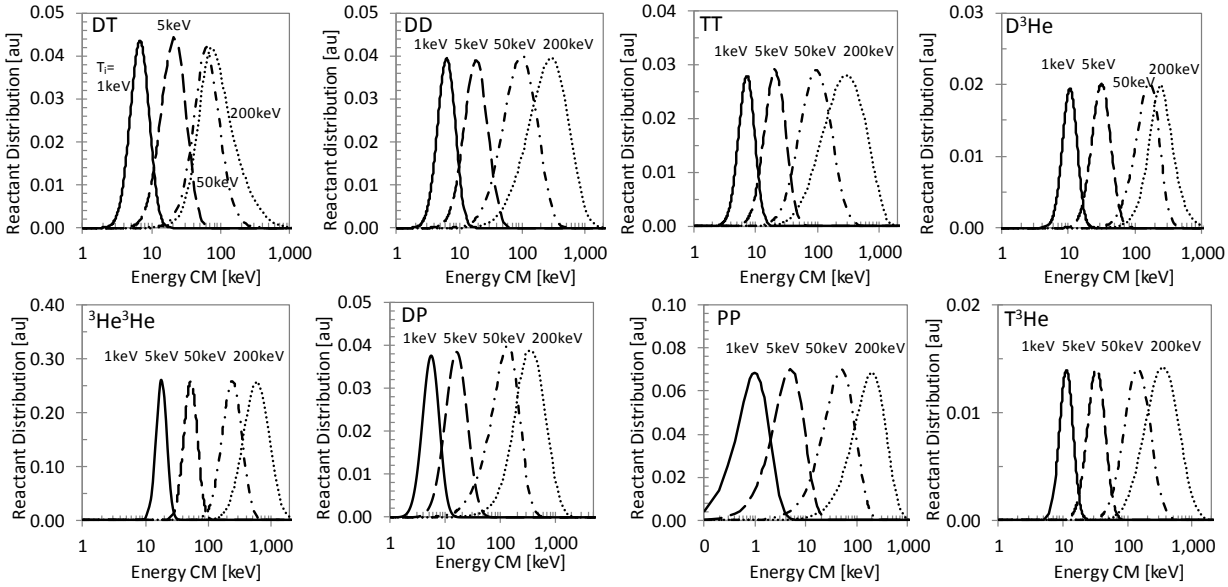

Figure B-9: Plot of the thermal reactant energy distributions (at four ion temperatures T_i=1keV, 5keV, 50keV, 200keV) as a function of CM reactant energy for the fusion reactions shown in Figure B-7. Note that these distributions have been individually scaled for easy comparison.

E_0 can also be calculated analytically for a non-resonant reaction* using the S-factor parameterization for the cross-section in Equation (1-2), as illustrated by

$$\langle \sigma v \rangle = \sqrt{\frac{8}{\pi\, m_r}} \frac{1}{T^{3/2}} \int_0^\infty S(E) e^{-\sqrt{E_G/E} - E/T} dE. \tag{B-2}$$

If S(E) is slow varying over the burn (non-resonant like the reactions shown in Figure B-6c and Figure B-6d) then it can be removed from the integral. Also, the quantity: $e^{-\sqrt{E_G/E} - E/T}$, can be approximated by a Gaussian distribution $\sim e^{-\frac{(E-E_0)^2}{\Delta/2}}$ using the method of steepest descent.[138] The peak of this distribution is $E_0 = (bT/2)^{2/3}$, where the $b = \sqrt{E_G}$ defined above. For TT, b =38.5 keV$^{1/2}$ and for ^{3}He^{3}He b=154 keV$^{1/2}$ (T_i and E_0 are expressed in keV). The 1/e full-width is $\Delta = 4(E_0 T_i/3)^{1/2}$. Table B-1 summarizes Gamow peak energies and Gamow penetration energies for several reactions of interest.

* Note near a strong resonance reaction $E_0 \sim E_{res}$, where E_{res} is the resonance energy. This is evident in the reactant distributions at T_i=50keV and 200keV for DT in Figure B-9.

Table B-1: Gamow penetration energies (E_G) for several reactions of interest. Also provided is the Gamow peak energy (E_0) normalized by $T^{2/3}$ where T is expected in keV.

	DT	DD	TT	D^3He	$^3He^3He$	PP	T^3He
E_G(MeV)	1.18	0.99	1.48	4.73	23.67	0.49	5.92
$E_0(keV)/T_{keV}^{2/3}$ †	6.66	6.27	7.18	10.58	18.09	4.98	11.39

† In principle, this only works far away from resonances

For a resonant reaction, the Breit-Wigner form for the cross-section can be used to analytically evaluate Equation (1-2).[10] A crude estimate of the reactivity can be obtained by assuming all reactions occur within a very narrow resonance where the width (Γ) is much less then the peak energy (E_{res}),[16, 138] which results in $\langle\sigma v\rangle_{narrow} \sim \sqrt{\frac{8}{\pi\, m_r}} \frac{E_{res}}{T^{3/2}} \frac{\pi\,\Gamma}{2} \sigma(E_{res})\, e^{-E_{res}/T}$. This estimate is compared to the numerically evaluated reactivity <σv> for the DT and D^3He reactions in Figure B-10. This estimate only works near the DT and D^3He resonances but is accurate to about a factor of two near each resonance (despite the fact that these are broad resonances).

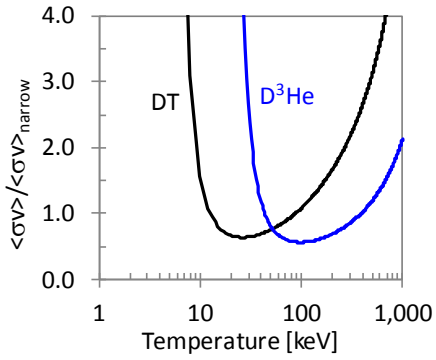

Figure B-10: A comparison between the numerically evaluated <σ*v*> for the resonant reactions DT and D^3He, and a simple analytical estimate of $<\sigma v>_{narrow}$, assuming narrow resonances.

Nuclear reaction cross-sections, like those shown in Figure B-6, are measured in the presence of electrons. Generally, the effect of electrons on the Coulomb barrier between reacting nuclei is negligible except at very low CM energies where the electrons effectively screen the repulsive Coulomb barrier and enhance the reaction cross-section. The enhancement, which is often significant in low-energy accelerator experiments, was modeled by Assenbaum et al.[15] This enhancement can be expressed as

$$f(E) = \frac{\sigma_{Screened}(E)}{\sigma(E)} \approx e^{\frac{U_e\sqrt{E_G}}{2E^{3/2}}}. \quad \text{(B-3)}$$

Here U_e is the electron-screening energy, which is tabulated and available in Assenbaum et al.[139] and Aldelberger et al.[15] This model shows excellent agreement with the measured D^3He reaction cross-section enhancement over the ENDF/B-VII.0 bare-nuclei cross-section (see Figure B-11a). When this model is applied to the DT and TT reactions, the predicted enhancement is negligible, except at energies much lower than relevant for ICF applications as shown in Figure B-11b. This means that screening effects are negligible in the reference DT and TT data, which have been obtained by laboratory accelerator experiments.

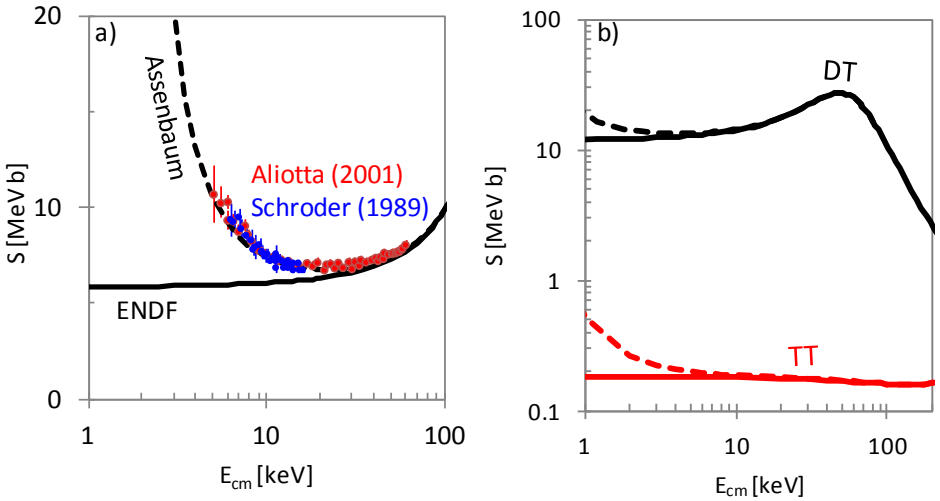

Figure B-11: a) The S-factor for the D^3He reaction as a function of the CM energy. The data sets were obtained by Aliotta et al.[140] and Schroder et al.[141], which are contrasted to the bare-nuclei S-factor (solid curve) and electron-screened S-factor (dashed curve). The bare-nuclei S-factor is from the ENDF/B-VII.0 database.[13] Electron-screening enhancement is taken from Assenbaum et al.[139] b) The S-factor for the DT and TT reactions as a function of CM energy with the predicted accelerator electron screening effect (dashed curve) from the Assenbaum[15] model. The model shows that accelerator electron screening for the DT and TT reactions is negligible in the energy range of most ICF implosions (>10keV).

The Salpeter model[15] characterizes the effect of plasma electron screening in the thermonuclear plasmas that exist in ICF experiments and in the sun. As shown by Equation (B-4), the plasma electron screening is a function of the plasma temperature (T) and plasma Debye radius (λ_D).

$$f(E) = \frac{\sigma_{Screened}(E)}{\sigma(E)} \approx e^{\frac{Z_1 Z_2 e^2}{4\pi\varepsilon_0 T \lambda_D}} \tag{B-4}$$

The reaction enhancement factor *f(E)*, is shown in Figure B-12 for the DT, TT, D^3He, and $^3He^3He$ reactions as a function of plasma ion temperature T_i, which illustrates that *f(E)* is negligible for all experiments described in this thesis (ρ~5g/cm^3) and even for much denser implosions (ρ~500g/cm^3), except for $^3He^3He$ where electron screening may be important.

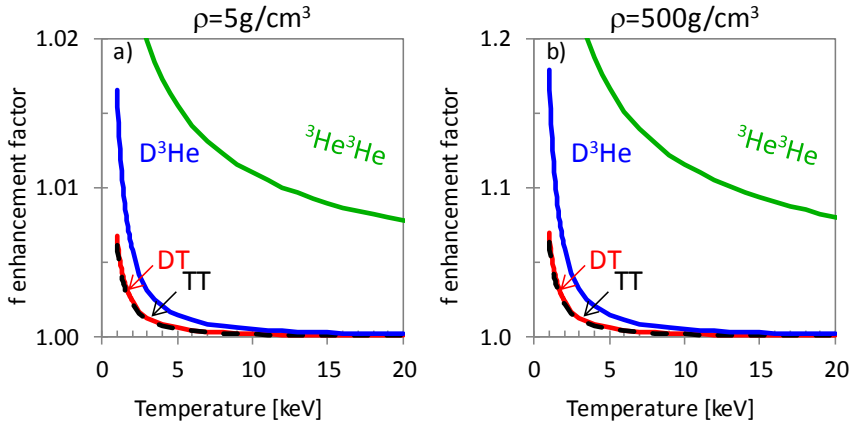

Figure B-12: Predicted enhancement for the DT, TT, D^3He, and $^3He^3He$ reactions due to plasma electron screening calculated using the Salpeter[15] model for ρ~5g/cm^3 in part a (achievable in an OMEGA implosion) and ρ~500g/cm^3 in part b (achievable in a NIF implosion). The predictions show that plasma electron screening is negligible in all measurements presented in this thesis.

Appendix C - OMEGA DSn Experimental Data Summary

Summary of OMEGA Cryogenic DT implosions diagnosed by the MRS

OMEGA shot	Y_{DTn} (X 10^{12})	T_i (keV)	MRS ρR_{tot} (mg/cm^2)	MRS $\sigma_{\rho R}$ (mg/cm^2)	CPS1 ρR_{tot} (mg/cm^2)	CPS1 $\sigma_{\rho R}$ (mg/cm^2)	CPS2 ρR_{tot} (mg/cm^2)	CPS2 $\sigma_{\rho R}$ (mg/cm^2)
53808	3.5	2.1	68	42	161	31	62	7
53879	6.0	2.3	94	27	22	5	47	4
54886	5.5	2.1	98	15	135	9	87	6
54926	3.9	1.8	83	9	128	10	62	5
55230	3.7	2.2	191	22	sat	sat	49	6
55231	3.4	2.2	179	34	sat	sat	sat	sat
55399	3.0	2.1	185	27	sat	sat	sat	sat
55468	2.8	2.1	221	36	170	23	sat	sat
55722	2.0	1.8	276	34	sat	sat	66	8
55723	1.9	1.8	295	47	sat	sat	sat	sat
55826	1.9	1.8	236	34	sat	sat	sat	sat
55947	7.6	2.2	64	15	na	na	49	6
55952	4.2	2.1	111	14	171	25	71	9
56043	2.8	2	179	26	sat	sat	sat	sat
56044	1.7	1.6	198	37	sat	sat	sat	sat
56046	2.2	1.9	168	31	sat	sat	sat	sat
57482	3.0	2.1	215	21	sat	sat	sat	sat
58197	2.3	1.8	178	50	160	24	178	50
58288	1.6	1.53	216	36	167	26	sat	sat
58970	1.9	1.98	114	21	143	22	49	12

OMEGA shot	Y_{DTn} (X 10^{12})	T_i (keV)	MRS ρR_{tot} (mg/cm^2)	MRS $\sigma_{\rho R}$ (mg/cm^2)	CPS1 ρR_{tot} (mg/cm^2)	CPS1 $\sigma_{\rho R}$ (mg/cm^2)	CPS2 ρR_{tot} (mg/cm^2)	CPS2 $\sigma_{\rho R}$ (mg/cm^2)
54886	5.5	2.1	98	15	135	9	87	6

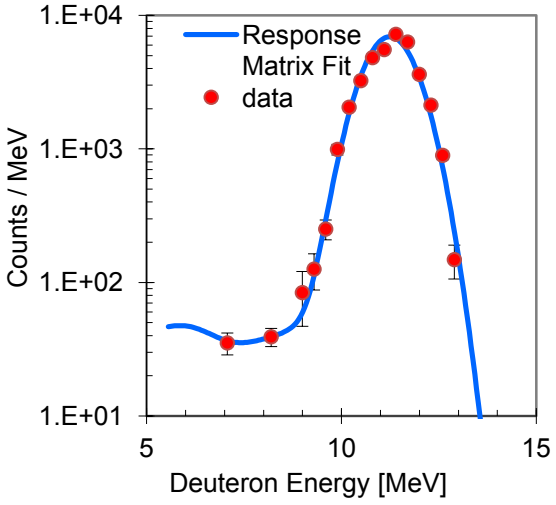

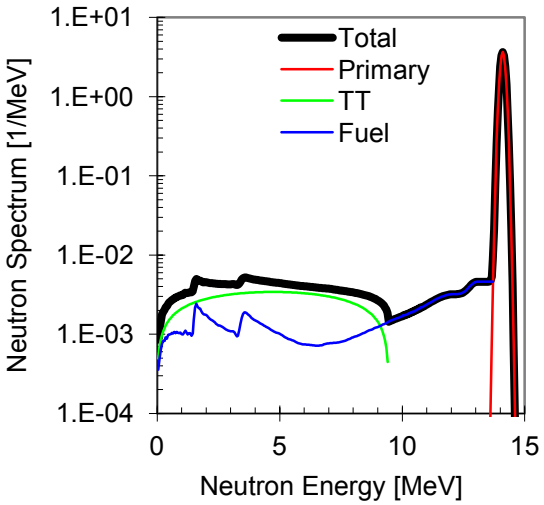

OMEGA shot	Y_{DTn} (X 10^{12})	T_i (keV)	MRS ρR_{tot} (mg/cm^2)	MRS $\sigma_{\rho R}$ (mg/cm^2)	CPS1 ρR_{tot} (mg/cm^2)	CPS1 $\sigma_{\rho R}$ (mg/cm^2)	CPS2 ρR_{tot} (mg/cm^2)	CPS2 $\sigma_{\rho R}$ (mg/cm^2)
54926	3.9	1.8	83	9	128	10	62	5

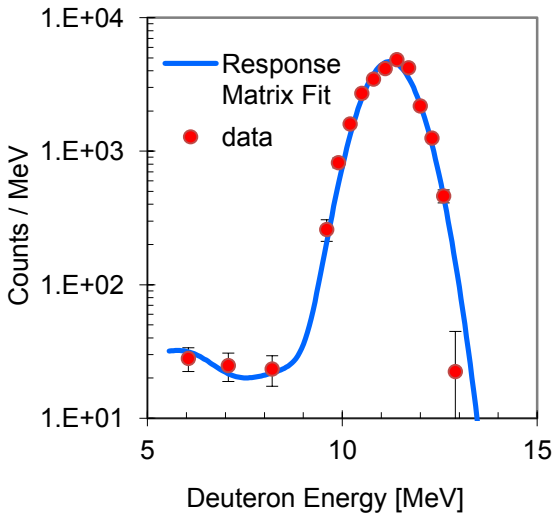

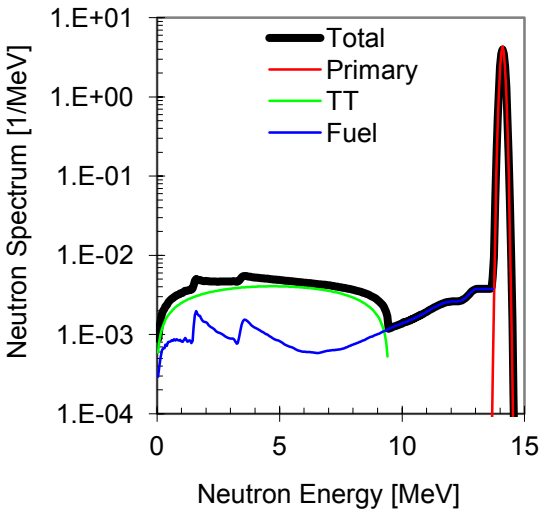

OMEGA shot	Y_{DTn} (X 10^{12})	T_i (keV)	MRS ρR_{tot} (mg/cm^2)	MRS $\sigma_{\rho R}$ (mg/cm^2)	CPS1 ρR_{tot} (mg/cm^2)	CPS1 $\sigma_{\rho R}$ (mg/cm^2)	CPS2 ρR_{tot} (mg/cm^2)	CPS2 $\sigma_{\rho R}$ (mg/cm^2)
55230	3.7	2.2	191	22	sat	sat	49	6

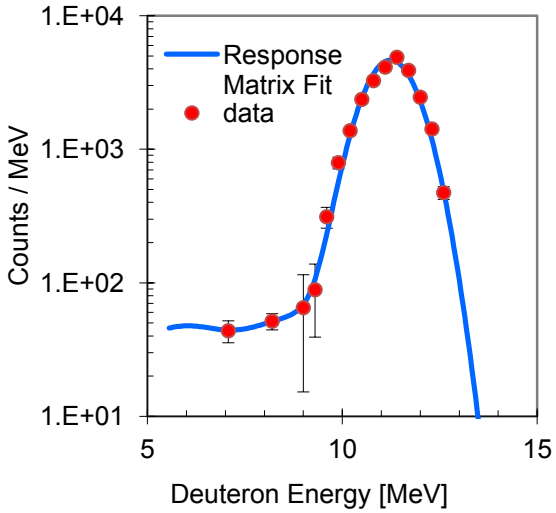

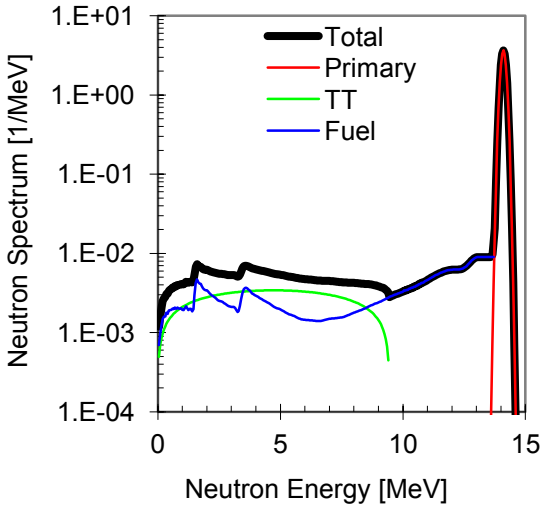

OMEGA shot	Y_{DTn} (X 10^{12})	T_i (keV)	MRS ρR_{tot} (mg/cm^2)	MRS $\sigma_{\rho R}$ (mg/cm^2)	CPS1 ρR_{tot} (mg/cm^2)	CPS1 $\sigma_{\rho R}$ (mg/cm^2)	CPS2 ρR_{tot} (mg/cm^2)	CPS2 $\sigma_{\rho R}$ (mg/cm^2)
55231	3.4	2.2	179	34	sat	sat	sat	sat

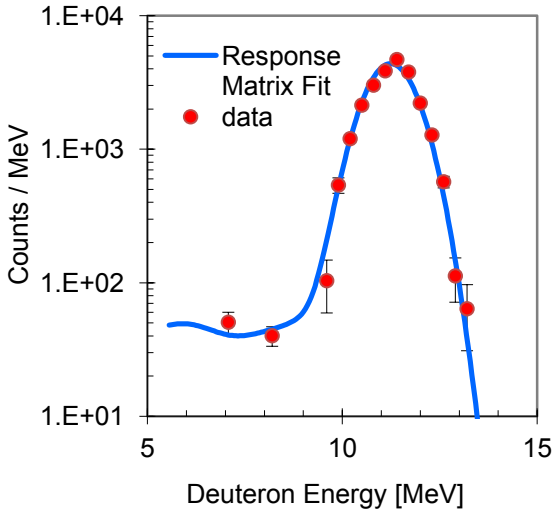

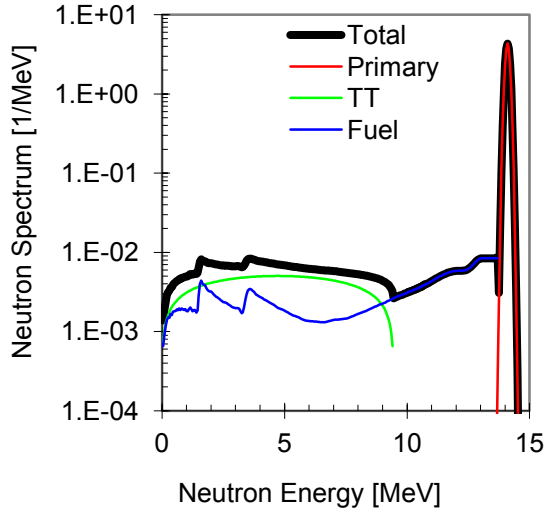

OMEGA shot	Y_{DTn} (X 10^{12})	T_i (keV)	MRS ρR_{tot} (mg/cm^2)	MRS $\sigma_{\rho R}$ (mg/cm^2)	CPS1 ρR_{tot} (mg/cm^2)	CPS1 $\sigma_{\rho R}$ (mg/cm^2)	CPS2 ρR_{tot} (mg/cm^2)	CPS2 $\sigma_{\rho R}$ (mg/cm^2)
55399	3.0	2.1	185	27	sat	sat	sat	sat

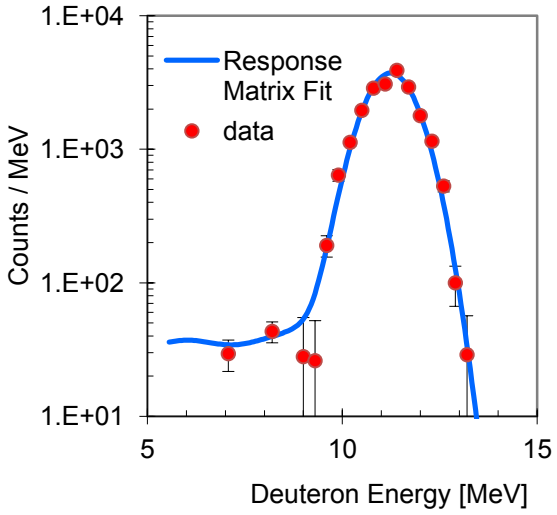

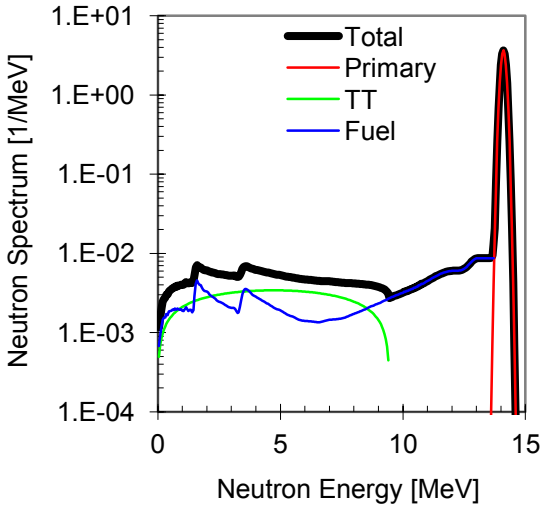

OMEGA shot	Y_{DTn} (X 10^{12})	T_i (keV)	MRS ρR_{tot} (mg/cm^2)	MRS $\sigma_{\rho R}$ (mg/cm^2)	CPS1 ρR_{tot} (mg/cm^2)	CPS1 $\sigma_{\rho R}$ (mg/cm^2)	CPS2 ρR_{tot} (mg/cm^2)	CPS2 $\sigma_{\rho R}$ (mg/cm^2)
55468	2.8	2.1	221	36	170	23	sat	sat

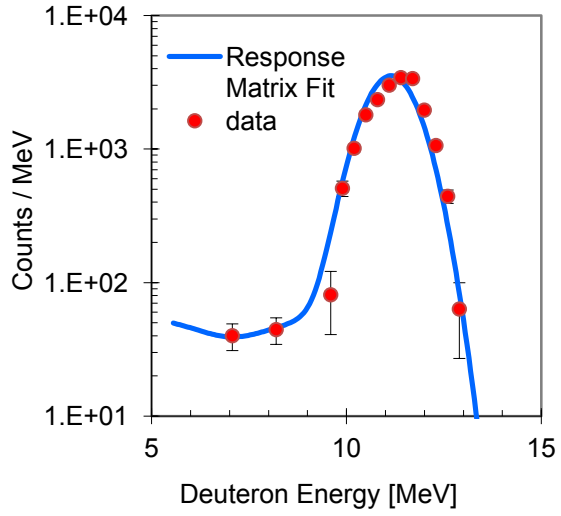

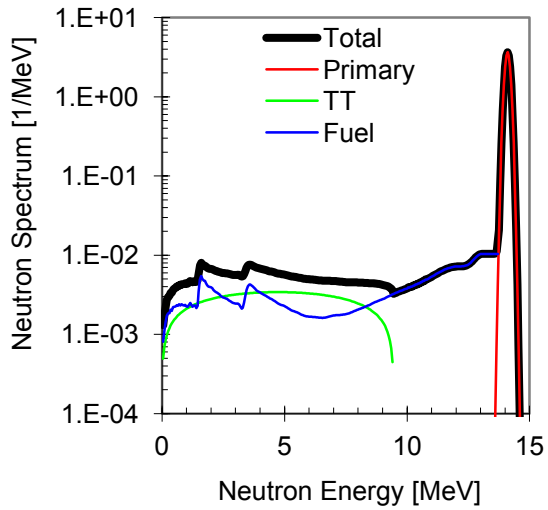

OMEGA shot	Y_{DTn} (X 10^{12})	T_i (keV)	MRS ρR_{tot} (mg/cm^2)	MRS $\sigma_{\rho R}$ (mg/cm^2)	CPS1 ρR_{tot} (mg/cm^2)	CPS1 $\sigma_{\rho R}$ (mg/cm^2)	CPS2 ρR_{tot} (mg/cm^2)	CPS2 $\sigma_{\rho R}$ (mg/cm^2)
55722	2.0	1.8	276	34	sat	sat	66	8

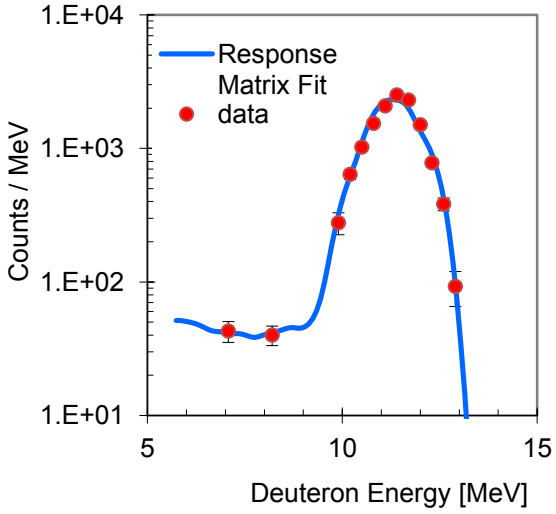

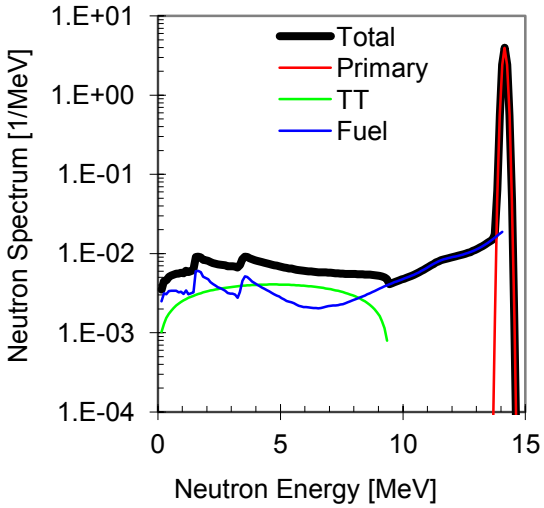

OMEGA shot	Y_{DTn} (X 10^{12})	T_i (keV)	MRS ρR_{tot} (mg/cm^2)	MRS $\sigma_{\rho R}$ (mg/cm^2)	CPS1 ρR_{tot} (mg/cm^2)	CPS1 $\sigma_{\rho R}$ (mg/cm^2)	CPS2 ρR_{tot} (mg/cm^2)	CPS2 $\sigma_{\rho R}$ (mg/cm^2)
55723	1.9	1.8	295	47	sat	sat	sat	sat

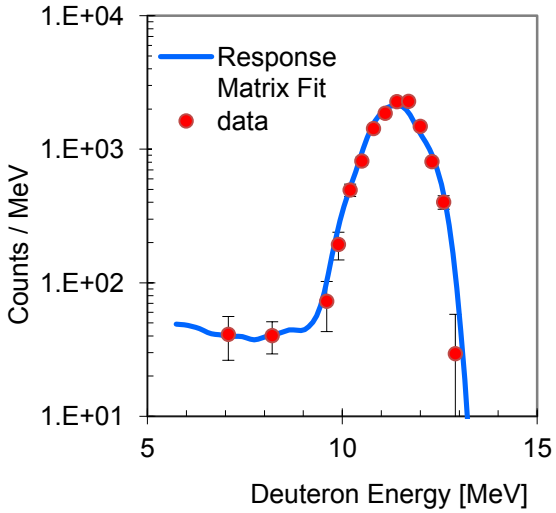

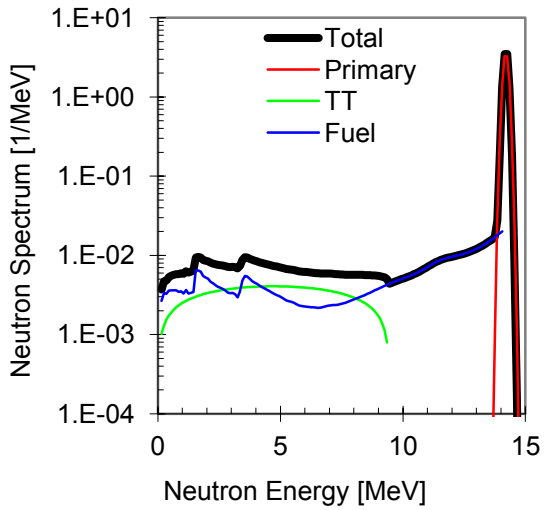

OMEGA shot	Y_{DTn} (X 10^{12})	T_i (keV)	MRS ρR_{tot} (mg/cm^2)	MRS $\sigma_{\rho R}$ (mg/cm^2)	CPS1 ρR_{tot} (mg/cm^2)	CPS1 $\sigma_{\rho R}$ (mg/cm^2)	CPS2 ρR_{tot} (mg/cm^2)	CPS2 $\sigma_{\rho R}$ (mg/cm^2)
55826	1.9	1.8	236	34	sat	sat	sat	sat

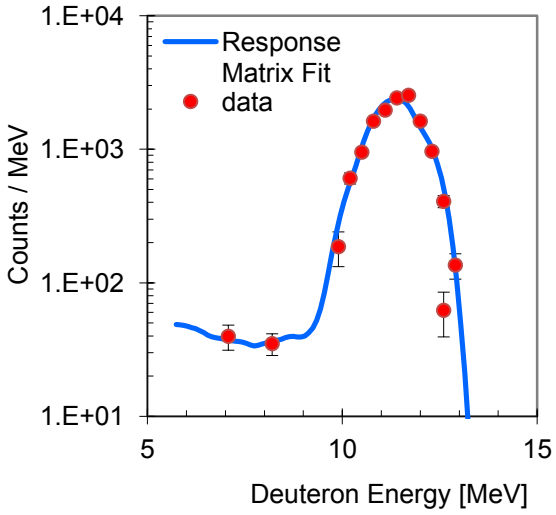

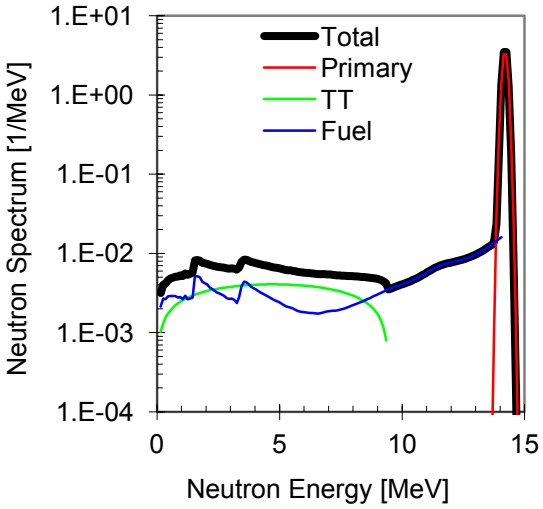

OMEGA shot	Y_{DTn} (X 10^{12})	T_i (keV)	MRS ρR_{tot} (mg/cm^2)	MRS $\sigma_{\rho R}$ (mg/cm^2)	CPS1 ρR_{tot} (mg/cm^2)	CPS1 $\sigma_{\rho R}$ (mg/cm^2)	CPS2 ρR_{tot} (mg/cm^2)	CPS2 $\sigma_{\rho R}$ (mg/cm^2)
55947	7.6	2.2	64	15	na	na	49	6

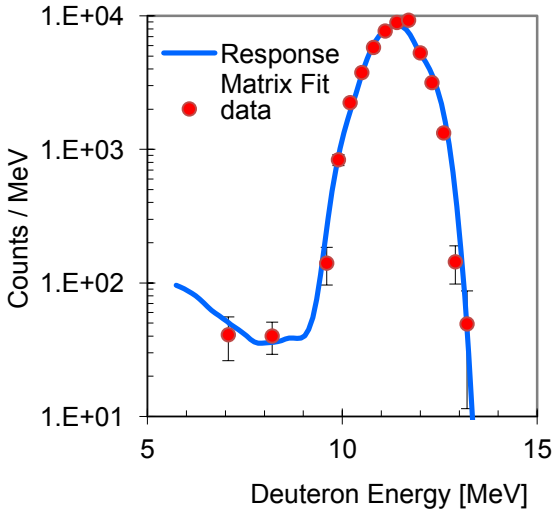

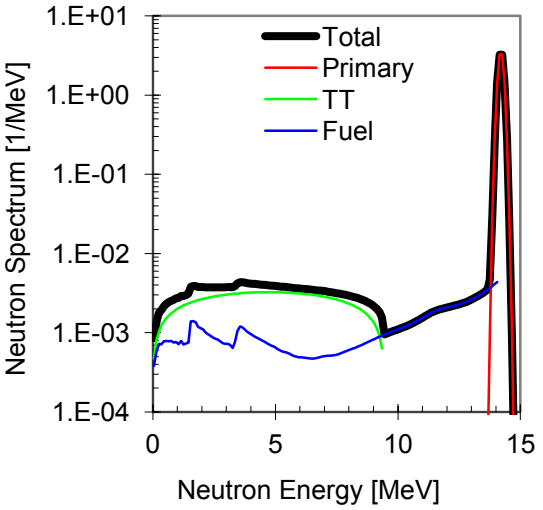

OMEGA shot	Y_{DTn} (X 10^{12})	T_i (keV)	MRS ρR_{tot} (mg/cm^2)	MRS $\sigma_{\rho R}$ (mg/cm^2)	CPS1 ρR_{tot} (mg/cm^2)	CPS1 $\sigma_{\rho R}$ (mg/cm^2)	CPS2 ρR_{tot} (mg/cm^2)	CPS2 $\sigma_{\rho R}$ (mg/cm^2)
55952	4.2	2.1	111	14	171	25	71	9

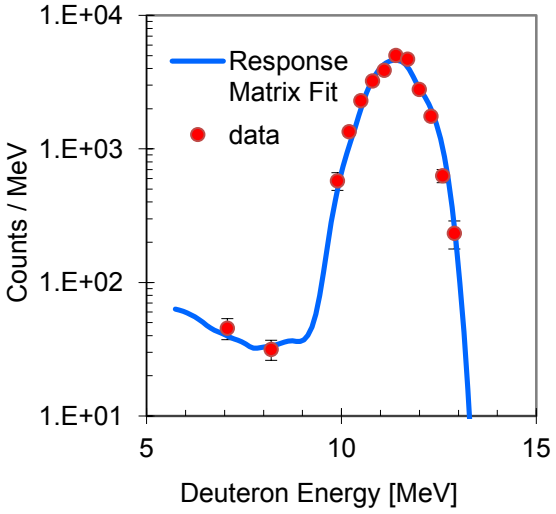

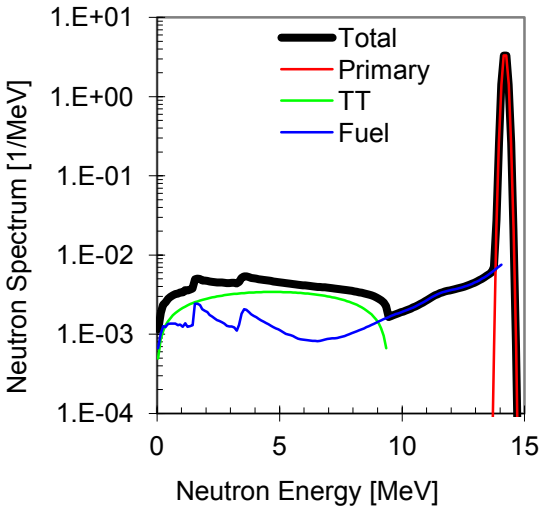

OMEGA shot	Y_{DTn} (X 10^{12})	T_i (keV)	MRS ρR_{tot} (mg/cm^2)	MRS $\sigma_{\rho R}$ (mg/cm^2)	CPS1 ρR_{tot} (mg/cm^2)	CPS1 $\sigma_{\rho R}$ (mg/cm^2)	CPS2 ρR_{tot} (mg/cm^2)	CPS2 $\sigma_{\rho R}$ (mg/cm^2)
56043	2.8	2	179	26	sat	sat	sat	sat

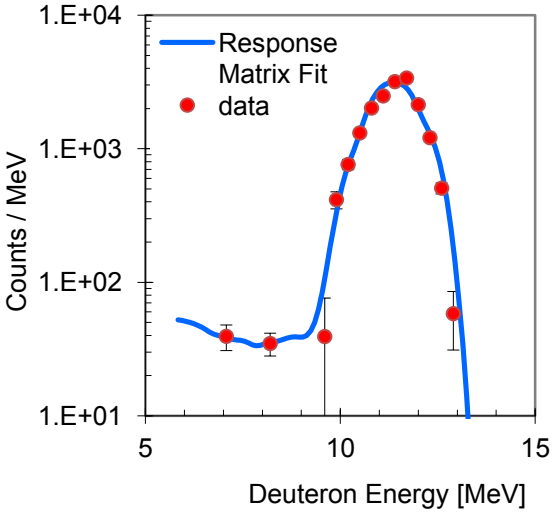

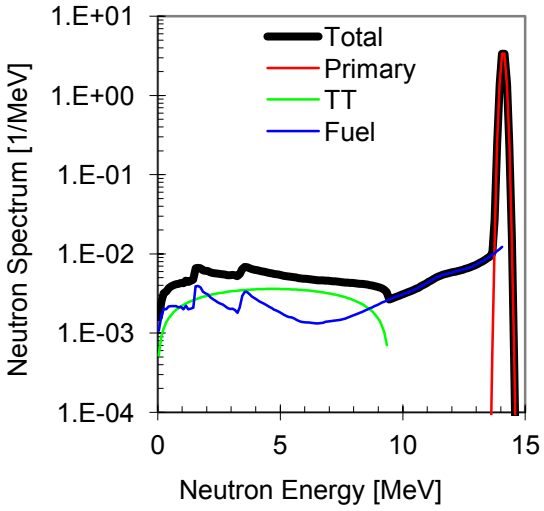

OMEGA shot	Y_{DTn} (X 10^{12})	T_i (keV)	MRS ρR_{tot} (mg/cm^2)	MRS $\sigma_{\rho R}$ (mg/cm^2)	CPS1 ρR_{tot} (mg/cm^2)	CPS1 $\sigma_{\rho R}$ (mg/cm^2)	CPS2 ρR_{tot} (mg/cm^2)	CPS2 $\sigma_{\rho R}$ (mg/cm^2)
56044	1.7	1.6	198	37	sat	sat	sat	sat

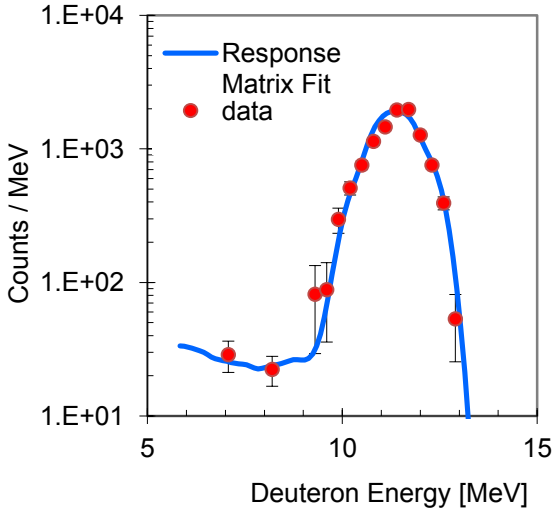

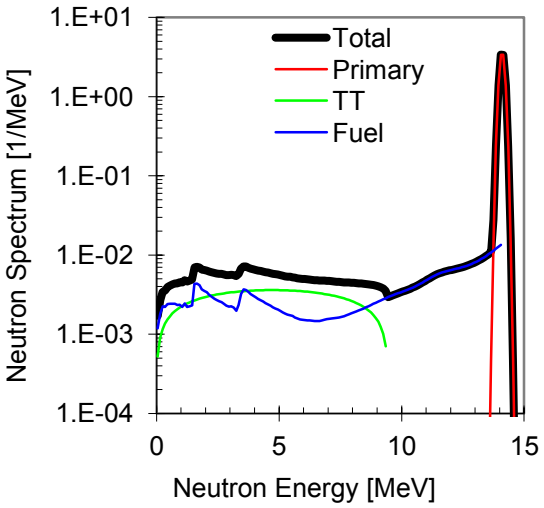

OMEGA shot	Y_{DTn} (X 10^{12})	T_i (keV)	MRS ρR_{tot} (mg/cm^2)	MRS $\sigma_{\rho R}$ (mg/cm^2)	CPS1 ρR_{tot} (mg/cm^2)	CPS1 $\sigma_{\rho R}$ (mg/cm^2)	CPS2 ρR_{tot} (mg/cm^2)	CPS2 $\sigma_{\rho R}$ (mg/cm^2)
56046	2.2	1.9	168	31	sat	sat	sat	sat

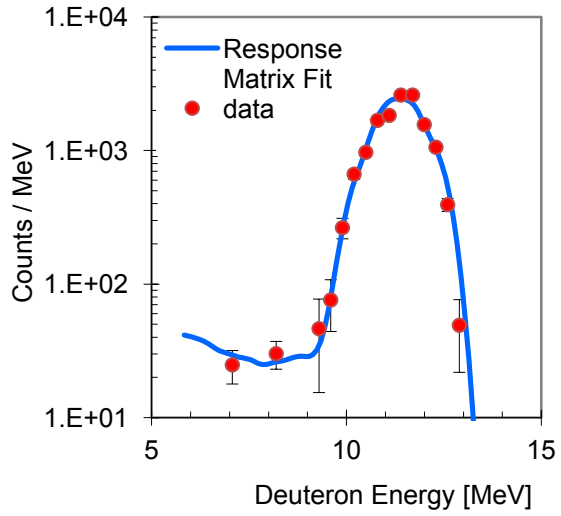

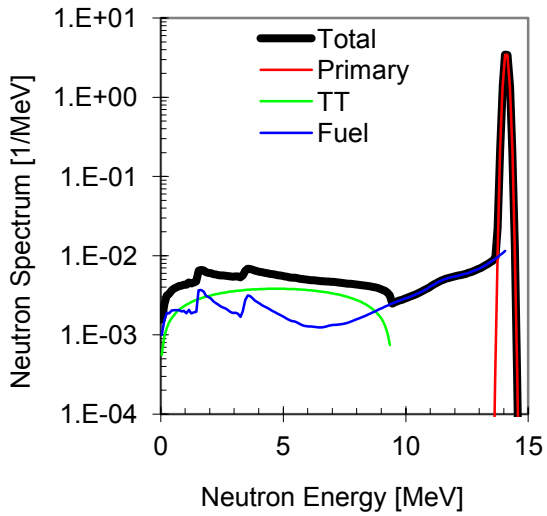

OMEGA shot	Y_{DTn} (X 10^{12})	T_i (keV)	MRS ρR_{tot} (mg/cm^2)	MRS $\sigma_{\rho R}$ (mg/cm^2)	CPS1 ρR_{tot} (mg/cm^2)	CPS1 $\sigma_{\rho R}$ (mg/cm^2)	CPS2 ρR_{tot} (mg/cm^2)	CPS2 $\sigma_{\rho R}$ (mg/cm^2)
57482	3.0	2.1	215	21	sat	sat	sat	sat

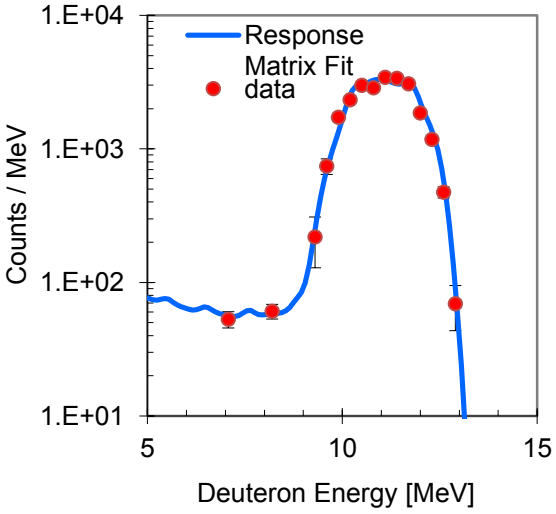

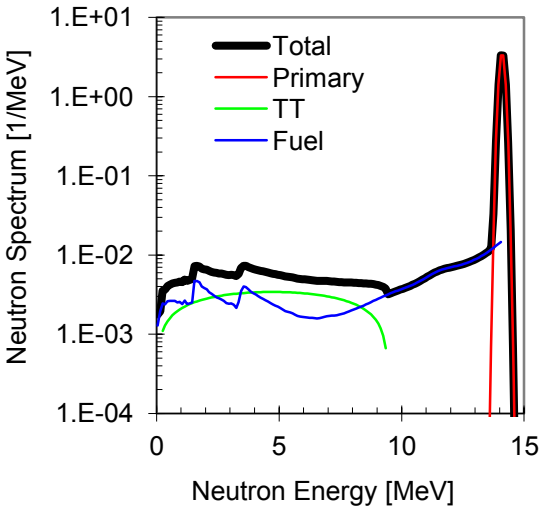

OMEGA shot	Y_{DTn} (X 10^{12})	T_i (keV)	MRS ρR_{tot} (mg/cm^2)	MRS $\sigma_{\rho R}$ (mg/cm^2)	CPS1 ρR_{tot} (mg/cm^2)	CPS1 $\sigma_{\rho R}$ (mg/cm^2)	CPS2 ρR_{tot} (mg/cm^2)	CPS2 $\sigma_{\rho R}$ (mg/cm^2)
58197	2.3	1.8	178	50	160	24	178	50

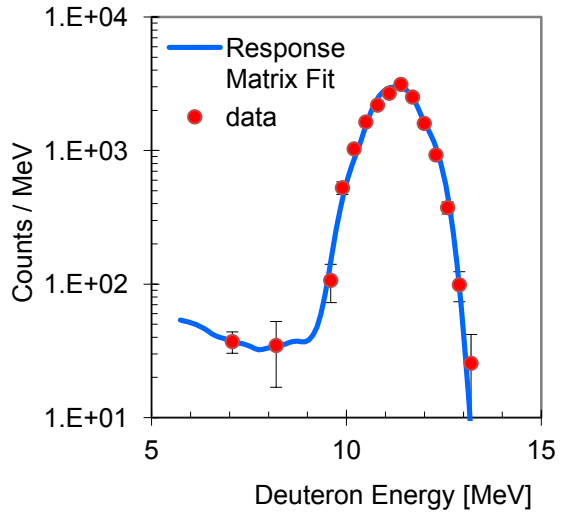

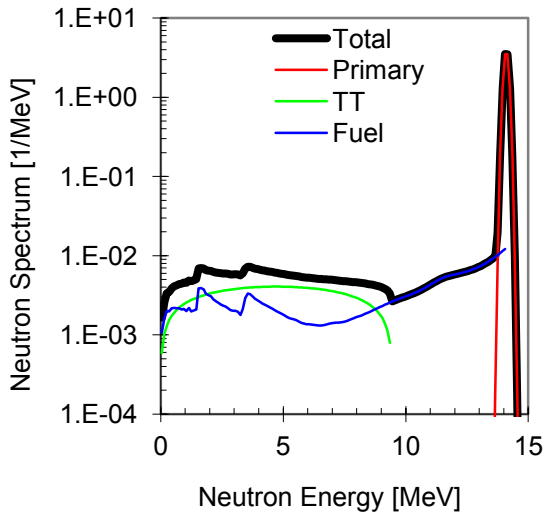

OMEGA shot	Y_{DTn} (X 10^{12})	T_i (keV)	MRS ρR_{tot} (mg/cm^2)	MRS $\sigma_{\rho R}$ (mg/cm^2)	CPS1 ρR_{tot} (mg/cm^2)	CPS1 $\sigma_{\rho R}$ (mg/cm^2)	CPS2 ρR_{tot} (mg/cm^2)	CPS2 $\sigma_{\rho R}$ (mg/cm^2)
58288	1.6	1.53	216	36	167	26	sat	sat

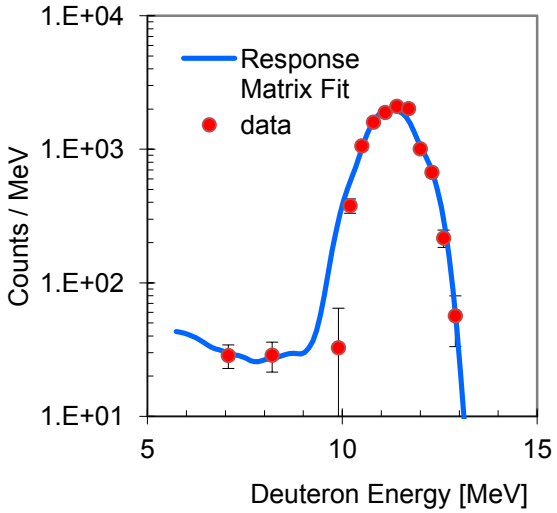

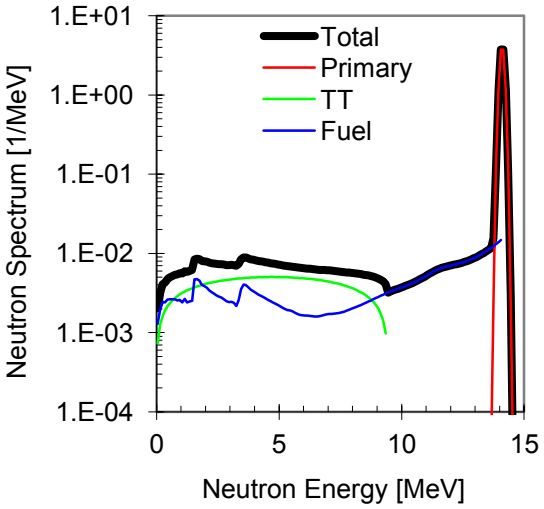

OMEGA shot	Y_{DTn} (X 10^{12})	T_i (keV)	MRS ρR_{tot} (mg/cm^2)	MRS $\sigma_{\rho R}$ (mg/cm^2)	CPS1 ρR_{tot} (mg/cm^2)	CPS1 $\sigma_{\rho R}$ (mg/cm^2)	CPS2 ρR_{tot} (mg/cm^2)	CPS2 $\sigma_{\rho R}$ (mg/cm^2)
58970	1.9	1.98	114	21	143	22	49	12

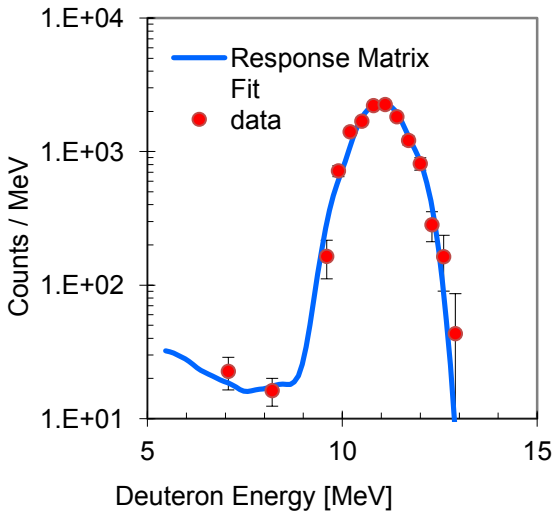

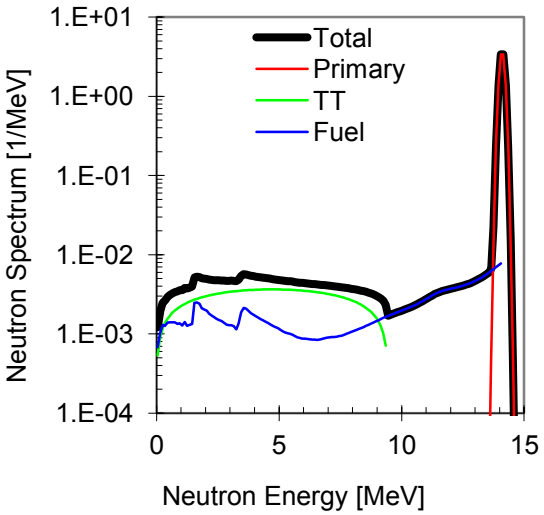

Appendix D– NIF DSn Experimental Data Summary

Summary of NIF Cryogenic DT and THD implosions diagnosed by the MRS:

NIF shot	MRS Y_{DTn} (X 10^{14})	MRS σ_{Yn} (%)	T_i (keV)	σ_{Ti} (keV)	MRS DSR (%)	DSR σ (%)	MRS ρR_{tot} (g/cm^2)	MRS $\sigma_{\rho R}$ (g/cm^2)
N110201	1.1	4.5	3.5	0.1	2.4	0.3	0.48	0.06
N110212	1.25	4.5	3.6	0.1	2.8	0.31	0.56	0.06
N110603	0.642	4.7	2.6	0.2	4.8	0.55	0.96	0.11
N110615	4.38	4.36	3.4	0.1	4	0.25	0.80	0.05
N110620	4.14	4.36	4.3	0.2	4.9	0.29	0.97	0.06
N110904	4.4	4.37	3.5	0.2	5.0	0.29	1.00	0.06
N110908	5.67	4.35	3.5	0.2	5.0	0.27	1.01	0.05

NIF shot	MRS Y_{DTn} (X 10^{14})	MRS σ_{Yn} (%)	T_i (keV)	σ_{Ti} (keV)	MRS DSR (%)	DSR σ (%)	MRS ρR_{tot} (g/cm^2)	MRS $\sigma_{\rho R}$ (g/cm^2)
N110201	1.1	4.5	3.5	0.1	2.4	0.3	0.48	0.06

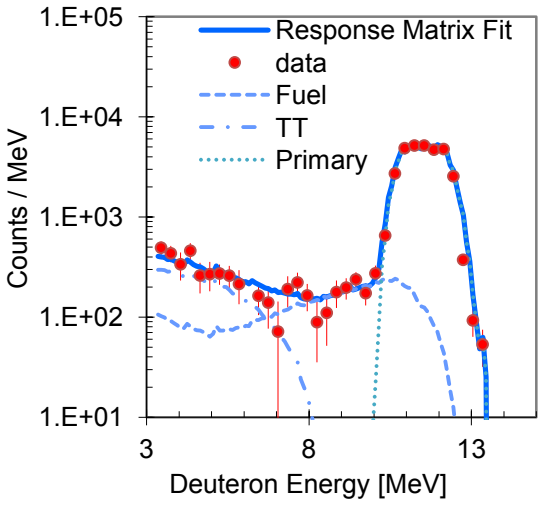

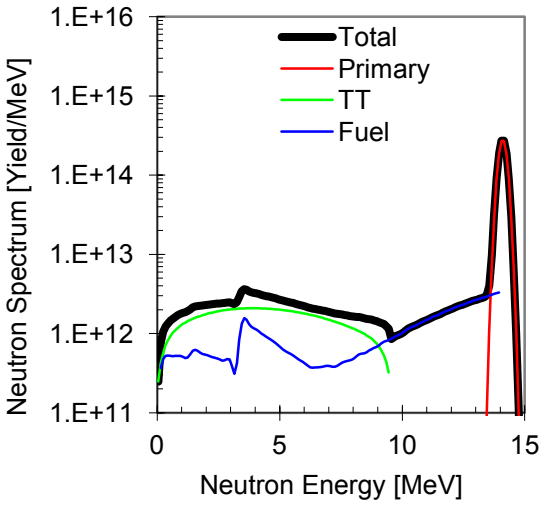

NIF shot	MRS Y_{DTn} (X 10^{14})	MRS σ_{Yn} (%)	T_i (keV)	σ_{Ti} (keV)	MRS DSR (%)	DSR σ (%)	MRS ρR_{tot} (g/cm^2)	MRS $\sigma_{\rho R}$ (g/cm^2)
N110212	1.25	4.5	3.6	0.1	2.8	0.3108	0.56	0.06216

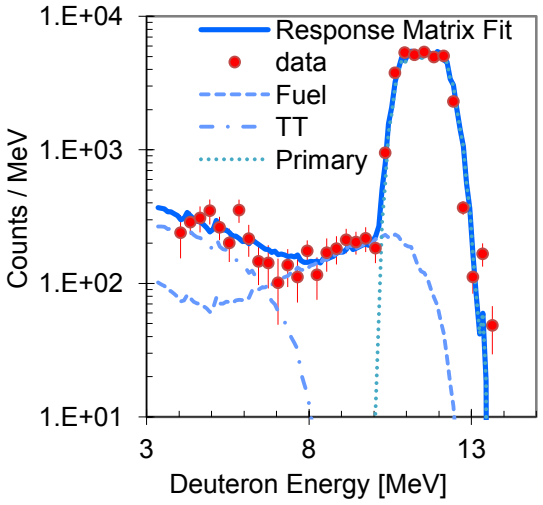

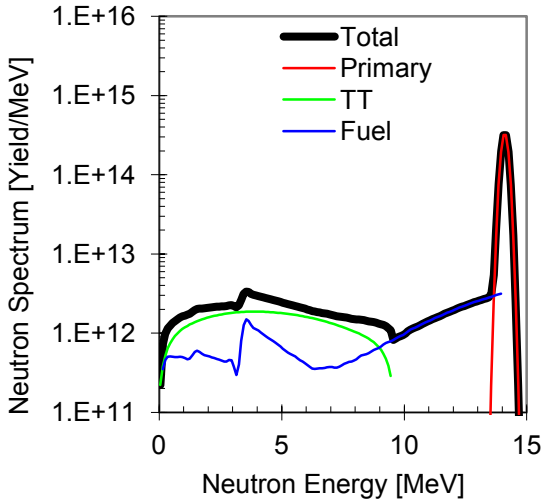

NIF shot	MRS Y_{DTn} (X 10^{14})	MRS σ_{Yn} (%)	T_i (keV)	σ_{Ti} (keV)	MRS DSR (%)	DSR σ (%)	MRS ρR_{tot} (g/cm^2)	MRS $\sigma_{\rho R}$ (g/cm^2)
N110603	0.642	4.7	2.6	0.2	4.8	0.5472	0.96	0.10944

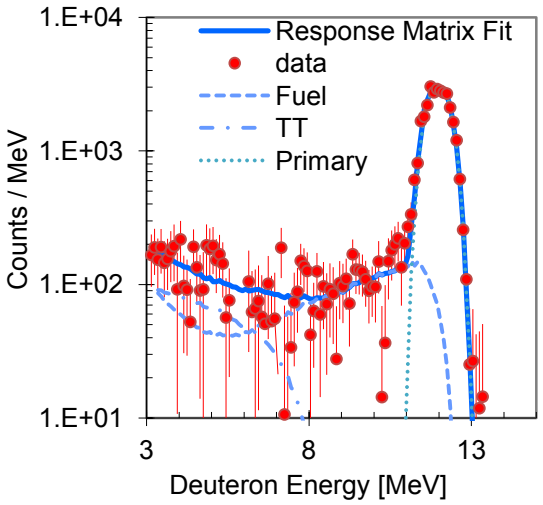

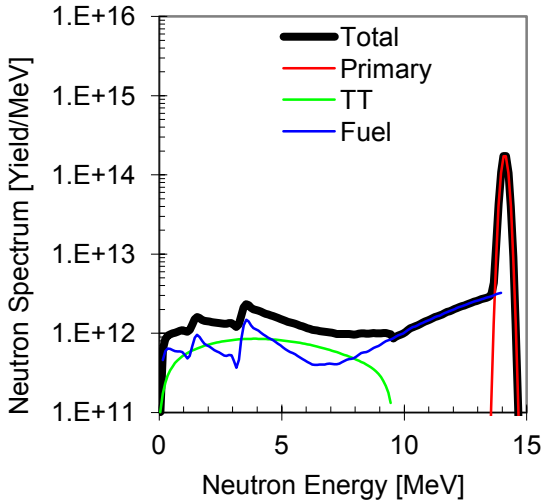

NIF shot	MRS Y_{DTn} (X 10^{14})	MRS σ_{Yn} (%)	T_i (keV)	σ_{Tt} (keV)	MRS DSR (%)	DSR σ (%)	MRS ρR_{tot} (g/cm^2)	MRS $\sigma_{\rho R}$ (g/cm^2)
N110615	4.38	4.36	3.4	0.1	4	0.2544	0.8	0.05088

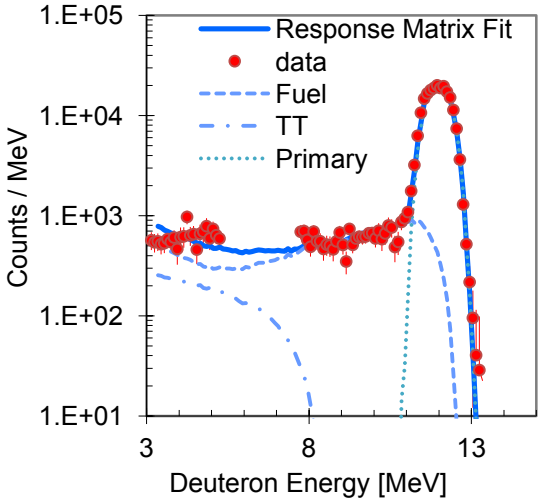

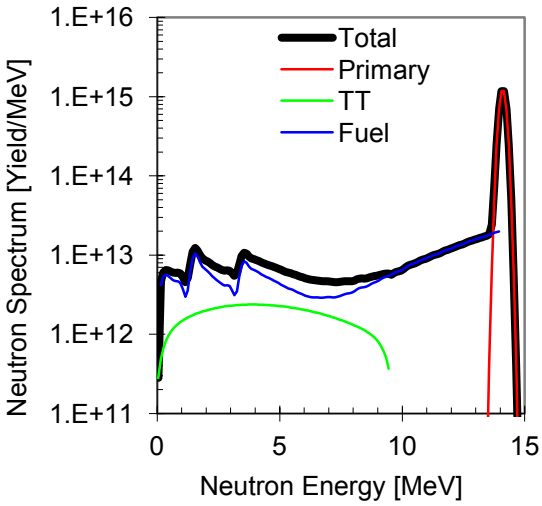

NIF shot	MRS Y_{DTn} (X 10^{14})	MRS σ_{Yn} (%)	T_i (keV)	σ_{Tt} (keV)	MRS DSR (%)	DSR σ (%)	MRS ρR_{tot} (g/cm^2)	MRS $\sigma_{\rho R}$ (g/cm^2)
N110620	4.14	4.36	4.3	0.2	4.87	0.2878	0.974	0.057563

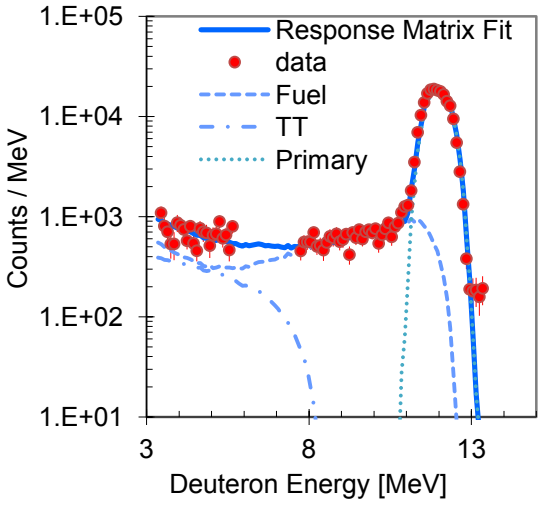

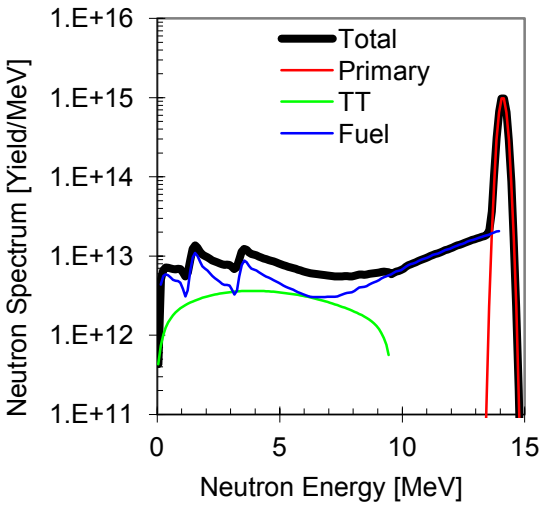

NIF shot	MRS Y_{DTn} (X 10^{14})	MRS σ_{Yn} (%)	T_i (keV)	σ_{T_i} (keV)	MRS DSR (%)	DSR σ (%)	MRS ρR_{tot} (g/cm^2)	MRS $\sigma_{\rho R}$ (g/cm^2)
N110904	4.4	4.37	3.5	0.2	5.02	0.2917	1.004	0.058332

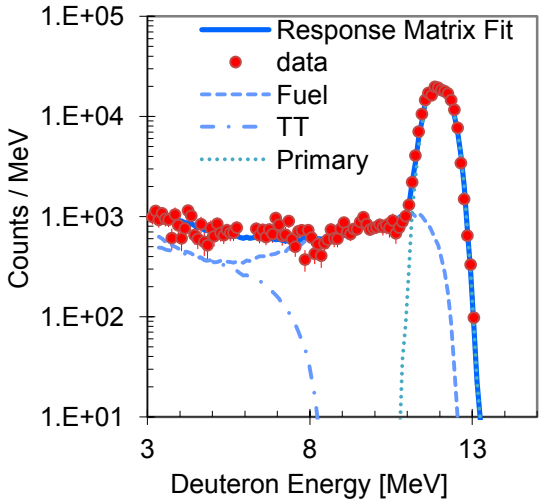

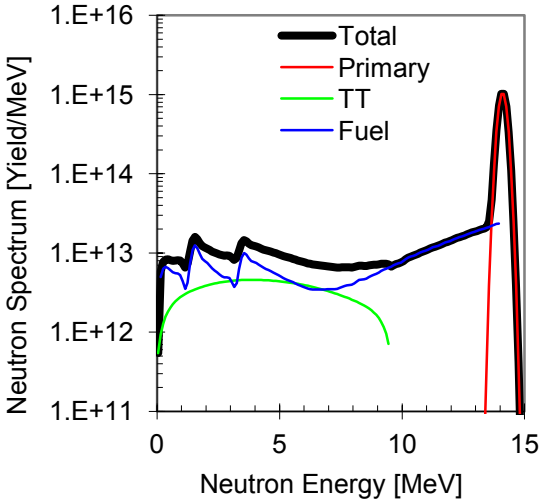

NIF shot	MRS Y_{DTn} (X 10^{14})	MRS σ_{Yn} (%)	T_i (keV)	σ_{T_i} (keV)	MRS DSR (%)	DSR σ (%)	MRS ρR_{tot} (g/cm^2)	MRS $\sigma_{\rho R}$ (g/cm^2)
N110908	5.67	4.35	3.5	0.2	5.03	0.2746	1.006	0.054928

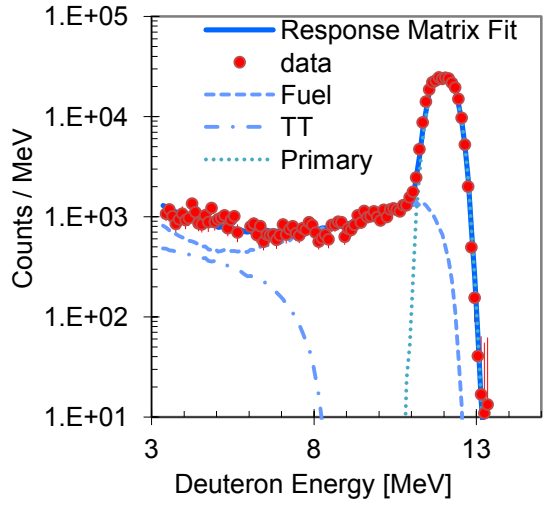

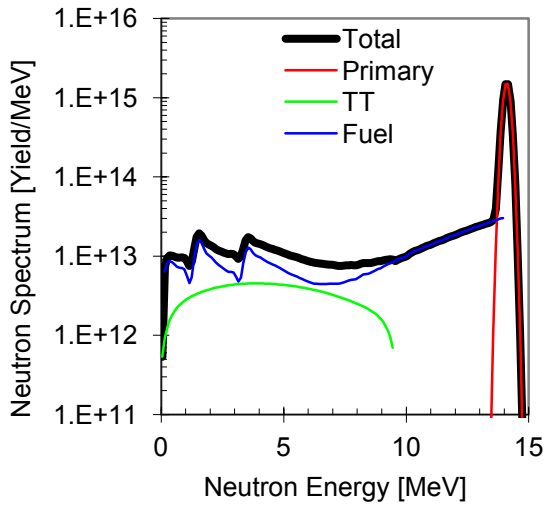

Appendix E - OMEGA TT Experimental Data Summary

OMEGA integrated shot numbers	Target Gas(atm)Shell[μm]	Y_{DTn} (X 10^{13})	T_i (keV)	E_{CM} (keV)	$Y_{TT\text{-}rx}/Y_{DT\text{-}rx}$ (X 10^{-3})
55983-55989	DT(17)CH19.7]	3.8	3.5	16.5 ± 1.6	3.7 ± 0.7
54472-54474	DT(17)CH[19.6]	3.2	3.8	17.5 ± 1.5	4.0 ± 0.7
58157-58159,58161-58162	DT(15)13CH[15]	7.4	5.1	21.3 ± 1.4	5.1 ± 0.7
55074-55083	DT(17.5)CH[15.8]	15.8	5.3	21.7 ± 1.4	4.1 ± 0.5
58165,58209-58210	DT(18.9)CH[14.1]	5.0	5.6	22.5 ± 1.4	4.8 ± 0.8
58163, 58208	DT(10.1)SiO2[3.8]	13.2	7.4	27.3 ± 1.2	5.6 ± 0.7
55641-55647	DT(12.1) CD[9.5]	25.5	8.0	28.7 ± 1.2	6.2 ± 0.5

OMEGA integrated shot numbers	Target Gas(atm)Shell[mm]	Y_{DTn} (X 10^{13})	Ti (keV)	E_{CM} (keV)	$Y_{TT\text{-}rx}/Y_{DT\text{-}rx}$ (X 10-3)
55074-55083	DT(17.5)CH[15.8]	15.8	5.3	21.7 ± 1.4	4.1 ± 0.5

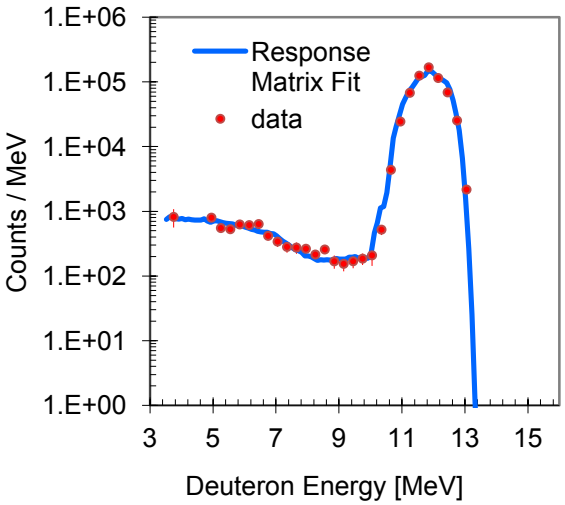

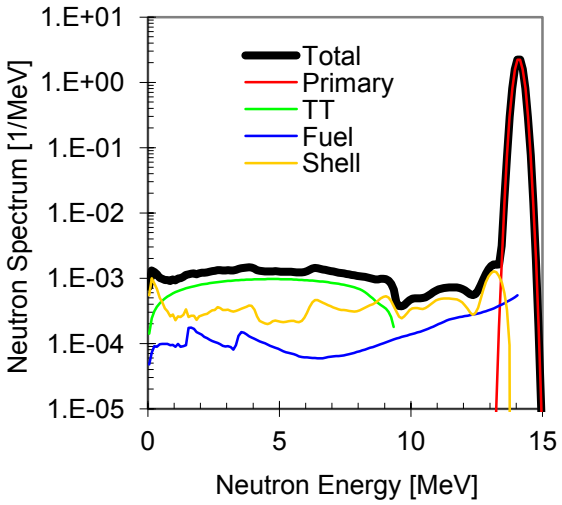

OMEGA integrated shot numbers	Target Gas(atm)Shell[mm]	Y_{DTn} (X 10^{13})	Ti (keV)	E_{CM} (keV)	$Y_{TT\text{-}rx}/Y_{DT\text{-}rx}$ (X 10-3)
55641-55647	DT(12.1) CD[9.5]	25.5	8.0	28.7 ± 1.2	6.2 ± 0.5

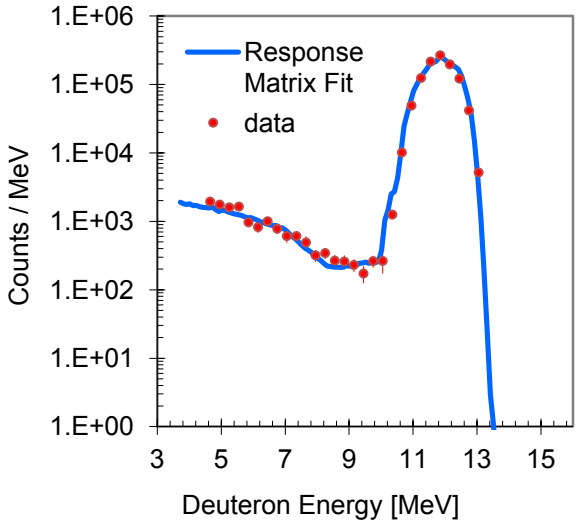

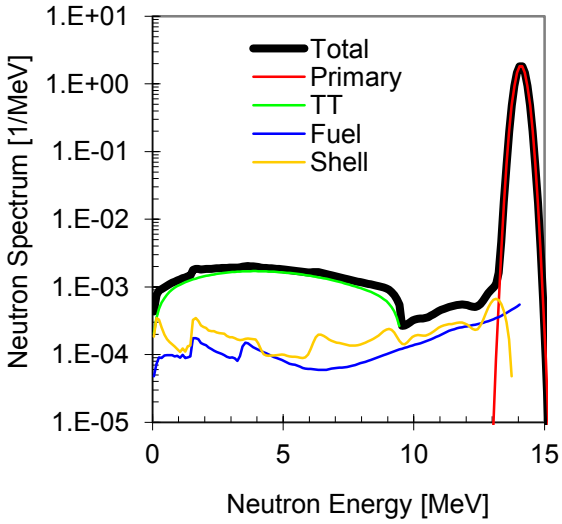

OMEGA integrated shot numbers	Target Gas(atm)Shell[mm]	Y_{DTn} (X 10^{13})	Ti (keV)	E_{CM} (keV)	$Y_{TT\text{-}rx}/Y_{DT\text{-}rx}$ (X 10-3)
58163, 58208	DT(10.1)SiO2[3.8]	13.2	7.4	27.3 ± 1.2	5.6 ± 0.7

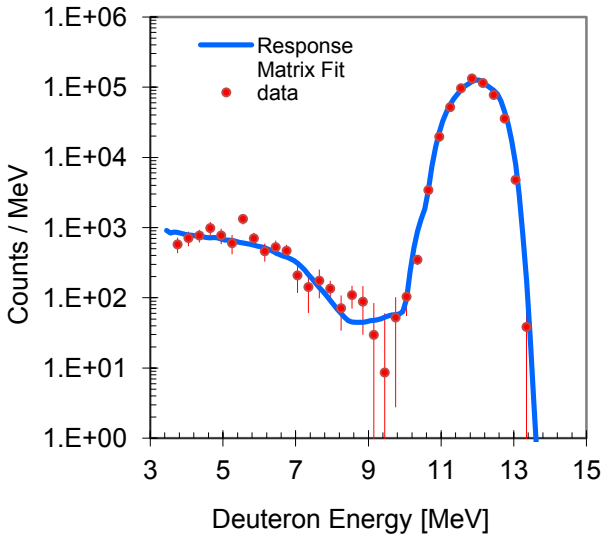

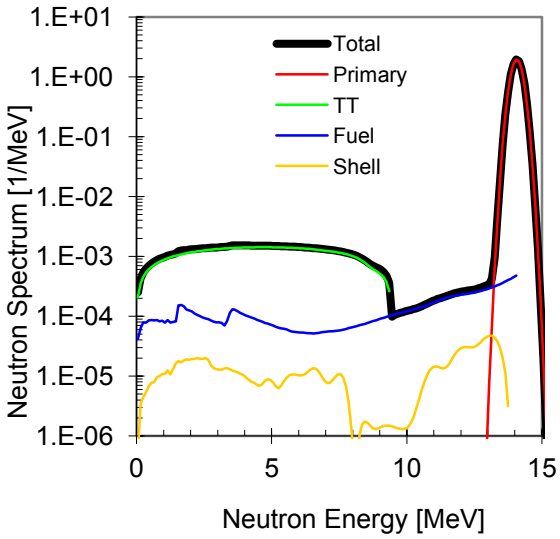

OMEGA integrated shot numbers	Target Gas(atm)Shell[mm]	Y_{DTn} (X 10^{13})	Ti (keV)	E_{CM} (keV)	Y_{TT-rx}/Y_{DT-rx} (X 10-3)
58165,58209-58210	DT(18.9)CH[14.1]	5.0	5.6	22.5 ± 1.4	4.8 ± 0.8

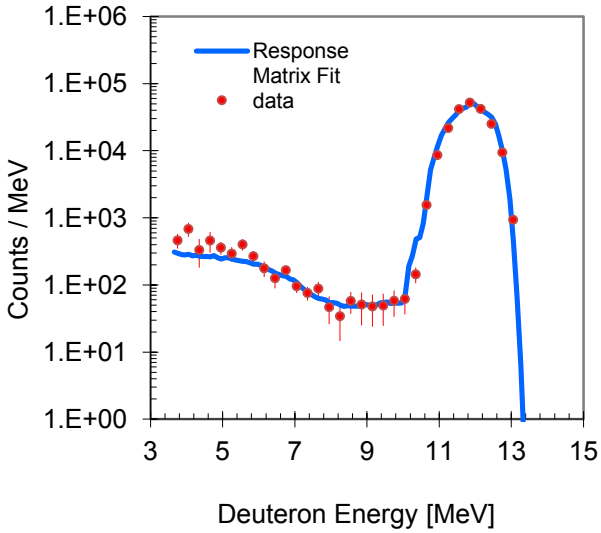

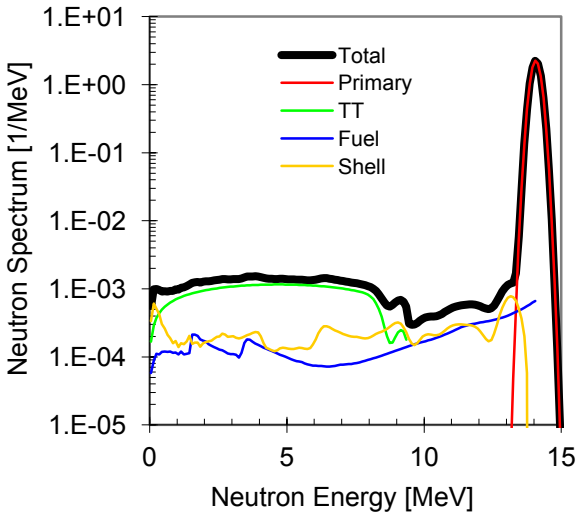

OMEGA integrated shot numbers	Target Gas(atm)Shell[mm]	Y_{DTn} (X 10^{13})	Ti (keV)	E_{CM} (keV)	Y_{TT-rx}/Y_{DT-rx} (X 10-3)
58157-58159.58161-58162	DT(15)13CH[15]	7.4	5.1	21.3 ± 1.4	5.1 ± 0.7

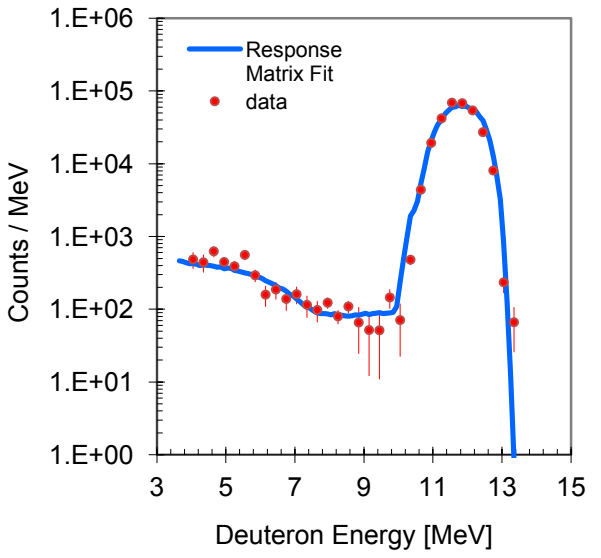

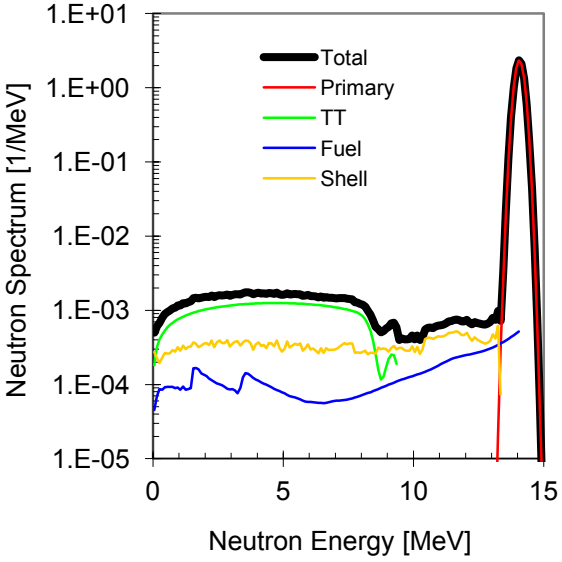

OMEGA integrated shot numbers	Target Gas(atm)Shell[mm]	Y_{DTn} (X 10^{13})	Ti (keV)	E_{CM} (keV)	$Y_{TT\text{-}rx}/Y_{DT\text{-}rx}$ (X 10-3)
55983-55989	DT(17)CH19.7]	3.8	3.5	16.5 ± 1.6	3.7 ± 0.7

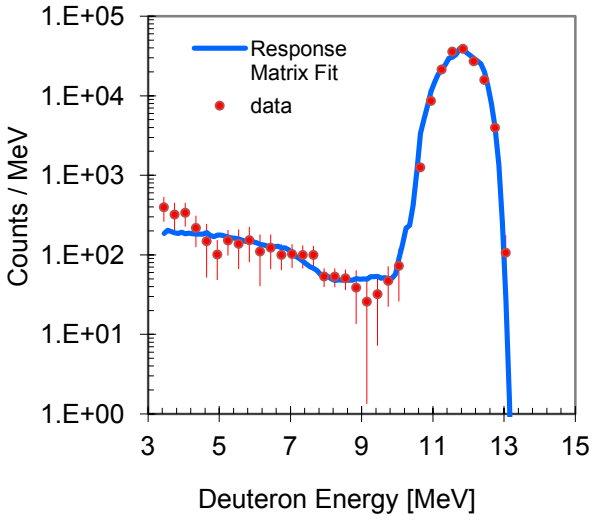

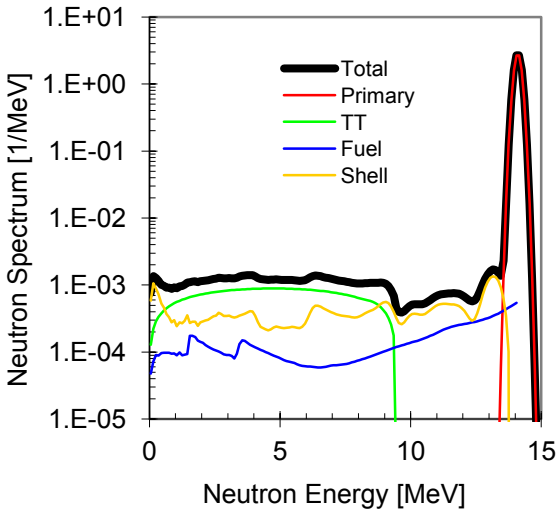

OMEGA integrated shot numbers	Target Gas(atm)Shell[mm]	Y_{DTn} (X 10^{13})	Ti (keV)	E_{CM} (keV)	$Y_{TT\text{-}rx}/Y_{DT\text{-}rx}$ (X 10-3)
54472-54474	DT(17)CH[19.6]	3.2	3.8	17.5 ± 1.5	4.0 ± 0.7

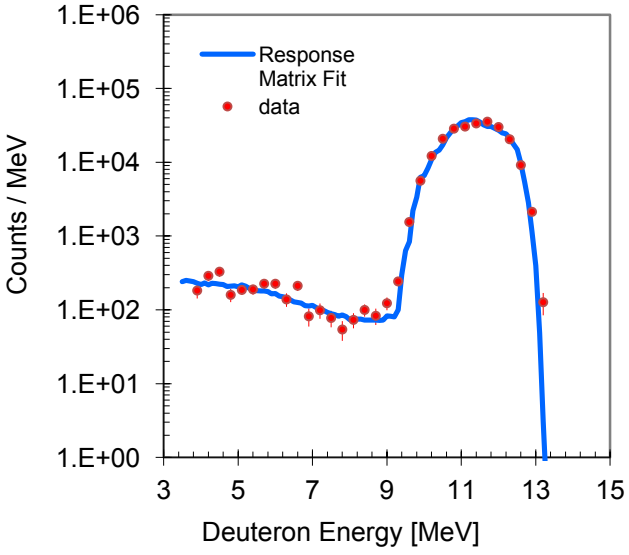

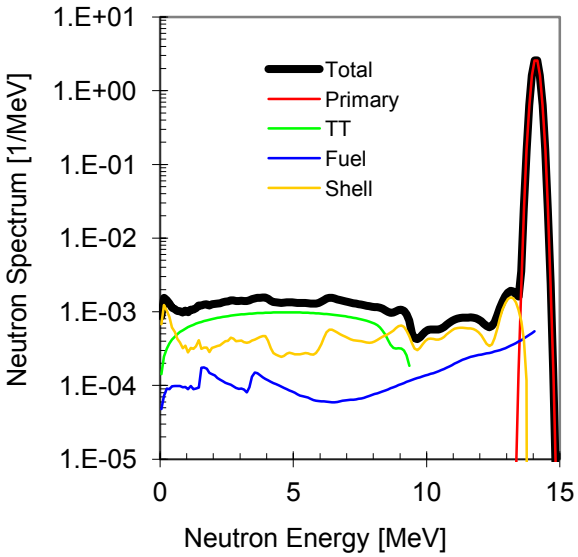

Appendix F – Fitting algorithm for analyzing MRS data

The minimum chi-square fitting method is used throughout this thesis to interpret the measured MRS recoil deuteron spectrum and the neutron spectrum that provides the best fit to the measured spectrum. The details of this fitting algorithm are illustrated in this Appendix. This method was adopted from the paper by Avni et al.[142], but the interested reader is referred to many excellent texts on the subject, such as the texts Bevington,[143] Taylor,[144] and Numerical Recipes.[145] The following example is a from OMEGA shots 55641-55647, described in detail in Chapters 8 and 9.

We can describe the chi-square fitting routine by first defining the chi-square (χ^2) metric

$$\chi^2 = \sum_i^N \frac{\left(y_i - fit(n)_i\right)^2}{\sigma_i^2}. \tag{F-29}$$

Here, N is the number of observables, y_i is the value for each observable, σ_i is the uncertainty for each observable, and $fit(n)_i$ is the model describing the observables, which is a function of n parameters. The number of degrees of freedom (d) is then given by

$$d = N - n. \tag{F-30}$$

If the $fit(n)_i$ requires normalization, the number of degrees of freedom is expressed as $d = N - n - 1$. A best fit is found by minimizing χ^2. The uncertainty in the best-fit parameters of the model can be determined from the variation of χ^2 (or $\Delta\chi^2$) from its minimum (χ_{min}^2), as described in Avni[142] and Bevington[143]. In the case of one fitting parameter, the 1σ uncertainty can be determined by varying the parameter until $\chi^2 = \chi_{min}^2 + 1$ or $\Delta\chi^2=1$ (for inferring uncertainty in more interesting parameters see Bevington[143]).

The reduced chi-square (χ_ν^2) metric is often used to evaluate a model of system and is defined as

$$\chi_\nu^2 = \frac{1}{d}\sum_i^N \frac{\left(y_i - fit(n)_i\right)^2}{\sigma_i^2}. \tag{F-31}$$

On average, χ_ν^2 is ~1 when a model describes the data well. A distribution of χ_ν^2 is expected as a function of d (see Bevington[143] and Taylor).[144] However, as a general rule of thumb a $\chi_\nu^2 >> 1$ indicates a poor model or an underestimated set of observable uncertainties, while $\chi_\nu^2 << 1$ indicates a model that over-fits the data or an overestimated set of observable uncertainties.

An example of a measured recoil deuteron spectrum from OMEGA shots 55641-55647 is depicted in Figure F-13a. The points are the measured data, while the black solid curve represents the best-fit to the data above ~8MeV (at deuteron energies below 8 MeV, the TTn spectrum is the dominating component, as discussed subsequently). Figure F-13b shows the neutron spectrum that best fits the measured recoil deuteron spectrum above ~8MeV. The absolute primary DT spectrum (red dashed curve) was determined by using the MRS detection efficiency and the number of observed counts in the primary peak (see Chapter 5). The DSn spectrum was adjusted in intensity (spectral shape fixed) until best fit to the solid data points was found in the deuteron-energy range 8-9.5 MeV (or when the minimum χ^2 was found). As shown in Figure F-13c, the best fit was found for a ρR_{tot} of 35±5mg/cm^2.

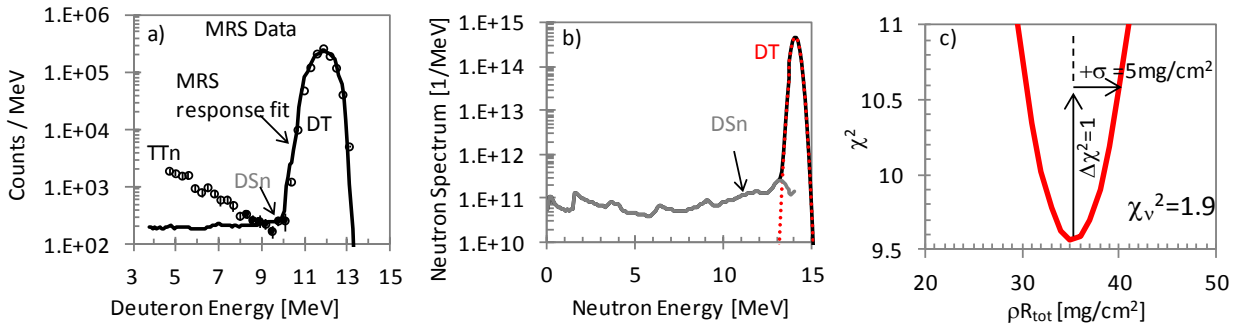

Figure F-13: a) Example recoil deuteron spectrum from OMEGA shots 55641-55647. The open and solid data points are the measured data, while the solid black data points are the data used in the fit to the DSn spectrum. The solid line represents the best-fit to the data and has been normalized by Y_{DT}. b) Best-fit neutron spectrum to the recoil deuteron spectrum in part a, excluding the TTn which is described in the subsequent figure. c) χ^2 distribution as a function of the fit parameter ρR_{tot}. The best fit ρR_{tot} = 35±5mg/cm^2.

After obtaining the best-fit DSn spectrum, the TTn spectrum can be determined, as shown in Figure F-14. A modeled TTn spectrum was used and adjusted in intensity (spectral shape fixed) to find the best fit to the measured data points below 8 MeV in Figure F-14a. Figure F-14b shows the neutron spectrum that best-fits the whole MRS measured spectrum. Figure F-14c shows the χ^2 as a function of the fit parameter Y_{TT}/Y_{DT}, which indicate that a best fit was found for a Y_{TT}/Y_{DT} of $(6.2 \pm 0.5)\times10^{-3}$.

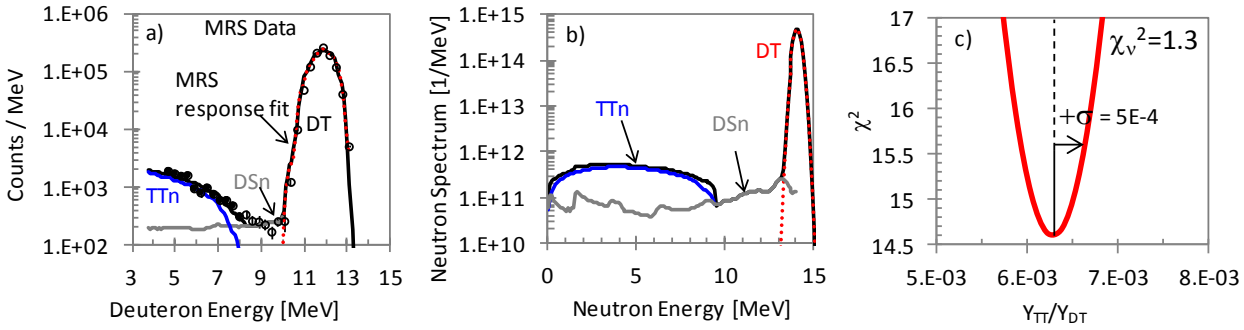

Figure F-14: a) Measured and modeled MRS recoil deuteron spectrum for OMEGA shots 55641-55647. b) Modeled neutron spectrum, which now includes the TTn, DSn, and primary components. The best-fit TTn spectrum was obtained from the solid data points. c) χ^2 as a function of the fit parameter Y_{TT}/Y_{DT}. The best fit was found for a Y_{TT}/Y_{DT} of $(6.2 \pm 0.5)\times10^{-3}$.

Appendix G - Description of coincidence counting analysis program

The coincidence counting analysis of the MRS data (described in detail in Chapter 6) is performed using a developed windows based C++ analysis program. The current version of this program and its main algorithm are described briefly in this section.

The CCT program reads binary scan files produced by the scan software developed by Seguin et al.[48] primarily for the processing of CR-39 data taken at OMEGA and the NIF. A screen capture of the user interface of CCT analysis program is shown Figure G-15. The CCT analysis program allows the user to plot coincidence distributions as a function of track-contrast, diameter, eccentricity, x and y coordinate distributions, and relative dx and dy locations (front coordinate minus back coordinates).

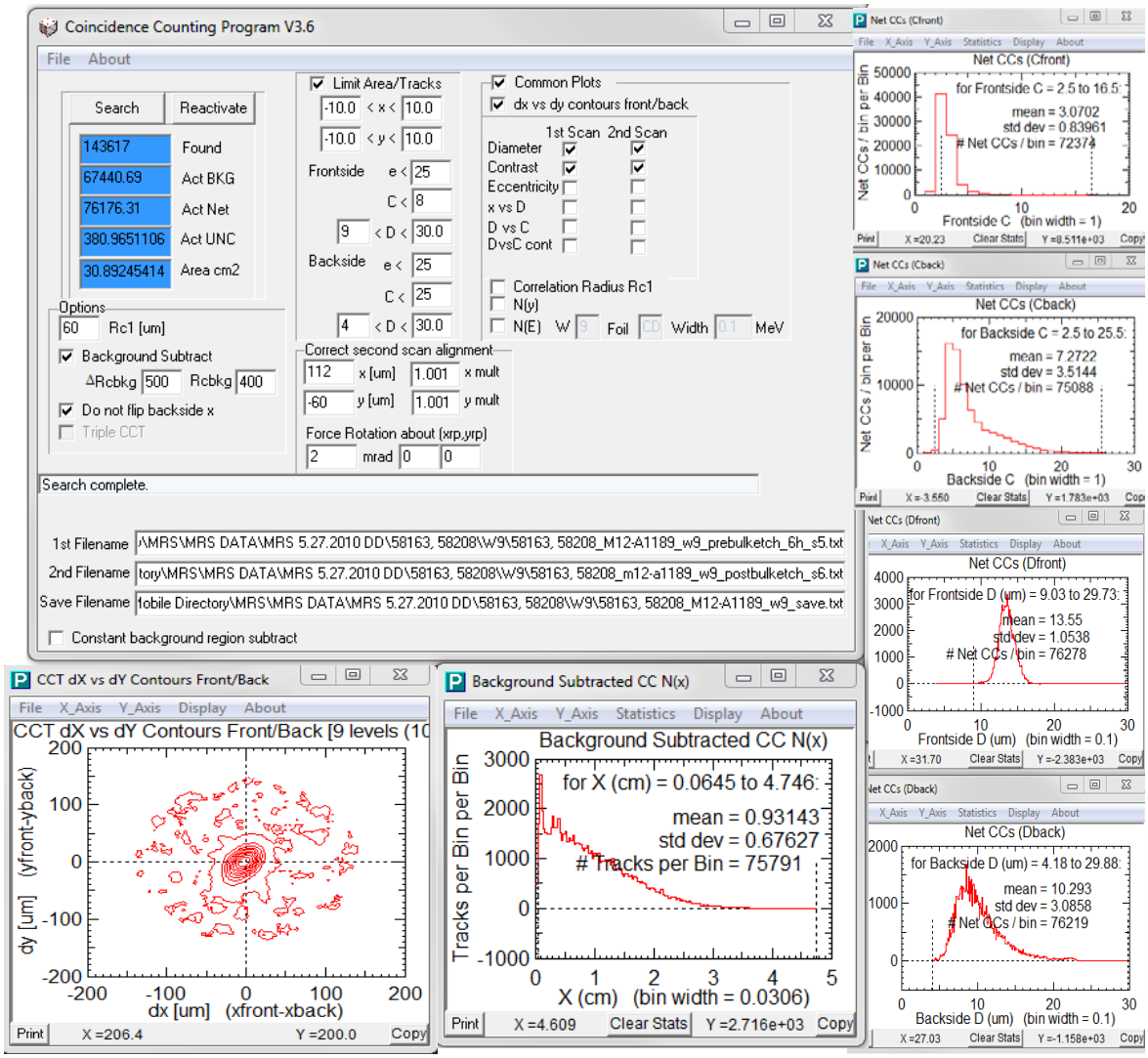

Figure G-15: User interface of the coincidence counting program. Several plots of diameter, contrast, dx/dy, and N(x) distribution of found coincidences are also shown.

The basic algorithm behind the CCT analysis program is as follows. The program opens the binary scan files, and then applies specified constraints, which allows regions of the CR-39 to be isolated spatially or cuts to be applied in contrast, diameter, and eccentricity. The coordinate system of the backside scan is then realigned using pin mark fiducials, as described in Chapter 6. A search for a correlated back-side track within the search radius (R_c) is performed for each found front-side track that meets the constraints. Every pair of correlated front-side and back-side tracks are recorded. When the search for correlated tacks is finished, several plots of the coincidence distribution are generated.

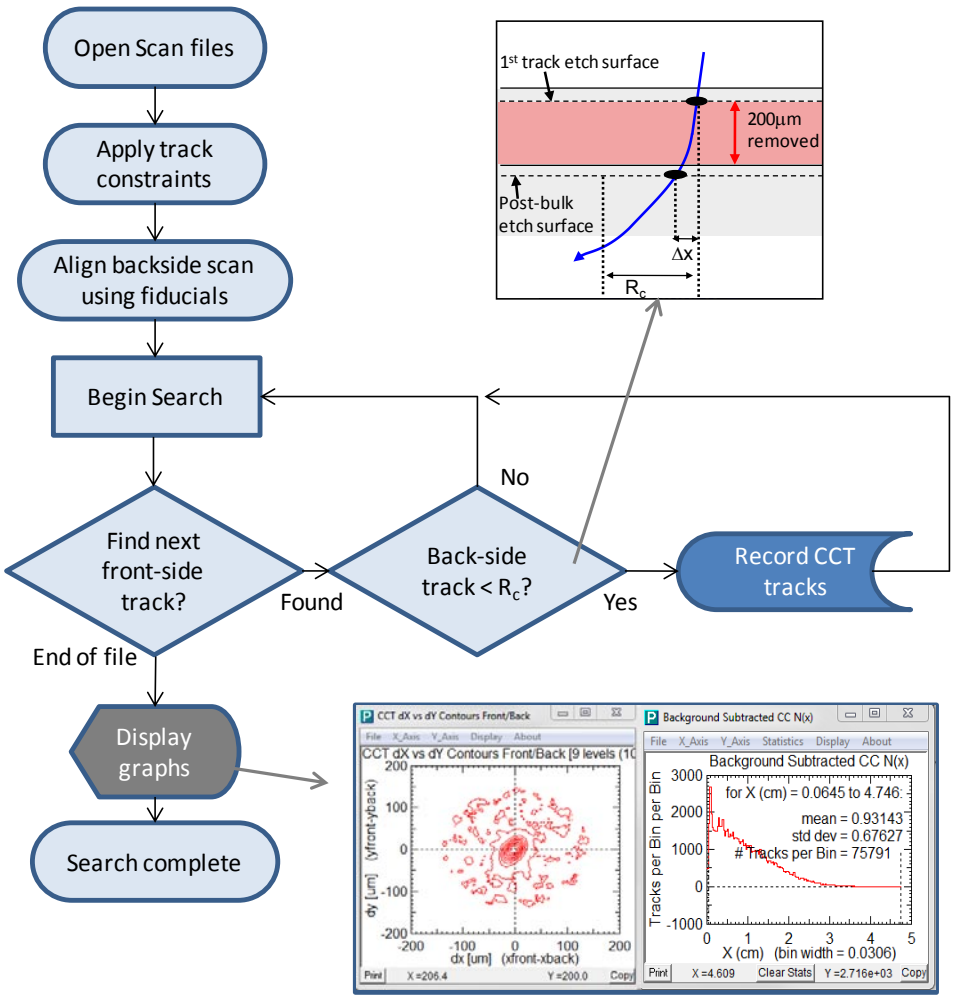

Figure G-16: Flow diagram describing the coincidence counting program algorithm.

Appendix H- LILAC simulations of select OMEGA implosions

Hydrodynamic simulations are often used to study ICF implosions or design ICF implosion experiments. These simulations provide detailed information of the implosion dynamics (such as time and space evolving density, temperature, and burn profiles). The following section shows three types of simulations relevant to the OMEGA data shown in thesis: simulation of a shock-driven exploding pusher, an ablative-driven plastic, and a low-adiabat cryogenic implosion. These simulations were performed using the 1D hydrodynamics code LILAC (LILAC simulations performed by P. B. Radha, LLE).[31]

In particular, this appendix presents numerous LILAC simulated capsule implosion parameters such as thermonuclear yield, n_i, T_i, Pressure, velocity, and acceleration as a function of time. Each parameter is color-mapped and superimposed on the simulated capsule radius versus time, described in detail in Figure 7-5. This allows the evolution of each parameter, in space and time, to be more easily visualized. In some cases, a parameter may undergo rapid change near stagnation. In these cases, a $\log_{10}$ plot is also included to better show the evolution.

H.1 Shock-driven exploding pusher

In a shock-driven exploding pusher, the capsule has typically a thin glass SiO_2 or a thin plastic ablator. This thin shell is completely ablated away, driving a single strong shock into the gas. This shock compresses the gas and converges to the center where it rebounds. The rebounding shock compresses gas once again and a shock-burn is produced. Shot 58163 is an example of such an implosion, which utilized a 10.1 atm DT gas-filled SiO_2 capsule with an 804 μm radius shell, which was 3.9μm thick. The short hand notation for this target type is: DT(10.1)SiO2[3.9]. The 1D LILAC simulation for shot 58163 is shown in Figure H-17 through Figure H-21. The lower plot in Figure H-17 shows the simulated trajectories of different fluid elements (of fixed mass) during the implosion. The thick black curve at largest radius is the outer boundary SiO_2 shell. The second thick black curve is the DT gas boundary with the SiO_2 shell.

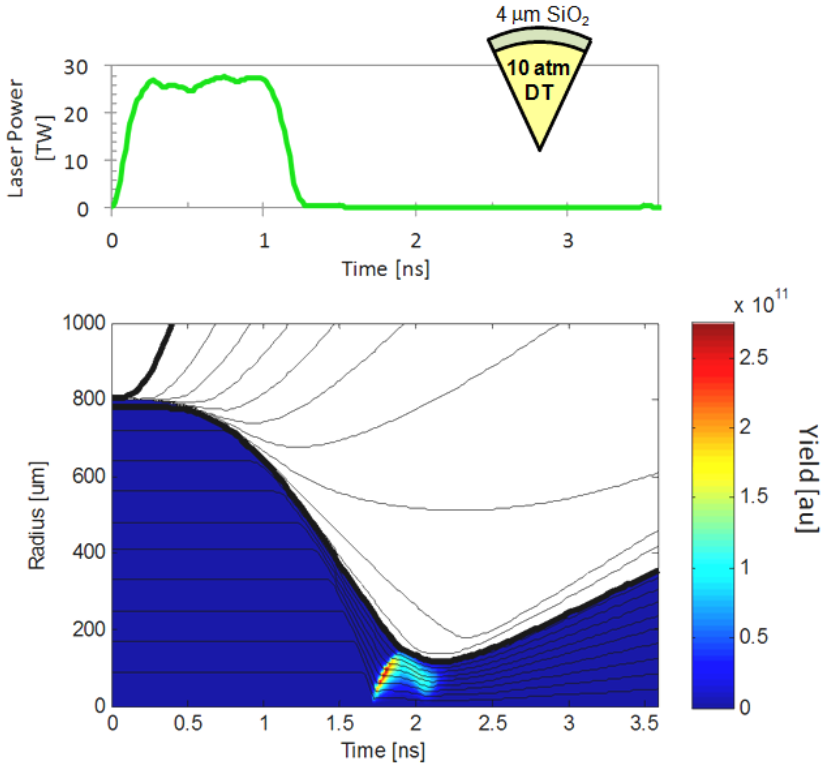

Figure H-17: Top: Laser pulse shape for the exploding pusher shot 58163, showing the laser power in TW, as a function of time. Bottom: Simulated capsule radius as a function of time. The burn profile as a function of radius and time is also plotted.

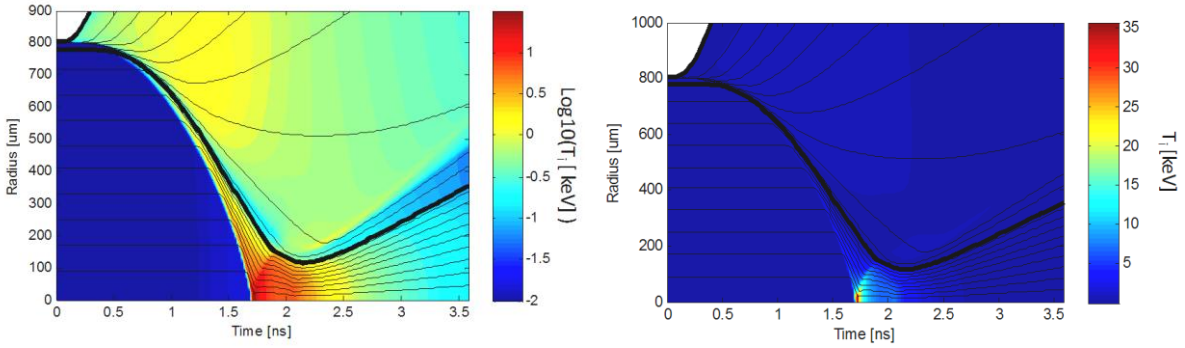

Figure H-18: Simulated ion temperature profile as a function of radius and time for shot 58163.

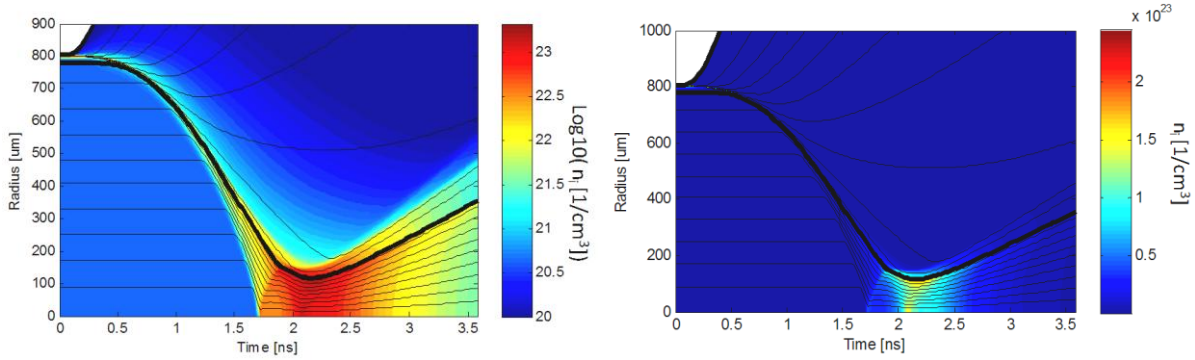

Figure H-19: Simulated ion density profile as a function of radius and time for shot 58163.

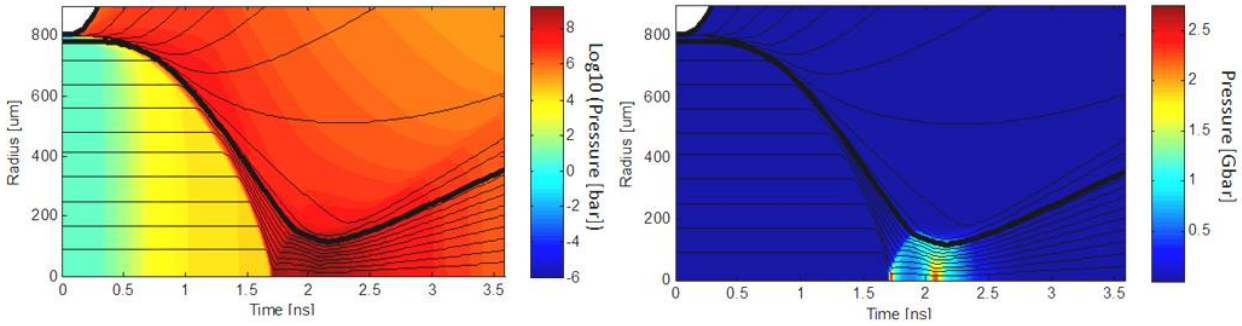

Figure H-20: Simulated pressure profile as a function of radius and time for shot 58163.

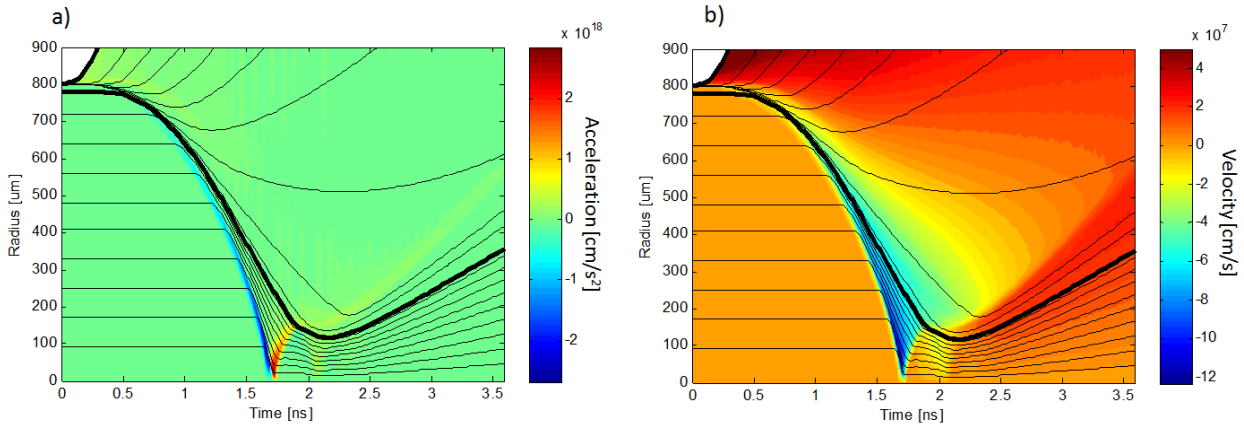

Figure H-21: Simulated acceleration (a) and velocity (b) profiles as a function of radius and time for shot 58163.

H.2 Ablatively-driven plastic shell implosion

In an ablatively-driven implosion, the laser ablates the outer parts of the plastic shell, forcing the remaining shell to implode inwards. The imploding shell compresses and heats the central gas through *pdV* work, producing a hot-spot. Shot 55983 utilized a 17atm DT gas-filled CH capsule, with a 446 μm radius shell, which was 19.8μm thick. The short hand notation for this target type is: DT(17)Ch[19.8]. In this type of the implosion, a thicker plastic shell is used to compress and heat the central gas. The 1D LILAC simulation for shot 55983 is shown in Figure H-22 through Figure H-26. The lower plot in Figure H-22 shows the simulated trajectories of different fluid elements (of fixed mass) during the implosion. The thick black curve at largest radius is the outer thin-Al coating. The second thick black curve is the CH-shell boundary, and the third inner-most thick black curve is the DT gas boundary.

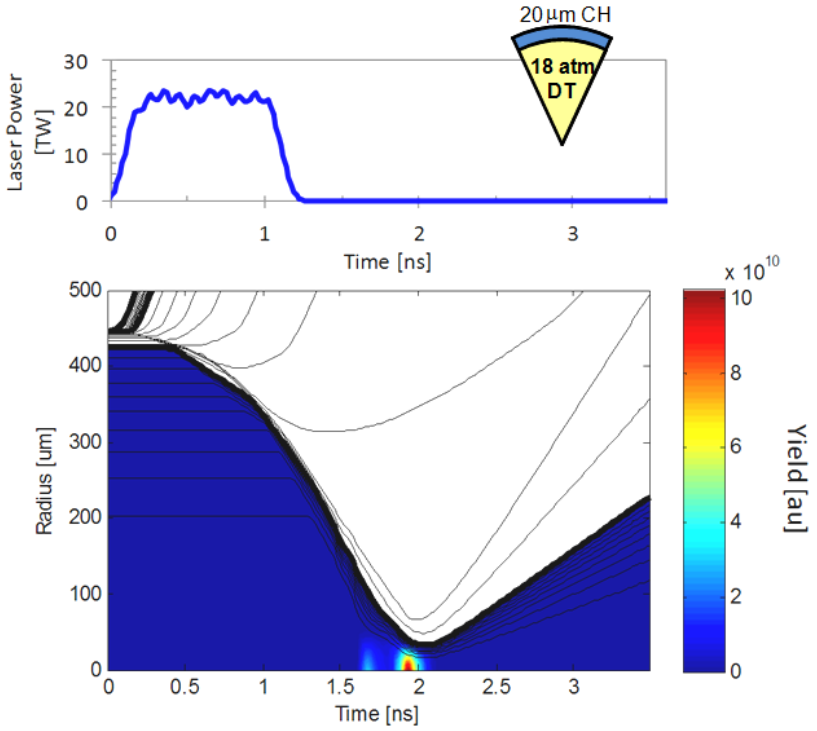

Figure H-22: Top: Laser pulse shape for ablatively-driven shot 55983, showing the laser power in TW, as a function of time in ns. Bottom: Simulated capsule radius as a function of time. The burn profile as a function of radius and time is also plotted.

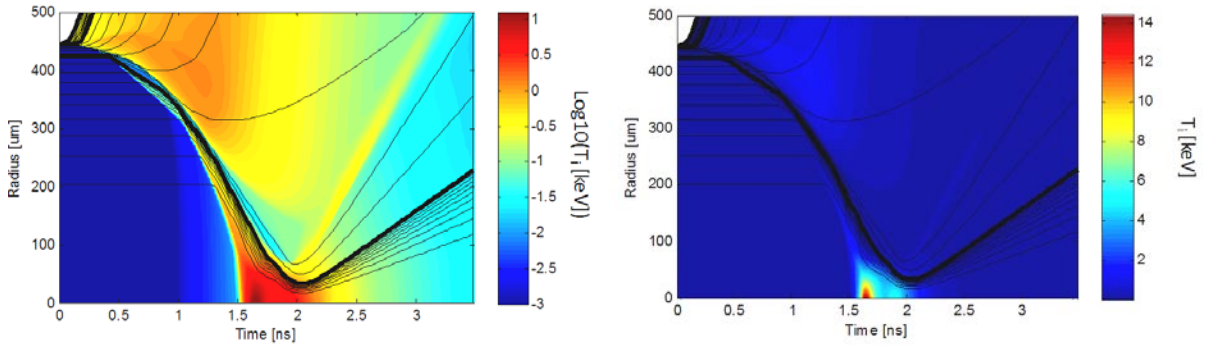

Figure H-23: Simulated ion temperature profile as a function of time for shot 55983.

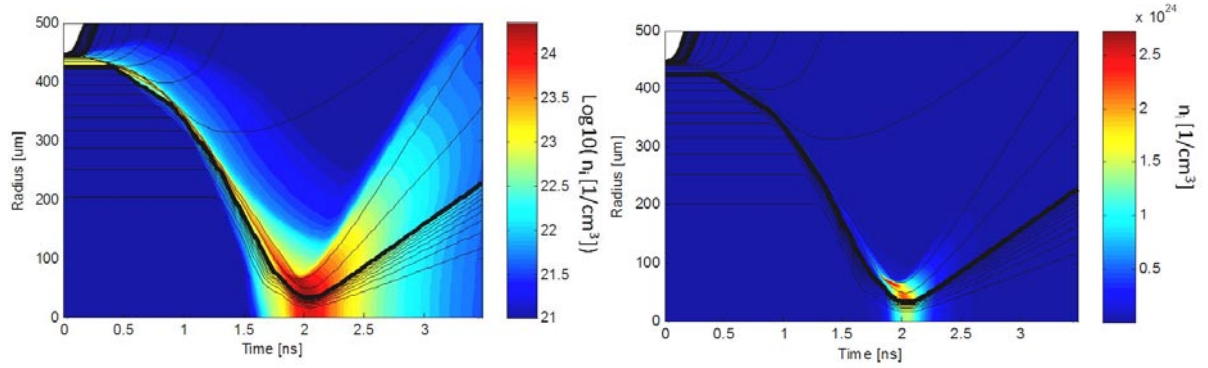

Figure H-24: Simulated ion density profile as a function of radius and time for shot 55983.

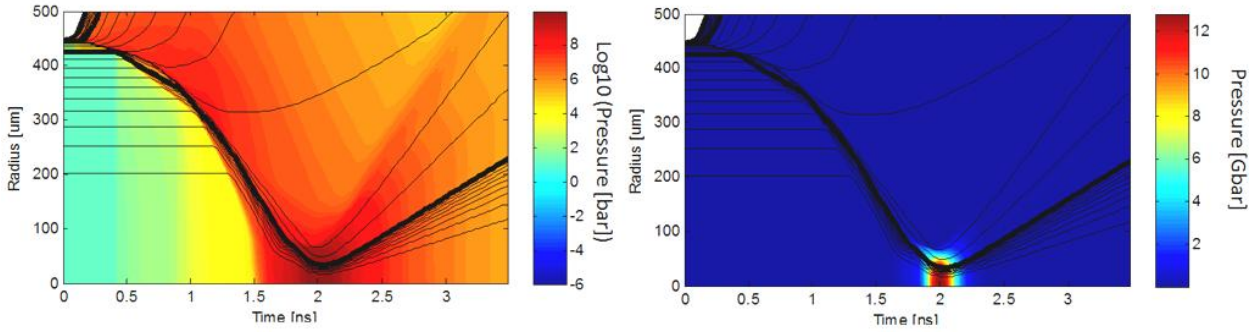

Figure H-25: Simulated pressure profile as a function of radius and time for shot 55983

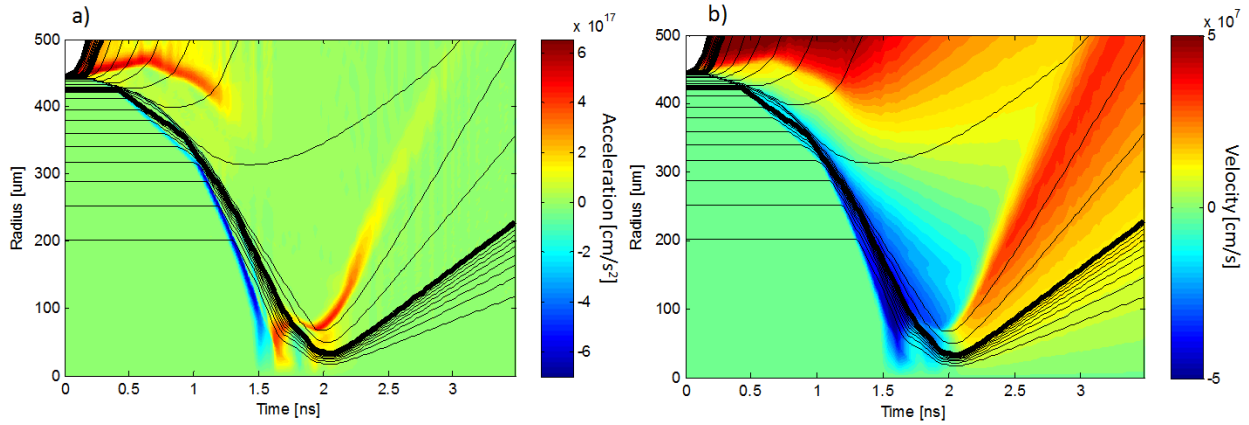

Figure H-26: Simulated acceleration (a) and velocity (b) profiles as a function of radius and time for shot 55983

H.3 Cryogenic DT implosion

In a low-adiabat cryogenic implosion, triple picket laser pulses in front of the main drive are often used. These pickets are designed to begin compressing the shell (as discussed Chapter 2) before the main pulse drives the implosion to maximum compression. This implosion also utilizes a thin 10.5μm CD ablator, followed by a 55.9μm cryogenic DT ice layer, filled to ~650 atm of DT gas. The total capsule radius was 438μm. The short hand notation for this target type is: CD[10.5]DT(55.9). The lower plot shows the simulated trajectories of different fluid elements (of fixed mass) during the implosion. The thick black curve at largest radius is the outer CD ablator boundary. The second thick black curve is the DT ice-shell boundary, and the third inner-most thick black curve is the DT gas boundary. The first picket at ~0.1ns begins ablating the outer CD layer and sends a shock through the DT ice that starts at 0.3ns. The second picket at 0.9ns launches a second shock, which travels faster than the first shock (because of higher temperature generated by the first shock). The third picket at ~1.6ns launches a third and even faster shock. The shocks from the three pickets approximately coalesce and break out of the DT ice shell at ~2.1ns. The shell begins to decelerate at around 3.6ns and peak compression and heating of the gas occur at ~3.8ns. The 1D LILAC simulation for shot 55952 is shown in Figure H-27 through Figure H-31.

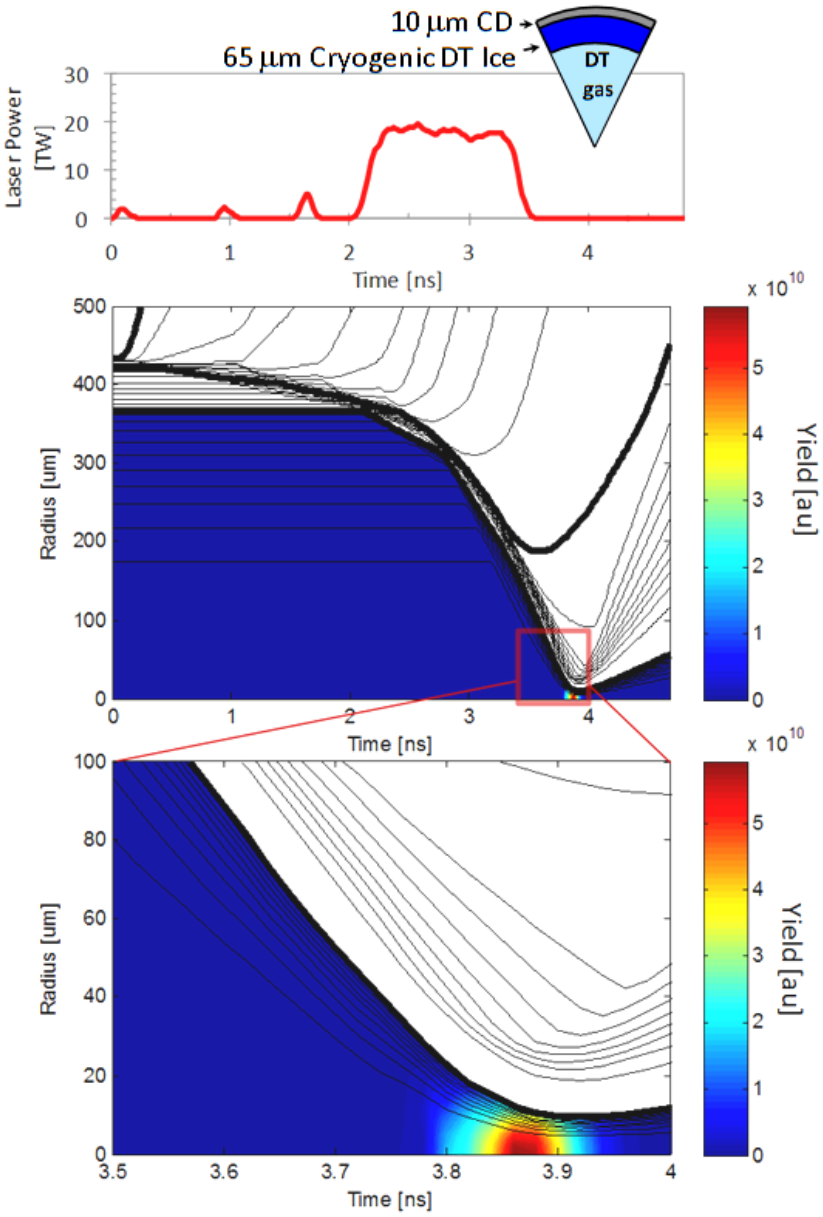

Figure H-27: Top: Laser pulse shape for cryogenic DT shot 55952, showing the laser power in TW, as a function of time in ns. Bottom: Simulated capsule radius as a function of time. The burn profile as a function of radius and time is also plotted. This implosion is discussed extensively in Chapter 7.

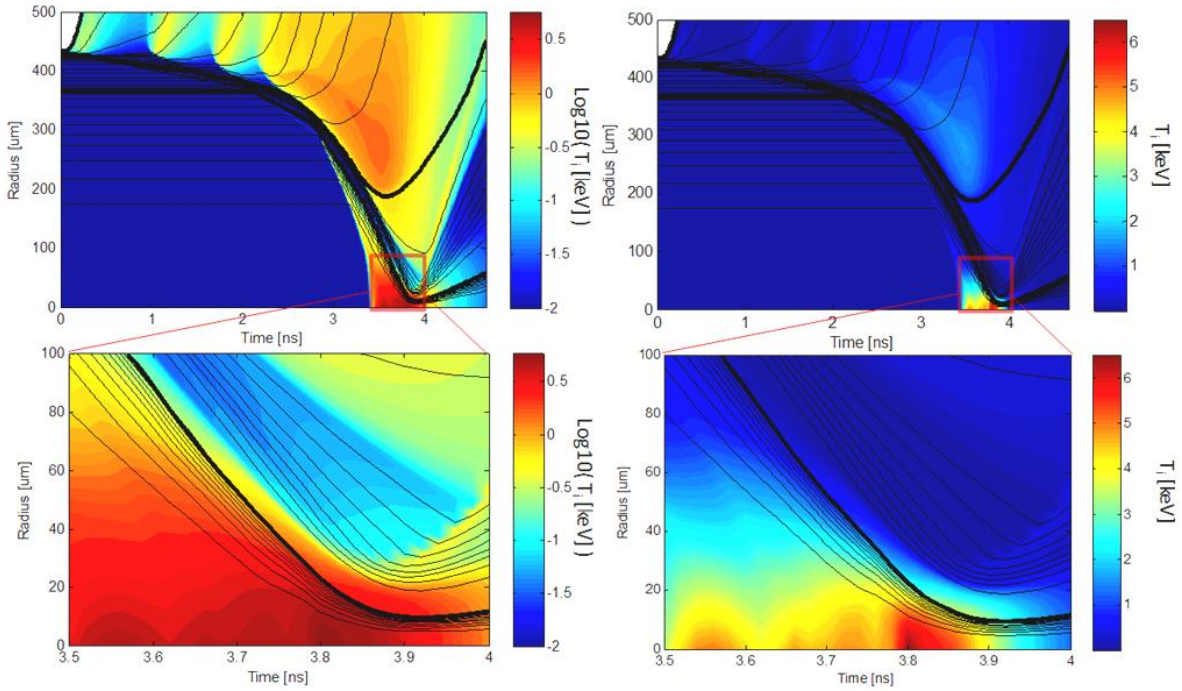

Figure H-28: Simulated ion temperature profile as a function of radius and time for shot 55952.

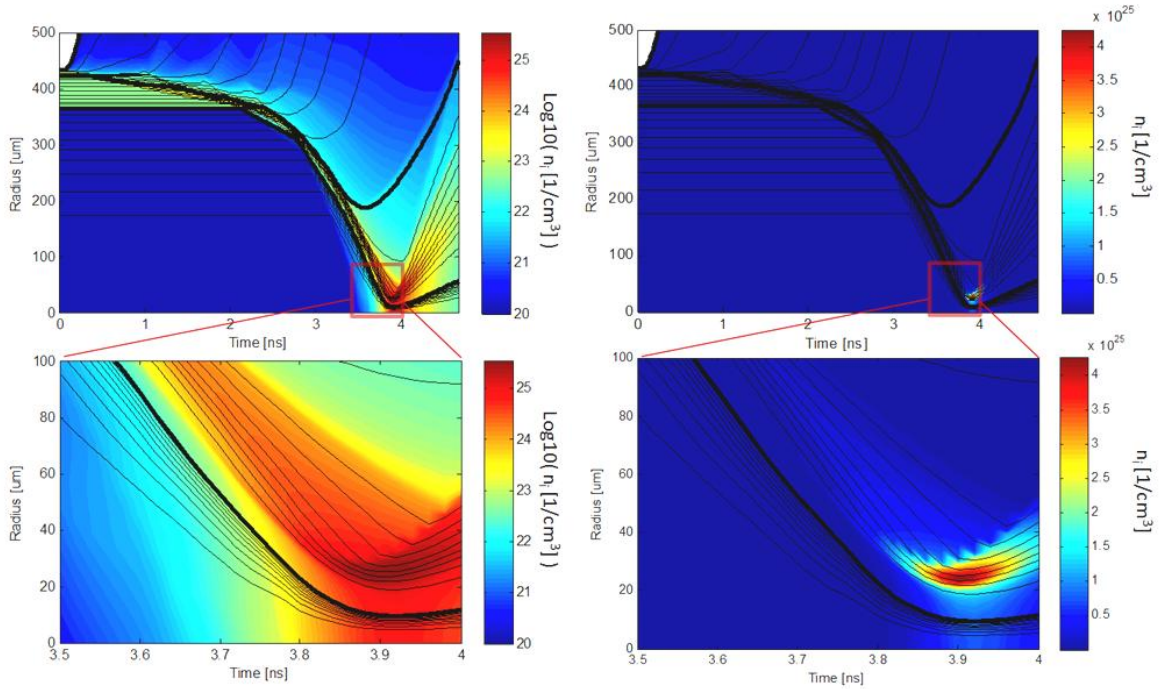

Figure H-29: Simulated ion density profile as a function of radius and time for shot 55952.

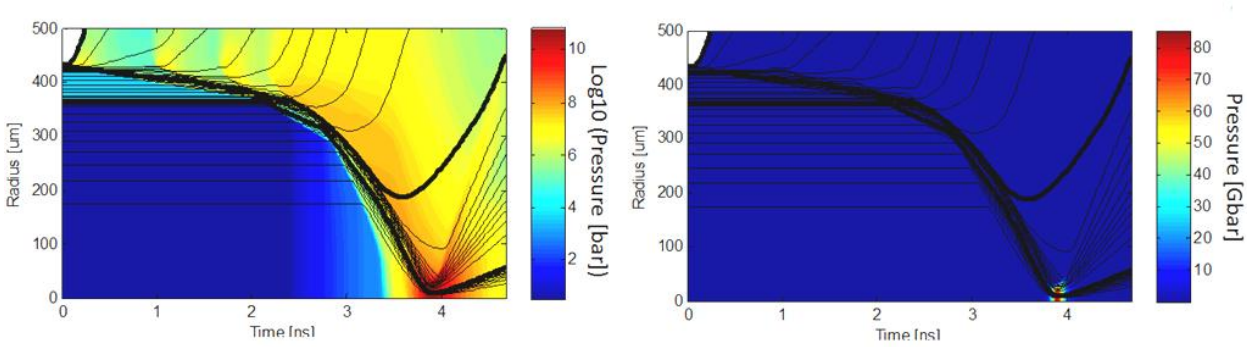

Figure H-30: Simulated pressure profile as a function of radius and time for shot 55952.

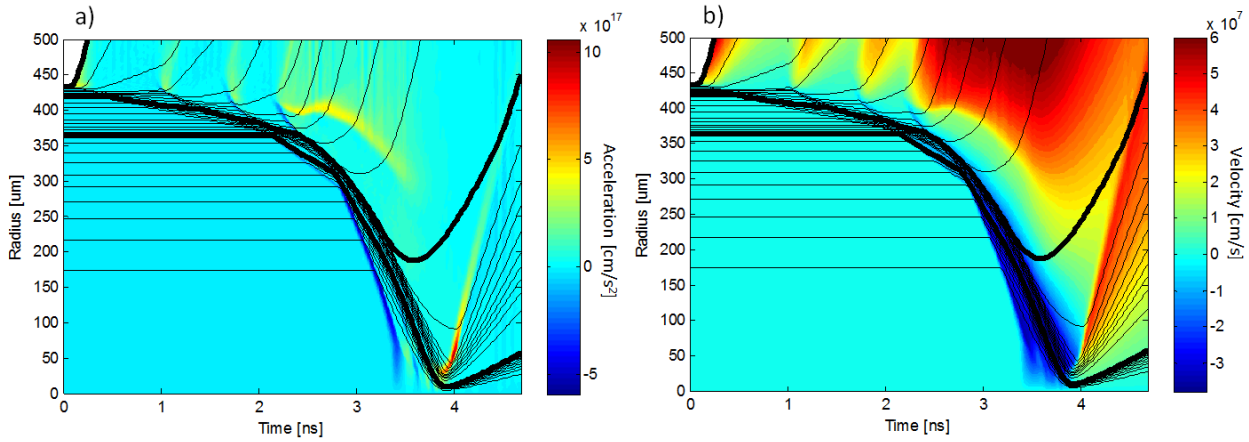

Figure H-31: Simulated acceleration (a) and velocity (b) profiles as a function of radius and time for shot 55952.